THE APPLICATION OF NON-THERMAL PLASMA-CATALYSIS IN FISCHER-TROPSCH SYNTHESIS AT HIGH PRESSURE

by

Byron B. Govender

BSc. Eng. (Chemical)

University of KwaZulu-Natal

Submitted in fulfilment of the academic requirements for the degree of Master of Science in Engineering (Chemical) in the School of Engineering; College of Agriculture, Engineering and Science; University of KwaZulu-Natal, Durban, South Africa.

June 2016

Supervisor: Professor D. Ramjugernath

Co-supervisor: Dr. S. A. Iwarere

DECLARATION

This dissertation constitutes my master's research undertaken in the Thermodynamic Research Unit, School of Engineering, at the University of KwaZulu-Natal, Durban from August 2013 to June 2016 under the supervision of Professor D. Ramjugernath and Dr S. A. Iwarere.

I declare that:

i. This dissertation except where otherwise indicated is my original work.
ii. The written expressions are in my own words, and where other written sources have been quoted, then:
    (a) their words have been re-written but the general information attributed to them has been referenced;
    (b) where their exact words have been used, their writing has been placed inside quotation marks, and referenced.

_____

B. B. Govender

As the candidate's supervisors, we approved this thesis for submission.

_____ _____

Professor. D. Ramjugernath Dr S. A. Iwarere

ACKNOWLEDEMENTS

This work could only have been realised with the assistance of several individuals and groups, to whom I am indebted. I wish to thank:

- The Department of Science and Technology (DST) and the National Research Fund (NRF) for funding this research project.
- My supervisor, Professor D. Ramjugernath. I appreciate your advice, feedback and endless expertise over the years. It has been an honour being a member of this research group.
- My co-supervisor, Dr S. A. Iwarere. Thank you for introducing me to this incredible field of plasma chemistry. I appreciate your patient guidance and always being willing to share your knowledge. Thank you for continuously availing yourself in the laboratory, and encouraging and assisting me when experiments and equipment were not co-operative.
- Dr A. Lebouvier. Your advice in the initial stages of this project was extremely helpful.
- Fiona Higginson. Thank you for proof reading my dissertation draft. Your journalistic editing expertise was invaluable.
- The postgraduate students at UKZN Westville Campus Chemistry Department: Sandeeran, Hari, Aziz, Shamla and Drushen, as well as Professor. H. Friedrich. Thank you for accommodating me in your labs and for those several discussions that helped focus my catalyst research.
- Our chief lab technician, Ayanda Khanyile. Your 'Tony Stark/Iron man' troubleshooting lab skills saved my project several times.
- The workshop technicians, Leon Augustine, Danny Padayachee and Sanjay Deeraj. Thank you for fabricating and modifying the equipment needed for this project.
- The instrument technicians at the Microscopy and Microanalysis Unit (MMU), Vishal Bharuth, Subashen Naidu and Phillip Christopher, and the XRD instrument technician, Pat Suthan; I appreciate your professional assistance with those expensive instruments.
- Colleagues at the Thermodynamics Research Unit (TRU), especially my office mate and friend Travis. You made this project a rested experience.
- Friends and band members at church. I am grateful for your prayer, encouragement and music.
- My friends: Veeran, Wesley, Peter and Ricardo. Thank you guys for keeping me sane.
- My family: Mum, Dad, Kathleen and Cherisse. Thank you for everything you have done for me. I truly appreciate your unfailing support and encouragement of my education and dreams.
- Jesus Christ, my friend and everything else. Without you I am nothing and through you I can do all things.

LIST OF CONFERENCES

The findings reported here were presented at the following international conferences:

- Govender, B.B., Iwarere, S.A. and Ramjugernath, D., "The application of low current non-thermal plasma-catalysis in Fischer-Tropsch synthesis at very high pressure: the effect of pressure on hydrocarbon product yields", Proceedings of the 22nd International Symposium on Plasma Chemistry (ISPC-2015), Antwerp, Belgium, 5-10 July 2015. [Full manuscript, peer reviewed].
- Govender, B.B., Iwarere, S.A. and Ramjugernath, D., "The application of low current non-thermal plasma-catalysis in Fischer-Tropsch synthesis at very high pressure: the effect of current on hydrocarbon product yields and energy efficiency", Proceedings of the 22nd International Symposium on Plasma Chemistry (ISPC-2015), Antwerp, Belgium, 5-10 July 2015. [Full manuscript, peer reviewed].
- Govender, B.B., Iwarere, S.A. and Ramjugernath, D., "The Application of High Pressure Plasma-Catalysis in Fischer-Tropsch Synthesis and Dry Reforming of Methane", Proceedings of the International Conference on Chemical Thermodynamics/South African Institute of Chemical Engineers National Conference (ICCT/SAIChE 2014), Durban, South Africa, 27 July-01 August 2014. [Abstract, peer reviewed].

The following manuscripts, encompassing the content of this dissertation, have been prepared for publication in plasma-related peer-reviewed journals:

- Govender, B.B., Iwarere, S.A. and Ramjugernath, D., "The application of non-thermal plasma-catalysis in Fischer-Tropsch synthesis at very high pressure". [Manuscript in preparation for submission to "Catalysis Science and Technology"].
- Govender, B.B., Iwarere, S.A. and Ramjugernath, D., "The application of non-thermal plasma-catalysis in Fischer-Tropsch synthesis at very high pressure: the effect of cobalt catalyst loading". [Manuscript in preparation for submission to "Catalysis Science and Technology"].

ABSTRACT

Until recently, when several studies demonstrated that non-thermal plasmas (NTPs) can be ignited and sustained in an arc discharge reactor at high pressures (P > 1MPa), weakly ionized or non-thermal plasmas (NTPs) generated at low currents (I < 1A), have been limited to ignition at low to atmospheric pressures (P ≤ 0.1 MPa). This innovation, obtaining ignition at high pressure, was as a result of technological developments. The new technology has been applied in non-reactive and reactive systems, such as in dry reforming of methane, fluorocarbon synthesis and Fischer-Tropsch synthesis, but no work has been reported on incorporating a catalyst in a high pressure arc reactor (high pressure plasma-catalysis), a synergy which shows promise in atmospheric pressure NTP applications. This, therefore, might be the first study to explore plasma-catalysis at high pressure, which, in turn, is harnessed to induce Fischer-Tropsch synthesis (FTS) - the leading industrial process for producing synthetic transportation fuels from natural gas or coal-derived synthetic gas (H_2 + CO).

Plasma-catalytic FTS using a Co-based catalyst, representative of an industrial FTS catalyst, was investigated. The primary objective was to improve product yields and energy consumption of pure plasma FTS (no catalyst) at various operating conditions, namely pressure (1 to 10 MPa), current (250 to 450 mA) and inter-electrode gap (0.5 to 2 mm). An additional objective was to determine the influence of different cobalt catalyst loadings on these performance factors. Finally, in an attempt to elaborate on potential plasma-catalytic interactions, the following catalyst characterisation tools were leveraged: Transmission electron microscopy (TEM), scanning electron microscopy (SEM), energy dispersive x-ray (EDX) and x-ray diffraction (XRD).

The catalyst employed in plasma-catalysis was formulated by coating active components onto a pre-formed mullite (72 wt%-Al_2O_3/SiO_2) ceramic substrate, designed and fabricated to fit precisely into the reactor. The mullite substrate was firstly washcoated with 5 wt%-γ-Al_2O_3, followed by the impregnation of 0 (blank catalyst), 2 or 6 wt% Co by wet incipient impregnation, calcination and reduction. After reduction, the catalyst was inserted into an arc discharge reactor capable of operating up to 20 MPa. The reactor was filled with syngas with a fixed H_2/CO ratio of 2.2:1, similar to that in conventional FTS. This was followed by ignition and stretching of the discharge to the desired inter-electrode gap, which was sustained by a high voltage DC power supply for a treatment period of up to 60 s.

The major hydrocarbon products were obtained in trace quantities due to the arc discharge (reactive) volume being more than 30 000 times less than the batch reactor volume. These gaseous C_1-C_3 hydrocarbons were

synthesized for pure plasma and plasma-catalytic FTS in the general order: methane >> ethane > ethylene > propane > propylene. The highest C_1-C_3 hydrocarbon yields were obtained for the cobalt catalytic systems in the order: 6 wt% Co > 2 wt% Co >> pure plasma > blank, results which extended to most operating conditions. The optimum chain growth conditions for the 2 and 6 wt% Co catalysts were: (i) 10 MPa at 10 s and 2 MPa at 60 s for the pressure variation study (0.5 to 10 MPa); (ii) 250 mA for the current variation study (200 to 450 mA) and; (iii) 2 mm for the inter-electrode gap variation study (0.5 to 2 mm).

The inter-electrode gap was the most influential operating parameter on hydrocarbon production and energy consumption, followed by current and pressure. Therefore, at the widest inter-electrode gap of 2 mm, the methane, ethane, ethylene and propane concentrations of 22 424 (2.24 mol%), 517, 101, 79 and 19 ppm, respectively, for the 6 wt% Co catalyst were 1.5, 1.5, 0.8 and 4 times greater than the 2 wt% Co catalyst concentrations and were 227, 210, 278, 1353 times greater than that of the pure plasma concentrations. In addition, the 6 wt% Co catalyst (specific required energy: 265 $MJ/mol_{methane,prod}$) used ~107 times less energy to produce a mole of methane than the pure plasma system.

In addition to the 6 wt% Co catalyst achieving the highest product yields and lowest specific required energy (SRE) values, this catalyst also produced propylene, which was not detected for the 2 wt% Co catalyst studies. These results indicated that the Co catalyst was activated by plasma (in the absence of external heating) to induce FTS reactions and that chain growth was promoted by a higher cobalt loading (as in conventional FTS). In addition, carbon nanotubes were detected on the 6 wt% Co catalyst via transmission electron microscopy (TEM) imaging, indicating further synergistic effects caused by the higher cobalt loading. X-ray diffraction (XRD) showed that graphite was deposited on the blank, 2 and 6 wt% Co catalysts, which is a precursor for carbon nanotube synthesis. Finally, scanning electron microscopy-energy dispersive x-ray (SEM-EDX) analysis revealed that the 2 and 6 wt% Co catalyst surfaces were modified by plasma treatment, producing a more uniform dispersion and possibly reducing cobalt oxides to metallic cobalt due to the reductive syngas environment, which may have contributed to the sustaining of the catalyst activity.

TABLE OF CONTENTS

LIST OF FIGURES

Appendix A: GC CALIBRATION

Appendix C: PRESSURE CALIBRATION

Appendix E: PRESSURE CALIBRATION

LIST OF PHOTOGRAPHS

LIST OF TABLES

Chapter 2: PLASMA-CATALYSIS

Chapter 3: FISCHER-TROPSCH SYNTHESIS

Chapter 4: EQUIPMENT DESCRIPTION

Chapter 5: CATALYST PREPARATION

Chapter 6: RESULTS AND DISCUSSION

Appendix B: EXPERIMENTAL UNCERTAINTIES

NOMENCLATURE

Abbreviations

APGD	Atmospheric pressure glow discharge
DBD	Dielectric barrier discharge
DC	Direct current
C_x	Hydrocarbon containing *x* number of carbon atoms
C_1	Methane
C_2	Ethane/ethylene
C_3	Propane/propylene
CH_x	Methylene monomer
CVD	Chemical vapour deposition
CNT	Carbon nanotube
EDS	Energy dispersive spectroscopy
EDX	Energy dispersive x-ray
FTS	Fischer-Tropsch synthesis
GAT	Glow-to-arc transition
GC	Gas chromatograph
GC-MS	Gas chromatograph mass spectrometer
HTFT	High temperature Fischer-Tropsch
LTE	Local thermal equilibrium
LTFT	Low temperature Fischer-Tropsch
MHD	Magnetohydrodynamic
NTP	Non-thermal plasma
PECVD	Plasma enhanced chemical vapour deposition
SEM	Scanning electron microscopy
TEM	Transmission electron microscopy
TRU	Thermodynamics Research Unit
UKZN	University of KwaZulu-Natal
VOCs	Volatile organic compounds
XRD	X-ray diffraction

Symbols

I	Current [mA]
n	Number of mols
P	Pressure [1MPa = 10 atm]
ppm	parts per million (molar)
R	Universal gas constant [$J.K^{-1}.mol^{-1}$]
SIE	Specific input energy [kJ/mol_{syngas})]
SRE	Specific required energy [$MJ/mol_{methane,prod}$]
T	Temperature [K or ^{o}C]
U	Expanded uncertainty
u	Standard uncertainty
u_c	Combined uncertainty
V	Volume [m^3]
V_{rms}	Root mean square voltage [V]

Chapter 1
INTRODUCTION

Non-thermal plasmas (NTPs) have typically been generated at low current (< 1 A) and atmospheric pressure (0.1 MPa) by electric discharges such as dielectric barrier and corona discharges. NTP generation at low current and very high pressure (P > 1 MPa) has only been recently explored, due to technological advances that enable an arc discharge to be ignited and sustained under high pressure conditions.

The originators of this new arc discharge technology, the plasma research group at Mines ParisTech (Sophia Antipolis, France), envisaged that high pressure NTPs could stimulate specific chemical reactions for use in applications such as lighting, chemistry and chemical synthesis. The research group initially utilized this technology to electrically characterize non-reactive gases. Later, in collaboration with the Thermodynamics Research Unit (TRU) at the University of KwaZulu-Natal (UKZN), they investigated reactive systems, namely dry reforming of methane, fluorocarbon and hydrocarbon synthesis. Hydrocarbon synthesis, in turn, led to the production of gaseous hydrocarbons from syngas (H_2 and CO), which resembled the gaseous products of Fischer-Tropsch synthesis (FTS) – the leading industrial process for producing synthetic transportation fuels (synfuels).

FTS provides a competitive alternative to oil-derived fuels [1], especially in view of the declining oil reserves, fluctuating oil prices and increasing energy demand. FTS synfuels are poised to play a significant role in the global energy mix in the upcoming decades. This is indicated by continued and escalating investments in FTS technology, infrastructure and feedstock exploration by the world's major energy corporations such as Sasol, Shell, ExxonMobil and Chevron [2, 3].

Plasma-based FTS technologies could provide a viable alternative to conventional processes as a result of the rapid reactions promoted by plasma species (seconds to minutes), and a reduction in space and maintenance required by the technology. Hence, the motivation for this research. However, in order to increase the product yields and energy efficiency obtained by two previous pure plasma FTS (no catalyst) investigations, undertaken by Iwarere et al. [4] and Rohani et al. [5], an industrially representative cobalt catalyst will be incorporated into the arc reactor, enabling the study of high pressure plasma-catalytic FTS.

The synergy of plasma and catalyst has shown promise in atmospheric pressure plasma-catalytic applications. In plasma-catalytic dry reforming of methane, the active plasma species generated by the discharge enabled the catalyst to convert the reactants at a much lower temperature compared to pure catalysis, which led to the restriction of catalyst deactivation. In addition, active plasma species have been shown to interact with the catalyst particles, enhancing surface reactions, resulting in higher energy efficiency and product selectivity compared to the pure plasma process. Similar plasma-catalytic interactions are expected in high pressure plasma-catalytic FTS in this work.

1.1 Objectives

FTS will be explored at high pressure (0.5 to 10 MPa) using a low-current arc discharge reactor combined with an industrially representative cobalt catalyst in order to improve the hydrocarbon product yields and energy efficiency of the pure plasma FTS process. This overall objective will be divided into the following three tasks: (i) Catalyst preparation; (ii) pure plasma and plasma-catalytic FTS experiments and; (iii) catalyst characterization.

1.1.1 Catalyst preparation

Due to the novelty of investigating plasma-catalysis at high pressure, the initial objective is to design and prepare a catalyst that will maintain catalytic activity in the high pressure plasma environment while sustaining or positively modifying the arc discharge.

1.1.2 Pure plasma and plasma-catalytic FTS experiments

In preliminary experiments, pure plasma FTS will be tested and compared with the literature. Thereafter, plasma-catalytic FTS will be undertaken using three prepared catalysts, one without cobalt (blank) and two catalysts with different cobalt loadings of 2 and 6 wt%. Multiple catalysts will be used to determine the influence of different cobalt loadings on the product yields and energy performance parameters.

The four systems to be investigated are;

i. Pure plasma (no catalyst);
ii. 5 wt%-γ-Al_2O_3 coated onto a mullite ceramic (no cobalt);
iii. 2 wt%-Co/5 wt%-γ-Al_2O_3 coated onto a mullite ceramic;
iv. 6 wt%-Co/5 wt%-γ-Al_2O_3 coated onto a mullite ceramic.

The performances of these four systems will be compared based on the product yields and energy consumption as functions of three varying operating parameters, which are;

a. Pressure: 0.5 to 10 MPa, for two different reaction times of 10 and 60 s;

b. Current: 250 to 450 mA;
c. Inter-electrode gap: 0.5 to 2 mm.

1.1.3 Catalyst characterization

Finally, the effect of the plasma on the catalyst will be evaluated by the characterization of the catalyst using the following diagnostic tools:

- Transmission electron microscopy (TEM)
- Scanning electron microscopy (SEM)
- Energy dispersive x-ray (EDX)
- X-ray diffraction (XRD)

1.2 Dissertation overview

This dissertation reports on outcomes of the objectives described above, as follows:

- The literature review section is subdivided into two chapters. In Chapter 2, the location of the high pressure arc reactor technology is described within the framework of the non-thermal plasma literature. Subsequently, the synergistic effect of plasma-catalysis in current applications are reviewed. Chapter 3 provides a discussion on Fischer-Tropsch synthesis, entailing a brief review of current industrial activity, chemistry and catalysts utilised
- The experimental section is subdivided into Chapters 4 and 5. Chapter 4 provides a discussion on the arc discharge reactor and peripheral equipment in addition to the experimental procedure. Chapter 5 discusses the various catalyst technologies and preparation techniques used in the literature and the integration and modification of these methods for preparation of the catalyst in this work.
- In Chapter 6, a discussion of the experimental results for pure plasma and plasma-catalytic Fischer-Tropsch synthesis at high pressure under various operating parameters is provided, followed by characterization of the tested catalysts.

Chapter 2
PLASMA-CATALYSIS

Literature review outline

Plasma-catalytic Fischer-Tropsch synthesis (FTS) - the combination of a high pressure (> 1 MPa) non-thermal plasma (NTP) and a cobalt FTS catalyst - is explored in order to improve the product yields and energy efficiency of pure plasma FTS (no catalyst). The literature review (Chapters 2 and 3) addresses the following components encompassing the research topic:

i. Non-thermal plasmas (Chapter 2),
ii. Non-thermal plasma-catalysis or simply plasma-catalysis (Chapter 2) and
iii. Fischer-Tropsch synthesis (Chapter 3).

In Chapter 2, non-thermal plasmas (NTPs) generated at low to atmospheric pressure (Section 2.1) are firstly discussed in order to understand the advancements made in the NTP field, which include the technologies that enabled the generation of high pressure NTPs. Thereafter, works published in the high pressure NTP field are reviewed (Section 2.2), with a focus on applying high pressure NTPs in Fischer-Tropsch synthesis (referred to as pure plasma FTS).

The current research attempts to extend the work of high pressure pure plasma FTS by introducing a cobalt FTS catalyst into the arc discharge reactor (high pressure plasma-catalytic FTS). Therefore, the only known work of plasma-catalytic FTS, undertaken at atmospheric pressure (Section 2.3.1), will be reviewed. However, due to the atmospheric pressure pure plasma FTS work being an exploratory study, it does not provide a detailed account of the plasma-catalytic interactions. Therefore, mature plasma-catalytic processes, pollutant treatment and hydrocarbon reforming, are discussed in Sections 2.3.2 and 2.3.3 in order to understand the interactions that could lead to improved product yields and energy efficiency in high pressure plasma-catalytic FTS. Because these interactions are dependent on the catalyst configuration, a brief review of the various plasma-catalytic configurations is provided in Section 2.3.4. Chapter 2 (Section 2.3.5) concludes with the consideration of the above-mentioned plasma-catalytic topics and their potential applicability in the current study.

In Chapter 3, a suitable catalyst for plasma-catalytic FTS will be screened from those used in conventional FTS. In addition, the industrial FTS trends, operating conditions, and reaction mechanisms are briefly discussed, in order to provide further insight into the influence of the catalyst in plasma-catalytic FTS interactions.

2.1 Non-thermal plasmas: Low to atmospheric pressure

Non-thermal plasmas (NTPs) generated by electric discharges are a branch of plasmas that are weakly ionised due to generation at low currents (I < 1A), and low to atmospheric pressures (P ≤ 0.1 MPa). As a result, the plasma is far from thermal equilibrium (or is in a state of non-equilibrium) in which the electrons have high temperatures in the range of 1–10 eV (10 000 to 100 000 K) and the bulk gas is close to ambient temperature.

The location of NTPs in the field of plasmas is illustrated in Figure 2.1, which also highlights the application of NTPs in Fischer-Tropsch synthesis (FTS) at atmospheric and high pressures, which will be discussed later.

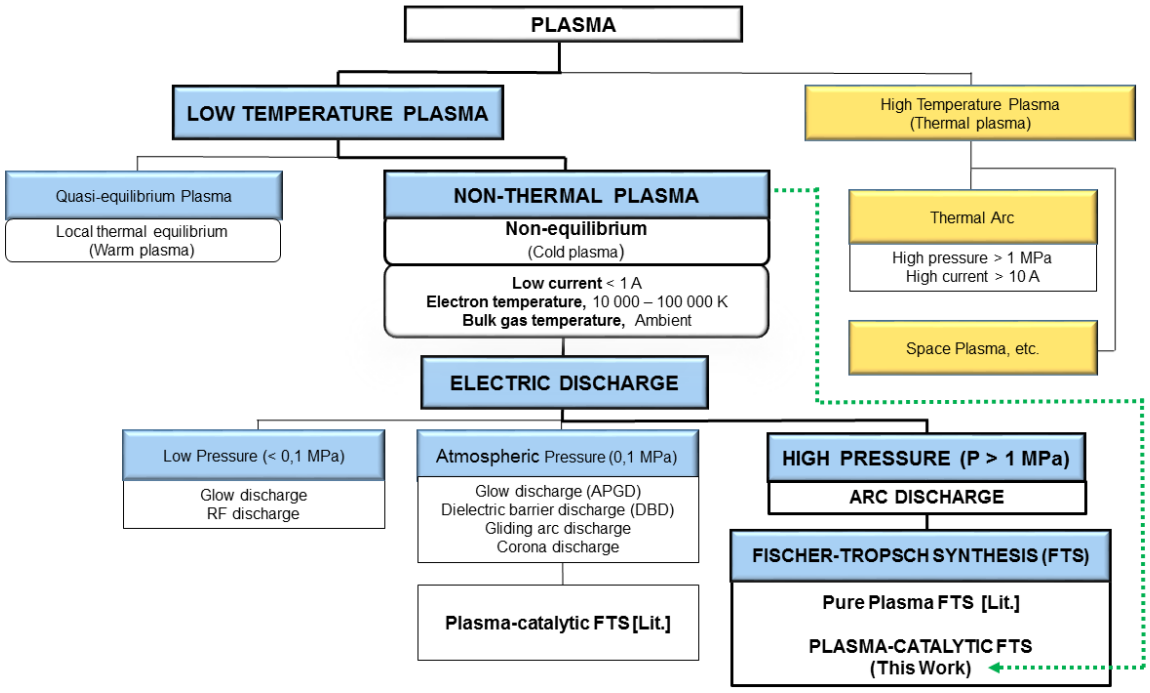

Figure 2.1: Hierarchy diagram of non-thermal plasmas (NTPs) generated using electric discharges at different pressures, and their applications in Fischer-Tropsch synthesis (FTS).

The non-equilibrium properties of NTPs, mentioned above, have been harnessed to promote specific chemical reactions in various fields including chemical production, pollutant treatment, surface

modification and lighting. These NTP applications are listed in Table 2.1, along with the discharges used to generate the NTPs. The characteristics of the discharges are governed by the operating pressure, amongst other factors, such as electrode geometry.

Table 2.1: Low and atmospheric pressure NTP applications and associated discharges.

Category	**Application**	**Discharge**
Chemical production	Methanol production	Corona [6], DBD [7]
	Hydrocarbon reforming	DBD [8]
	Oxidation reactions	RF [9]
	Industrial ozone production	DBD [10]
Pollutant treatment	Aromatic pollutants	Corona [11], DBD [12]
	Aliphatic pollutants	DBD (FPD) [13-15]
	Halogenated pollutants	[16-18]
	Inorganic pollutants (NO_x, SO_2 and H_2S)	DBD [19], corona [20]
Surface modification	Heat-sensitive polymers and biological tissues	RF [21], APGD [22], DBD [23, 24]
	Synthetic fabrics (manufacture of clothing)	Corona [25]
	Etching/deposition processes (micro-electronics)	RF [26]
	Thin-film deposition	DBD [27, 28]
	Substrate and surface cleaning	DBD [29]
	Catalyst modification	DBD [30] and others [30-35]
Lighting	Fluorescent lamps	Glow [36-38]
	High-power CO_2 lasers	DBD [39]
	Ultraviolet lamps	DBD [40]
	Plasma display panels	DBD [41]

At low (sub-atmospheric) pressure, glow and radio frequency (RF) discharges are formed, and at atmospheric pressure, atmospheric pressure glow discharge (APGD), corona, gliding arc and dielectric barrier discharges are ignited.

NTP generation has been limited to low and atmospheric pressure due to the constraints imposed by Paschen's Law [42-48]. The law describes the dependency of the breakdown voltage (minimum voltage required for electric breakdown of a gas), on the product of the operating pressure and discharge gap length, shown in equation 2.1 below.

$$V_b \approx P \times d \tag{2.1}$$

For atmospheric pressure NTPs, the discharge gap ranges between millimetres and centimetres, which provides a relatively large treatment volume, incentivising their use in industrial applications [49]. However, at pressures near and beyond atmospheric pressure, the plasma approaches thermal equilibrium as the electron and bulk gas temperature begin to homogenise as illustrated in Figure 2.2. By further increasing the pressure, the plasma tends closer towards a thermal equilibrium state, eventually forming a thermal (strongly ionised) plasma, which is known as a thermal arc when coupled with a flow of gas. Thermal arcs are typically generated at high currents (> 10 A) in order to sustain the thermal nature at high pressures [50-55], with applications in various industrial sectors including aerospace engineering [56].

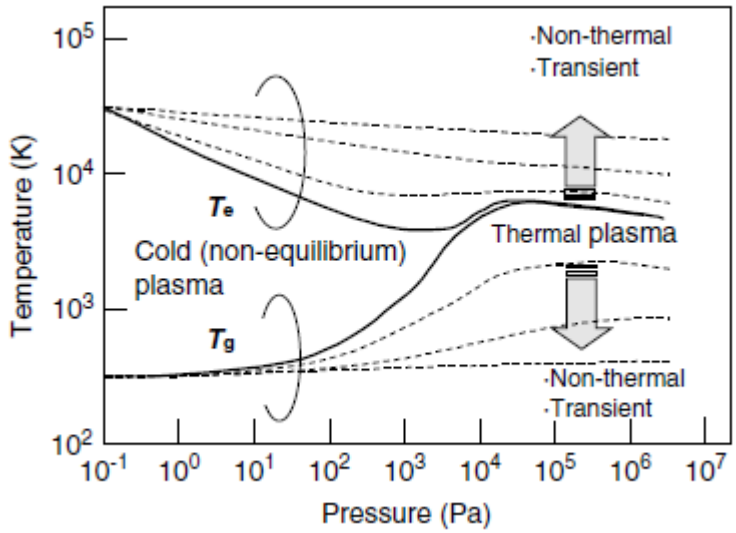

Figure 2.2: Bulk gas and electron temperature as a function of gas pressure in plasmas (extracted from [57]). (N.B. 10^5 Pa = 0.1 MPa = 1 bar).

Due to their thermal-equilibrium nature, thermal plasmas possess more thermal energy than NTPs. This can lead to the destruction of targeted chemical species, amongst other undesired effects. In contrast, NTPs have the ability to selectively induce specific chemical and physical reactions at ambient temperature and low input power. Hence the appeal of NTPs in industrial applications and the desire to produce them at high pressures.

In order to produce a NTP above atmospheric pressure, and to avoid the formation of a thermal plasma, the discharge gap had to be reduced in accordance with Paschen's law. Researchers reduced the discharge gap to the micrometre range [57], forming a branch of NTPs known as microplasmas. The resulting extremely narrow discharge gap enabled microplasmas to maintain their NTP nature at high pressure (> 1 MPa) and low current (< 1 A).

Besides microplasmas, another route for generating high pressure NTPs was realised in the mid-2000s as a result of advances in plasma reactor technology; advances such as electrode materials, high pressure reactor materials of construction, power supply and reactor gas tightness. These innovations led to the design and construction of an arc discharge reactor (by the plasma research group at Mines ParisTech, in Sophia Antipolis, France), that had the capability of igniting and sustaining a non-thermal arc discharge at low currents (< 1A), high pressures (> 1 MPa) and at wider discharge gaps (up to 2.5 mm) than microplasmas,

The main feature of the arc discharge reactor was a mobile anode that enabled a variable discharge gap. To ignite a discharge, the mobile anode was initially in contact with a fixed cathode i.e. no inter-electrode gap. Subsequently, the anode was manually retracted to the desired inter-electrode gap via an axial positioning system. The system of extending the arc discharge gap from an anode-cathode contact point, enabled ignition at high pressures up to 15 MPa, thus overcoming the constraints imposed by Paschen's law. A similar arc discharge will be used to undertake plasma-catalytic Fischer-Tropsch synthesis in this work. Published studies undertaken using the arc reactor technology will be discussed in the next section.

2.2 Non-thermal plasmas: High pressure (review)

Preliminary experiments using the high pressure arc discharge reactor investigated the electrical behaviour and sustainability of an arc discharge in the presence of various non-reactive gases, namely, pure argon [58], argon/H_2 mixture [59] and pure helium [60]. The operating conditions used in these studies are listed in Table 2.2.

Two important findings were obtained from the non-reactive studies. Firstly, the results showed that an inert gas arc discharge could be ignited and sustained at pressures up to 15 MPa at low currents (≤ 500 mA), with the stability of the arc improving above 5 MPa. Secondly, operating condition ranges (particularly current and inter-electrode gap), were obtained, which revealed the operable ranges and the limitations of the technology.

Table 2.2: High pressure non-thermal plasma (NTP) applications using a recently developed arc discharge reactor.

System	Feed gas ratio	Pressure (MPa)	Current (mA)[a]	Inter-electrode gap (mm)	Discharge time[b] (s)	Reaction products	Year	Author
			Non-reactive systems					
Ar	-	≤ 10	0.1-500	-	-	-	2008	Izquierdo et al. [58][c]
H_2/Ar	H_2/Ar (0, 0.33, 1.4 and 2)	≤ 14	≤ 400 mA	0.5-1.5	-	-	2009	Izquierdo et al. [59][c]
He	-	0.1-15	250-400	0.25-2.5	-	-	2010	Fulcheri et al. [60][d]
			Reactive systems					
Hydrocarbon (Fischer-Tropsch) synthesis (H_2 + CO)	H_2/CO (4:1) / 40% He	2.2	350	1.25	100	C_1-C_2 hydrocarbons	2011	Rohani et al. [5][d]
	H_2/CO (2.2:1)	0.5-15	350	1	60	C_1-C_3 hydrocarbons	2014	Iwarere et al. [4][d]
	H_2/CO (2.2:1)	5	200-400	1	60	C_1-C_3 hydrocarbons	2014	Iwarere et al. [4][d]
Fluorocarbon synthesis (CF_4)	CF_4/He (2/3)	2	350	0.4	80	C_2F_6 and C_3F_8	2014	Iwarere et al. [61][d]
Dry reforming of methane (CH_4 + CO_2)	CH_4/CO_2 (1.8:1)	0.5-7.8	350	0.4	60	Syngas (H_2 + CO), C_2-C_3 hydrocarbons	2015	Iwarere et al. [62][d]

[a] The ignition voltage was typically 8 kV, [b] denotes a continuous treatment period, [c] previous reactor prototypes, [d] current reactor prototype.

The above mentioned factors, pertaining to non-reactive systems, provided crucial information that enabled the application of the arc discharge in reactive systems. The reactive systems investigated were hydrocarbon synthesis [4, 5], dry reforming of methane [62] and fluorocarbon synthesis [61]. These studies showed that chemical species can be successfully synthesised in the high pressure NTP environment. The products obtained for each process are listed in Table 2.2.

All reactive studies produced interesting results; however, hydrocarbon (Fischer-Tropsch) synthesis is discussed in detail as this process is the focus of the current research. Fischer-Tropsch synthesis (FTS) was explored using the high pressure arc discharge technology due to the positive influence of high pressure (2 to 4 MPa) in conventional Fischer-Tropsch synthesis (FTS). In conventional FTS, an increase in pressure, usually in the range of 1 to 6 MPa [63, 64], favoured the formation of heavier hydrocarbon products [65]. A detailed discussion of conventional FTS is provided in Chapter 3.

Utilising similar operating conditions to conventional FTS in the arc discharge reactor, Rohani et al. [5] and Iwarere et al. [4] produced hydrocarbons resembling that of FTS. Rohani et al. [13] conducted the first FTS experiments. They produced minute quantities (ppm range) of methane, ethane and ethylene from syngas with a H_2/CO ratio of 4:1 diluted with 40% helium at a fixed pressure of 2.2 MPa and current of 350 mA. Different treatment modes were investigated: a continuous treatment period of 100 s and two different intermittent treatment periods (treatment-relaxation cycles). The results of the continuous treatment mode are presented in Table 2.2.

Subsequently, Iwarere et al. [14] studied a wider pressure range than Rohani et al. [5] of 0.5 to 15 MPa at a fixed current of 350 mA, inter-electrode gap of 1 mm, continuous discharge period of 60 s and H_2/CO ratio of 2.2:1. They also varied current between 200 to 400 mA at a fixed pressure of 0.5 MPa and inter-electrode gap of 1 mm. They found that the concentrations of C_1-C_3 hydrocarbons increased with increasing pressure and decreasing current with the optimal hydrocarbon yields and energy efficiency coinciding at 12 MPa for the pressure study and at 200 mA for the current study.

The two FTS studies showed that hydrocarbon chain growth was promoted by very high pressure operation and that hydrocarbons could be synthesised using pure plasma without the presence of a conventional FTS catalyst.

This work attempts to increase the product yields and improve the energy efficiency of the high pressure non-thermal plasma FTS explored by Rohani et al. [5] and Iwarere et al. [4], by incorporating an industrially representative FTS catalyst in the high pressure arc discharge reactor - a hybrid process commonly known

as plasma-catalysis. Plasma-catalysis, which was recently applied in FTS at atmospheric pressure, is reviewed in Section 2.3.

2.3 Plasma-catalysis

2.3.1 Plasma-catalytic FTS at atmospheric pressure

Plasma-catalysis applied in FTS has only been conducted at near atmospheric pressure by Al-Harassi et al. [66]. They used a catalyst that was comprised of Cu/Co coated onto an Al_2SiO_5 ceramic foam monolith, which was crushed and inserted into the annular discharge gap of a coaxial DBD reactor. Plasma-catalytic FTS and pure catalytic FTS (no plasma) were investigated in order to determine the dependency of CO conversion and hydrocarbon product selectivities on variable operating parameters such as input power (50 to 90 W), H_2/CO ratio (0.33 to 1) and pressure (1 to 6 bar or 0.1 to 0.6 MPa).

In the plasma-catalytic FTS study using a Cu/Co, an increase in pressure (0.1 to 0.6 MPa) and H_2/CO ratio (0.5 to 2) led to an increase in the selectivity of C_{2-4} and C_{5+} hydrocarbons, verifying the influence of pressure on chain growth. It was also reported that no methane was produced in plasma-catalytic FTS under all variable conditions tested; whereas under pure catalytic conditions (230ºC, 6 bar, no plasma), which were more representative of conventional FTS conditions, a methane selectivity of up to 42% was obtained using a similar Cu/Co catalyst. The suppression of methane formation and improved chain growth by plasma-catalytic compared to pure catalytic FTS revealed the positive contribution of plasma to the catalytic process at atmospheric pressure.

However, Al-Harassi et al. [66] did not investigate pure plasma FTS – plasma-assisted FTS without a catalyst present – which was investigated by Iwarere et al. [4] and Rohani et al. [5] at high pressure, and is also investigated in this work. Due to this limitation and the exploratory nature of the novel study by Al-Harassi et al., they could not determine the influence of the catalyst on the plasma, and therefore the plasma-catalytic interactions could not be fully described.

Consequently, more mature plasma-catalytic applications are reviewed in Sections 2.3.2 and 2.3.3 in order to gain a more comprehensive understanding of these interactions, which could be responsible for improved chain growth in the present high pressure plasma-catalytic FTS study.

2.3.2 Plasma-catalytic synergy

In the previous section it was shown by Al-Harassi et al. [66] that atmospheric pressure plasma-catalytic FTS improved certain performance factors of pure catalytic FTS (no plasma). This improvement by plasma-

catalysis over the pure catalytic process is referred to as the synergistic effect of plasma-catalysis. The synergy between the plasma and catalyst has also led to improvements over the pure plasma process (no catalyst) or the sum or product of the pure plasma and pure catalytic processes. Hence, the attractiveness of plasma-catalysis over the pure processes.

Positive synergistic effects have also been reported in several other plasma-catalytic applications; most notably, pollutant treatment and hydrocarbon reforming. A few examples showcasing the synergy between the plasma and catalyst in these applications are discussed below.

Pollutant treatment

In trichloroethylene (TCE) removal, Vandenbroucke et al. [67] found that when coupling a DC glow discharge with a post-plasma located Pd/γ-Al_2O_3 catalyst, 12 to 22% more TCE was decomposed than compared to the product of the pure plasma and pure catalyst systems. When Whitehead [68] coupled plasma with a TiO_2 catalyst, a threefold increase in the destruction of toluene was achieved compared to the sum of the individual plasma and catalytic processes. Chae et al. [69] found that the pure plasma treatment of air was harmful to humans due to the formation of CO and ozone, which was reduced by factors of 10 and 5, respectively, when a catalyst was present, revealing plasma-catalysis as a promising method for indoor air control.

Hydrocarbon reforming

Bromberg et al. [70] investigated the reforming of ethanol and bio-oils using a low-current plasmatron combined with ceramic-supported and metal catalysts. They obtained higher conversion rates, and in one case, double the hydrogen yields than the corresponding pure plasma reforming process. Whitehead and co-workers [71, 72] observed that the methane conversion and hydrogen yields almost doubled when a nickel-based catalyst was introduced to an atmospheric pressure DBD plasma.

The complex interactions between the plasma and catalyst are the source of the synergistic effect revealed in the above studies. These interactions are discussed in Section 2.3.3 as they may describe the potential interactions in plasma-catalytic FTS in the current communication.

2.3.3 Plasma-catalytic interactions

The plasma-catalytic synergistic effect, usually observed as improvements in the process selectivity and energy efficiency, mainly arises from the interactions between the short-lived NTP species and catalyst surface [73]. These interactions have been known to modify both the plasma and catalyst properties [74,

75]. The individual roles of the plasma and catalyst in plasma-catalytic interactions and the resulting plasma/catalyst modifications are discussed in Sections 2.3.3.1 and 2.3.3.2.

2.3.3.1 The influence of the plasma in plasma-catalysis

Catalyst activation

In plasma-catalysis, the pre-dissociation of the reactants by the high voltage discharge enables the catalyst to adsorb the reactants (usually the rate limiting step) and desorb the products at a much lower temperature compared to pure catalysis [75-77]. Many studies indicated that the higher internal energies of the pre-dissociated species (such as radicals, etc.) in plasma-catalysis (compared to the stable ground-state molecules in conventional catalysis), are responsible for lowering the catalyst activation temperature [78-83].

Plasma-catalytic dry reforming of methane, combining a Ni, Ni-Ca or Rh catalyst and a DBD reactor, was effective at relatively low temperatures between 40 and 230^{o}C; whereas pure catalytic experiments and thermodynamic equilibrium calculations showed that there should be no production of syngas below 300^{o}C [8]. Similar temperature reductions were observed in several other reforming investigations [84-86]. In some plasma-catalytic reforming cases, NTPs have been proven to decrease the catalyst activity temperature from 750^{o}C (required in pure catalysis) to as low as ambient temperature [87, 88].

The significantly lower catalyst temperature in dry reforming of methane, as a result of the pre-dissociation of CO_2 and CH_4 reactant molecules, has been reported to reduce the carbon deposition on the catalyst surface and increase the catalyst lifetime [75, 76]. The lowering of the catalyst activation temperature was also observed in plasma-catalytic pollutant treatment processes such as methane [89] and toluene [90] oxidation.

Several other catalyst activation routes arising from plasma species interactions have been reported in plasma-catalytic pollutant processing. These activation routes include: local heating, UV, activation of lattice oxygen, variations in work function, formation of electron-hole pairs and the interaction of radicals with adsorbed pollutants [91].

Catalyst surface properties

In addition to influencing the catalyst temperature, the active plasma species have been believed to electrically charge the catalyst particles or form micro-discharges in the catalyst pores; thus modifying the

catalyst surface and enhancing its chemisorption properties for the promotion of additional surface reaction pathways, which can influence product selectivities and distribution [35].

In addition to enhancing the chemisorption catalytic properties, the active plasma species in NTPs have also been employed to enhance the dispersion of the active catalytic materials in catalyst preparation processes [92, 93]. For instance, in toluene removal, Mn_3O_4 was formed when a Mn_2O_3 catalyst was exposed to a DBD discharge for an extended period [94]. In another toluene process, an alumina supported Pd catalyst exposed to plasma formed new active catalytic sites such as stable Al-O-O* in the alumina pores [95]. It was also shown that the catalytic surface area and structure could be modified via plasma exposure [92, 94, 96]. Catalysts preparation methods using plasmas have been comprehensively reviewed by Kizling et al. [97] and Liu et al. [35].

As discussed in this section, plasma species contribute to plasma-catalysis in several ways, including lowering the activation temperature, enhancing adsorption properties and improving the dispersion of active catalytic materials. The next section describes the role of a catalyst in plasma-catalysis.

2.3.3.2 The influence of the catalyst in plasma-catalysis

The introduction of a solid catalyst in a plasma discharge region resembles some of the effects of dielectric materials in a DBD reactor, in which the type of dielectric barrier materials and the geometry of the material inserted between the electrodes have been used to control the electron energy and adjust the electrical properties of the generated NTP for use in specific applications [98]. For instance, the insertion of ferroelectric pellets between the dielectric-covered electrodes in DBD reactors, known as ferroelectric packed discharge (FPD), was shown to amplify the electric field by a factor of 10 to 250 [99], thus generating higher energetic electrons in the discharge region.

Discharge properties

In a similar manner to DBDs, the introduction of a metal catalyst in the discharge zone of a plasma reactor can enhance the electrical properties such as the electric field strength, etc., thus varying the composition of the plasma species [100]. The plasma properties may also be modified by the catalyst, changing the discharge nature; for example, from filamentary to surface charges in the case of DBDs [100].

Modifications of the discharge nature may arise from increasing the catalyst surface area, altering the catalyst oxidation state, reducing the metal oxides to the metallic state, activating the catalyst by photo irradiation, forming hotspots that may possibly lead to thermal activation of the catalyst and decreasing the

activation energy barrier [74]. These factors have been investigated by various researchers. Kim et al. [101] indicated that hot spot formation in a catalyst bed can occur due to localized heating by strong micro-discharges that run along the boundaries of adjacent pellets. Cheng et al. [102] reported that NiO could be reduced to Ni in an argon glow discharge.

Discharge residence time

In addition to the catalyst influencing the discharge nature, the effect of the catalyst porosity on the discharge residence time was observed. Roland et al. [103] found that in plasma-catalytic pollutant treatment, the porosity of the Al_2O_3 and SiO_2 catalytic materials, compared to non-porous materials, enhanced the oxidation of the VOCS (toluene and phenol), as well as the resulting CO_2/CO selectivity. The enhancement was suggested to arise from the short-lived species, such as atomic oxygen, being adsorbed in the catalyst pores, indicating that the porosity promoted the pre-concentration (adsorption) of plasma VOC species on the catalyst surface.

It is believed that the adsorption of plasma species on the catalyst surface (pores) increases their concentration and residence time in the discharge zone [73, 104], leading to enhanced collisional activity and conversion [103, 104]. Similar effects of catalyst porosity were suggested to enhance pollutant removal in other studies [73, 105].

Product Selectivity

The catalyst in plasma-catalysis can also reduce the activation energy barrier of the rate limiting step and aid in directing the selectivity of the process towards the desired products [74], which are typical roles of the catalyst in traditional (pure) catalysis. Tao et al. [106] found that in plasma-catalytic reforming of toluene, the plasma improved the toluene decomposition rate while the Ni/SiO_2 reforming catalyst focused the reaction towards H_2 and CO formation.

Process energy efficiency

The electric field on the catalyst surface, modified by the plasma species (discussed in Section 2.3.3.1), may, in turn, enhance the plasma electric field, potentially sustaining or increasing the non-equilibrium properties of the plasma and improving the energy efficiency [74, 75].

Plasma-catalytic decomposition of benzene with a Ag/TiO_2 catalyst was reported to significantly improve the energy efficiency compared to the pure plasma process [101]. Van Durme et al. [107] also reported an improvement in the energy efficiency in comparison to the pure plasma process. Chao et al. [108] reported

that the energy efficiency for the plasma-catalytic partial oxidation of methane was ~20 % higher than a methane-fueled gas turbine. They additionally found that the catalyst temperature was maintained by the plasma-heated gas as well as by the exothermic nature of the reaction.

The various effects of the catalyst in plasma-catalysis were discussed above. A summary of the individual contributions of the plasma and catalyst in plasma-catalysis, discussed in Sections 2.3.3.1 and 2.3.3.2, are listed in Table 2.3. These plasma-catalytic interactions could be responsible for higher product yields and energy efficiency in plasma-catalytic FTS, discussed in Chapter 6.

Table 2.3: A summary of the individual roles of the plasma and catalyst in plasma-catalysis.

Influence of plasma on catalyst	**Influence of catalyst on plasma**
Lower catalyst activation temperature	Enhance discharge electric field
Thermally activate (heat) catalyst	Modify discharge/plasma nature
Improve catalytic chemisorption	Increase concentration of plasma species in discharge zone
Reduce active catalytic material	Increase residence time of plasma species in discharge zone
Disperse active catalyst material	
Increase catalyst work function	

Because a major objective in the present study is the preparation of a FTS catalyst and its configuration within an arc discharge reactor, various configurations of catalyst within plasma reactors are discussed in Section 2.3.4.

2.3.4 Plasma-catalytic configurations

The plasma-catalytic interactions and synergistic effects, described in the previous sections, strongly depend on the configuration of the catalyst in the plasma reactor. The catalyst configuration factors to be considered are the form of the catalyst used (Section 2.3.4.1) and the location of the catalyst in the discharge chamber (Section 2.3.4.2). These factors will be carefully examined in order to determine the most suitable form and arrangement of the catalyst in the arc discharge reactor in the current research.

2.3.4.1 Forms of catalyst

A catalyst is typically inserted into a plasma reactor in several forms: Packed bed (comprised of pellets or powder) [80, 109], foam [110], honeycomb monolith [111], powder layer or coating on the reactor walls/ electrodes [112]. These various catalyst forms are illustrated in Figure 2.3.

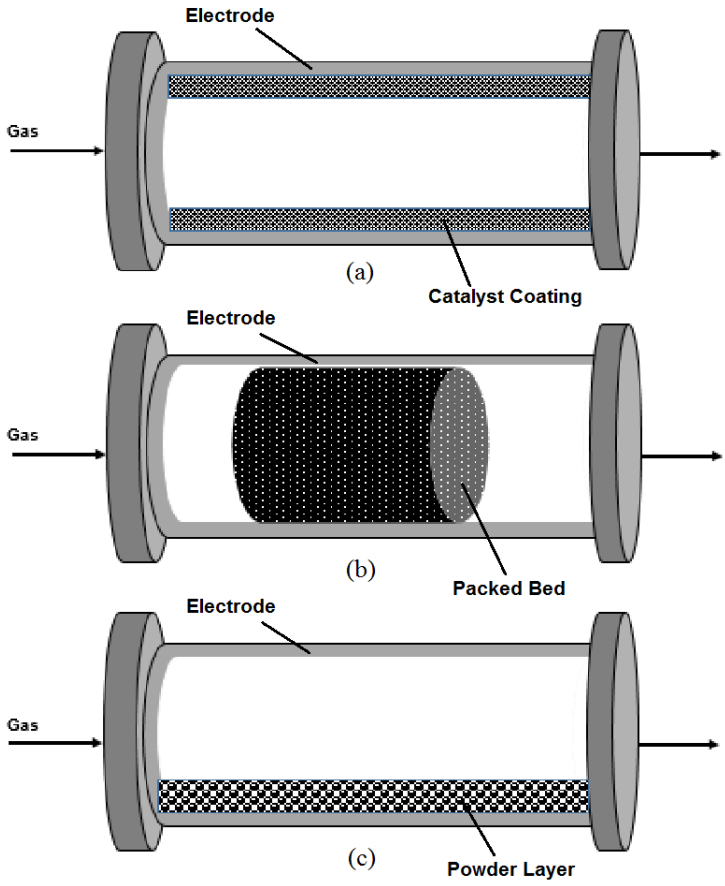

Figure 2.3: Different forms of catalysts used in plasma-catalytic applications;
(a) coated catalyst, (b) packed bed and (c) powder catalyst.

2.3.4.2 Arrangement of catalyst

In addition to the physical form of catalyst, there are two common arrangements of the catalyst within the plasma reactor in terms of proximity to the discharge zone [75, 109]: In-plasma catalysis and post plasma catalysis.

(i) In-plasma catalysis (IPC)

In in-plasma catalysis (IPC), illustrated in Figure 2.4.b, the solid catalyst is introduced into the discharge region of the reactor allowing direct contact and interaction between the catalyst and plasma. The complex

plasma-interactions described in Sections 2.3.3.1 and 2.3.3.2 are usually associated with IPC due to the direct exposure of catalyst particles to the active plasma species, especially short-lived plasma species (excited species, radicals, ions and photons) [68].

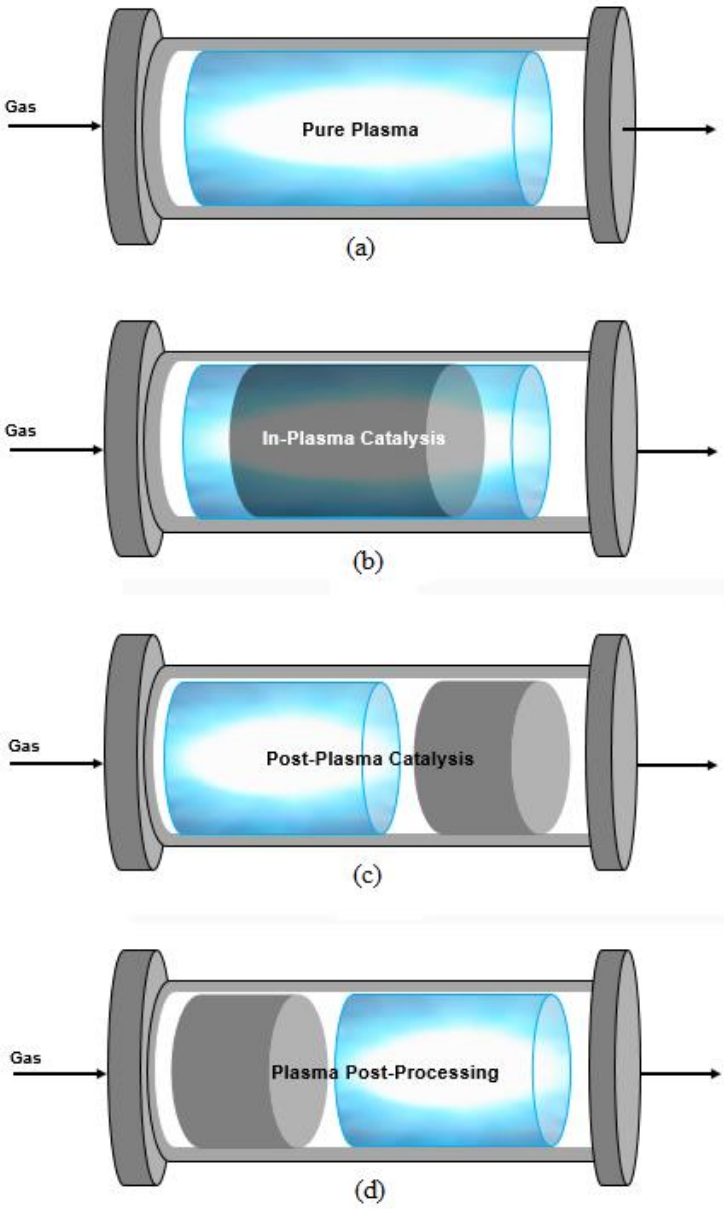

Figure 2.4: Different arrangements of catalysts in plasma-catalytic applications; (a) pure plasma, (b) in-plasma catalysis (IPC), (c) post-plasma catalysis (PPC) and (d) plasma post-processing.

Several other terms are used in the literature for the IPC configuration: single-stage plasma-catalysis (SPC) [100], plasma-driven catalysis (PDC) [113], combined plasma-catalysis (CPC) [114, 115], in-plasma catalysis reactor (IPCR) [73] or plasma and catalyst integrated technologies (PACT) [116].

(ii) Post-plasma catalysis (PPC)

In post-plasma catalysis (PPC), illustrated in Figure 2.4.c, the catalyst is introduced at a distance downstream or upstream of the discharge zone and usually has no direct contact with the discharge itself. The catalyst is only exposed to the plasma-generated end-products, long lifetime plasma intermediate species (for example ozone in plasma-processing of pollutants) and vibrationally excited species, which are all suggested to participate in plasma-chemical reactions [68]. However, Chen et al. [77] reported that the lifetime of vibrationally excited species are between 1 and 100 ns at atmospheric pressure, which is too short for catalytic interaction in the PPC configuration. Other terms used for the PPC configuration include: Two-stage plasma-catalysis (TPC) [100], plasma-enhanced catalysis (PEC) [113] and post-plasma catalysis reactor (PPCR) [73].

Wang et al. [84] investigated the IPC and PCC catalyst arrangements using a Ni/Al_2O_3 commercial catalyst and dielectric barrier discharge (DBD) for dry reforming of methane. Three different contact modes between the catalyst and the plasma were studied in which the catalyst was placed either 15 mm away from the discharge region (PPC), at the boundary of the discharge zone or directly in the discharge zone (IPC). Reactant conversion and selectivity results showed that the synergistic effect was only achieved when the catalyst was loaded directly into the annular discharge gap (IPC), indicating the advantage of this configuration in reforming processes.

Despite the advantages of the IPC configuration in certain processes, the complexity of the arc discharge reactor internals and the hybrid nature of the arc discharge (existing at non-thermal and local thermal equilibrium) used in the current study, does not permit either a stringent IPC or PCC arrangement of the catalyst, but requires a variation of these configurations, which is extensively described in Chapter 5.

2.3.5 Plasma-catalysis in this work (objectives)

In view of the benefits arising from the combination of a plasma and catalyst, as discussed in Section 2.3, it is anticipated that plasma-catalysis applied in FTS under high pressure, in this work, will improve hydrocarbon production and reduce energy consumption beyond that of pure plasma FTS. In order to test this proposition, both pure plasma and plasma-catalytic FTS will be used to investigate the influence of three operating parameters - pressure (0.5 to 10 MPa), current (200 to 450 mA) and inter-electrode gap (0.5

to 2 mm) - on hydrocarbon yields and energy consumption. A similar high pressure arc discharge reactor to that previously tested by Iwarere et al. [4] (discussed in Section 2.2) will be used.

In pure plasma FTS it is expected that the arc discharge should be solely accountable for hydrocarbon synthesis, whereas in plasma-catalytic FTS, synthesis will be enhanced by the interaction between the arc discharge and industrially representative Co/Al_2O_3 FTS catalyst.

In order to better understand the interactions between the cobalt catalyst and plasma in the current work, the role of the cobalt catalyst in conventional FTS will be discussed in the next chapter. Chapter 3 also includes a discussion of the current and future industrial FTS trends, industrial catalyst technologies and process chemistry. These topics will provide support for the method of catalyst selection and the preparation techniques discussed in Chapter 5. It will also provide a framework for evaluating the performance of the cobalt catalyst in plasma-catalytic FTS in Chapter 6.

Chapter 3
FISCHER-TROPSCH SYNTHESIS

As discussed in Chapter 2, the only known studies of Fischer-Tropsch synthesis (FTS), induced by non-thermal plasmas (NTPs), have been high pressure pure plasma FTS (no catalyst) using an arc discharge reactor [4, 5], and atmospheric pressure plasma-catalytic FTS using a combination of a DBD discharge and Co/Cu catalyst [66]. The arc discharge reactor technology used in high pressure pure plasma FTS [4, 5] will be used to investigate high pressure plasma-catalytic FTS in the current study, with the anticipation that introducing an industrially representative catalyst into the discharge zone will improve product yields and energy efficiency.

Since an industrially representative catalyst will be employed in plasma-catalytic FTS, it is beneficial to understand the role of various catalysts in conventional FTS. These and other relevant topics are reviewed in Chapter 3, which focuses on the following themes: Chemistry and major FTS products (Section 3.3), industrial catalysts (Section 3.4), operating conditions (Section 3.5) and catalytic surface mechanisms (Section 3.6). Emphasis is given to the cobalt catalyst, which is to be screened from several other FTS catalysts for use in high pressure plasma-catalytic FTS. But firstly, the need for FTS in the global energy mix (Section 3.1) and the current and future trends (Section 3.2) are discussed.

In each section, conventional FTS trends are discussed in relation to the results obtained in high pressure pure plasma FTS undertaken by Iwarere et al. [4], herein simply referred to as pure plasma FTS. Moreover, both of the conventional and pure plasma FTS trends are used to predict the performance of plasma-catalytic FTS in Chapter 6.

3.1 The importance of FTS in the global energy mix

Diversification of the global energy mix is desirable from a political, commercial and environmental perspective. A promising, contemporary alternative to oil-derived transportation fuels is synthetic fuels (or synfuels) produced by Fischer-Tropsch synthesis (FTS). FTS fuels are competitive with oil-derived fuels for several reasons.

Firstly, the FTS process is capable of converting syngas ($CO + H_2$), generated by the reforming of carbon-based feedstocks such as natural gas, coal or biomass, into a wide range of hydrocarbons. The hydrocarbon

products are easily refined into end-products, namely gasoline, diesel, wax and other liquid products. In industry, both reforming and FTS operations are incorporated in the same facility. It is known as a gas-to-liquid (GTL) facility when natural gas is the feedstock; and a coal-to-liquid (CTL) facility when coal is the feedstock.

GTL processes, using natural gas - the lowest cost feedstock [117] - is becoming more viable due to technological developments that enable extraction of natural gas reserves at remote sites, which are however considered too confined for liquefied natural gas (LNG) operations or pipeline (stranded gas) projects [1]. Moreover, at higher oil to natural gas cost ratios [118], which seems to be the current trend, GTL conversion operations become more feasible.

Secondly, FTS products are of high quality and are free of contaminants, such as sulphur, nitrogen and aromatic compounds, all found in petroleum products [1].

Finally, since FTS-derived fuels possess similar properties to oil-derived petroleum fuels, they can be blended with petroleum fuels [119] and can employ existing petroleum-based transportation, storage and refueling infrastructure, and they are compatible with current vehicular technologies [1].

The above factors motivate continued investment in the FTS industry by the world's major energy corporations. The activities of these corporations are discussed in Section 3.2, along with the current and future industry and research trends.

3.2 Development of FTS

Fischer-Tropsch (FT) synthetic fuel has been an alternative to oil-derived fuels for around 90 years. It was discovered in the early 1920s [120] and patented in 1925 [121] by German chemists Franz Fischer and Hans Tropsch. Commercial production began from 1935 and by the 1940s, 600 kilotons per annum of liquid fuels were produced using cobalt-based catalysts [122, 123].

In the 1950s, Sasol, a South African energy company, adopted the process for two major reasons. Firstly, to reduce the county's dependence on foreign oil as a result of isolation and sanctions during the apartheid era. Secondly, the process was profitable due to the country's abundant coal resources. Sasol has since been a major developer of the process and associated technologies [123]. FTS synthetic fuels (or synfuels) are currently produced in South Africa from coal by Sasol and from natural gas by PetroSA, both leaders in the

global FTS synfuel industry. In the future, it is expected that the technological contributions of these companies will drive development and growth in Africa [1].

Apart from South Africa's utilization of FTS synfuels, global interest was renewed during the oil crisis of the 1970s, which prompted extensive developments in FTS technologies for converting coal and natural gas into synfuels [123, 124]. The major FTS plants that emerged from that period, and operational developments, are listed in Table 3.1.

Besides research and industrial investment in FTS towards the production of automobile transportation fuels, governmental institutions have recently investigated synfuel uses in other sectors. Since the beginning of this decade, attention has turned to the production of FTS synthetic jetfuels as alternative fuels for use in commercial [125] and military aviation [126, 127]. In addition, the National Aeronautics and Space Administration (NASA) has been researching the FTS middle distillate (C_8-C_{18} hydrocarbons) for use in aerospace technologies [128, 129].

Industrial and research interests in FTS, and its role in the global energy mix, discussed in Sections 3.1 and 3.2, provided impetus for research and development of alternative production methods. Non-thermal plasma-based technologies are considered to provide a viable alternative to conventional FTS technologies. The small-sized plasma reactors are likely to reduce equipment and space costs, and the short reaction periods may potentially lower operating costs. The current research in plasma-catalytic FTS could therefore provide insight into the practicality of a plasma-based process.

In the next section, the reaction chemistry and product distribution of conventional FTS are discussed, as similar reactions and products are anticipated in plasma-catalytic FTS.

Table 3.1: Present and future GTL (FTS) operations [2, 3].

Company	Country	Technology	Production rate (bpd)	Investment (bn. USD)	Start-up year
PetroSA	South Africa	Sasol's slurry phase technology	20 000	1.5	1992
Shell Bintulu	Malaysia	Shell middle distillate synthesis (SMDS) fixed-bed technology	15 000	0.85	1993
Sasol/Qatar Petroleum, in alliance with Chevron, Oryx GTL	Qatar	Sasol's slurry phase technology	34 000	-	2005
Chevron Nigeria (Sasol/Chevron alliance) and Nigeria National Petroleum Company	Nigeria	Sasol's slurry phase technology	34 000	-	2007
Shell and Qatar Petroleum, Pearl GTL	Qatar	Shell middle distillate synthesis (SMDS) fixed-bed technology	140 000	19	2009
ExxonMobil/Qatar Petroleum	Qatar	Advanced gas conversion for the 21th centure (AGC- 21) technology	154 000	-	2011
Sasol/Chevron/NNPC, Escravos GTL	Nigeria		34 000	8.4	2013
Sasol/Uzbekneftegaz/Petronas GTL	Uzbekistan		38 000	2.5	2016-2017
Sasol, Lake Charles	USA		96 000	16	2018-2019

3.3 General chemistry and selectivity

FTS is a polymerisation process involving the conversion of syngas (H_2 + CO), with a typical H_2/CO feed ratio of 2:1, into a multicomponent mixture of hydrocarbons, oxygenates and water in the presence of a nickel, iron, cobalt or ruthenium catalyst. The main FTS reaction schemes are presented in Table 3.2.

Table 3.2: Main reaction pathways of Fischer-Tropsch synthesis [130-134].

Primary reactions			
Methylene:	$CO + 2H_2 \rightarrow -CH_2 - + H_2O$	ΔH = -165 kJ.mol^{-1} (Fe catalyzed)	(3.1)
Methanation:	$CO + 3H_2 \rightarrow CH_4 + H_2O$	ΔH = -206 kJ.mol^{-1}	(3.2)
Paraffins:	$nCO + (2n + 1)\ H_2 \rightarrow C_nH_{2n+2} + nH_2O$		(3.3)
Olefins:	$nCO + 2n\ H_2 \rightarrow C_nH_{2n} + nH_2O$		(3.4)
Water-gas shift:	$CO + H_2O \leftrightarrow CO_2 + H_2$	ΔH = 41.3 kJ.mol^{-1} (Fe catalyzed)	(3.5)
Secondary reactions			
Alcohols:	$nCO + 2n\ H_2 \rightarrow C_nH_{2n+1}OH + (n-1)H_2O$		(3.6)
Boudouard reaction:	$2CO \rightarrow C_s + CO_2$	ΔH = -172 kJ.mol^{-1}	(3.7)
Catalyst (metal) modification			
Bulk carbide formation:	$yC + xM \rightarrow M_xC_y$		(3.8)
Catalyst oxidation/reduction:	$M_xO_y + yH_2 \leftrightarrow yH_2O + xM$		(3.9)
	$M_xO_y + yCO \leftrightarrow yCO_2 + xM$		(3.10)

M denotes a metal particle.

The FTS selectivity and product distribution based on the reactions listed in Table 3.2 are highly dependent on the type of catalyst used and accompanying reaction conditions. The process selectivity is usually described by the Anderson-Schulz-Flory (ASF) distribution in which FTS is assumed to be an ideal polymerization reaction characterised by a single parameter, the chain growth probability, α. The distribution of n-paraffins, described by the ASF model is shown below [133].

$$m_n = (1-\alpha)\alpha^{n-1} \tag{3.11}$$

Where m_n represents the mole fraction of hydrocarbons of chain length n and α is the chain growth probability, described by:

$$\alpha^{n-1} = \frac{R_p}{R_p + R_t} \tag{3.12}$$

Where the R_p and R_t are the rates of chain propagation and termination respectively. The chain growth probability, dependent on catalyst type and process conditions, determines the hydrocarbon chain length distribution. The distribution is graphically represented in Figure 3.1, which shows a general trend of decreasing selectivity with increasing carbon number, calculated using equation 3.12.

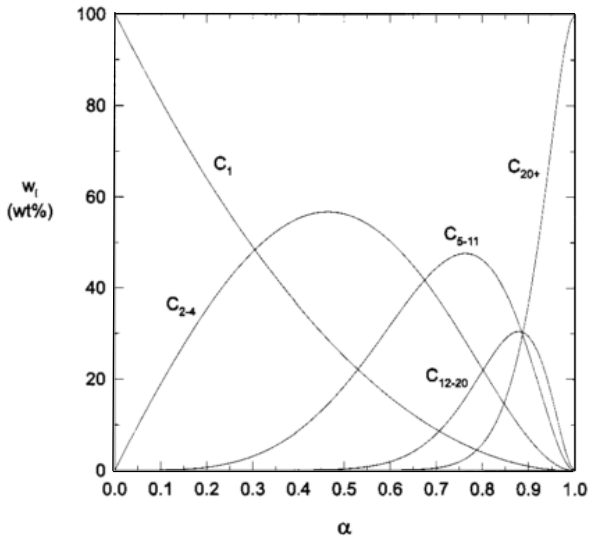

Figure 3.1: The dependence of hydrocarbon selectivity on the chain growth probability, α (extracted from [133]).

Common deviations from the ASF model in industrial practice are high methane [135] and low ethylene [136] yields, arising from the high surface mobility and reactivity of their precursors and the rapid re-adsorption and reinsertion of ethylene to form longer chains [133]. These phenomena, coupled with active plasma species, may explain the high methane concentrations (relative to the C_2 and C_3 hydrocarbons) in high pressure pure plasma FTS, explored by Iwarere and co-workers [4, 5].

The product selectivity and distribution, discussed in this section, are governed by the catalyst type and operating conditions used in conventional FTS. These topics are discussed in Sections 3.4 and 3.5 respectively.

3.4 FTS catalysts

In Section 3.4, the most suitable catalyst for use in plasma-catalytic FTS is screened from the four catalysts tested in conventional FTS: Nickel, iron, cobalt and ruthenium. Nickel catalysts promote methanation, which is undesirable in commercial FTS [137-139], whereas iron, cobalt and ruthenium catalysts promote chain growth to produce higher carbon number paraffins and olefins. Despite ruthenium having the highest

olefin and C_{5+} selectivity, it is too scarce and costly for industrial applications [140]. Therefore, much research and industrial attention has been afforded to iron and cobalt - commercially proven FTS catalysts used by ExxonMobil, Shell, Sasol, Statoil and Chevron.

Sasol employs a Fe-based catalyst in high temperature FTS (300 to 350ºC) or HTFT to produce gasoline comprised of C_5-C_{11} hydrocarbons and a Fe or Co-based catalyst in low temperature FTS (200 to 240ºC) or LTFT to produce higher hydrocarbons including high quality diesel (C_{12}-C_{18} hydrocarbons with a high cetane number) and waxes ($\geq C_{19}$ hydrocarbons) [122-124, 141].

Typical product selectivities for Sasol's low and high temperature FTS processes using an iron catalyst are presented in Table 3.3. FTS using iron catalysts have been extensively reviewed in the literature [142, 143].

Table 3.3: Product selectivities for Sasol processes (data from [63]).

Product	LTFT (Fixed bed)	HTFT (Synthol)
CH_4	4	7
C_2-C_4 olefins	4	24
C_2-C_4 paraffins	4	6
Gasoline (C_5-C_{11})	18	36
Middle distillate	19	12
Heavy oils and waxes	148	9
Water soluble oxygenates	3	6

In contrast to the wide product distribution of the iron and cobalt-based conventional FTS processes, a narrow C_1-C_3 distribution of gaseous products was obtained in pure plasma FTS experiments at high pressure [4, 5]. This is potentially due to the high temperatures in the arc core impeding chain growth. The addition of a cobalt catalyst into the arc discharge reactor in the present study may improve chain growth and increase the product distribution of pure plasma FTS.

So far, nickel and ruthenium catalyst have been eliminated, and cobalt and iron have been considered as potential catalysts for employment in plasma-catalytic FTS. Screening of cobalt and iron is deliberated in the next section.

3.4.1 Cobalt versus iron catalysts

A cobalt catalyst is preferred to iron in this work as it is three times more active [2], provides better selectivity to linear paraffins, has lower water gas shift (WGS) activity and offers a longer catalyst lifetime (more resistant to deactivation) [134, 144]. In addition, the anticipated operating conditions in plasma-catalytic FTS – pressures up to 10 MPa and operating temperatures around 25ºC (due to the catalyst bed not being externally heated in the arc discharge reactor) – are more suited to cobalt. This arises from cobalt catalyst working at higher pressures (up to 4 MPa) and lower temperatures (225ºC) than iron catalyst (2 MPa and 340ºC) in conventional FTS [134].

Furthermore, the required H_2/CO ratio for a cobalt catalyst is 2.15 [132, 140], which is similar to the ratio of 2.2 used by Iwarere et al. [4] in high pressure pure plasma FTS. In contrast, the ratio for an iron catalyst is usually < 2 but has ranges between 1.7-2.5 [140]. In addition, in industrial FTS (GTL) plants, cobalt is favoured over cheaper iron when natural gas is the feedstock as syngas with a high H_2/CO ratio is produced, thus eliminating the need for generating additional hydrogen by the Fe-promoted WGS reaction [118].

The several similarities, of operating parameters, between conventional FTS and pure plasma FTS mentioned in Section 3.4.1, support the selection of a cobalt catalyst in plasma-catalytic FTS. Various cobalt catalyst formulations will be touched upon in Section 3.4.2, providing a direction for catalyst preparation in Chapter 5.

3.4.2 Cobalt catalyst formulation

The major focus of industrial cobalt catalyst formulation and operation is to improve catalyst activity and stability, which are dependent on the cobalt loading, dispersion and reduction, as well as the support and promoters used. Various combinations of cobalt loadings, promoters and supports have been extensively tested for the production of proprietary commercial cobalt catalysts. Some of these formulations are discussed here.

Since cobalt is a more expensive transition metal than iron, smaller concentrations, between 15 and 30 wt% [145], are dispersed onto a high surface area refractory support (Al_2O_3, SiO_2 or TiO_2) in order to reduce metal usage; whereas ≤ 60 wt% iron is used in bulk iron catalyst. However, lower cobalt loadings, between 0 and 10wt%, are anticipated in these initial studies of high pressure plasma-catalytic FTS in order to understand the influence of the cobalt catalyst on plasma. If the results show promise, higher cobalt loadings should be investigated in the future.

In addition to the refractory oxide support (Al_2O_3, SiO_2 or TiO_2) reducing metal usage, it also provides a degree of mechanical strength and is usually modified with the addition of Zr, La or Si to further increase the structural strength and provide chemical inertness to the support [144]. Furthermore, a small amount (0.05 to 1 wt%) of a precious metal, such as Pt, Re or Ru, is often added in industrial formulations to promote reduction [146]. However, the promoter significantly elevates the costs of the catalyst [147]. Due to the complexity of the high pressure plasma-catalytic interactions and in order to determine the influence of the cobalt loading on the process, the above-mentioned promoters will not be used. However, future catalyst formulations used in plasma-catalytic FTS should benefit from promoter usage.

Many different formulations of the cobalt catalyst have been patented by Sasol [148], Shell [149], ExxonMobil [150], and Statoil [151]. Oukaci et al. [152] reproduced several patented catalysts comprised of cobalt loadings between 12-20 wt%, a metal promoter (Re or Ru) and an oxide promoter supported on Al_2O_3, SiO_2 or TiO_2, which were investigated under FTS conditions using a fixed bed reactor and slurry bubble column reactor. Several cobalt catalyst formulations and their corresponding technology provider are listed in Table 3.4.

Table 3.4: Commercial cobalt catalysts (data from [147]).

Technology provider	Support/Modifier	Promoter	Reactor	Production (bbl/day)	Relative activity
Sasol	γ-Alumina/Si**	Pt	Slurry	16 000	
Shell	Titania	Mn; V	Fixed	6 000	0.3
GTL.F1	Aluminate/α-Alumina	Re	Slurry	1 000	0.9
ENI/IFP/Axens	γ-alumina/SiO2; spinel	?	Slurry	20	0.19
Nippon Oil	Silica/Zirconia	Ru	Slurry	500	0.16
Syntroleum	γ-Alumina/Si**; La	Ru	Slurry	80	
BP	ZnO	?	Fixed		
ExxonMobil	Titania/γ-Alumina	Re	Slurry	200	
ConocoPhillips	γ-Alumina/Boron	Ru/Pt/Re	Slurry	400	0.68
Compact GTL	Alumina?	Re?	Micro	500	
Oxford cat./Velocys	Titania-Silica	Re	Micro	1 000	

The conventional FTS catalyst formulations discussed above provide a template for catalyst preparation in plasma-catalytic FTS. However, due to the complexity of the internal structure of the arc discharge reactor used in plasma-catalytic FTS, modifications to the preparation method are required. The modified preparation method is fully described in Chapter 5.

In Section 3.4, the selection, formulation and preparation of a cobalt catalyst were discussed. The activity of the cobalt catalyst in conventional FTS is mainly influenced by the reactor type (discussed in Chapter 5) and the operating conditions (discussed in Section 3.5).

3.5 Operating conditions

The activity and stability of a FTS catalyst, in addition to catalyst formulation, are dependent on three main operating conditions: Pressure, temperature and H_2/CO feed ratio.

An increase in pressure in FTS, usually in the range of 1 to 6 MPa [63, 64], increases the reaction rate and favours the formation of heavier hydrocarbon products [65]. The influence of pressure was also demonstrated in pure plasma FTS, investigated between 0.5 and 15 MPa. The methane product yield generally increased with pressure from 2 to 12 MPa and the C_2 and C_3 yields (indicative of chain growth), improved between 6 and 12 MPa [4]. This influence of pressure on chain growth is expected to be enhanced by the presence of a catalyst in high pressure plasma-catalytic FTS.

Similar to the effect of pressure, an increase in the catalyst temperature or H_2/CO ratio also increases the reaction rate of FTS, but conversely shifts the product distribution towards the lighter hydrocarbons for both iron [153] and cobalt [65] catalysts. In contrast to conventional FTS, the catalyst in plasma-catalytic FTS will not be externally heated. However, catalyst heating should arise solely from the plasma-catalyst interactions, which may be similar to the interactions that occur in plasma-catalytic hydrocarbon reforming and pollutant treatment, discussed in Sections 2.3.2 to 2.3.3.

Thus far in Chapter 3, the catalyst has been discussed in relation to its basic chemistry, formulation and operating conditions. The final section below, Section 3.6, expands on the reactions (discussed in Section 3.3), that occur on the catalyst surface in conventional FTS, which when coupled with the plasma-catalytic interactions in Chapter 2, provides a comprehensive forecast of reactions that could occur in plasma-catalytic FTS, as covered in Chapter 6.

3.6 Reaction mechanisms

As mentioned in Section 3.3, FTS is a complex polymerisation reaction involving the hydrogenation of carbon monoxide. The complex process encompasses multiple reaction pathways described by several proposed mechanisms: The carbene (CO dissociation) mechanism, hydroxy-carbene mechanism and CO insertion mechanism [134, 154]. The carbene mechanism, the most widely supported FTS mechanism, is described by the following elementary steps that occur on the catalyst surface [133, 134]. Similar mechanisms could occur on the catalyst in high pressure plasma-catalytic FTS.

i. Adsorption and dissociation of CO on the catalyst surface to form adsorbed C and O-atoms.

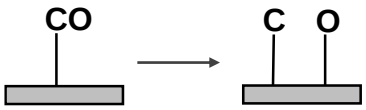

ii. Adsorptive dissociation of H_2 on the catalyst surface to form adsorbed H atoms.

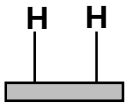

iii. Reaction of H-atoms and adsorbed carbon to form adsorbed CH_x (x=1-3) species; where CH_2, known as methylene, is a monomer vital for chain growth.

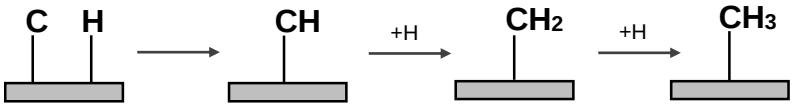

iv. Hydrogenation of adsorbed methyl radials, CH_x (x=3), to form methane.

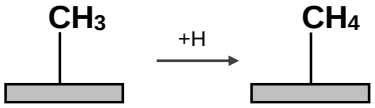

v. Chain growth via the addition of CH_2 monomers to form methyl, ethyl and alkyl radicals.

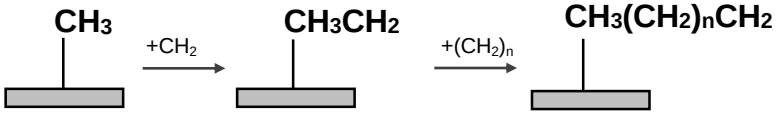

vi. Alkene formation via termination of an alkyl radical.

vii. Alkane formation via irreversible hydrogenation of an alkyl radical.

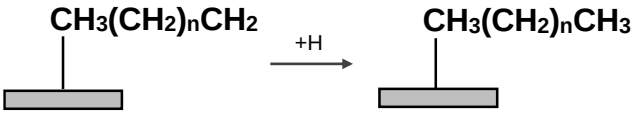

Primary products formed via these mechanisms, especially olefins, may be re-adsorbed onto available catalytic sites, and participate in secondary reactions, prior to exiting the reactor. Olefins are susceptible to the following secondary reactions [133, 134]:

i Hydrogenation to form linear paraffins.
ii Isomerization.
iii Cracking and hydrogenolysis to lower molecular weight hydrocarbons.
iv Insertion into longer chains.
v Readsorption and chain initiation.

The conventional FTS reaction schemes mentioned in this chapter are likely to occur on the catalyst surface during plasma-catalytic FTS experiments in the current work. These reactions are expected to be enhanced by the high pressure arc discharge with a synergistic effect similar to that encountered in atmospheric pressure plasma-catalytic processes described in Sections 2.3.1 to 2.3.4.

This chapter also discussed the various catalysts used in conventional FTS and listed the incentives for the selection of cobalt as the active catalytic material. The cobalt catalyst preparation method is fully described in Chapter 5, but firstly a detailed description of the high pressure arc discharge reactor and peripheral equipment are presented in Chapter 4.

Chapter 4
EQUIPMENT DESCRIPTION

In Chapter 4, the high pressure arc discharge reactor used to generate non-thermal plasma (NTP), constructed and developed by Fulcheri and co-workers [59, 60], is briefly reviewed in Section 4.1. Thereafter the experimental setup will be discussed in Section 4.2, which includes the preparation of syngas, reactor specifications, power supply and the diagnostic instruments required for discharge ignition and analysis; in addition to product analysis using a gas chromatograph. Finally, the orchestration of these components to induce Fischer-Tropsch synthesis (FTS) via high pressure non-thermal plasma (NTP) is discussed in the experimental procedure (Sections 4.3 and 4.4).

4.1 Arc discharge reactor: Review

The high pressure tip-to-tip arc discharge reactor used in this work was designed and constructed by the Plasma Group at MINES ParisTech (Sophia Antipolis, France) for the Thermodynamics Research Unit (TRU) at the University of KwaZulu-Natal (Durban, South Africa) as part of a bilateral collaboration. The reactor currently used by both research groups is a third generation prototype that possesses several operational improvements over the previous two prototypes. The challenges experienced during operation of the earlier prototypes are discussed in Table 4.1.

Initial experimental work using the present reactor was undertaken by Fulcheri et al [60]. They investigated a pure helium arc discharge with varying current (250 to 400 mA), pressure (0.1 to 15 MPa) and inter-electrode gap (0.25 to 2.5 mm). Iwarere et al. [4] used similar operating conditions in hydrocarbon synthesis (Fischer-Tropsch synthesis). Based on the good arc stability at these operating ranges, similar conditions were employed for high pressure plasma-catalytic FTS in the current research undertaken at the Thermodynamics Research Unit (TRU).

Table 4.1: Past and present high pressure arc discharge reactors and operating conditions.

Evolution of Reactor	System investigated	Max. operating pressure (MPa)	Inter-electrode gap (mm)	Input current (mA)	Reactor volume (cm^3)	Notes [155]
First prototype		10	-	-	2.65	(i) Actual maximum working pressure of 3 MPa due to improper sealing. (ii) Inaccurate measurement of inter-electrode gap due to electrode tip erosion. (iii) Aluminium electrode base melted during experimentation.
Second prototype	Ar/H_2 gas mixture [59]	0.1-15	0.5-1.5	100-350	2.53	No sightglass due to pressure limitations.
Current setup	Helium [60], Hydrocarbon synthesis(FTS) [4, 5], Dry reforming of methane [62], Fluorocarbon synthesis [61].	20	0.25-2.5	600	2.56	Capable of measuring discharge voltage and current (power).

4.2 Experimental setup

The present experimental setup is comprised of the following subsystems:

i. Syngas preparation system constituting a gas mixing vessel;
ii. Reactor chamber in which the discharge is generated and plasma treatment occurs;
iii. Electrical circuit encompassing the power supply, voltage and current diagnostic instruments;
iv. Gas Chromatograph for chemical quantitative analysis.

An overall process scheme is presented in Figure 4.1 and the actual experimental setup is shown in Photograph 4.1. A detailed description of the reactor and peripheral equipment are discussed below.

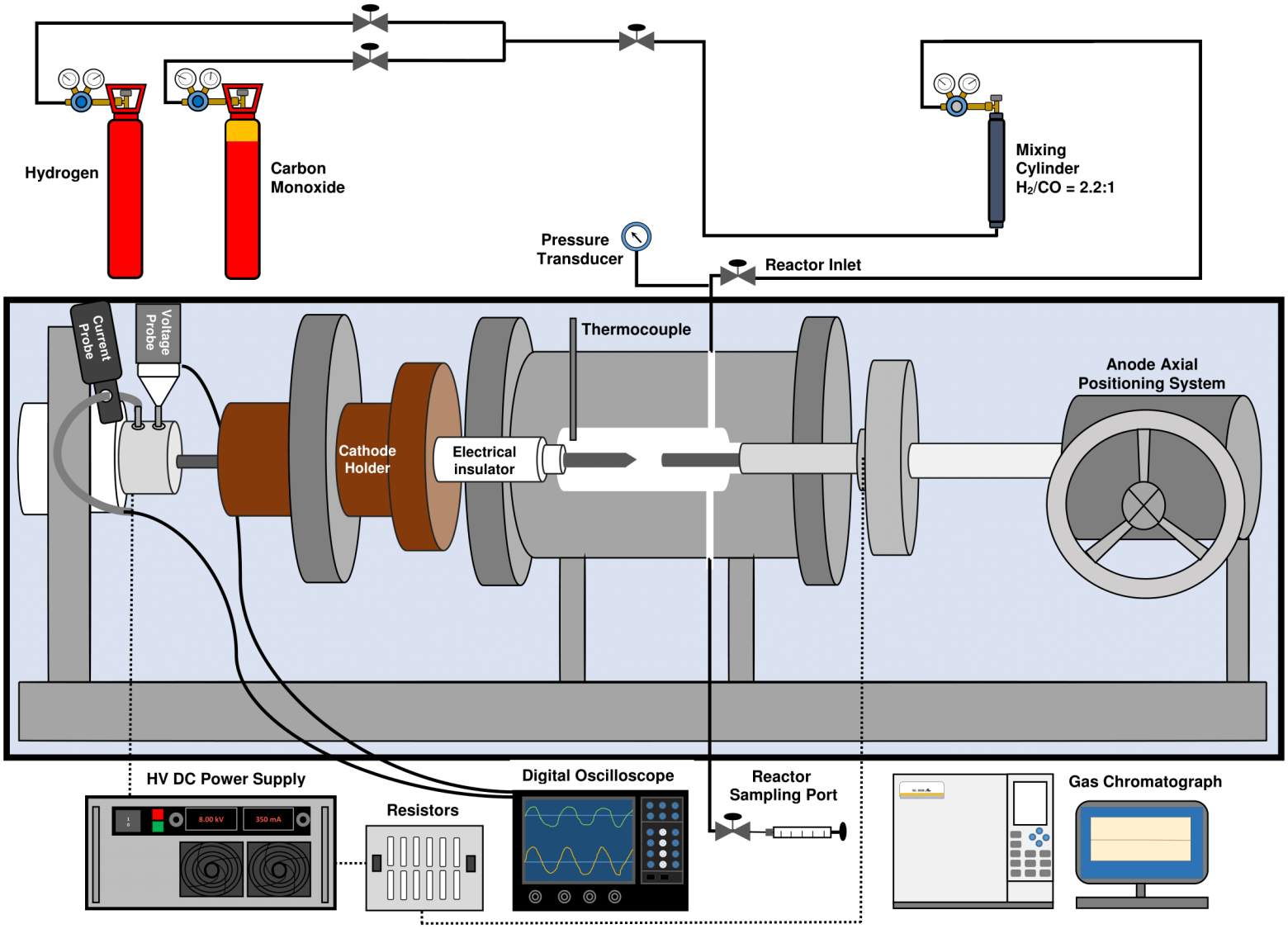

Figure 4.1: Schematic of the arc discharge reactor and auxiliary equipment.

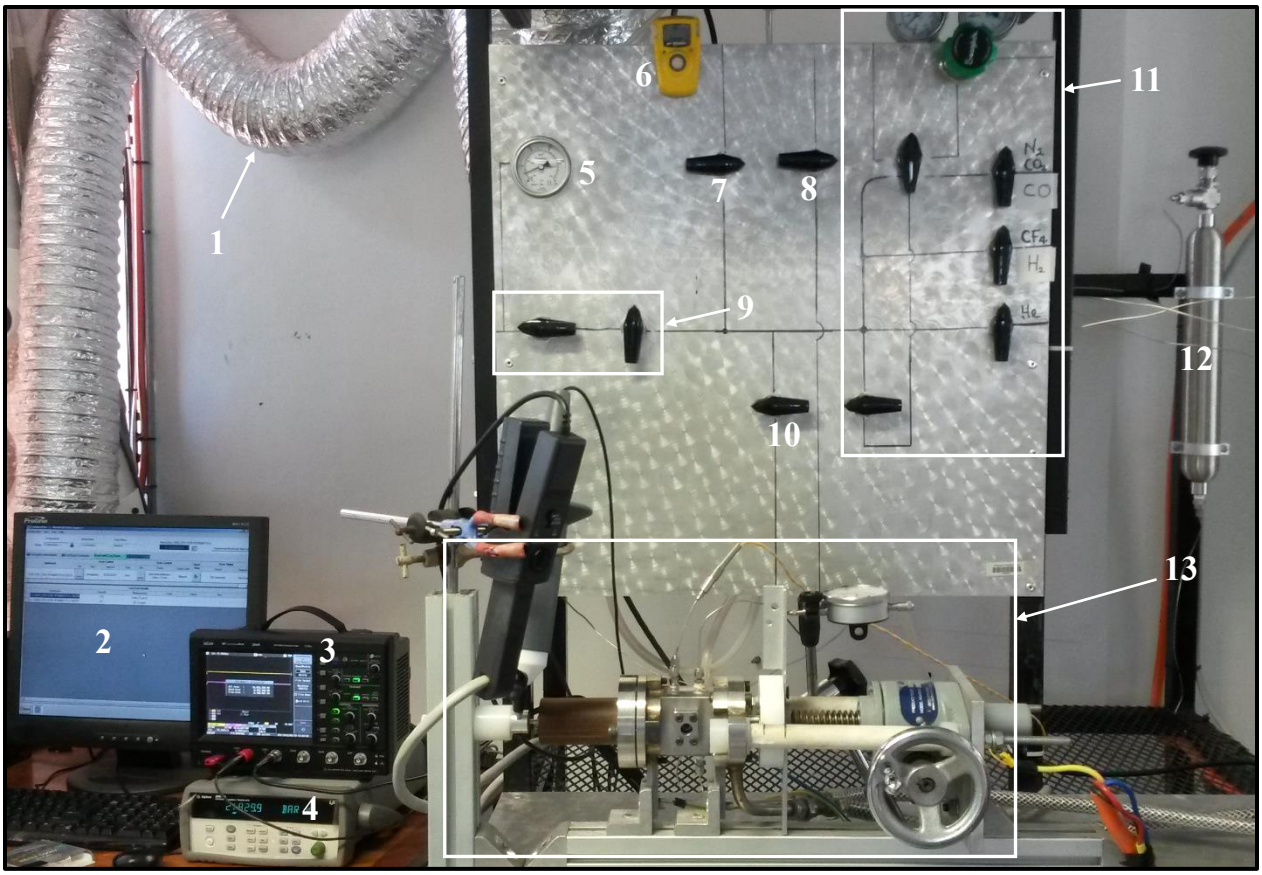

Photograph 4.1: Image of the arc discharge reactor and auxiliary equipment; (1) extractor vent line, (2) data acquisition software, (3) digital oscilloscope, (4) data acquisition instrument, (5) reactor pressure gauge (linked to pressure transducer), (6) CO detector, (7) reactor evacuation line, (8) reactor sampling line, (9) reactor supply lines, (10) vacuum pump line, (11) mixing cylinder feed circuit, (12) mixing cylinder, (13) reactor setup (described in Photograph 4.2).

4.2.1. Syngas preparation

The gases that constitute syngas, H_2 and CO, were procured from Afrox, South Africa. In the first high pressure pure plasma FTS study, Rohani et al. [13] used syngas with a H_2/CO ratio of 4:1 diluted with 40% helium. However, Iwarere et al. [14] later found that pure syngas with a H_2/CO ratio of 2.2:1, similar to conventional FTS, led to a more stable arc discharge; therefore this ratio was used in the current work. The method of mixing the reactant gases included introducing pure CO (99.999 mol%) followed by pure H_2 (99.999 mol%) into a 300 cm^3 Swagelok mixing cylinder to achieve a H_2/CO ratio of 2.2:1 based on the partial pressures of the gases. The gases did not spontaneously react in the mixing cylinder as H_2 and CO are stable molecules as described by their high dissociation energies (11.16 eV for CO and 4.25 eV for H_2 4.25 eV), thus requiring high energy input to initiate the reaction. This gas blend was allowed to mix and homogenize overnight in the mixing cylinder. The syngas composition ratio was verified by analysing three

samples using a Shimadzu 2010 Plus gas chromatograph (GC). In the occurrence of an inaccurate syngas ratio, adjustments were implemented by introducing additional quantities of the individual gases.

4.2.2. Arc discharge reactor description

In this work, a very high pressure low current tip-to-tip arc discharge reactor, similar to that described by Fulcheri et al. [60], was used to facilitate the FTS process. A schematic of the batch reactor is presented in Photograph 4.2. The reactor or discharge chamber, constructed from 316 L stainless steel, was cylindrical with an inner diameter of 12 mm and length of 24 mm. The reactor was capable of operating up to 20 MPa.

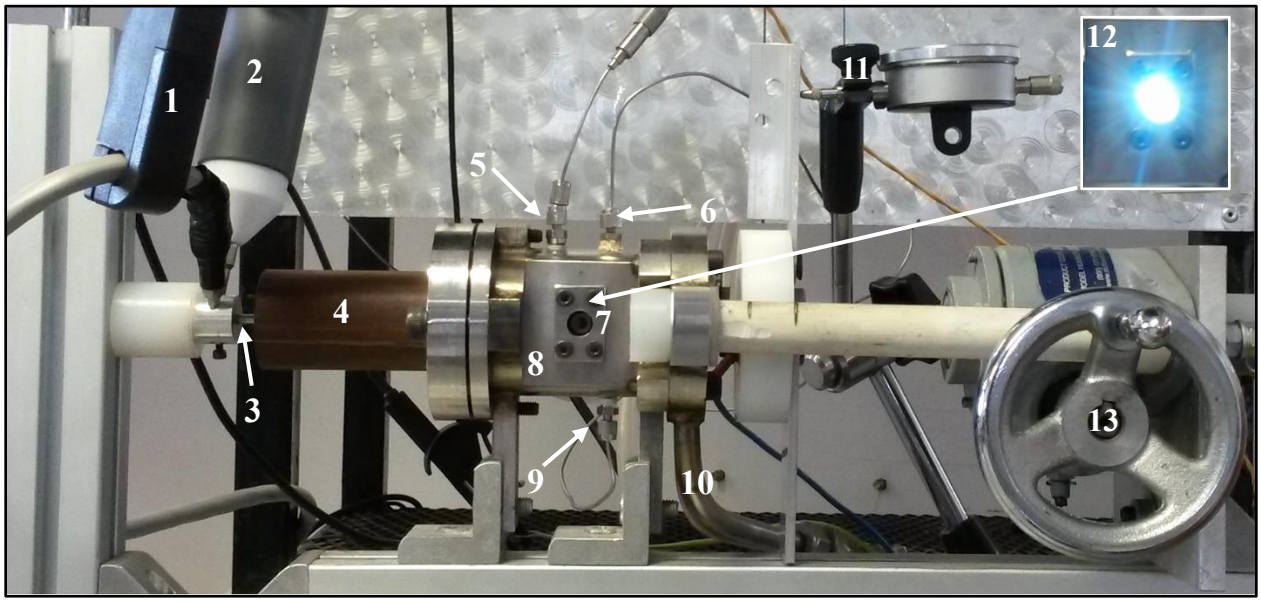

Photograph 4.2: Photographic image of the arc discharge reactor; (1) current probe, (2) voltage probe, (3) fixed electrode (cathode), (4) fixed electrode holder, (5) thermocouple, (6) reactor inlet (gas feed line), (7) sightglass, (8) discharge chamber, (9) reactor outlet (sampling line), (10) water cooling line, (11) Gear wheel actuator, (12) syngas arc discharge observed via the sightglass (without optical filters), (13) crank for mobile electrode (anode).

Two pure tungsten TIG electrodes, both with a diameter of 4 mm, were inserted axially into the reactor. The cathode was 150 mm in length and had a conical tip that was milled at an angle of 60^{o} from the tip point to the tip base, while the anode was 19 mm in length and had a flattened tip. The cathode was fixed in position while the anode was axially mobile in order to adjust the inter-electrode gap using a hand wheel with a pitch of 0.25 mm per revolution. When the inter-electrode gap was 1 mm, a reactor volume of approximately 2.56 cm^3 was obtained.

A ceramic holder, fabricated by Ceradvance Engineering Ceramics (Johannesburg, South Africa), was used to hold the cathode in position. It also provided good electrical insulation that ensured stability of the arc discharge. In addition, the ceramic insulator afforded high mechanical strength for operation beyond 10 MPa. At these high pressures, the discharge chamber was sealed using O-rings. Two face-to-face borosilicate Pyrex^{TM} sightglasses enabled visual observation of the arc discharge.

The reactor was fitted with a thermocouple to measure the bulk gas temperature, which was located at an approximate distance of 8.5 to 9 mm from the tip of the cathode where the arc discharge was initiated. However, no instrument was installed to measure the temperature of the arc discharge generated between the electrodes. A WIKA S-10 (0-250 bar) high pressure transmitter (calibration curve presented in Appendix C) was used to determine the reactor operating pressure via an Agilent 34972A data acquisition instrument. A cooling jacket with water as the cooling fluid was used to regulate the bulk gas temperature within the reactor.

4.2.3. Electrical circuit architecture

An arc discharge was ignited between the electrodes at high pressure by applying a high voltage to the cathode using a high voltage direct current (DC) power supply. The cathode was connected to the negative polarity and the anode to the neutral point of the power supply, which was a Technix-SR-10R-5000 (Photograph 4.3) with a maximum output voltage and current of 10 kV and 500 mA respectively. The current in the circuit was measured using a Chauvin-Arnoux E3N Clamp Hall-effect current probe with a bandwidth between 0 and 100 kHz and an offset of 0.3 mV/A to 100 mV/A. The discharge voltage was measured using a Metrix HX0027 high-voltage probe with a voltage rating of up to 20 kV, bandwidth of up to 30MHz and offset of 0.2 mV. The current and high-voltage probes were directly connected to the cathode. A BNC connector was used to network the probes to a Teledyne LeCroy Wavejet WJ354A 4 channel digital oscilloscope with a bandwidth of 500 MHz and real-time sampling rates of up to 2 GS/s. The oscilloscope generated a graph (Lissajous curve) of the instantaneous voltage and current signals as a function of time, which also reflected the minor voltage fluctuations due to changes in the reactor load.

The regulated power supply enabled the operator to precisely fix the current while the output voltage was actively controlled in order to continuously compensate for variations in the input voltage, current and load resistance. In order to maintain a fixed current throughout the system, the reactor and ballast resistors were connected in series to the power supply i.e. the load current in series is always equal to the current supplied, whereas the voltage is maintained in a parallel network. The two 1 kilo-Ohm ballast resistors were installed in series between the power supply and the discharge reactor in order to limit and regulate the amount of

current flowing in the electrical circuit. The resistors were also positioned in close proximity to the reactor in order to minimise the stray capacitance (stored charge) of the circuit, thereby improving the stability of the discharge. A comprehensive description of the electrical architecture is presented by Fulcheri et al. [60], which includes details of a similar Technix-SR power source, specifically a Technix-SR-15R-10000, capable of operating up to 15 kV and 660 mA.

Photograph 4.3: Image of the high voltage DC power supply.

4.3 Experimental procedure: Reactor

In order to remove impurities remaining in the system from previous experiments, the reactor discharge chamber was purged using helium followed by evacuation using an Edwards two stage vacuum pump. After purging, the syngas mixture was transferred from the mixing cylinder to the discharge chamber of the reactor at the desired operating pressure, between 0.5 and 10 MPa, via a series of Swagelok valves. The mixture composition ratio was verified prior to every experiment using a Shimadzu 2010 Plus gas chromatograph (GC). GC analysis revealed that the unreacted syngas contained methane (impurity) with a maximum concentration of 15 ppm, whereas no detectable quantities of ethane, ethylene, propane or proplyene were found. Prior to reaction, a Polyscience circulator (with a programmable temperature controller) was engaged in order to circulate water (maintained at ambient temperature) through the stainless steel cooling jacket, which enveloped the reactor chamber. Cooling of the reactor was necessary due to the highly exothermic Fischer-Tropsch reactions and a high temperature arc discharge.

Subsequent to filling the reactor with syngas, the mobile electrode was moved axially towards the fixed electrode using an axial positioning system until contact of the electrodes was achieved. Electrode contact was verified via the continuity function on a multimeter.

Direct contact of the electrodes was mandatory to overcome the limitations imposed by Paschen's Law under the low current and very high pressure conditions. Upon electrode contact, a three phase power was switched on, followed by the high voltage DC power supply. The power supply could only be engaged using a physical activation key, which ensured public safety by preventing unauthorised access. The power supply was pre-set at the desired ignition current and driving voltage.

After activation of the power supply, the arc was ignited as the mobile electrode was retracted. When an inter-electrode gap of 1 mm was attained, a stopwatch was activated to measure the elapsed treatment time, which was either 10 or 60 s in this work. After this period, the power supply was switched off and the arc was instantaneously extinguished. The arc discharge could only be sustained by the power supply for the duration of all experiments.

As a safety precaution, an insulated copper wire was used to transfer residual charge from the experimental apparatus to the ground. After discharging the system, a voltmeter was used to verify that there was no residual charge in the system, only then did post-reaction analysis proceed. A post-reaction sample was withdrawn from the reactor at a sampling point using a 500 uL Hamilton Gas-tight syringe and was analysed off-line by a gas chromatograph.

4.4 Experimental procedure: Reaction products analysis

The FTS product sample, extracted from the arc discharge reactor, was comprised of a multi-component spectrum containing syngas (H_2 and CO) in high percentage levels up to 99 mol% and C_1-C_3 hydrocarbons in trace levels (< 2.5 mol%), which made separation of these components (with similar physical properties) problematic for a single column and detector. Therefore, this product spectrum was analysed (off-line) using a Shimadzu 2010-Plus Gas Chromatograph (GC) equipped with two channels with each channel incorporating a carrier gas/column for component separation and a detector for identification of the different compound classes. A detailed list of the GC parameters are presented in Table 4.2 below.

In the first GC channel, the injected sample was transferred through the GC by a nitrogen carrier gas, separated on a Poropak-Q packed column and detected by a calibrated thermal conductivity detector (TCD). Nitrogen (0.026 $W.m^{-1}.K^{-1}$ at 300 K) was employed as the carrier gas for H_2 (0.18 $W.m^{-1}.K^{-1}$ at 300 K) detection due to the large difference in thermal conductivities of these gases, whereas detection using helium (0.15 $W.m^{-1}.K^{-1}$ at 300 K) was impractical due to similar thermal conductivities. The GC was originally designed for capillary columns, therefore Shimadzu column adaptors were fitted to accommodate a packed column.

In the second GC channel, the injected sample was transferred through the GC by a helium carrier gas, separated on a HP Al_2O_3 PLOT column and detected by a calibrated flame ionisation detector (FID). Because the FID has a higher sensitivity for trace levels of hydrocarbons than the TCD, it was used to detect methane, ethane ethylene, propane and propylene. Prior to FTS experimentation, the first and second GC channels were calibrated for the detection of permanent gases and hydrocarbons respectively. The GC calibration charts are presented in Appendix A. GC-solution was the software data package used to generate the chromatogram report after sample analysis.

Table 4.2: Gas chromatograph settings used in this work.

		Channel 1	Channel 2
Analytes	Compound class	Permanent gases	Hydrocarbons
	Gases	H_2, CO	CH_4, C_2H_6, C_2H_4, C_3H_8, C_3H_6
Injector	Type	SPL-2010 (Direct mode)	SPL-2010 (Split mode)
	Carrier gas type	Nitrogen	Helium
	Carrier gas flow	30 ml.min^{-1}	83 ml.min^{-1}
	Temperature	250^{o}C	200^{o}C
	Split ratio	-	15:1
	Linear velocity	-	38.4 cm.sec^{-1}
	Gas volume injected	500 µL	500 µL
Column	Type	Packed	Capillary
	Make	Supelco	HP
	Model	Carboxen 1000 (60/80)	Al_2O_3 PLOT
	Length	4.5 m	30 m
	Inner diameter	2.10 mm	0.53 mm
	Film thickness	-	15 µm
	Max. temperature	400^{o}C	200^{o}C
	Operating temperature	40^{o}C (Isothermal)	40^{o}C (10 mins)-170^{o}C (ramp)
	Retention time	10 mins	30 mins
Detector	Type	TCD	FID
	Temperature	275^{o}C	250^{o}C
	Flame	-	35 ml.min^{-1} H_2
		-	350 ml.min^{-1} Air

The experimental apparatus and procedures discussed in this chapter were employed in both the pure plasma and plasma-catalytic FTS studies, with a catalyst being integrated into the system for the plasma-catalysis studies. A detailed description of the catalyst preparation and configuration in the reactor is provided in Chapter 5.

Chapter 5
CATALYST PREPARATION

As has been previously explained, this enquiry set out to study the synergistic effect of non-thermal plasma (NTP) with a catalyst, in Fischer-Tropsch synthesis (FTS), at high pressure. Although catalyst formulation was not the focus of this work, a suitable catalyst had to be sourced. This was complicated by the intricacy and minute volume of the arc discharge reactor (compared to typical laboratory reactors), which gave rise to the question of how to attain the most suitable configuration of the catalyst.

As a result, it was decided to integrate the plasma-catalytic configuration used in gliding arc discharge reactors with the catalyst preparation method used for monolithic catalysts. The monolith preparation method entailed washcoating of a mullite (ceramic) substrate with high surface area γ-Al_2O_3, followed by the dipcoating of cobalt according to the classical wet impregnation method.

A detailed description of the conventional FTS (Section 5.1) and plasma-catalytic (Section 5.2) catalyst configurations (Sections 5.1 and 5.2) and preparation methods (Section 5.3) used in the literature are discussed in this chapter, followed by the integration and modification of these methods in plasma-catalytic FTS at high pressure (Section 5.4). Finally, the various catalyst characterisation tools used to understand the plasma-catalytic interactions in Chapter 6 are discussed in Section 5.5.

5.1 Conventional catalyst configuration

The Co/Al_2O_3 catalyst, which is used in the current study, is representative of that in industrial Fischer-Tropsch synthesis. Cobalt is the active component in catalysing FTS, while the support serves to increase the catalytic activity by increasing the surface area for metal dispersion. It also provides high thermal and mechanical strength, and physical and chemical stability. Cobalt was selected, instead of iron, for reasons discussed in Section 3.4.

Co/Al_2O_3 is typically prepared using the following procedure: Incipient wetness impregnation, drying, calcination and reduction [140]. These steps are vital in order to obtain a high dispersion of cobalt on the support. In order to ensure good catalytic activity and stability, various arrangements of the prepared catalyst are implemented in industrial and laboratory FTS reactors.

In industrial FTS reactors, the prepared catalyst is arranged as a packed bed in fixed bed reactors or is dispersed in slurry bubble column reactors. There are four commercially proven reactors that are currently in use, namely the tubular fixed bed, circulating fluidized bed, fluidized bed and slurry bed reactors [156, 157]. Tables 3.1 and 3.4 (presented in Chapter 3) list the reactors and companies that employ them in commercial FTS. FTS reactors are designed to rapidly remove heat liberated by the highly exothermic process (liberating about 10 times more energy than catalytic reactions in oil refining [157]). Heat removal is vital in order to maintain near-isothermal catalyst conditions, control the product distribution, and to impede excessive methane production, carbon deposition and sintering of catalyst particles.

In laboratory FTS investigations, the catalyst powder or pellets are often packed midway in a tube and suspended by an inert and high temperature material such as glass wool. The tube is then inserted into a heating apparatus.

Despite the effective configuration of the catalyst in industrial and laboratory reactors, neither of these arrangements, especially the packed bed format, were available for application in the arc discharge reactor. This was mainly due to the limited space in the reactor: 2.56 cm^3. Additionally, a packed bed could not be inserted between the electrodes as configured in other plasma-catalytic reactors (discussed in Section 2.3.4), due to the narrow discharge gap of 0.5 to 2 mm as well as the high temperature nature (10 000 to 20 000 K) of the arc discharge.

Apart from a packed catalyst bed arrangement, other options for suspending the catalyst in the arc discharge reactor were deliberated. For instance, allowing the catalyst powder particles to freely drift within the reaction chamber in a manner similar to that in fluidised beds was considered. But this was impractical because contact of the particles with the hot arc would lead to an unstable discharge. Alternatively, coating the powdered catalyst onto the reactor inner walls was also considered, but the limited space in the reactor chamber made it difficult to obtain a uniform coating.

5.2 Plasma-catalytic configuration

A particular source of difficulty in finding a suitable catalytic arrangement in the arc discharge reactor, in addition to the low volume, was the dual nature of the plasma; where the arc core is typically in local thermal equilibrium (LTE) reaching temperatures similar to that of thermal plasmas while the background gas is minimally heated corresponding to non-thermal plasmas (NTPs). The arc core temperature was estimated to be 16 200 K at the cathode and 12 700 K at the anode for a helium arc discharge using magnetohydrodynamic (MHD) modelling [158]. This arc core is hotter than other typical non-thermal

plasmas such as the dielectric barrier and corona discharges due to the high pressure operation. In addition, the arc ignition current is lower than that used to generate high temperature plasmas (I >> 1A), leading to a lower degree of bulk gas heating (near room temperature) than that in warm plasmas (1000-3000 K) [159] and thermal plasmas (10 000-40 000 K) [97].

This dual nature (non-thermal and local equilibrium) of the high pressure arc discharge is similar to that of a gliding arc discharge. In a gliding arc reactor, the arc is initially generated at the narrowest gap between two divergent electrodes, at which point the plasma is in a thermal state. As the arc moves upwards due to gas flow around the electrodes, the arc length increases and the gas temperature decreases as a result of heat losses; however, the electron temperature is maintained leading to a non-thermal plasma. Conveniently, gliding arc discharges have been coupled with catalysts in the literature, providing a template for the configuration of the catalyst in this work.

The gliding arc-catalyst configuration by Rueangjitt and co-workers [160, 161] was the most transferrable to this work. They investigated methane reforming using a combination of a gliding arc micro-reactor and a catalyst comprised of nickel loaded onto a porous alumina-silica ceramic plate. The nickel coated ceramic was positioned away from the electrodes in order to avoid direct contact between the hot arc and catalyst as shown in Figure 5.1.

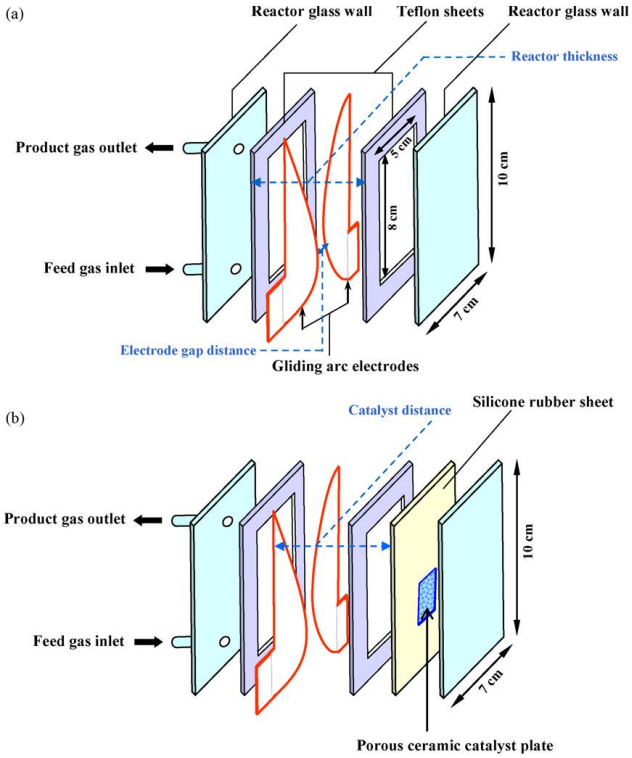

Figure 5.1: Configuration of a gliding arc discharge microreactor;
(a) without a catalyst and (b) with a catalyst (extracted from [160, 161]).

The nickel was dispersed onto the ceramic surface by wet impregnation, which involved immersion of the plate in a nickel nitrate solution, followed by drying, calcination and reduction. This catalyst configuration, entailing a ceramic substrate coated with the active catalytic material along with the assembly of the catalyst in the reactor, was adapted for use in this work.

5.3 Monolithic catalyst preparation

A ceramic substrate, used to hold the active catalytic material for the gliding arc-catalyst configuration discussed above, was prepared for plasma-catalytic FTS in accordance with the method employed for honeycomb monolithic FTS catalysts. Honeycomb monoliths have been tested in FTS for over a decade in response to the catalyst mass transfer limitations of fixed bed and slurry reactors [162-164]. Monoliths have been shown to overcome these mass transfer problems by providing a short diffusion distance without reducing the catalytic material used (due to the material being coated onto the thin walls of the monolith) [162, 163]. Additional benefits of monolithic catalysts are described in the literature [162, 163, 165-167].

Monolithic catalysts used in FTS are comprised of long parallel channels with internal diameters between 0.5 and 3 mm, separated by thin walls with a thickness between 0.1 and 0.3 mm [166]. These monoliths usually have square-shape channels (presented in Photograph 5.1) as these are the simplest shapes to manufacture [168]. In contrast to these complex channelled structures, the ceramic substrate used in this work was a hollow cylinder containing a single channel (presented in Figure 5.2, Section 5.4.1).

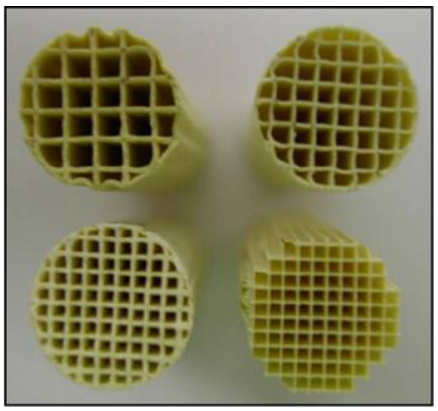

Photograph 5.1: Ceramic honeycomb monoliths
with different cell densities (extracted from [168]).

Strictly speaking, the single channel ceramic substrate (Figure 5.2) was not a monolith as described above and the typical benefits of a monolith are not applicable. Monolithic catalysts are intended to address mass transfer limitation issues in continuous reactors, which does not apply to this work as the arc discharge

reactor is operated in a batch mode. However, the monolith preparation technique was adopted and modified for use in this work. This method involves washcoating a ceramic monolithic substrate (usually made of low surface area cordierite, silica or alumina) with a high surface area support, followed by the dispersion of active metals, which are catalytically active for promoting FTS reactions [162, 163, 166, 167, 169-172]. Several methods of applying the active phase onto the monoliths have been reviewed by Avila et al. [173].

So far, in Chapter 5, it has been shown from the literature, that the catalyst configuration used in the gliding arc discharge reactor (Section 5.2) and the technique used for preparing monolithic catalysts (Section 5.3) are most suited for undertaking FTS in the high pressure arc discharge reactor. The application of these methods are discussed in Section 5.4, which includes the experimental procedure used for cobalt catalyst preparation.

5.4 Plasma-catalysis configuration: This work

5.4.1 Ceramic catalyst substrate

A mullite ceramic, representing the monolithic supports described above, was used as the support for the catalytically active cobalt. A LINE-OX® porous mullite substrate (illustrated in Figure 5.2), fabricated by Ceradvance Engineering Ceramics (Johannesburg, South Africa), was designed specifically for this application. The face-to-face perforations of 5 mm on the substrate were designed to align with the windows of the reactor for visualization of the arc discharge. Three cut-outs, each with a radius of 2.5 mm, were made at the edges of the cylinder to accommodate the thermocouple line, and reactor inlet and outlet lines.

The mullite substrate outer diameter of ~12 mm enabled a precise fit in the discharge chamber of the reactor (12 mm in diameter) with the outer cylindrical surface of the ceramic directly contacting the reactor surface, providing radial support for high pressure operation. The ceramic inner diameter of 7 mm allowed a radial clearance between the electrodes and catalyst when the electrodes axially contacted each other within the annulus of the catalyst (illustrated in Figure 5.3). The distance between the catalyst inner surface and the anode outer surface was approximately 1.5 mm and the distance between the catalyst inner surface and the conical tip of the cathode, where the arc was initiated, was approximately 3.5 mm. This configuration differs from the atmospheric pressure dielectric barrier discharge where the low temperature nature enables the introduction of a catalyst bed directly within the discharge region, and therefore facilitates direct contact of the plasma with the discharge.

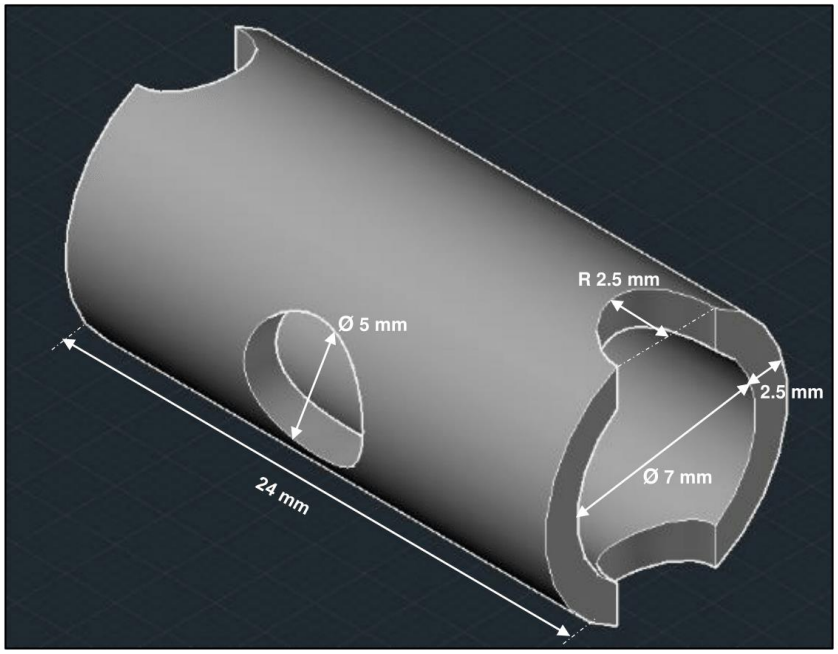

Figure 5.2: SE Isometric view of the LINE-OX® porous mullite substrate.

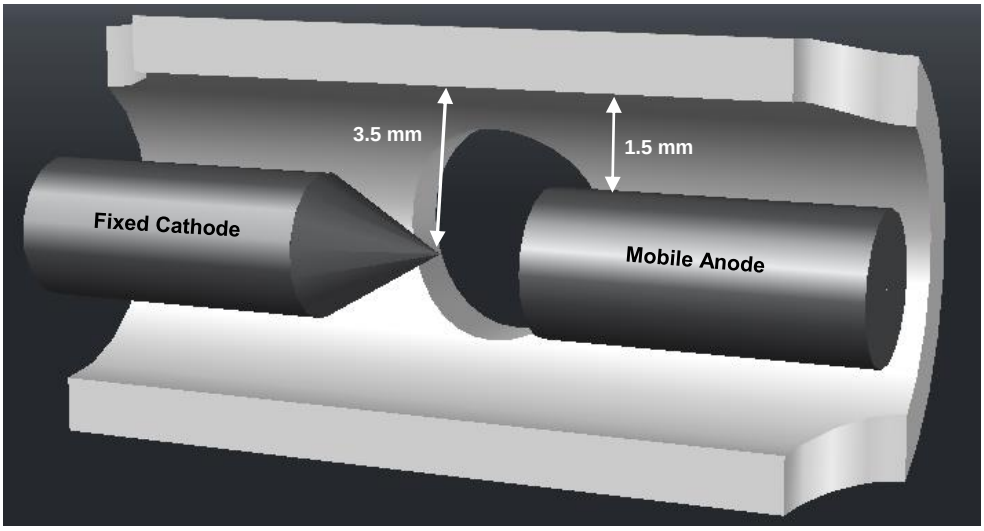

Figure 5.3: SE cross sectional isometric view of the LINE-OX® porous mullite substrate with electrodes.

Mullite was selected as the material for the catalyst substrate due to its excellent physical properties: Thermal stability [174], needed for exposure to the high temperature arc; mechanical strength [174], required for high pressure operation up to 10 MPa; porous structure, for binding of the washcoat onto the substrate surface; and high electrical resistivity (10^{13} ohm-cm at room temperature to 10^{4} ohm-cm at 1400°C [175]), required for high voltage operation. In addition, oxygen vacancies are abundant in mullite [176], which assists in promoting certain reactions.

A few studies on mullite as a catalyst support have been reported, such as the partial oxidation of ethanol [177]; decomposition of N_2O propellant [178] and; synthesis of phthalic anhydride [179]. These studies revealed the ability of mullite to enhance mass transfer due to its porous structure, and to maintain thermal stability in high temperature environments.

Mullite was preferred to the commonly used cordierite ceramic, owing to its superior thermal and mechanical properties (listed in Table 5.1), which were required for the high pressure and high temperature plasma environment. Ceramic supports are usually selected based on the operating conditions and not on the products desired.

Table 5.1: Properties of mullite and other advanced oxide ceramics [176].

Compound	**Tieillite**	**Cordierite**	**Spinel**	**Zirconia**	**Mullite**
Composition	$Al_2O_3 \cdot TiO_2$	$2MgO \cdot 2Al_2O_3 \cdot 5SiO_2$	$MgO \cdot Al_2O_3$	ZrO_2	$3Al_2O_3 \cdot 2SiO_2$
Melting point (^oC)	1860	1465	2135	2600	~1830
Density ($g.cm^{-3}$)	3.68	2.20	3.56	5.60	~3.2
Strength (MPa)	30	120	180	200	~200
Fracture toughness, K_{lc} ($MPa.m^{0.5}$)	-	~1.5	-	~2.4	~2.5

The thermo-mechanical properties of the mullite used in this work (supplied by Ceradvance Engineering Ceramics) are listed in Table 5.2.

Table 5.2: Thermo-mechanical properties of mullite supplied by Ceradvance Engineering Ceramics.

Mechanical		**Thermal**	
Alumina content	72 wt%	Max. temperature	1400^{o}C
Other constituents	Silica (bound)	Thermal conductivity	5 $Wm^{-1} K^{-1}$
Bulk density	2.7-2.8 g/cm^3	Thermal expansion:	
Porosity	15%	at 400^{o}C	$4.68x10^{-6}$ $^oC^{-1}$
Water absorption	6-8%	at 800^{o}C	$5.54x10^{-6}$ $^oC^{-1}$
Modulus of rupture	100 MPa	at 1000^{o}C	$5.88x10^{-6}$ $^oC^{-1}$
Modulus of elasticity	140 GPa		

Section 5.4.1 discussed the reasoning behind the selection of mullite as the catalyst carrier in plasma-catalytic FTS. In the next section, the experimental procedure for applying the active catalyst materials onto the mullite substrate is described.

5.4.2 Catalyst washcoating

A mullite substrate coated with γ-Al_2O_3 and cobalt was used as the FTS catalyst in this work. The support material, γ-Al_2O_3, was favoured over TiO_2 and SiO_2 due to stronger interactions with cobalt resulting in improved metal dispersion [180]. There are several methods for coating the active catalyst material onto a monolith [173].

Bakhtiari et al. [171] investigated two different coating methods for FTS catalysts. The first method involved the dispersion of cobalt on γ-Al_2O_3 by wet incipient impregnation, followed by drying and calcination. The calcined Co/γ-Al_2O_3 catalyst powder was ground in a ball mill in an aqueous environment to form a slurry, which was washcoated onto the ceramic support. In the second method, two separate coatings were applied, where γ-Al_2O_3 was washcoated onto the ceramic followed by impregnation of cobalt.

Washcoating the ceramic with Co/γ-Al_2O_3 in the first method probably led to some cobalt particles being submerged in the coating layer instead of being exposed on the surface, rendering those cobalt particles inactive in FTS; whereas in the second method, washcoating with only γ-Al_2O_3 provided a large surface area for dispersion of cobalt on the surface of the catalyst, ensuring maximum exposure of the active material. These results could explain why the second preparation method occasioned higher conversion and C_{5+} selectivity in the study by Bakhtiari et al [171]. In addition, washcoating was suggested to impart roughness and microporosity to the ceramic surface, which in partial oxidation of hydrocarbons, was suggested to increase mixing of reactant gases and improve mass transfer on the catalytic surface [165]. After consideration of these factors, the second preparation method was employed.

In this work, cobalt and γ-Al_2O_3 were deposited separately as thin layers onto the surface of the pre-formed mullite substrate. The uncoated mullite substrates, used to formulate three catalysts, weighed between 3.1643 and 3.3333 g. An image of the mullite substrate before γ-Al_2O_3 washcoating and cobalt dipcoating is presented in Photograph 5.2.a below.

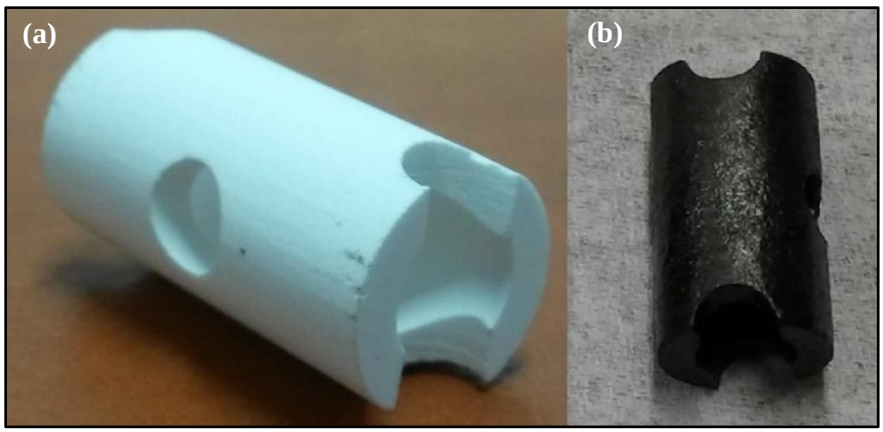

Photograph 5.2: Photographic images of the LINE-OX® porous mullite catalyst substrate; (a) before Al_2O_3 and Co coating, (b) after Al_2O_3 and Co coating, drying and calcination.

The γ-Al_2O_3 washcoating technique developed by Villegas et al. [181], a benchmark method in regards to monolith catalyst preparation, along with the method for deposition of cobalt onto monoliths in FTS [162, 163, 166, 167, 169-172], were modified for adoption in this work. Firstly, γ-Al_2O_3 powder with an average particle size of 3 µm, supplied by Alpha-Aesar, was mixed with water to form a slurry (Al_2O_3/H_2O = 20-25 wt%) with the addition of HNO_3 (HNO_3/Al_2O_3 = 2.2 mol.g^{-1}) to aid alumina dispersion. The slurry was mixed by a magnetic stirrer for 15 hours at room temperature. A mullite substrate was immersed vertically into the prepared slurry for between 5-15 minutes. After removing the precursor, the excess suspension was removed using a stream of compressed air. The precursor was dried and calcined in a static furnace at 600°C for 15 minutes and then weighed. The coating process (dipping and drying) was repeated until a 5 wt%-γ-Al_2O_3 washcoat was achieved. Washcoating with γ-Al_2O_3 was followed by cobalt impregnation.

The γ-Al_2O_3 washcoated mullite was dipped in a cobalt nitrate hexahydrate ($Co(NO_3)_2.6H_2O$) solution for 15 minutes (cobalt nitrate hexahydrate was procured from Sigma Aldrich in the crystalline form). The excess solution was removed from the mullite substrate using compressed air. The cobalt impregnated substrate was then dried in an oven at 120°C for between 30-60 minutes and weighed. The different drying times yielded very similar mass increases, demonstrating that 30 minutes was sufficient for effective drying. This short drying period was due to the simple design of the single-channel mullite substrate compared to the multiple micro-channel honeycomb monoliths which usually require several hours for complete drying.

The dried substrate was calcined in air at 450°C for 4 hours in order to decompose the cobalt nitrate hydrate into cobalt oxide, which was then reduced ex-situ at 350°C for 3 hours in pure hydrogen with a flow of 30 ml.min^{-1}. Cobalt is typically reduced in hydrogen at temperatures between 200 and 450°C [130, 131] in

order to convert cobalt oxides into metallic cobalt, which is the active phase for FTS [182, 183]. The activated catalyst was weighed and immediately inserted into the reactor. An image of the catalyst subsequent to γ-Al_2O_3 washcoating, cobalt impregnation, drying and calcination is presented in Photograph 5.2.b above.

This catalyst preparation procedure was used to prepare three coated mullite catalysts: A blank catalyst, coated with only γ-Al_2O_3 (no cobalt), and a 2 and 6 wt% cobalt catalyst containing γ-Al_2O_3 and cobalt. The composition of these catalysts are listed in Table 5.3. Each catalyst was retained in the reactor for the entire period of investigation, which included the pressure, current and inter-electrode gap variation studies that amounted to approximately 40-50 experiments using each catalyst.

Table 5.3: Composition of coated mullite catalysts.

Catalyst	γ-Al_2O_3 (wt%)		Co (wt%)	
	Target	Actual	Target	Actual
Blank	5	5,1	0	0
2 wt% Co	5	5,4	2	2,1
6 wt% Co	5	5,4	6	6,3

In the next section, the catalyst characterisation tools used to probe the catalyst will be discussed.

5.5 Catalyst Characterisation

Characterisation of the blank, 2 and 6 wt% cobalt catalysts was essential for understanding the effect that plasma has on the catalyst. Transmission electron microscopy (TEM) was used to estimate the cobalt particle size distribution and detect the deposition of carbonaceous species. Scanning electron microscopy coupled with energy dispersive x-ray (SEM-EDX) were used to analyse the catalyst surface morphology, coating thickness and elemental distribution at the sub-micron level. SEM differs from TEM imaging in that an image is produced based on the electrons reflected instead of absorbed. The crystalline phase structures and molecular composition were determined using x-ray diffraction (XRD).

5.5.1 Transmission electron microscopy (TEM)

The catalyst was prepared for TEM imaging by grinding the mullite coated substrate into a fine powder, which was mandatory for analysis. Less than a gram of powder was mixed with ethanol in a vial and sonicated for at last 10 minutes to facilitate dispersion of the powder. A drop of suspension was deposited onto an Agar 200 mesh copper grid and analysed under vacuum using a JEOL JEM-1010 TEM instrument.

5.5.2 Scanning electron microscopy (SEM) - Energy dispersive x-ray (EDX)

The fresh and used catalyst samples were prepared for SEM analysis by breaking the catalyst into pieces, small enough to mount onto a SEM stage. Carbon tape was used to secure the catalyst pieces onto the stage. The samples were then coated with a thin film of gold using a Quorum Tech Q150RES sputter coater in order to reduce undesired electron charging effects commonly encountered during imaging. The sample stages were placed in the microscope chamber, which was evacuated using a turbomolecular vacuum pump. This low pressure environment aided in the transfer of electrons between the emission source and detector.

Once the sample was mounted on the stage, a focused electron beam scanned the catalyst surface with reflected electrons that were collected by a detector to produce an image. Contrasts in the image varied according to the orientation of the sample surface in relation to the beam, where a surface normal pointing towards the detector formed bright images and the surface normal pointing away formed dark images.

SEM imaging was performed using a Zeiss Ultra Plus FEG with SmartSEM image capture software. In this work, samples were analysed using a magnification of up to 30 000. In addition to SEM imaging, EDX (based on x-ray fluorescence spectroscopy), was coupled to the SEM microscope to determine the elements comprising the catalyst. The EDX instrument was an Oxford X-Max 80mm SDD with Aztec analysis software.

5.5.3 X-ray diffraction (XRD)

Powdered catalyst samples were analysed using a Panalytical Empyrean x-ray powder diffractometer equipped with a Co-K_α radiation source. About 1 g of powder was placed in a sample holder, which was fitted onto the instrument stage. The holder was rotated during analysis in order to maintain the focus of the x-rays. Incident x-rays emitted from the radiation source bombarded the sample, either scattering off or diffracting from different planes of the powdered particle's crystal lattices. The x-rays were detected when the x-ray source, sample and detector were oriented to give Bragg diffraction. This produced an x-ray diffraction pattern, represented as a plot of x-rays diffracted from a sample, that possessed a certain energy (or intensity), versus the diffraction angle of 2θ.

This concludes the experimental section.

The cobalt catalyst, prepared according to the methods described in Chapter 5, was incorporated into the arc discharge reactor, described in Chapter 4, in order to induce Fischer-Trospch synthesis (FTS). The FTS experimental results are discussed in Chapter 6.

Chapter 6
RESULTS AND DISCUSSION

6.1 Chapter outline

6.1.1 Systems and operating conditions investigated

Chapter 6 presents the experimental results for Fischer-Tropsch synthesis (FTS) induced by non-thermal plasma (NTP), which was generated within an arc discharge batch reactor at high pressure (0.5–10 MPa). FTS experiments using non-thermal plasma (NTP) without a catalyst (herein referred to as pure plasma FTS), were undertaken prior to experiments combining NTP and a catalyst (herein referred to as plasma-catalytic FTS).

The catalysts employed in plasma-catalytic FTS consisted of mullite ceramics coated with either γ-Al_2O_3 (a blank sample) or γ-Al_2O_3 and cobalt. Different cobalt loadings were tested to determine the contribution of cobalt in plasma-catalytic FTS. The constituents of the three catalysts were:

i. 5 wt%-γ-Al_2O_3 (no cobalt) coated onto a mullite ceramic;
ii. 2 wt%-Co and 5 wt%-γ-Al_2O_3 coated onto a mullite ceramic;
iii. 6 wt%-Co and 5 wt%-γ-Al_2O_3 coated onto a mullite ceramic.

These three catalysts used in plasma-catalytic FTS experiments are herein referred to as:

i. Blank;
ii. 2 wt% Co;
iii. 6 wt% Co.

Pure plasma and plasma-catalytic FTS were investigated under the scope of three varying operating parameters, as follows:

a. Pressure: 0.5 to 10 MPa, at different reaction times of 10 and 60 s (Section 6.2);
b. Current: 250 to 450 mA (Section 6.3);
c. Inter-electrode gap: 0.5 to 2 mm (Section 6.4).

The hydrocarbon product yields (reported as ppm) and energy consumption (reported as $MJ/mol_{methane,prod}$) at these operating conditions were used to compare the performances of the four systems investigated: Pure

plasma, blank, 2 and 6 wt% Co. Firstly, the pressure variation study discussed in Section 6.2 was undertaken at discharge times of 10 and 60 s and at a fixed current of 350 mA and an inter-electrode gap of 1 mm. A pressure of 2 MPa was fixed for the current and inter-electrode gap variation studies as it produced a stable arc discharge at low currents (< 350 mA) and at a wide range of inter-electrodes gaps (0.5-2.0 mm), discussed in Sections 6.3 and 6.4. A detailed list of the operating parameters for the parametric studies are presented in Table 6.1.

Table 6.1: List of operating conditions used in pure plasma and plasma-catalytic FTS.

Operating parameters	**Pressure variation study**		**Current variation study**	**Electrode gap variation study**
Discharge time (s)	10	60	60	60
Ignition current (mA)	350	350	250, 300, 350, 400, 450	350
Ignition voltage (kV)	8	8	8	8
Electrode gap (mm)	1	1	1	0.5, 1.0, 1.5, 2.0
Pressure (MPa)	0.5, 1, 2, 3, 4, 5, 6, 7, 8, 9, 10	0.5, 1, 2, 3, 4, 5, 6, 7, 8, 9, 10	2	2
H_2/CO ratio	2.2:1	2.2:1	2.2:1	2.2:1

6.1.2 Reaction products

Trace quantities of C_1-C_3 gaseous hydrocarbons were synthesised in the reactor for the pure plasma, blank, 2 and 6 wt% Co systems. Trace products were the result of the arc discharge volume, determined by Rohani et al. [5], being considerably smaller than the total volume of the arc discharge reactor.

Rohani et al. [5] used a CCD camera with optical filters to observe the arc core volume (the volume containing active plasma species responsible for inducing FTS reactions), which was estimated to be a cylinder with an average radius between 0.15 and 0.16 mm and a length of 1 mm (for an inter-electrode gap of 1 mm). Based on these measurements, the arc core volume (between 0.071 and 0.080 mm^3) was approximated to be more than 30 000 times smaller than the total volume of the reactor (2.56 cm^3).

This volume difference, coupled with the low current operation, was responsible for large temperature gradients between the hot arc core and the ambient temperature bulk gas. The arc temperature ranged between 16 200 K at the cathode and 12 700 K at the anode for a helium arc discharge, determined using

magnetohydrodynamic (MHD) modelling [158]. This wide temperature gradient, assumed to be in effect in the current study, induced a convective effect that caused circulation of syngas in the batch reactor, thus enabling continuous treatment of the bulk gas. The circulation also led to mixing of C_1-C_3 hydrocarbons (most likely produced within the arc core) with unreacted bulk syngas (syngas that may have not been introduced to the discharge region during the discharge period), resulting in a mixture containing < 1 mol% (10 000 ppm) total hydrocarbons and > 99 mol% syngas for the pressure variation study and approximately ≤ 2.5 mol% (25 000 ppm) hydrocarbons for the inter-electrode gap study. The trace hydrocarbons produced by all four systems - pure plasma, blank catalyst, 2 wt% and 6 wt% Co catalysts - in order of concentration, were C_1 (methane) >> C_2 (ethane + ethylene) > C_3 (propane + propylene).

The above mentioned hydrocarbon product concentrations were determined using the following equations:

$$n_i(mols) = (GC\ Calibration\ slope)_i \times (GC\ peak\ area)_i \tag{6.1}$$

$$C_i(ppm) = \left(\frac{n_i}{\sum_{i=1}^{tot} n_i + n_{CO} + n_{H2}}\right) \times 1\ 000\ 000\ ppm \tag{6.2}$$

$$C_{i,prod}(ppm) = C_{i,final} - C_{i,initial} \tag{6.3}$$

Where *i* denotes the C_1-C_3 hydrocarbon species, C_i is the concentration of species *i* present in the gas mixture before and after reaction, and $C_{i,prod}$ is the concentration of species *i* produced by the reaction.

The expanded experimental uncertainty (*U*) of ±11% for $C_{i,prod}$ was determined from the uncertainty contributions of two major error sources: Sample measurement (u_{rep}) and GC calibration (u_{calib}). A complete evaluation of the combined and expanded uncertainties is presented in Appendix B.

$$U(ppm) = f\left(u_{rep}, u_{calib}\right) \approx \pm 11\% \tag{6.4}$$

The expanded uncertainties are represented by the vertical error bars in the concentration versus operating parameter (pressure, current or inter-electrode gap) plots in Sections 6.2 to 6.4. The influence of varying pressure, the main parameter investigated in this work, is discussed in the following section.

6.2 Pressure variation study

6.2.1 The influence of pressure on FTS product yields

Operating Conditions

The effect of very high pressures (0.5–10 MPa), on gaseous hydrocarbon yields and energy consumption for pure plasma and plasma-catalytic FTS, was determined at a fixed current of 350 mA and a fixed inter-electrode gap of 1 mm for different discharge times of 10 and 60 s using a syngas mixture with a H_2/CO ratio of 2.2:1.

These operating conditions were selected from the literature and their utilisation is justified as follows:
The specified current and inter-electrode gap were used because they provided a stable arc discharge at high pressures in previous pure plasma FTS studies [4, 5]. This current also allowed process flexibility as it resided within the middle of the operable current range in this work. That is, the maximum output current of the power supply was 500 mA and the minimum current at which a stable arc can be ignited was above 200 mA at a low pressure of 2 MPa.

In addition, a H_2/CO ratio of 2.2:1 was utilised, as Iwarere et al. [4] found that this syngas composition, similar to that used in conventional FTS, led to a more stable arc discharge than the He/H_2/CO mixture used by Rohani et al. [5]. Moreover, helium in the He/H_2/CO mixture would consume electron energy, causing a reduction in the fractional electron energy spent on syngas (H_2/CO) dissociation, conversion and hydrocarbon chain growth processes. A detailed list of operating conditions used in the pressure variation study are presented in Table 6.1.

6.2.1.1 Pure plasma: Comparison with the literature

Prior to elaborating on the phenomena responsible for the pressure variation results in this work (discussed in Section 6.2.1.2), the results are compared with those in the literature.

The C_1-C_3 hydrocarbons products obtained for pure plasma FTS in this work were previously reported by Rohani et al. [5] and Iwarere et al. [4]; however, there were discrepancies between their results and this work in terms of yields produced and input voltage (discussed here). The C_1–C_3 hydrocarbon concentration versus pressure (1 to 10 MPa) curves for the current work and that by Iwarere et al. [4] and Rohani et al. [5] are presented in Figures 6.1.a to 6.1.e.

The study by Iwarere et al. [4] and this work were undertaken using a similar arc discharge reactor and operating conditions i.e. H_2/CO ratio of 2.2:1, a current of 350 mA, inter-electrode gap of 1 mm and reaction

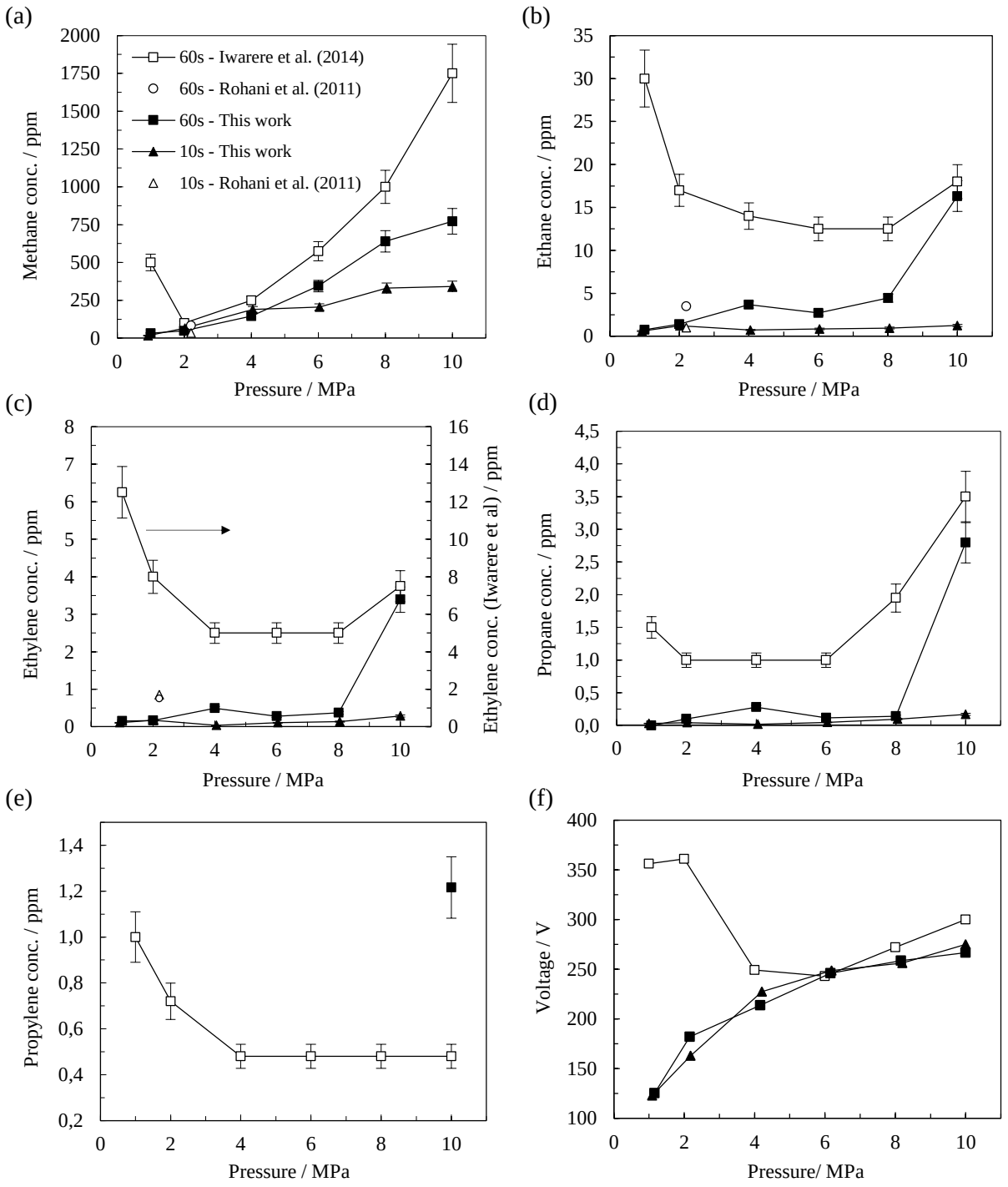

Figure 6.1: The influence of pressure on hydrocarbon concentration and voltage for pure plasma FTS at discharge times of 10 and 60 s; (a) methane, (b) ethane, (c) ethylene, (d) propane, (e) propylene and (f) voltage**. Legend:** □ - Iwarere et al. (60 s); ○ - Rohani et al. (60 s); ■ - This work (60 s); ▲ – This work (10 s); ∆ – Rohani et al. (10 s). **Operating conditions:** *This work and Iwarere et al*.: H_2/CO ratio: 2.2:1; current: 350 mA; inter-electrode gap: 1 mm; wall temperature: 25^{o}C. *Rohani et al.*: He/H_2/CO ratio: 40%/48%/12%; current: 350 mA, inter-electrode gap: 1.25 mm; pressure: 2.2 MPa. **Error bars (vertical):** Expanded experimental hydrocarbon concentration uncertainty of ±11%.

(discharge) time of 60 s. Iwarere et al. [4] investigated a pressure range of 0.5 to 15 MPa, but only their results between 1 to 10 MPa are shown here for the purpose of comparison.

Rohani et al. [5], who undertook the first pure plasma FTS study, used different operating conditions such as a $He/H_2/CO$ ratio of 40%/48%/12%. They also experimented with continuous treatment (no relaxation period) and pulsed treatment, which cycled between discharge ignitions and relaxation. Their results based on the most similar operating conditions to this work are presented in Figures 6.1.a to 6.1.e i.e. current of 350 mA, discharge gap of 1.25 mm and pressure of 2.2 MPa. In addition, the concentrations at discharge times of 10 and 60 s (in the continuous treatment mode) were interpolated from their work. Even though their syngas feed composition, pressure and inter-electrode gap parameters differed, their hydrocarbon yields resided in the domain of this work and that by Iwarere et al. [4] at 2 MPa.

The methane concentrations from 2 MPa upwards for this work and that by Iwarere et al. [4] showed similar trends of increasing concentration with increasing pressure. However, their methane concentrations were more than double with the difference between concentrations increasing as pressure increased. Their methane concentration of ~100 ppm at 2 MPa was ~2.1 times higher than this work (48 ppm); whereas at 10 MPa, their methane concentration of ~1750 ppm was ~2.3 times higher than this work (772 ppm). Their results showed that in the pressure range of 1 to 10 MPa, the maximum concentrations of ethane, ethylene and propylene were obtained at 1 MPa with the ethane and ethylene (C_2 hydrocarbons) concentrations generally decreasing from 1 to 8 MPa and slightly increasing at 10 MPa. Whereas, propylene decreased from 1 to 4 MPa and remained constant up to 10 MPa. Their trends contrasted with this work, where the maximum ethane, ethylene and propylene concentrations were obtained at 10 MPa, with trends that generally increased from 1 to 4 MPa, remaining relatively constant in the moderate pressure range of 4 to 6 MPa, and increased significantly from 8 to 10 MPa.

A major factor contributing to the discrepancies in hydrocarbon yields for these two studies was the input voltage (power), which is presented by the rms voltage versus pressure curves in Figure 6.1.f. In the study by Iwarere et al. [4], the trend of the voltage-pressure plot closely corresponded to the concentration-pressure plots of ethane, ethylene and propylene, where the highest concentrations of these hydrocarbons were obtained at the highest applied voltages (> 350 V). This trend implied that the high energy input at lower pressures were focused on ethane, ethylene and propylene production, whereas methane and propane production were favoured between 6 and 10 MPa.

In contrast to their voltage-pressure behaviour; in this work the voltage monotonically increased from 125 to 256 V in the range of 1 to 10 MPa at 60 s. The input voltages for both works significantly differed at 1 and 2 MPa, where input voltages of 125 V at 1 MPa and 182 V at 2 MPa in this work were almost 2 and 3 times lower, respectively, than that obtained by Iwarere et al. [4].

Their voltage-pressure behaviour corresponded to that observed for a pure helium arc discharge studied by Fulcheri et al. [60], who used a current of 300 mA and inter-electrode gap of 1.25 mm for a pressure range of 0.5 to 15 MPa. They found that a decreasing voltage-pressure trend occurred between 0.5 and 5 MPa, where a glow discharge formed between 0.1 and 1 MPa followed by the formation of an unstable arc between 1 and 5 MPa. At 5 MPa, an arc jump occurred leading to a voltage drop of almost 100 V. Thereafter, the voltage monotonically increased from this minimum voltage at 5 MPa up to 15 MPa.

Similarly to the work of Fulcheri et al. [60], Iwarere et al. [4] observed a decrease in voltage with increasing pressure between 2 and 6 MPa with a voltage drop of almost 100 V between 2 and 4 MPa and a minimum voltage at 6 MPa. The similar voltage behaviours observed by these authors could infer that the high voltages at low pressures in the study by Iwarere et al. [4] was due to the formation of a glow discharge or glow-to-arc transitional (GAT) discharge. These types of discharges have inherently larger treatment volumes than an arc discharge, which could have resulted in higher C_1-C_3 yields at lower pressures (1 to 2 MPa).

The reason for the formation of a potential glow discharge in their work and an arc discharge in this work was not clear but could have been due to the response of the different power supplies to the reactor load i.e. the output current of the constant-current regulated supplies used in both works were maintained at the current set-point of 350 mA due to the supplies actively adjusting the output voltage in order to continuously compensate for variations in the load resistance (temperature, etc.).

Despite the contrasting voltage trends between 1 and 6 MPa, the voltage output in the study by Iwarere et al. [4] and this work behaved similarly between 6 and 10 MPa with analogous voltages at 6 MPa. However, regardless of this similarity, all hydrocarbon concentrations differed even though the qualitative concentration-pressure behaviours appeared similar. This discrepancy was accredited to the methane impurity present in the feed syngas prior to reaction. Iwarere et al. [4] reported syngas containing 200 ppm of methane as an impurity in the syngas. However, in this work, a maximum of 15 ppm of methane was detected using a gas chromatograph; whereas 200 ppm, initially present in their syngas, was only produced

above 4 MPa for a discharge time of 60 s. A higher concentration of the methane impurity would have also contributed to their overall higher yields of C_2 and C_3 hydrocarbons, especially at lower pressures.

6.2.1.2 Pure plasma: This work

The previous section compared the general trends for pure plasma FTS in this work with studies in the literature, in order to validate the accuracy of the experimental techniques and instruments used in the plasma-catalytic FTS study. Armed with a clarification of the reasons for some differences in results, a more comprehensive analysis of the pure plasma FTS outcomes in this research was undertaken.

The methane concentration curves (Figure 6.1.a) for pure plasma at 10 and 60 s showed a consistent trend of increasing concentration with increasing pressure. In the 60 s study, there was a minimum of 32 ppm at 1 MPa and a maximum of 772 ppm at 10 MPa. In the 10 s study, there was a minimum of 17 ppm at 1 MPa and a maximum of 342 ppm at 10 MPa. The methane concentrations for the 10 and 60 s studies were similar between 1 and 4 MPa, but these began to diverge at 6 MPa as methane production increased at a faster rate at 60 s than at 10 s; whereas, considerable divergence in the ethane, ethylene and propane concentration-pressure plots only occurred at 10 MPa.

These results suggested that the longer treatment time of 60 s was beneficial for production at pressures above 4 MPa. The probable cause of this concentration-pressure behaviour was that at higher pressures there were higher density gradients between the high temperature gas at the arc core and the cold surrounding bulk gas. This would have caused greater convective forces resulting in higher gas velocities and improved circulation of the surrounding gas through the arc core, leading to larger quantities of the bulk gas being treated. In contrast, at lower pressures, $\leq$ 4 MPa for methane and $\leq$ 2 MPa for ethane, ethylene and propane, gas mixing was poor and led to the 10 and 60 s treatment times yielding similar product concentrations, rendering the longer treatment time ineffective. This was especially evident at 2 and 4 MPa where the concentration of methane at 10 s exceeded that at 60 s.

As mentioned above, the discharge period of 60 s was more effective for production between 4 and 10 MPa. However, between 4 and 8 MPa, the ethane concentration remained relatively constant, and ethylene and propane concentrations decreased, whereas the methane yield increased by more than a factor of 4; suggesting that the pressure range of 4 to 8 MPa did not significantly improve chain growth, especially when factoring in the ±11% expanded experimental uncertainty for ethane.

A significant improvement in C_2 and C_3 hydrocarbon concentrations were only achieved at 10 MPa, where the maximum ethane (16.3 ppm), ethylene (3.4 ppm) and propane (2.8 ppm) concentrations were obtained. These were approximately 4, 9 and 20 times greater, respectively, than that produced at 8 MPa. However, propylene (1.2 ppm) was only detected at 10 MPa, although it was possible for the propylene concentration to have resided below the detection limit of the gas chromatograph for experiments at lower pressures. These results confirmed the observation that higher pressures favoured the production of longer chain hydrocarbons in accordance with Arrhenius principle and conventional FTS trends [63-65].

In conclusion of the discussion of pure plasma FTS, the following trends of interest were observed: Firstly, plasma-enhanced syngas circulation rendered the 60 s treatment period to be more effective than the 10 s period between 4 and 10 MPa and; secondly, for the 60 s treatment period, chain growth to form C_2 and C_3 hydrocarbons was considerably improved at 10 MPa.

Reaction mechanisms

Despite the positive influence of increasing pressure in pure plasma FTS, the C_1-C_3 hydrocarbon concentrations obtained were low, and chain growth was poor, compared to conventional FTS. This was probably due to the arc core having a local thermal nature, where temperatures could have ranged between 10 000 and 20 000 K (estimated to be 16 200 K at the cathode and 12 700 K at the anode for a helium arc discharge, determined using MHD modelling [158]). These temperatures could have led to thermal CO dissociation (rate limiting step) into C and O radicals (occurring above 5000 K), which could cause an increase in the electron density of the plasma [184, 185]. In addition, the energy required to dissociate CO (11.16 eV) was a factor of 2.6 higher than that to dissociate H_2 (4.25 eV) [66]; therefore, hydrogen should have dissociated more rapidly than CO and the rate of hydrogenation could have exceeded CO dissociation, thus impeding chain growth and solid carbon formation, and favouring methanation.

This explains the high methane yields as well as the narrow gaseous C_1-C_3 hydrocarbon product distribution for the pure plasma FTS and plasma-catalytic FTS systems (Sections 6.2.1.3 to 6.2.1.6). In contrast, catalytic activity occurring at much lower temperatures (200 to 240^{o}C) in commercial low temperature FTS operations, resulted in a wide (C_1 to at least C_{30}) hydrocarbon product spectrum, forming liquid synthetic fuels (C_6 to C_{18}) and solid waxes ($\geq C_{19}$) [63, 140].

Farther away from the thermal arc core, a more non-equilibrium behaviour was prevalent, evidenced by the close to ambient bulk gas temperatures. In this non-equilibrium region ($T_{translational} = T_{rotational} < T_{vibrational} <$

$T_{electronic}$), it was likely that highly energetic electron impact could have stimulated the dissociation of H_2 and CO by vibrational and electronic excitation, as indicated by Fridman [38].

Vibrational excitation typically takes effect for electron energies between 1 and 3 eV, specifically 2 eV for CO [38], whereas electronic excitation is effective above 10 eV. Since the electron energy in and around the borders of the arc discharge could range between 1 and 10 eV, it was likely that these collisional phenomena, with vibrational excitation being dominant, were responsible for H_2 and CO dissociation in and near the arc core. In addition, rotational excitation of CO and H_2 reactant molecules were shown in the literature to occur via collisions with heavier particles as electrons have too low mass to control these processes. Hence, the rotational temperature is an estimation of the bulk gas temperature [186], which increased by merely ~6^{o}C for a pressure increase from 1 to 10 MPa in this work, indicating that the plasma probably retained its non-equilibrium nature throughout the pressure range investigated.

Due to the absence of a catalyst in pure plasma FTS, the plasma species mentioned above were solely responsible for producing hydrocarbons. In an attempt to improve the hydrocarbon product yields and distribution, plasma-catalytic FTS was explored using a mullite substrate coated with either 5 wt%-γ-Al_2O_3 (blank), 2 or 6 wt% Co/5 wt%-γ-Al_2O_3. Prior to presenting the findings of the blank and cobalt coated mullite catalytic processes, the effect of introducing a mullite substrate into the reactor is discussed in the next section.

6.2.1.3 Plasma-catalysis: Mullite Substrate

A mullite substrate was used exclusively as a carrier for the active catalytic materials in plasma-catalytic FTS. The physical properties and spatial dimensions of the substrate were fully described in Chapter 5 (Section 5.4.1). The introduction of the substrate into the reactor caused a 54 % reduction of the total reactor volume from 2.56 cm^3 to 1.20 cm^3. The same catalyst volume was used for the γ-Al_2O_3 and Co/γ-Al_2O_3 coated ceramics as the coating thicknesses (< 100 nm measured via SEM, discussed in Section 6.5.2.1), were negligible compared to the 2.5 mm thickness of the ceramic.

This reduction in the reactor volume, whilst the discharge volume was assumed to remain the same, inferred that the concentration of hydrocarbon products for plasma-catalysis would be more than twice that obtained for pure plasma FTS (where no catalyst was present). In other words, if 1000 ppm of methane was produced in a pure plasma system, more than 2000 ppm would be expected for plasma-catalysis assuming a linear relationship between reactor volume and syngas-product dilution. However, hydrocarbon concentrations varied widely from that obtained by pure plasma FTS for the pressure, current and inter-electrode gap

studies, suggesting that the presence of a catalyst affected synthesis beyond that caused by the reduction of the reactor volume by the catalyst.

Due to the mixing cylinder's limited storage pressure of 17 MPa, experiments were undertaken from high to low pressure (from 10 to 1 MPa) for the pressure variation study to ensure that the same syngas mixture was used for all experiments. A new syngas batch was used for the current or inter-electrode gap experiments. A single coated mullite catalyst was kept in the reactor for the entire duration of the pressure, current and inter-electrode gap variation studies. Therefore, the effect of the individual pressures, currents and inter-electrode gaps on the catalyst could not be directly investigated. However, observation via the sightglass and physical property measurements showed that higher pressures, currents, and inter-electrode gaps caused greater heating of the bulk gas and mullite catalyst surface; phenomena which are discussed later (Section 6.2.2). But first, plasma-catalysis using a blank catalyst is discussed in Section 6.2.1.4.

6.2.1.4 Plasma-catalysis: Blank catalyst

A γ-Al_2O_3 coated mullite substrate without cobalt was tested in order to: firstly, observe the effect of introducing a ceramic to the arc discharge region, and to understand its associated effects on the arc stability and pure plasma FTS and; secondly, to provide a control study for determining the performance of the cobalt loaded ceramic (as all the preparation parameters were kept constant).

The 10 and 60 s methane concentration curves, shown in Figure 6.2.a below, diverged from 1 MPa onwards as opposed to 4 MPa for pure plasma. This was probably a result of the reduced volume of the reactor, which improved gas circulation at lower pressures. As in the case of pure plasma, the pressure range of 4 to 8 MPa was not effective for promoting chain growth as compared to 8 to 10 MPa. The blank's methane qualitative trend was similar to that of pure plasma, but methane yields were lower for the pressure range investigated. For instance, at 10 MPa and 60 s, the methane yield for the blank catalyst (269 ppm) was ~2.9 times lower than that for pure plasma (772 ppm).

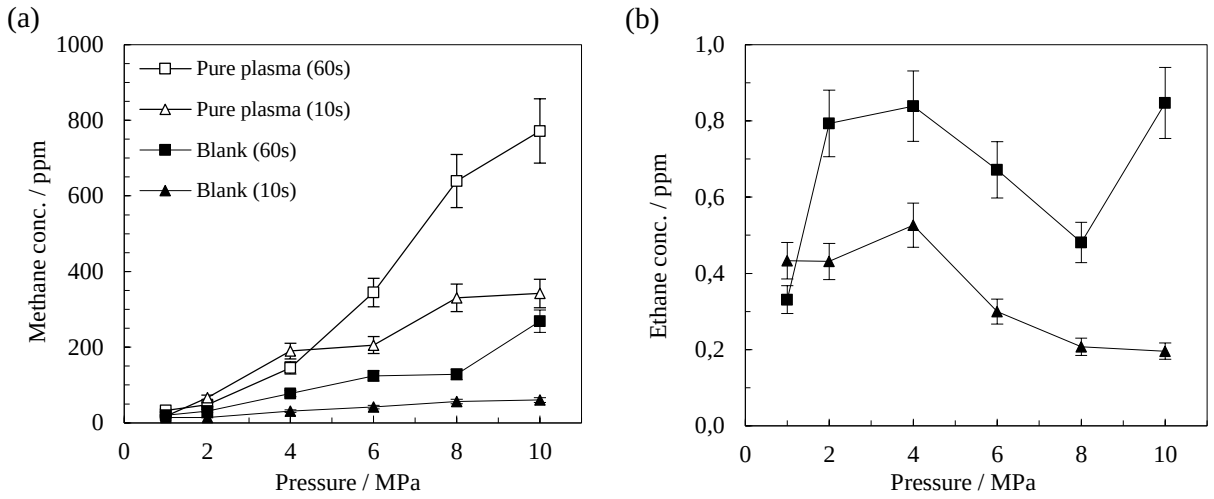

Figure 6.2: The influence of pressure on the hydrocarbon concentration for plasma-catalytic FTS (NTP + Blank catalyst) at discharge times of 10 and 60 s; **(**a) methane and (b) ethane. **Legend:** □ - Pure plasma (60 s); ∆ – Pure plasma (10 s); ■ – Blank (60 s); ▲ – Blank (10 s). **Operating conditions:** Syngas ratio: 2.2:1; current: 350 mA; inter-electrode gap: 1 mm; wall temperature: 25ºC. **Error bars (vertical):** Expanded experimental hydrocarbon concentration uncertainty of ±11%.

A lower methane yield than that produced in pure plasma FTS may imply lower CO conversions; thus a reduction in methylene monomers - the building blocks for chain growth. Monomer reduction, in turn, could have been responsible for lower C_2-C_3 hydrocarbon yields as seen by the low ethane concentrations (< 1 ppm) throughout the pressure range investigated (Figure 6.2.b). In addition, extremely low ethylene yields (< 0.1 ppm) were detected (not shown here), and propane and propylene were not produced (or may have existed below the gas chromatograph detection limit).

The γ-Al_2O_3 washcoated mullite catalyst was not expected to enhance hydrocarbon production as cobalt is the active material in conventional FTS. However, Al_2O_3 has been proven to possess good catalytic activity related to the acid/base surface properties and metal-oxygen bond strength [187-190], which enables this refractory material to promote various acid catalyzed reactions [189, 191].

In this work, it was likely that the adsorptive properties of γ-Al_2O_3 (washcoated onto mullite) caused a decline in FTS activity, where adsorption was assumed to be related to pressure drop. The pressure drop immediately after the treatment period, denoted by ΔP_{drop}, is presented as a function of operating pressure in Table 6.2 for the pure plasma and plasma-catalytic FTS systems at discharge times of 10 and 60 s.

At 10 MPa and at a discharge period of 10 s, the operating pressure for the pure plasma system increased by 0.01 MPa (denoted by the negative ΔP_{drop} value), suggesting that an increase in the inter-electrode gap

from 0 mm (before reaction, t < 0 s) to 1 mm (at the start of reaction, t = 0 s) had a negligible effect on the reactor volume and the associated pressure drop. However, at 10 MPa and 60 s, the operating pressure for the pure plasma system decreased by 0.07 MPa, probably due to an increase in the yields of C_1-C_3 hydrocarbons, which had lower partial pressures than the reactants, H_2 and CO.

A similar decreasing pressure trend was observed for the blank catalyst at 10 MPa, where the pressure drop values of 0.16 and 0.3 MPa at 10 and 60 s, respectively, were more than 16 and 4 times higher than the pure plasma values. However, the higher pressure drops in the blank catalyst experiments were not the result of lower partial pressure products, as the blank catalyst produced significantly lower hydrocarbon yields than pure plasma FTS. Therefore, it was reasonable to assign the decrease in operating pressure to the adsorption of CO (probably in the molecular, radical or vibrationally excited states), followed by surface reactions to form carbonaceous species. This was a plausible reaction pathway as graphite was detected via x-ray diffraction (presented in Section 6.5.4) on the blank, 2 wt% and 6 wt% Co catalysts. The influence of adsorption on the Co-based catalytic processes are discussed later in Sections 6.2.1.5 and 6.2.1.6.

These claims of CO adsorption on the blank catalyst could be supported by the adsorption properties of γ-Al_2O_3 and mullite (72 wt%-Al_2O_3/SiO_2). Cabrejas Manchado et al. [190] showed that CO was more strongly adsorbed on γ-Al_2O_3 than hydrogen and oxygen, which takes place through the weak carbonyl bonds being easily converted into formate. Their adsorption and readsorption-kinetic experiments revealed that CO possessed a low activation energy leading to a 90% surface coverage and irreversible adsorption.

CO adsorption in this work may have been further accelerated by the thermal activation of the catalyst by the discharge, possibly producing radicals and vibrationally excited CO species that could be more easily adsorbed than ground state CO molecules.

It was shown in other plasma-catalytic applications, namely pollutant treatment and dry reforming of methane, that the active plasma species can electrically enhance the chemisorption properties of porous catalytic materials, including Al_2O_3 [35, 192]. Porous Al_2O_3 may also increase the concentration of plasma species (pre-concentration) on the catalyst surface, leading to a longer residence time in the discharge zone [73]. These modifications by the presence of Al_2O_3 could lead to higher collisional activity and additional surface reaction pathways [103, 104], which in this work may have translated to enhanced CO adsorption and impeded hydrocarbon chain growth.

In addition to CO adsorption, the deficiency of hydrogen adsorption could have also impeded chain growth and hydrocarbon synthesis in this work. It has been postulated in classical catalytic processes that hydrogen dissociation on an active metal, followed by spillover onto a catalyst support, generates a hydrogen reservoir for synthesis [134, 193], which would be absent in the blank catalytic experiments due to the absence of active cobalt. It is therefore reasonable to attribute the CO conversion and low methane yields to strongly or irreversibly adsorbed CO coupled with the scarcity of adsorbed hydrogen (required for hydrogenation). These claims were supported by the formation of trace quantities of graphite-containing C-C bonds detected by XRD analysis, as discussed above. Furthermore, the components of mullite, which are silica and alumina, may have contributed to low C_2 and C_3 yields, and possibly graphite formation, as silica-alumina are known to catalyse cracking reactions, enhanced by low quantities of water [189]. These conditions, present during experimentation, could have led to catalytic cracking of ethylene (known to be susceptible to cracking [194]).

An additional source of the low hydrocarbon yields could have been the strong oxidative properties of Al_2O_3. In plasma-catalytic pollutant treatment, the oxidation of aromatic compounds to form CO_2, CO, and various other hydrocarbons, was enhanced by the porosity of the alumina, suggesting that short-lived species, such as atomic oxygen, may be adsorbed in the catalyst pores [73, 103, 105]. In plasma-catalytic dry reforming, methane was oxidised to CO using a DBD discharge coupled with a γ-Al_2O_3 catalyst [89]. Based on the oxidative nature of Al_2O_3, it is plausible that hydrocarbons produced in the arc core, with quantities similar to that achieved in pure plasma FTS, could have been oxidised by oxygen radicals and excited oxygen species to form CO or CO_2 within the alumina pores. However, this theory was difficult to support as an increase in CO yields and the formation of CO_2 were too low to detect by GC analysis.

All the above factors attributed to the presence of Al_2O_3 and mullite in the blank catalyst, namely higher CO chemisorption, hydrogen shortage, hydrocarbon cracking and hydrocarbon oxidation, could have led to plasma-catalytic interactions that modified the reaction pathways of pure plasma FTS; thereby leading to lower C_1-C_3 hydrocarbon yields than pure plasma FTS as shown by the concentration-pressure plots in Figure 6.2. Therefore, the use of a γ-Al_2O_3 coated mullite catalyst without cobalt is not recommended in plasma-catalytic FTS.

As mentioned above, the blank catalyst mainly served as a control for determining the influence of different cobalt loadings on the γ-Al_2O_3 coated mullite. The results for a 2 and 6 wt% Co catalysts are discussed in the subsequent sections.

6.2.1.5 Plasma-catalysis: 2 wt% Co catalyst

Comparison with the literature

The application of plasma-catalysis in FTS was first investigated by Al-Harrasi et al. [66] under near atmospheric pressure conditions (0.01-0.06 MPa) using a Cu/Co catalyst inserted into the annular discharge gap of a coaxial DBD reactor. The experimental details were described in Section 2.3.1.

Only a single experiment by Al-Harrasi et al. used a typical H_2/CO ratio of 2:1, which was undertaken at atmospheric pressure (0.1 MPa), with a wall temperature of 100^{o}C, and input power of 90W. At these conditions, the selectivity of higher hydrocarbons (C_{2-4} and C_{5+}) approached 90%. Interestingly, no methane was produced.

In addition, they investigated the effect of pressure on hydrocarbon production, where an increase in pressure from 0.01 to 0.06 MPa (at fixed conditions of 100^{o}C, H_2/CO ratio of 1:1 and 90 W), resulted in an increase in the selectivity of higher hydrocarbons (C_{2-4} and C_{5+}) from approximately 80 to 95%, and a decrease in CO conversion from 24% to 8%, which was attributed to a reduction in mean electron energy with increasing pressure.

The high selectivity of C_{2-4} and C_{5+} hydrocarbons in their work was due to the discharge occupying the entire reactor volume, typical of a DBD discharge, whereas in this work the discharge volume was more than 30 000 times smaller than the reactor volume, leading to dilution of products (discussed in detail in Section 6.1.2 above). Furthermore, their discharge (reactor) volume of 100 ml, determined for a discharge gap with a radius of 7.5 mm and length of 175 mm, was approximately 39 times greater than the reactor volume of 2.56 ml, and 4 000 000 times greater than the discharge volume in this work. This demonstrates the effect that the discharge/reactor volume ratio has on production, indicating that an increase in the arc discharge/reactor volume ratio in this work should significantly improve hydrocarbon production.

It is important to note that the DBD reactor is a mature technology in the field of non-thermal plasmas (NTPs), whereas the arc discharge reactor is a prototype, which is still in the developmental stages. Up to now, it has been used purely as a tool to explore the fundamental phenomena occurring in high pressure NTPs under gaseous non-reactive and reactive conditions. The reactive conditions (listed in Table 2.2 in Chapter 2), were only investigated from around 2011 [5]. Since that period, minor modifications have been implemented, such as the improvement of the reactor sampling port. In order for this technology to be utilised beyond exploratory purposes, it is vital that future reactor developments address the discharge/reactor volume ratio limitation.

The current enquiry, apart from the study by Al-Harrasi et al., seems to be the only other work to have explored plasma-catalytic FTS, and the first to investigate it at high pressure. A Co/Cu catalyst was used in their study, whereas a Co/Al_2O_3 catalyst was screened for this work. The results for high pressure plasma-catalytic FTS using a cobalt-based catalyst are discussed next.

This work

Co-based catalysts were comprised of mullite substrates washcoated with γ-Al_2O_3 and impregnated with cobalt. Several successive coating steps led to the agglomeration of cobalt particles to form nano-sized cobalt clusters resulting in 2 wt% of cobalt being loaded onto a γ-Al_2O_3 mullite carrier. These cobalt clusters, not present on the blank catalyst, were active for catalysing FTS reactions and facilitated the migration and adsorption of chain growth monomers.

The C_1-C_3 hydrocarbon yields obtained for the 2 wt% Co catalyst were higher than that for pure plasma in the pressure range of 0.5-10 MPa at both discharge periods of 10 and 60 s as shown in Figures 6.3.a to 6.3.d below.

In addition, the 2 wt% Co catalyst's hydrocarbon yields at 10 s were generally higher than that for pure plasma FTS at 60 s, indicating that the Co catalyst was active for FTS. For the 10 s experiment, there was a trend of increasing methane, ethane, ethylene and propane concentrations between 4 and 10 MPa; similar to that for pure plasma FTS at the same conditions, but with higher yields. The longer discharge time of 60 s improved yields to a lesser extent between 3 and 7 MPa as in the case of pure plasma between 4 and 8 MPa, suggesting that this moderate pressure range for plasma-catalysis was not favourable for chain growth.

A significant increase in C_1-C_3 concentrations occurred at 8 MPa for the 2 wt% Co catalyst compared to 10 MPa for C_2 and C_3 hydrocarbons by pure plasma FTS, suggesting that the catalyst lowered the pressure required for hydrocarbon production. In contrast to pure plasma FTS, where the methane concentration increased monotonically with pressure, for the 2 wt% Co catalyst, there was a local maximum for methane at 2 MPa with corresponding increases in ethane, ethylene and propane yields. In fact at 2 MPa, the maximum ethylene yield (52 ppm) was achieved, and the ethane yield (95 ppm) was close to the maximum yield attained at 8 MPa (109 ppm). These results clearly indicated that the cobalt catalyst altered the product selectivity of pure plasma FTS, with its influence being more dominant at 2 MPa.

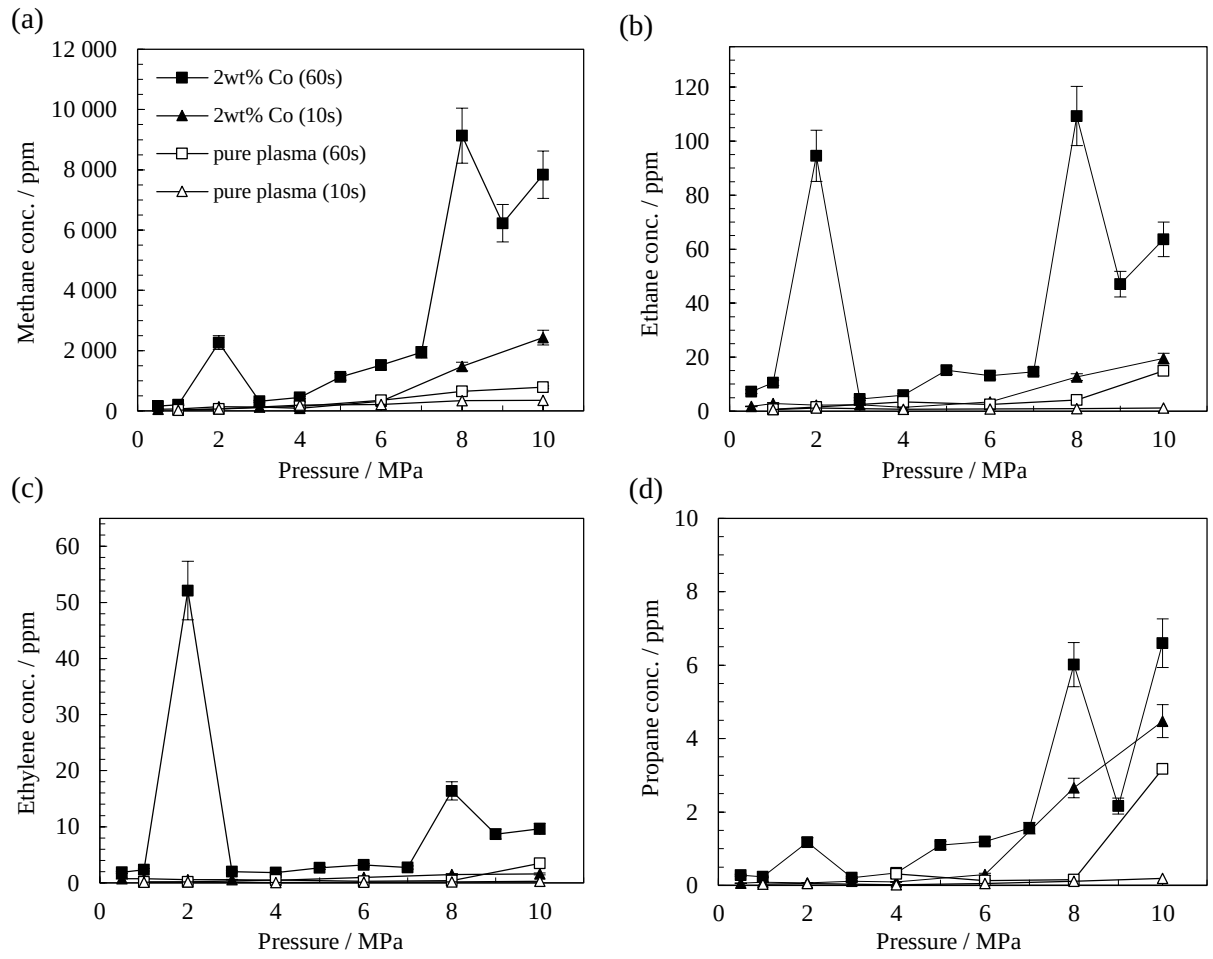

Figure 6.3: The influence of pressure on the hydrocarbon concentration for pure plasma and plasma-catalytic FTS (NTP + 2 wt% Co catalyst) at discharge times of 10 and 60 s; (a) methane, (b) ethane, (c) ethylene and (d) propane. **Legend:** ■ – 2 wt% Co (60 s); ▲ – 2 wt% Co (10 s); □ - Pure plasma (60 s); ∆ – Pure plasma (10 s). **Operating conditions:** Syngas ratio: 2.2:1; current: 350 mA; inter-electrode gap: 1 mm; wall temperature: 25^{o}C. **Error bars (vertical):** Expanded experimental hydrocarbon concentration uncertainty of ±11%.

These trends at 2 MPa could be explained by the effect of pressure on hydrocarbon production in conventional FTS. Zabidi et al. [195] tested various Co-based catalysts supported on carbon nanotubes under FTS conditions (220^{o}C, H_2/CO ratio of 2:1). They found that an increase in pressure from 0.1 to 2 MPa led to an increase in CO conversion (higher reaction rate) and an increase in C_{5+} selectivity of 60 and 57%, respectively, as well as a decrease in methane selectivity by around 50%. In addition, Jager et al. [63] using kinetic models predicated an increase in syngas conversion of up to 40% for an increase in pressure from 2 to 5 MPa. The increase in CO conversion with pressure could be due to an increase in the concentration of syngas species on the catalyst surface and an associated increase in CO collisional activity resulting in improved CO adsorption [196].

Similar concentration-pressure trends to conventional FTS were observed in the current work, where the ethane, ethylene and propane yields increased with pressure from 0.5 to 2 MPa. However, a contrasting (increasing) methane trend was obtained in this work, which was probably due to an increase in heating of the catalyst caused by an increase in the arc temperature with operating pressure. This result confirmed that the plasma and catalyst temperatures were directly influenced by the operating pressure in plasma-catalytic FTS, unlike in conventional FTS, where the pressure and temperature are independently controlled.

In contrast to the increase in C_1-C_3 hydrocarbon yields from 0.5 to 2 MPa, a substantial decrease occurred between 2 to 4 MPa (Figure 6.3), which could be partially explained by the work of de la Pena O'Shea et al. [197]. They showed that an increase in pressure from 2 to 4 MPa using a 10 wt% Co/SiO_2 under conventional FTS conditions (230ºC, H_2/CO ratio of 2:1) resulted in a decrease in gaseous C_1 to C_5 hydrocarbons. This was due to improved chain growth forming liquid C_{6+} hydrocarbons as a result of an increase in the H_2 and CO solubility with pressure. An increase in the active catalytic surface area due to particle segregation caused by an increase in CO chemisorption with pressure was also observed.

However, in this work, the formation of liquid (C_{5+}) hydrocarbon products was probably inhibited by the high temperature arc core. The hot arc appeared to have instead directed chain growth towards long C-C chains that formed solid carbonaceous species which were visibly observed as a thin film on the electrodes, specifically on the conical cathode tip and flat anode surface. Additionally, carbon species were detected on the catalyst via various microscopic analysis (discussed in Section 6.5).

The literature studies discussed above offer an explanation for the findings of the maximum concentration of ethane and local maximum of other gaseous hydrocarbons at 2 MPa. FTS is not conventionally studied beyond 4 MPa [134], with the exception of experiments using supercritical fluids such as hexane, where pressures around 6 MPa are explored [198].

As mentioned above, liquid hydrocarbons were not detected; however, liquid water was produced between 8 and 10 MPa for the 2 wt% Co catalyst. Water was seen as liquid droplets on the sightgass, which was verified using GC-MS analysis. This phenomena, not observed in the pure plasma and blank catalyst processes, was exclusively attributed to the presence of cobalt on the catalyst. Furthermore, water was not quantified, but the relationship between water yields and operating pressure could be estimated from conventional FTS.

Water is always a product of conventional FTS, formed by associatively dissociated hydrogen bonding with oxygen, which is released through CO dissociation. Therefore, an increase in CO conversion with pressure or residence time leads to an increase in water partial pressure, a trend commonly observed in conventional FTS [180, 199-201]. Similarly, at lower pressures (below 8 MPa) in this work, low concentrations of water would have been produced, which remained in the gaseous phase. Whereas, at higher pressures between 8 and 10 MPa, water condensation occurred as a result of higher water partial pressures, probably due to higher CO conversions.

The high water yields between 8 and 10 MPa could also explain the solid carbon formation and the decrease in methane yields (Figure 6.3.a) in this pressure range. Yang et al. [202] indicated that the formation of methane by hydrogenation of methane precursors may be inhibited by water production at relatively high CO conversion levels. As water production increases with pressure due to the presence of the catalyst (as is the trend in conventional FTS [180, 199-201]), the H_2/CO ratio decreases, including near the catalyst surface. As a result, there is less hydrogen for methane formation, which in this work translated to a reduction in the methane concentration from 9317 ppm at 8 MPa to 7995 ppm at 10 MPa. This lower hydrogen availability coupled with higher pressures may have also contributed to solid carbon formation on the catalyst surface, as mentioned above.

The formation of liquid and solid phases, discussed above, corresponded to a higher pressure drop than that observed for the blank catalyst as shown in Table 6.2 above (Section 6.2.1.4). For the 2 wt% Co catalyst, pressure drops of 0.31 and 0.87 MPa were obtained for the 10 and 60 s studies, respectively, which were approximately 2 and 3 times higher than the blank catalyst's pressure drops.

Table 6.2: Pressure drop (immediately after the treatment period) for the pure plasma, blank catalyst, 2 and 6 wt% Co catalysts systems at different operating pressures and discharge times of 10 and 60 s.

	ΔP_{drop} / MPa							
Operating	Pure plasma		Blank		2 wt% Co		6 wt% Co	
Pressure / MPa	10 s	60 s	10 s	60 s	10 s	60 s	10 s	60 s
1	0,00	0,00	0,01	0,01	0,00	0,01	0,00	0,00
2	0,01	0,00	0,01	0,01	0,01	0,03	0,00	0,03
4	0,03	0,00	0,03	0,02	0,02	0,03	0,00	0,03
6	-0,01	0,01	0,03	0,05	0,03	0,07	0,02	0,15
8	0,00	0,02	0,05	0,12	0,11	0,17	0,04	-
10	-0,01	0,07	0,16	0,30	0,31	0,87	0,31	0,95*

*Arc discharge extinguished at 12 s.

The results presented in Section 6.2.1.5 showed that the 2 wt% Co catalyst significantly improved the hydrocarbon yields compared to the blank catalyst and pure plasma FTS systems. In addition, carbon deposition was reported. Subsequently, a higher cobalt loading of 6 wt% was investigated in an attempt to reduce deposition, increase the FTS activity and understand the fundamental effects of different cobalt loadings on plasma-catalytic interactions. These findings are discussed in the next section.

6.2.1.6 Plasma-catalysis: 6 wt% Co catalyst

For the pure plasma, blank and 2 wt% Co catalyst studies, the arc discharge was stable throughout the pressure range of 1 to 10 MPa at both discharge periods of 10 and 60 s. However, for plasma-catalysis at 60 s using a 6 wt% Co catalyst, the arc discharge was unstable beyond 6 MPa and it extinguished before completion of the 60 s discharge period. Extinguishing of the arc was due to condensation of water at higher pressures.

Liquid water was also observed for the 2 wt% Co catalyst but the arc remained stable. However, arc instability for the 6 wt% Co catalyst was due to the production of higher yields of water, related to an increase in CO dissociation (inferring that more oxygen was available for water production) as a result of the higher Co loading. Since the arc was ignited by contact of the electrodes, re-striking of the arc instantaneously after extinguishing was practically impossible under the low current and very high pressure conditions in accordance with Paschen's law.

The arc extinguished more rapidly as pressure increased i.e. the arc extinguished at ~30 s for the 7 MPa experiment and at ~12 s for the 10 MPa experiment. At 10 MPa and ~12 s, the methane, ethane, ethylene, propane and propylene concentrations were 32 598, 268, 61, 51 and 30 ppm, respectively, shown in Figures 6.4.a to 6.4.e below.

.

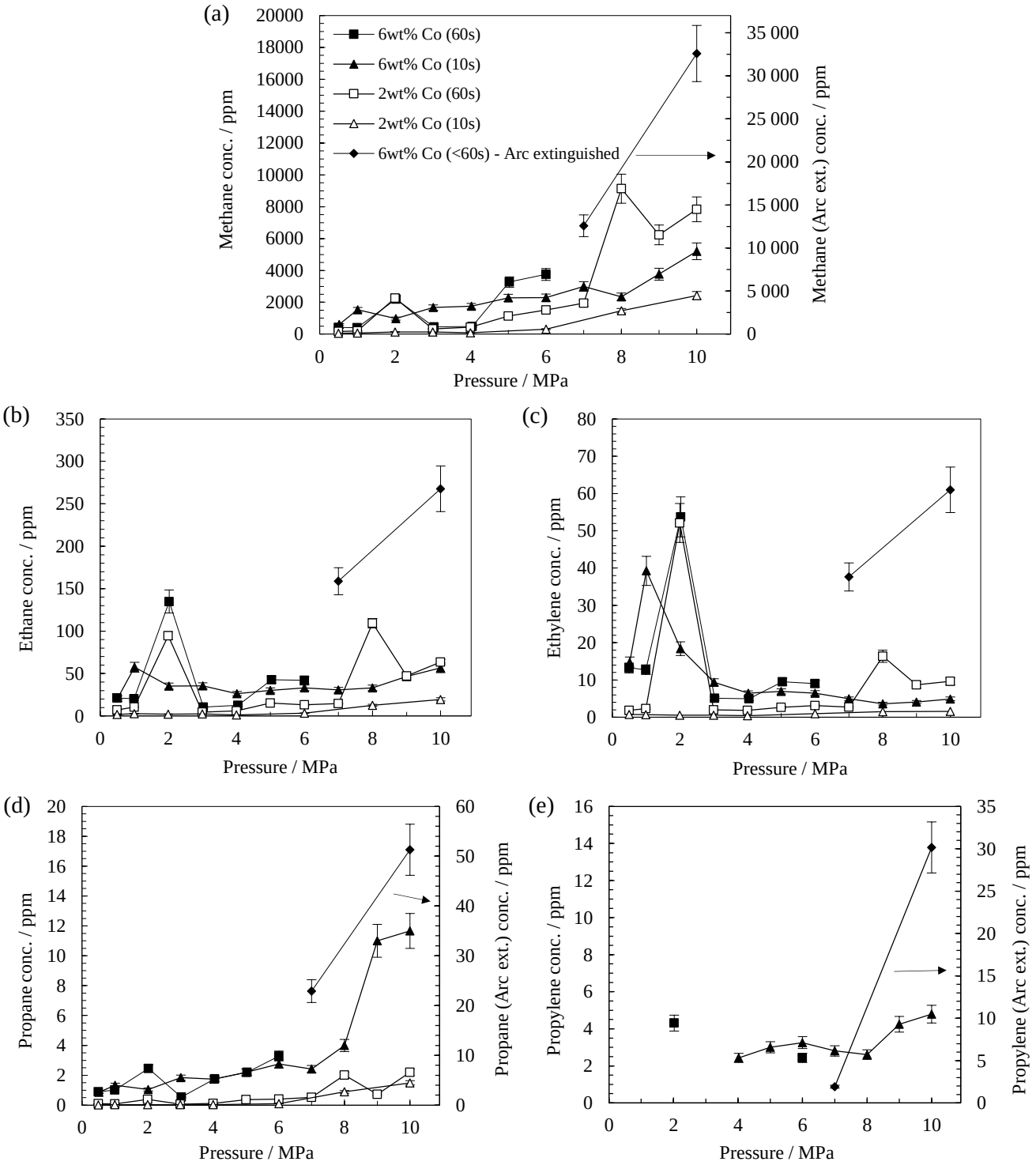

Figure 6.4: The influence of pressure on hydrocarbon concentration for plasma-catalytic FTS (NTP + 2 or 6 wt% Co catalyst) at discharge times of 10 and 60 s; (a) methane, (b) ethane, (c) ethylene, (d) propane and (e) propylene. **Legend:** ■ – 6 wt% Co (60 s); ▲ – 6 wt% Co (10 s); □ – 2 wt% Co (60 s); ∆ – 2 wt% Co (10 s); ♦ - 6 wt % Co (arc extinguished < 60 s). **Operating conditions:** Syngas ratio: 2.2:1; current: 350 mA; inter-electrode gap: 1 mm; wall temperature: 25ºC. **Error bars (vertical):** Expanded experimental hydrocarbon concentration uncertainty of ±11%.

Although these were the highest hydrocarbon yields obtained in the entirety of this project, operating at this pressure was avoided due to extinguishing of the arc, which was caused by the arc unhinging from the anodic root and jumping to the ceramic insulator that held the cathode, resulting in 'burning' of the insulation material as shown in Photograph 6.1. The insulator could not be re-used as it prohibited ignition of the arc in subsequent experiments, thus requiring a replacement insulator.

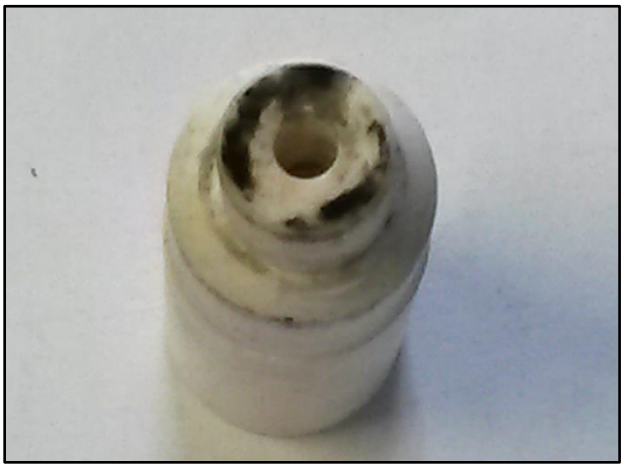

Photograph 6.1: Image depicting the cathode ceramic insulator (supplied by Ceradvance Engineering Ceramics), which was 'burnt' during the 6 wt% Co catalytic experiments at 60 s and between 7-10 MPa.

Owing to these limitations and to avoid instrumentation damage, plasma-catalysis using the 6 wt% Co catalyst for the discharge time of 60 s was restricted to the pressure range of 1 to 6 MPa. However, for plasma-catalysis at 10 s, the arc was stable between 0.5 and 10 MPa due to lower water yields as a result of the reduced discharge time.

The 6 wt% Co catalyst produced higher hydrocarbon yields for the 10 and 60 s experiments than the 2 wt% Co catalyst, as shown by the concentration-pressure plots in Figures 6.4.a to 6.4.e above. At 2 MPa, there was a sharp rise in all yields for the 6 wt% Co catalyst similar to the 2 wt% Co catalyst results. The longer 60 s treatment time for the 6 wt% Co catalyst was expected to lead to higher product yields than at 10 s, as in the case of the previous pure plasma, blank catalyst and 2 wt% Co catalyst systems investigated.

However, at 0.5, 1, 3 and 4 MPa the C_1 to C_3 hydrocarbon concentrations at 60 s were considerably lower than that at 10 s, inferring that within the additional 50 s, secondary reactions such as cracking or hydrogenolysis occurred that reduced the methane, ethane, ethylene and propane concentrations. Besides secondary reactions, which seemed much more prominent for the 10 s study (discussed in detail below), an increase in water formation due to the longer residence time of 60 s could have led to methane reduction.

Many studies reported a decrease in methane selectivity with increasing CO conversion (longer residence time), explained by an increase in H_2O formation causing a decrease in the H_2/CO ratio [180, 199-201], thus reducing the availability of hydrogen for hydrogenation to methane.

For the 6 wt% Co catalyst study at 10 s, where the arc remained stable up to 10 MPa; methane, propane and propylene concentrations generally increased with increasing pressure, especially at higher pressures between 8 and 10 MPa. However, the concentration of ethane decreased from 57 ppm at 1 MPa to 26 ppm at 4 MPa and increased to 57 ppm at 10 MPa. The ethylene concentration also decreased sharply from 39 ppm at 1 MPa to 6 ppm at 4 MPa and decreased marginally up to 10 MPa. This behaviour of ethylene formation differed from that of the previous studies at 10 s, where the ethylene yield increased at higher pressures.

This reduction of ethylene for the 10 s study and the decrease of the C_1 to C_3 hydrocarbon concentrations at 0.5, 1, 3 and 4 MPa for the 60 s study may be described by trends observed in conventional FTS using Co catalysts. There, the reduction of primary olefins occurred due to readsorption of olefins onto the catalyst surface, followed by secondary reactions (as mentioned above), such as hydrogenation to paraffins, reinsertion into growing chains, hydrogenolysis, cracking and isomerization [133, 194]. The type of secondary reaction that occurred depended on the process conditions, namely temperature, pressure and residence time. It has been reported that at 0.1 MPa (atmospheric pressure), secondary hydrogenation causing chain termination by paraffin formation is dominant, whereas at 1 and 2 MPa (a typical FTS operating pressure), reinsertion into growing chains becomes dominant [203-206].

In this work, maximum ethylene was produced at 1 MPa for the 10 s study and at 2 MPa for the 60 s. Ethylene generally decreased as pressure increased, especially for the 10 s study; whereas propane and propylene yields increased with pressure. This indicated that the secondary reinsertion of ethylene into C_3 hydrocarbon chains may have occurred.

Another potential secondary reaction involving readsorbed ethylene (and other olefins) was hydrogenolysis, indicated as the dominant secondary reaction above 550 K (277^{o}C) in conventional FTS. This reaction route reportedly caused a dramatic increase in methane selectivity with increasing CO conversion (longer residence time in conventional FTS) [207, 208]. It is likely that hydrogenolysis and cracking may have contributed to the high methane selectivity between 8 and 10 MPa, as it is believed that the cobalt catalyst could be heated to beyond 277^{o}C by plasma at these higher pressures i.e. the arc discharge temperature increased with operating pressure. However, it was shown in the literature that the catalyst activation

temperature could be significantly reduced by the active plasma species (pre-dissociated reactants) [75-88]. This topic is further discussed in Section 6.6.

It has been shown that ethylene was susceptible to readsorption and secondary reactions as in the literature. This was due to its high surface mobility and low activation energy barrier [194]. However, in addition to the secondary reactions, Bodke et al. [165] proposed the possibility of ethylene being trapped in the micro-pores on washcoated catalysts resulting in decomposition to form graphite. This could be the case here as graphite and carbon nanotubes (synthesized from graphite precursors) were detected on the catalyst surface as presented in Section 6.5.1.2.

In contrast to ethane, ethylene and propane being produced at all pressures for both discharge periods investigated, propylene was only formed between 4 and 10 MPa at 10 s (Figure 6.4.e), indicating that chain growth was directly influenced by pressure. In addition, it was only produced at 2 and 6 MPa (the highest pressure investigated) at 60 s (Figure 6.4.e) corresponding to the high ethane, ethylene and propane yields at these pressures. For the longer treatment time of 60 s, the absence of propylene at 4 and 5 MPa, and the lower yields at 6 MPa compared to the 10 s study, implied that propylene decomposition occurred during the additional 50 s. This trend could be explained by conventional FTS behaviour, where similarly, longer residence times were reported to decrease olefinicity (olefin to paraffin ratio) due to olefins being readsorbed and reinserted into growing chains [209].

In this work, propylene may have been readsorbed and hydrogenated to paraffins, especially propane, which slightly increased in concentration (by ~1 ppm) between 4 and 6 MPa (Figure 6.4.d). Furthermore, propylene was formed at lower pressures for the 6 wt% Co catalyst at 10 and 60 s as compared to only 10 MPa for pure plasma FTS (Figure 6.1.e).

These C_3 hydrocarbon results suggested that plasma-catalysis reduced the pressure required for chain growth. Propylene produced by the 6 wt% Co catalyst, absent for the 2 wt% Co catalyst, also suggested that a higher cobalt loading promoted chain growth. In addition, the 6 wt% Co catalyst only produced carbon deposits at the apex of the electrode tip compared to carbon coating the entire conical tip for the 2 wt% Co catalyst (as depicted in Photograph 6.2 below), again suggesting that the 6 wt% Co catalyst was more selective in producing chain growth monomers (CH_x) than compared to the 2 wt% Co catalyst producing more C-C chains.

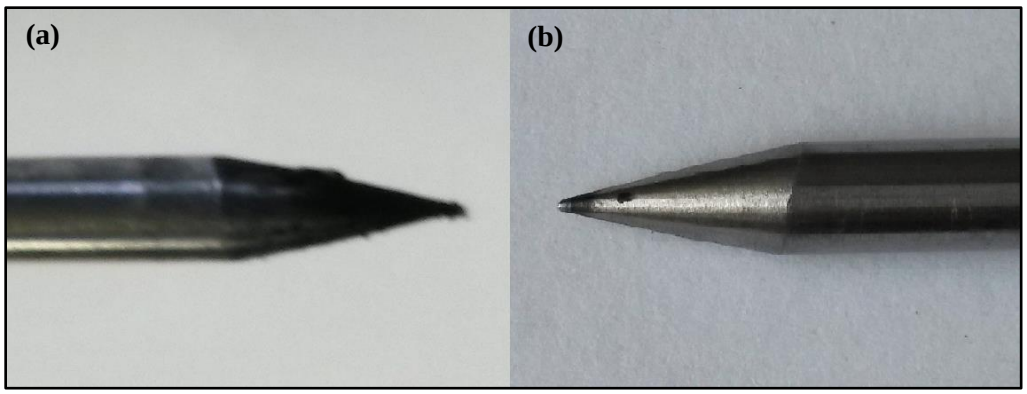

Photograph 6.2: Carbon deposits observed on the cathode's 60° conical tip for the (a) 2 wt% and (b) 6 wt% Co catalytic systems.

The results discussed in Section 6.2.1.6 showed that the 6 wt% Co catalyst was superior to the lower cobalt of 2 wt% in respect to chain growth, product yields and carbon deposition. A summary of the most promising results for the four systems investigated under the scope of the pressure variation study is presented in Section 6.2.1.7.

6.2.1.7 Summary of the pressure variation study

The previous sections (6.2.1.1 to 6.2.1.6) were dedicated to discussing the effects of pressure on hydrocarbon yields at discharge times of 10 and 60 s; where the focus was on describing the phenomena behind the concentration-pressure behaviour. This section provides a quantitative comparison of all four systems investigated at 10 and 60 s.

As discussed, for the pure plasma and blank catalyst systems, hydrocarbon yields generally increased with increasing pressure at both discharge periods of 10 and 60 s, with the maximum C_1-C_3 yields being obtained at 10 MPa. Furthermore, the blank catalyst study led to lower concentrations of hydrocarbons at all pressures investigated, producing less than 1 ppm of ethane and ethylene and no C_3 hydrocarbons at 10 and 60 s. The remainder of this section will focus on the improvement of these hydrocarbon yields by the 2 and 6 wt% Co catalytic systems.

Pressure variation study at 10 s

For the 10 study, the increasing concentration-pressure trends for the 2 wt% Co catalyst resembled that of the pure plasma and blank catalyst systems. The 6 wt% Co catalyst deviated from this behaviour, as discussed in Section 6.2.1.6, with the maximum ethylene and local maximum ethane yields being obtained at 1 MPa along with propylene being produced, which was not noticeable in other systems. Therefore, the

most favourable pressures for chain growth for the 10 s study were 1 MPa (especially for the 6 wt% Co catalyst) and 10 MPa (for the 2 and 6 wt% Co catalysts), which are presented in Table 6.3.

Table 6.3: Hydrocarbon concentrations for the pure plasma, blank, 2 and 6 wt% Co systems investigated at 1 and 10 MPa for a discharge time of 10 s. (Syngas ratio: 2.2:1; current: 350 mA; inter-electrode gap: 1 mm; wall temperature: 25^{o}C; expanded experimental hydrocarbon concentration uncertainty: ±11%).

Product	Conc. / ppm							
	Pure plasma		Blank		2 wt%Co		6 wt%Co	
	1 MPa	10 MPa	1 MPa	10 MPa	1 MPa	10 MPa	1 MPa	10 MPa
Methane	17	342	14	60	68	2428	1526	5200
C_2 hydrocarbons								
Ethane	0,6	1,3	0,4	0,2	2,8	19	57	57
Ethylene	0,1	0,3	0,05	0,1	0,7	1,6	39	5
C_3 hydrocarbons								
Propane	0,0	0,2	0,0	0,0	0,1	4,5	1,3	11,7
Propylene	0,0	0,0	0,0	0,0	0,0	0,0	0,0	4,8
Product ratio								
Methane/ ethane	29	270	32	308	24	125	27	92
Ethane/ ethylene	5,6	4,4	8,7	2,4	4,0	12,2	1,5	11,5

At 1 MPa and 10 s, the 6 wt% Co catalyst's methane, ethane, ethylene concentrations of 1526, 57 and 39 ppm, respectively, were 22, 20 and 56 times higher than that of the 2 wt% Co catalyst and 90, 95 and 390 times higher than that of pure plasma. At 10 MPa and 10 s, the 6 wt% Co catalyst's methane, ethane, ethylene and propane concentrations of 5200, 57, 5 and ~12 ppm, respectively, were 2, 3, 3 and 2 times higher than that of the 2 wt% Co catalyst and 15, 44, 17 and 59 times higher than that of pure plasma.

As mentioned, 1 and 10 MPa were the most favourable pressures for chain growth at 10 s. An additional chain growth indicator was the methane/ethane ratio (ratio of the two major products), listed in Table 6.3 above, which was used to determine the pressure at which methane was a minimum, due to methane being the least desired product in conventional FTS.

The methane/ethane ratio at 1 MPa for the pure plasma, blank catalyst, 2 and 6 wt% Co catalysts systems of 29, 32, 24 and 27, respectively, were 9, 10, 5 and 3 times less than that at 10 MPa. The higher ratios at 10 MPa were probably due to the higher arc temperature favouring methanation. Furthermore, the 2 and 6 wt% Co catalysts had the lowest ratios, indicating the promotion of chain growth.

In concluding the 10 s study, the 6 wt% Co catalyst was shown to be the optimal system and it provided the option of higher C_2 hydrocarbons at 1 MPa or higher C_3 hydrocarbons at 10 MPa.

Pressure variation study at 60 s

In general, the longer residence time of 60 s led to higher C_1-C_3 hydrocarbon concentrations, exhibited in the pure plasma and plasma-catalytic FTS experiments. These trends concurred with those of conventional FTS, in which the quantities of olefins and paraffins with higher carbon numbers and water partial pressure increased as the CO conversion increased with residence time [202, 210].

The concentration-pressure trends for the 2 and 6 wt% Co catalysts at 60 s were more complex and did not closely follow the pure plasma behaviour in that maximum hydrocarbons were produced at either 2 or 10 MPa. For the 2 wt% Co catalytic study at 60 s, the highest paraffin yields (methane, ethane and propane) were obtained at 10 MPa with local maxima at 2 MPa. At this pressure the maximum ethylene yield was also attained. For the 6 wt% Co catalytic study at 60 s, the maximum methane and propane yields were obtained at 6 MPa (due to the arc discharge extinguishing above 6 MPa), whereas the maximum ethane, ethylene and propylene yields were obtained at 2 MPa. Therefore, the most favourable pressures for chain growth for the 60 s study were 2 MPa (for the 2 and 6 wt% Co catalysts) and 10 MPa (for the 2 wt% Co catalyst), which are presented in Table 6.4 below.

At 2 MPa and 60 s, the 6 wt% Co catalyst's methane, ethane, ethylene and propane concentrations of 2194, 135, 54 and 2.5 ppm, respectively, were similar to the yields of 2266, 95, 52, 1.2 ppm for the 2 wt% Co catalyst; apart from the 6 wt% Co catalyst producing 1.4 times more ethane. In addition, these 6 wt% Co catalyst's methane, ethane, ethylene and propane yields were 46, 96, 270 and 25 times higher than that of pure plasma. At 10 MPa and 60 s, the 2 wt% Co catalyst's methane, ethane, ethylene and propane yields of 7836, 64, 9.6 and 6.6 ppm, respectively, were 10, 4, 3 and 2 times higher than that of pure plasma.

Table 6.4: Hydrocarbon concentrations for the pure plasma, blank, 2 and 6 wt% Co systems investigated at 2 and 10 MPa for a discharge time of 60 s. (Syngas ratio: 2.2:1; current: 350 mA; inter-electrode gap: 1 mm; wall temperature: 25°C; expanded experimental hydrocarbon concentration uncertainty: ±11%).

Product	Conc. / ppm							
	Pure plasma		Blank		2 wt%Co		6 wt%Co	
	2 MPa	10 MPa	2 MPa	10 MPa	2 MPa	10 MPa	2 MPa	6 MPa
Methane	48	772	31	269	2266	7836	2194	3749
				C_2 hydrocarbons				
Ethane	1,4	16	0,8	0,8	95	64	135	42
Ethylene	0,2	3,4	0,1	0,1	52	9,6	54	9,0
				C_3 hydrocarbons				
Propane	0,1	2,8	0,0	0,1	1,2	6,6	2,5	3,3
Propylene	0,0	1,2	0,0	0,0	0,0	0,0	4,3	2,4
				Product ratio				
Methane/ ethane	34	47	39	317	24	123	16	89
Ethane/ ethylene	8,2	4,8	11,1	10,9	1,8	6,6	2,5	4,7

Similarly to the 10 s study, a lower methane/ethane ratio was achieved at the lower pressure for the 60 s study, in this case 2 MPa. The methane/ethane ratio at 2 MPa for the pure plasma, blank catalyst, 2 and 6 wt% Co catalysts systems of 34, 39, 24 and 16, respectively, were 1.4, 8, 5 and 5.6 times lower than the ratios at 10 MPa. A similar trend was seen for the ethane/ethylene or paraffin/olefin ratio (where the olefin/paraffin ratio was typically used as a performance factor in conventional FTS). The lowest ethane/ethylene ratios for the 2 and 6 wt% Co catalysts were obtained at 2 MPa, indicating that this pressure favoured olefin formation, which was desired in conventional FTS.

Furthermore, the 6 wt% Co catalyst had the highest C_3 hydrocarbon yields at 2 MPa, indicating that an increase in cobalt loading promoted chain growth. In conclusion, for the 60 s study, optimal chain growth and olefinicity was achieved at 2 MPa using the 6 wt% Co catalyst.

The highest product yields and the corresponding pressures were discussed in Section 6.2.1.7, with the phenomena behind these trends being described in Sections 6.2.1.1 to 6.2.1.6. However, in order to determine the most energy efficient system and the optimum operating conditions, the energy consumption of the pure plasma and plasma-catalytic FTS processes are compared in Section 6.2.2.

6.2.2 The influence of pressure on energy consumption

Energy consumption is one of the most important performance factors for plasma-chemical processes. The electrical energy for non-thermal plasmas (NTPs) is usually selectively focused on the discharge generation without significantly heating the bulk gas. This is evident from the maximum bulk gas temperature increase of 11°C above room temperature for an arc core temperature that was usually in the range of 10 000 to 20 000 K [158, 211]. The energy requirements were evaluated by means of the specific input energy per mole of syngas (SIE), and the specific required energy per mole of methane produced (SRE), which were calculated using the following equations:

$$E\ (kJ) = V_{rms} I_{rms} \Delta t \tag{6.5}$$

$$SIE\left(kJ/n_{syngas}\right) = \frac{E}{n_{syngas}} \text{ , where } n_{syngas} = \frac{PV_{reactor}}{RT} \tag{6.6}$$

$$SRE\left(MJ/n_{CH_4,produced}\right) = \frac{E}{n_{CH_4,after} - n_{CH_4,before}} \tag{6.7}$$

Where V_{rms} and I_{rms} are the rms voltage and current, respectively; Δt is the discharge period of 10 or 60 s; E represents the electrical energy supplied to generate the arc discharge; n_{syngas} is the moles of syngas, which is dependent on the universal gas constant (R) as well as the syngas pressure (P), volume ($V_{reactor}$) and (ambient) temperature (T); and lastly n_{CH4} denotes the concentration of methane in the reactor before and after the discharge period of 10 or 60 s.

Ignition of the arc discharge could not be undertaken at an initial inter-electrode gap of 1 mm due to the high electrical resistance of the gas between the electrodes at high pressure. Therefore, the arc was ignited with the electrodes initially in contact. Since the electrical resistance of the gas was negligible when the electrodes were in contact, the input voltage reported below was assumed to be the breakdown voltage - the minimum voltage required for electrical breakdown of a gas in order to generate a plasma.

Voltage

For the pressure variation study, the ignition current was fixed at 350 mA and the input voltage was fixed

at 8 kV. The voltage of 8kV was set as a safety measure in order to provide sufficient time for the operator to manually shut down the power supply in the event of a sudden voltage surge. Since the direct current (DC) power supply was a constant current system, the voltage applied across the electrodes was automatically self-adjusted in order to maintain the fixed current. The variation of the self-adjusted rms voltage with pressure is presented in Figures 6.5.a and 6.5.b. The rms voltage (evaluated in Appendix D) was the average of the voltage signal recorded by the digital oscilloscope, which consisted of 10 000 and 60 000 voltage values acquired during the 10 s and 60 s discharge periods respectively.

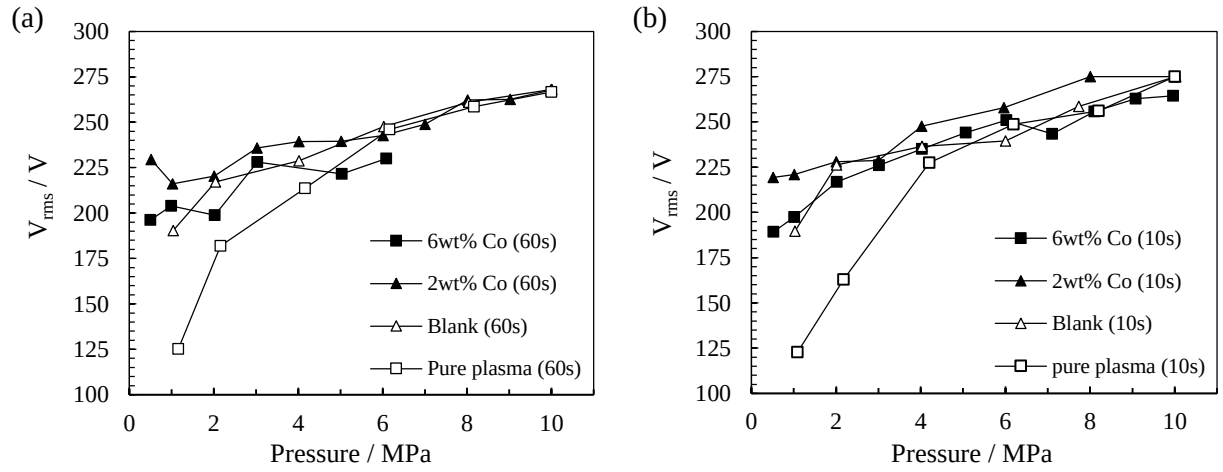

Figure 6.5: The influence of pressure on rms voltage for pure plasma FTS and plasma-catalytic FTS (NTP + Blank, 2 or 6 wt% Co catalyst) at discharge times of (a) 60 s and (b) 10 s. **Legend:** ■ – 6 wt% Co; ▲ – 2 wt% Co; ∆ – Blank; □ – Pure plasma. **Operating conditions:** Syngas ratio: 2.2:1; current: 350 mA; inter-electrode gap: 1 mm; wall temperature: 25^{o}C.

For all four systems tested, the general trend was that higher voltages were required at higher operating pressures for the electrical breakdown of syngas and ignition of an arc discharge. Similar trends were also reported by Fulcheri et al. [12] for a helium arc discharge and by Iwarere et al. [14] for a syngas arc discharge. The phenomena responsible for these voltage/concentration-pressure behaviour are discussed below.

At higher pressures (higher mass density), the collisional frequency between the electrons and syngas molecules increased. As a result of the higher plasma resistivity, a hotter and wider arc column was generated [43, 60]. The higher the arc temperature, the greater the density gradients between the arc (10 000 to 20 000 K) and cold bulk gas, thus leading to greater convective heat losses. In response to these convective losses, which caused greater load variations, the power supply automatically increased the input

voltage in order to maintain the supply current set-point of 350 mA. From a physics standpoint, this meant that the voltage increased in order to sustain electrical breakdown by increasing the electron density and mean electron energy of the gas and the related stability of the arc in response to the convective losses.

In addition to the operating pressure affecting the voltage behaviour, the supply voltage was also influenced by the presence of the catalyst in the reactor as seen in Figures 6.5.a and 6.5.b above. Below 6 MPa, lower voltages were required for pure plasma than plasma-catalysis. At 1 MPa, the voltage of 125 V for pure plasma was 52, 73 and 63% lower than the voltages of 190, 216 and 204 V for the blank, 2 and 6 wt% Co catalysts respectively. This pure plasma voltage increased more rapidly (by 121 V) between 1 and 6 MPa than the blank (57 V), 2 wt% Co (27 V) and 6 wt% Co (26 V) catalysts. The rapid increase in the pure plasma voltage by more than twofold between 1 and 6 MPa was probably due to the reactor (syngas) volume being more than double that of the plasma-catalytic systems i.e. the reactor volume was reduced by the presence of the catalyst. The larger volume (with the catalyst absent) meant that greater temperature gradients existed between the hot arc and cold bulk gas, making the pure plasma system more sensitive to pressure variations; hence the relatively steep voltage-pressure curve.

In contrast to the varying voltage-pressure trends for pure plasma and plasma-catalytic FTS below 6 MPa; between 6 and 10 MPa, all systems required similar input voltages (power) as seen by the plateauing voltage-pressure plots in Figure 6.5. For these similar input powers, the 2 and 6 wt% Co catalytic systems produced significantly higher hydrocarbon yields than pure plasma and the blank catalyst at 10 and 60 s. These results suggested that the cobalt catalysts contributed significantly to the FTS activity, revealing the plasma-catalyst synergistic effects.

The voltage-pressure relationship discussed above was mirrored by the bulk gas temperature-pressure behaviour, presented as the change in reactor temperature (ΔT) in Figure 6.6 below, i.e. the difference between the maximum and initial temperatures measured during the 60 s experiment. The rapid increase in input voltage (synonymous with power) from 1 to 6 MPa, shown in Figure 6.5 above, led to a greater heating of the bulk gas by 3.5^{o}C (from 1 to 6 MPa) for pure plasma, compared to 2.3^{o}C, 0.2^{o}C and 1.3^{o}C for the blank catalyst, 2 and 6 wt% Co catalytic systems respectively.

Temperature

It was shown above that the pure plasma system was the most sensitive to voltage-pressure variations, which was also reflected in the temperature-pressure behaviour. This temperature relationship has implications for the plasma-catalytic systems. That is, the degree of bulk gas heating (as reflected by ΔT in

Figure 6.6 below) for the plasma-catalytic systems, were lower than that for pure plasma, especially at higher pressures between 6 and 10 MPa where the input voltages were similar (as mentioned above). These lower bulk gas temperatures for the plasma-catalytic systems indicated that heat was consumed by the catalyst - both the catalyst and bulk gas were heated by the hot arc in plasma-catalysis leading to a lower ΔT - with greater catalyst heating occurring at higher pressures. Whereas, only the bulk gas was heated in pure plasma FTS.

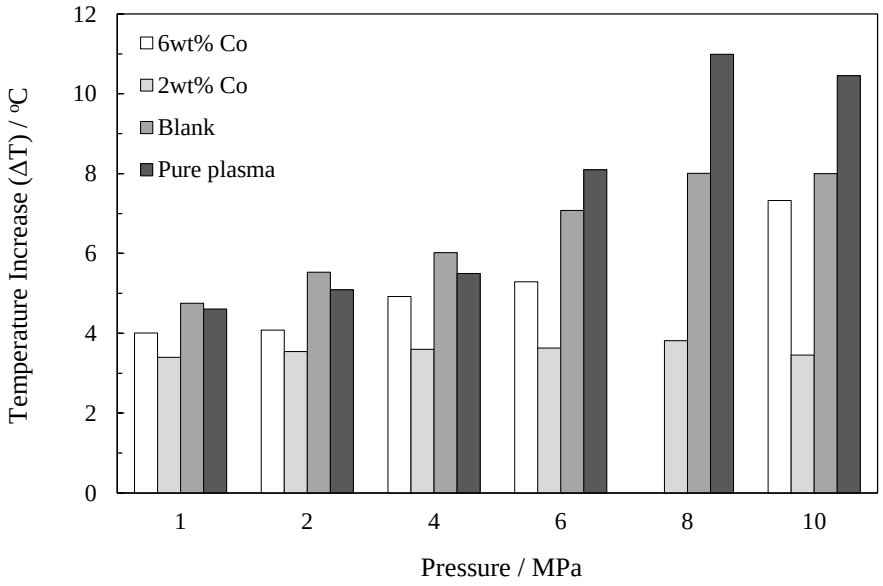

Figure 6.6: The temperature increase (ΔT) as a function of operating pressure for pure plasma and plasma-catalytic FTS (NTP + Blank, 2 or 6 wt% Co catalyst) at a discharge time of 60 s (N.B. the discharge time for the 6 wt% Co catalyst at 10 MPa was ~12 s). **Legend:** □ – 6 wt% Co; ■ – 2 wt% Co; ■ – Blank; ■ – Pure plasma. **Operating conditions:** Syngas ratio: 2.2:1; current: 350 mA; inter-electrode gap: 1 mm; wall temperature: 25ºC.

According to the ΔT-pressure trends in Figure 6.6 above, the order of decreasing catalyst heating was: Blank > 6 wt% Co > 2 wt% Co. The greater heating of the 6 wt% Co catalyst compared to the 2 wt% Co catalyst (implying a higher degree of thermal activation), compounded with the larger active cobalt sites (due to the higher loading), were the most probable factors that led to the highest quantities of hydrocarbon products being produced by the 6 wt% Co catalyst (as shown in Figure 6.4, and Tables 6.3 and 6.4).

In contrast, the blank catalyst was heated to a greater degree than the 2 and 6 wt% Co catalysts but produced the lowest yields of hydrocarbon. This was due to the absence of active Co active sites needed to promote FTS as well as the presence of γ-Al_2O_3 and mullite in the blank catalyst that promoted other reaction

pathways. The potential reaction pathways for the blank catalyst, discussed in Section 6.2.1.4, included enhanced CO chemisorption and carbonaceous species formation.

In addition to the bulk gas temperature increase (ΔT), the bulk gas pressure increase (ΔP), presented in Figure 6.7, as well as the discharge volume and luminosity (observed via a sightglass), generally increased with operating pressure. The escalation of these phenomena with pressure are typical of arc discharges.

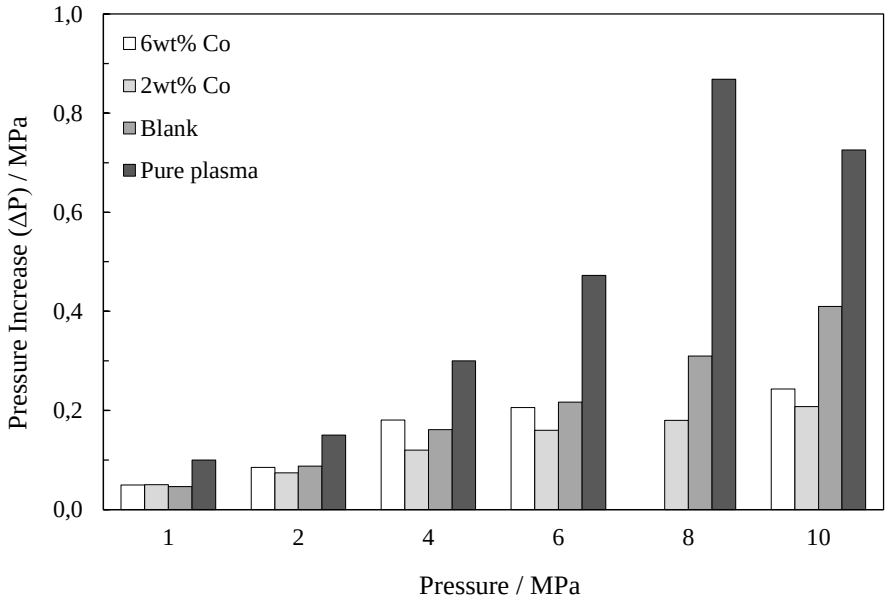

Figure 6.7: The pressure increase (ΔP) as a function of (initial) operating pressure for pure plasma and plasma-catalytic FTS (NTP + Blank, 2 or 6 wt% Co catalyst) at a discharge time of 60 s. **Legend:** □ – 6 wt% Co (N.B. the discharge time for the 6 wt% Co catalyst at 10 MPa was ~12 s); ■ – 2 wt% Co; ■ – Blank; ■ – Pure plasma. **Operating conditions:** Syngas ratio: 2.2:1; current: 350 mA; inter-electrode gap: 1 mm; wall temperature: 25ºC.

Specific input energy (SIE)

The specific input energy (kJ/mol$_{syngas}$) or SIE represented the electrical energy injected per mole of syngas. The SIE versus pressure plots for the pure plasma and plasma-catalytic systems are presented in Figure 6.8. The SIE values were directly related to the treatment time. That is, the SIE values for the 60 s treatment time were an average of 6 times greater than that for the 10 s treatment. All trends also showed that more energy was injected per mole of syngas at lower pressures (lower mass density). The higher SIE values and corresponding lower product yields at lower pressures suggested that more energy was spent on heating the bulk gas. Whereas, at higher pressures the opposite trends were observed with energy consumption improving as energy was more selectively focused on synthesising hydrocarbons.

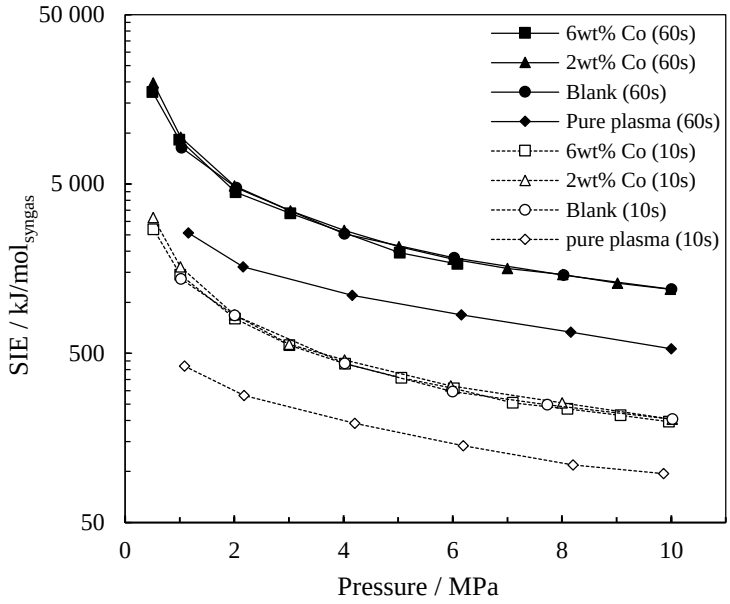

Figure 6.8: Specific input energy (kJ/mol$_{syngas}$) as a function of pressure for pure plasma and plasma-catalytic FTS (NTP + Blank, 2 or 6 wt% Co catalyst) at discharge times of 10 and 60 s. **Legend:** ■ – 6 wt% Co (60 s); ▲ – 2 wt% Co (60 s); ● – Blank (60 s); ♦ – Pure plasma (60 s); □ – 6 wt% Co (10 s); ∆ – 2 wt% Co (10 s); ○ – Blank (10 s); ◊ – Pure plasma (10 s). **Operating conditions:** Syngas ratio: 2.2:1; current: 350 mA; inter-electrode gap: 1 mm; wall temperature: 25ºC.

Specific required energy (SRE)

The final factor for determining the energetic performance was the specific required energy (MJ/mol$_{methane,prod}$) or SRE, which indicates the amount of energy required for the production of a single mole of methane. The SRE was determined for methane as it was the major synthesis product. A lower SRE value corresponded to a higher energy efficiency for the process. The energy efficiency is usually measured as a ratio of power consumed by plasma chemical-processes to the power on the supply terminals. This is usually low in electrical discharges because a large portion of the electrical energy is converted into heat and light instead of being transferred into chemical energy.

The general trend of the plots in Figure 6.9 below showed that less energy was required to produce methane at higher pressures; where the plateauing of the voltage-pressure curves (Figure 6.7 above) between 8 and 10 MPa for the 10 and 60 s studies were indicative of higher energy efficiency at higher pressures. For example, for the pure plasma study at 60 s the SRE (688 MJ/mol$_{CH4,prod}$) at 10 MPa was 116 times lower than the SRE at 1 MPa (79 828 MJ/mol$_{CH4,prod}$). This was because at higher pressures (higher mass densities), the electron-molecule collisions were more frequent due to shorter collisions paths, thus reducing the energy required for reactant (H_2 + CO) ionisation, dissociation and chain growth.

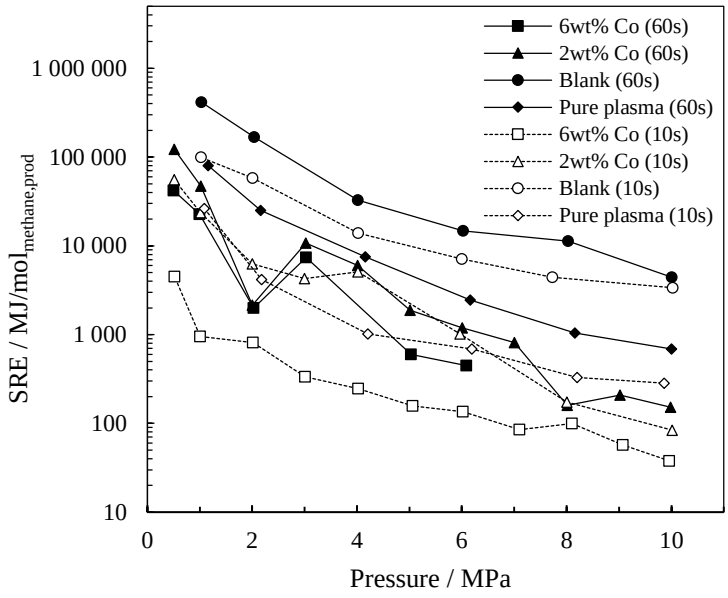

Figure 6.9: Specific required energy (MJ/$mol_{methane,prod}$) as a function of pressure for pure plasma and plasma-catalytic FTS (NTP + Blank, 2 or 6 wt% Co catalyst) at discharge time of 10 and 60 s. **Legend:** ■ – 6 wt% Co (60 s); ▲ – 2 wt% Co (60 s); ● – Blank (60 s); ♦ – Pure plasma (60 s); □ – 6 wt% Co (10 s); ∆ – 2 wt% Co (10 s); ○ – Blank (10 s); ◊ – Pure plasma (10 s). **Operating conditions:** Syngas ratio: 2.2:1; current: 350 mA; inter-electrode gap: 1 mm; wall temperature: 25^{o}C.

Optimum conditions

The minimum SIE and SRE values and the maximum concentrations for the C_1-C_3 hydrocarbons at 10 s, corresponded to the highest operating pressure of 10 MPa, which was considered the optimum operating pressure. At these conditions, the most energy efficient system was the 6 wt% Co catalyst as determined by the SRE value of 38 MJ/$mol_{CH4,prod}$, which was ~2.2 times lower than 2 wt% Co catalyst (84 MJ/$mol_{CH4,prod}$), 7.5 times lower than pure plasma (284 MJ/$mol_{CH4,prod}$) and 89 times lower than the blank catalyst (3307 MJ/$mol_{CH4,prod}$).

For the 60 s study, the highest C_2 and C_3 yields were obtained at 2 MPa for the 6 wt% Co catalyst corresponding to a SRE value of 1991 MJ/$mol_{CH4,prod}$. This was not a minimum SRE value for the 60 s study, which was obtained at 6 MPa (448 MJ/$mol_{methane,prod}$). The primary objective at this exploratory stage of FTS research was to improve chain growth and yields. Therefore, a trade-off between product yields, chain growth and energy consumption favoured 2 MPa as the optimum operating pressure for the 60 s study.

The optimum operating conditions related to the highest product yields and lowest energy consumption, or a trade-off of these factors, were reported in Section 6.2.2. The pressure variation study was discussed in extensive detail as pressure is a vital parameter in conventional FTS. But more importantly, a major focus of experimentation, using the recently developed arc discharge reactor, has been to understand the influence of high pressures on reactivity. The second parameter studied, current, is briefly discussed in the following section.

6.3 Current variation study

6.3.1 The influence of current on FTS products yields

In the current variation study, the supply current was varied between 250 and 450 mA for a discharge time of 60 s, a fixed pressure of 2 MPa and a fixed inter-electrode gap of 1 mm. Higher pressures led to an unstable arc or ultimately extinguishing of the arc. The latter arc behaviour was the case for the pressure variation study using the 6 wt% Co catalyst above 6 MPa and at a fixed current of 350 mA (discussed in Section 6.2.1.6). Therefore, the pressure of 2 MPa was used as a low pressure allowed ignition and good stability of the arc discharge at the lower currents (< 350 mA) in the range investigated. In addition, by operating at 2 MPa for the pressure variation study at 350 mA, 1 mm and 60 s, maximum concentrations of ethane, ethylene and propylene and local maxima for methane and propane were obtained. In addition, the lowest methane/ethane and ethane/ethylene ratios were also achieved at 2 MPa.

In pure plasma FTS, a stable arc discharge was generated throughout the current range of 250 to 450 mA for a discharge time of 60 s. The C_1-C_3 hydrocarbon concentrations shown in Figures 6.10.a to 6.10.d below are generally higher at lower currents with the maximum yields of methane (97 ppm), ethane (4 ppm), ethylene (14 ppm) and propane (0.3 ppm) obtained at the lowest current of 250 mA. The methane concentration at 250 mA was twice that obtained at 350 mA (the fixed current used in the pressure variation study). The reason for this trend was that at lower currents the bulk gas and electrons were further from thermal equilibrium, enabling electrons to focus their energy on plasma reactions instead of heating the bulk gas. The yields for the blank catalyst, which generally decreased with increasing current, were lower than that for pure plasma in the current range investigated. In addition, the blank catalyst only produced propane at 450 mA, verifying that the blank catalyst was ineffective in promoting chain growth, probably due to the reasons explained in the pressure variation study (Section 6.2.1.4).

The effect of cobalt loading could be seen by the improvement in C_1-C_3 hydrocarbon concentrations for the 2 and 6 wt% Co catalysts. For the 6 wt% Co catalyst, a glow-like transition discharge or arc-to-glow transition discharge (emitting a pale orange light at the cathode tip), was generated at 250 and 300 mA, whereas an arc discharge (seen as a bright blue/white column), was generated at 350, 400 and 450 mA.

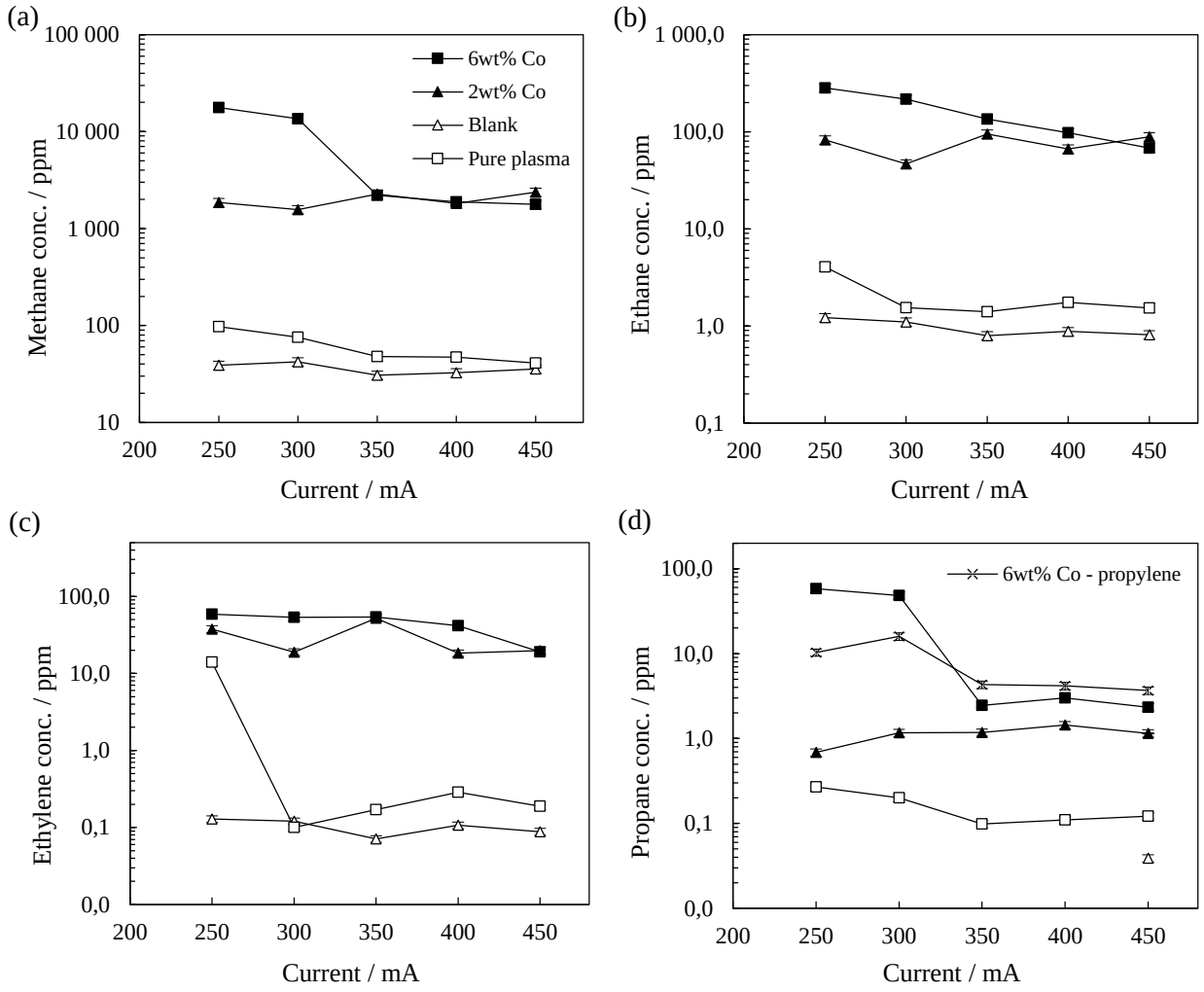

Figure 6.10: The influence of current on hydrocarbon concentration for pure plasma and plasma-catalytic FTS (NTP + Blank, 2 or 6 wt% Co catalyst) at a discharge time of 60 s; (a) methane, (b) ethane, (c) ethylene and (d) propane/propylene. **Legend:** ■ – 6 wt% Co; ▲ – 2 wt% Co; ∆ – Blank; □ – Pure plasma; x – 6 wt% Co (propylene). **Operating conditions:** Syngas ratio: 2.2:1; pressure: 2 MPa; inter-electrode gap: 1 mm; wall temperature: 25°C. **Error bars (vertical):** Expanded experimental hydrocarbon concentration uncertainty of ±11%.

Much research has focussed on the transition from a glow-to-arc discharge due to the attractiveness of the glow discharge in research and industrial applications. Kunhardt [212] stated that the glow–to–arc transition (GAT) occurs due to the instability of the glow discharge at near and above atmospheric pressure owing to the discharge contracting and tending towards thermal equilibrium, caused by heating of the neutral particles as well as the cathode overheating, which result in thermionic emission of electrons from the cathode, thus replacing secondary electron emission [49].

Since an opposite transition seems to occur in this work - an arc-to-glow transition, converse phenomena were valid in which the arc tended to traverse further away from thermal equilibrium towards the glow region. In addition, GAT in glow discharges occurred as a result of increasing the current at constant pressure or increasing the pressure at constant current [213]. An Inverse of this trend, decreasing the current (from 350 mA studied in the pressure variation study to 250 and 300 mA in the current variations study) at a constant pressure of 2 MPa, was aligned with the arc-to-glow transition in this work. This transitional behaviour was not observed in pure plasma FTS, and was therefore assigned to plasma-catalytic interactions modifying the electrical characteristics of the plasma as suggested by van Durme et al. [109] and other authors [74, 100].

In the 6 wt% Co catalyst study, the highest methane (17 729 ppm), ethane (282 ppm), ethylene (59 ppm), propane (58 ppm) and propylene (10 ppm) yields were obtained at the lowest pressure of 250 mA (glow-like discharge). These were approximately 8, 2, 1, 24 and 2.4 times higher, respectively, than that obtained in the arc discharge regime at 350 mA, which was due to the volumetric nature (larger treatment volume) of the glow-like discharge. The results also showed that C_3 hydrocarbon production, especially propane, was favoured in the lower current range of 250 to 350 mA. In addition, propylene was only produced for the 6 wt% Co catalyst proving that a higher Co loading promoted chain growth. The effects of plasma-catalysis were also clearly noticeable in that the maximum methane, ethane, ethylene and propane concentrations obtained at 250 mA, were 182, 69, 4 and 215 times greater, respectively, than the pure plasma concentrations obtained at the same current.

The concentration-current behaviour for the 2 wt% Co catalyst was more complex and did not follow the trend obtained for the pure plasma and 6 wt% Co catalyst. The trend deviated in that the maximum methane (2266 ppm), ethane (95 ppm) and ethylene (52 ppm) concentrations were obtained at 350 mA rather than at 250 mA. Hence, production at lower currents was less effective for the 2 wt% Co catalyst.

The 2 wt% Co catalyst's concentration-current behaviour cannot be attributed to an anomaly in the supply voltage as all systems displayed similar voltage-current trends as shown in Figure 6.11 (discussed in Section 6.3.2 below). Therefore, this deviation could probably have been due to the deposition of carbon on the electrode tip (as shown in Photograph 6.2 in Section 6.2.1.6), which was either absent or minutely present in the pure plasma, blank and 6 wt% Co catalytic systems. Carbonaceous species, formed by the 2 wt% Co catalyst system, could have either competed with hydrocarbons for carbon monomer species or could have attracted electrons and charged particles due to their electrical conductive nature [214], thus minimising the interaction of plasma species with syngas and causing a decline in the paraffin yields at 250 and 300 mA.

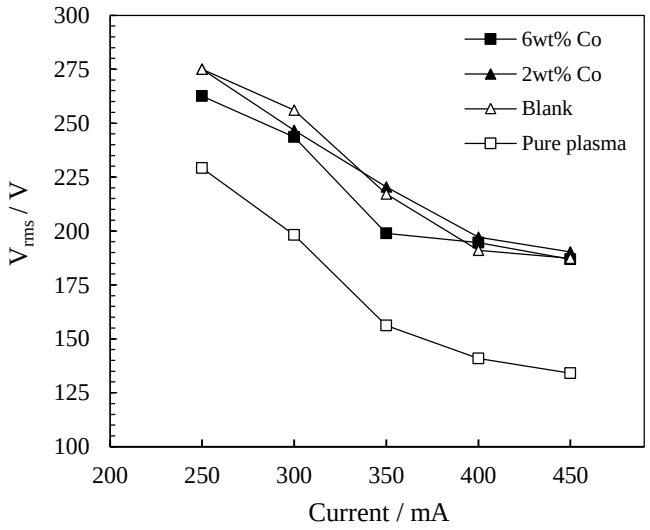

Figure 6.11: The influence of current on rms voltage for pure plasma and plasma-catalytic FTS (NTP + Blank, 2 or 6 wt% Co catalyst) at a discharge time of 60 s. **Legend:** ■ – 6 wt% Co; ▲ – 2 wt% Co; ∆ – Blank; □ – Pure plasma. **Operating conditions:** Syngas ratio: 2.2:1; pressure: 2 MPa; inter-electrode gap: 1 mm; wall temperature: 25^{o}C.

6.3.2 The influence of current on energy consumption

As in the pressure variation study; the pure plasma FTS results for the current variation study from this work were compared to that by Iwarere et al. [4] in order to validate the accuracy of the experimental techniques and instruments used in the plasma-catalytic FTS study. While Iwarere et al. achieved higher supply voltages (power) of approximately 450-250 V for a current range of 0.25-0.4 mA at a fixed pressure of 0.5 MPa, 250-134 V at 2 MPa were achieved in this work for the same current range. The higher input power and higher pressure used by Iwarere et al. contributed to higher hydrocarbon concentrations. For example, ~2500 ppm of methane was produced at 250 mA compared to ~100 ppm in this work.

As mentioned in Section 6.3.1, 2 MPa was selected for the current variation study in this work due to the high hydrocarbon yields obtained for the plasma-catalytic systems in the pressure variation study, as well as the increased arc stability and lower water partial pressures observed at this pressure.

The decreasing voltage-current characteristic curves obtained for all four systems (Figure 6.11 above) was also expressed by Ayrton's empirical formula, in which the voltage drop was a function of the inter-electrode gap and supply current [60] and corresponded to that of a classical non-thermal arc discharge generated at high pressure [4, 60, 215].

The plots in Figure 6.11 above showed a decrease in voltage with an increase in current, which also led to an increase in the electric field energy and specific input energy (SIE), presented in Figure 6.12 below. The increased electric field could have caused the traversing of the arc further away from non-equilibrium to a thermal arc. In the more thermal state, the plasma energy would be less selectively focused on discharge generation (or reactant conversion). This thermal behaviour was indicated by the decrease in hydrocarbon concentrations as seen in the concentration-current plots in Figures 6.10.a to 6.10.d above, which corresponded to an increase in SIE with current. As in the pressure variation study, the SIE values for plasma-catalysis were higher than that of pure plasma due to the reduction in the reactor volume caused by the presence of the catalyst.

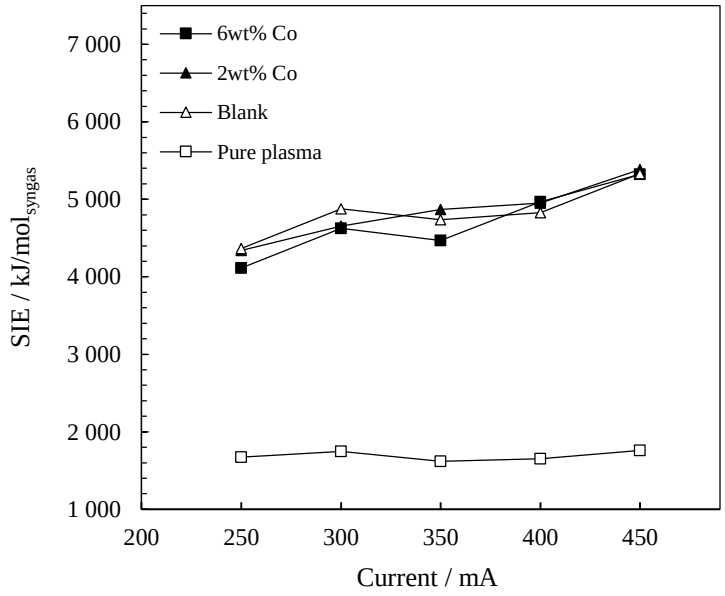

Figure 6.12: Specific input energy (kJ/mol$_{syngas}$) as a function of current for pure plasma and plasma-catalytic FTS (NTP + Blank, 2 or 6 wt% Co catalyst) at a discharge time of 60 s. **Legend:** ■ – 6 wt% Co; ▲ – 2 wt% Co; ∆ – Blank; □ – Pure plasma. **Operating conditions:** Syngas ratio: 2.2:1; pressure: 2 MPa; inter-electrode gap: 1 mm; wall temperature: 25^{o}C.

The final plasma performance factor, the specific required energy (SRE), presented in Figure 6.13, significantly increased from 232 MJ/mol$_{methane,prod}$ at 250 mA (glow-like discharge) to 3002 MJ/mol$_{methane,prod}$ at 450 mA (arc discharge) for the 6 wt% Co catalyst. This trend was indicative of the higher energy consumption of a discharge moving away from the glow to the arc region. In this transitional region, the 6 wt% Co catalyst's SRE values at 250 and 300 mA were 10 and 8.7 times lower, respectively, than that of the 2 wt% Co catalyst due to this latter discharge existing as an arc at these currents.

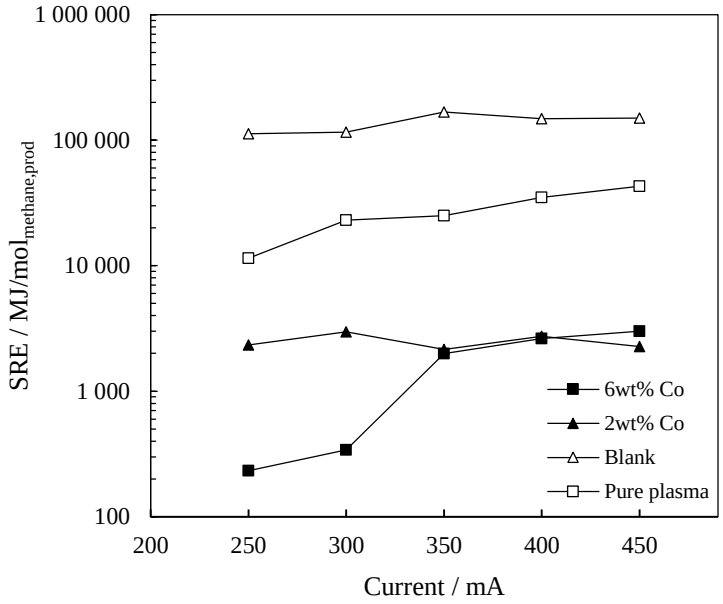

Figure 6.13: Specific required energy ($MJ/mol_{methane,prod}$) as a function of current for pure plasma and plasma-catalytic FTS (NTP + Blank, 2 or 6 wt% Co catalyst) at a discharge time of 60 s. **Legend:** ■ – 6 wt% Co; ▲ – 2 wt% Co; ∆ – Blank; □ – Pure plasma. **Operating conditions:** Syngas ratio: 2.2:1; pressure: 2 MPa; inter-electrode gap: 1 mm; wall temperature: 25°C.

Furthermore, the discharge transition of the 6 wt% Co catalytic system to a stable arc was apparent in its SRE values approaching that of the 2 wt% Co catalyst between 350 and 450 mA. This transitional state was also described by the arc stability. The stability was signified by the voltage fluctuations [60], which were represented by the standard deviation errors, determined using 60 000 voltage values that were recorded during the 60 s reaction period at each current set-point between 250 to 450 mA. The voltage errors for the individual currents were then averaged for each system. The average voltage errors for the 6 wt% Co catalyst were approximately 9 and 6% in the transitional region at 250 and 300 mA, respectively, compared to 1.7 % in the stable arc region at 350 mA. In contrast, the average voltage errors for the blank and 2 wt% Co catalysts were both ~0 and 1.9% at 250 mA and 300 mA (the transitional region for the 6wt% Co catalyst) respectively. This was much lower than the 6 wt% Co catalyst's errors, verifying that the 6 wt% Co catalyst had a greater influence on the electrical properties of the discharge in the glow-like region.

In conclusion, for the current variation study, the SRE value at 250 mA for the 6 wt% Co catalyst (mentioned above) was ~50 times lower than that of pure plasma (11 483 $MJ/mol_{methane,prod}$), verifying that this plasma-catalytic system and current were the most favourable parameters for hydrocarbon production and energy efficiency. The final parameter investigated, the inter-electrode, is discussed below.

6.4 Inter-electrode gap variation study

6.4.1 The influence of the inter-electrode gap on FTS product yields

The plots in Figures 6.14.a to 6.14.d showed a general trend of increasing hydrocarbon yields with an increase in the inter-electrode gap from 0.5 to 2 mm for a fixed pressure of 2 MPa and fixed current of 350 mA.

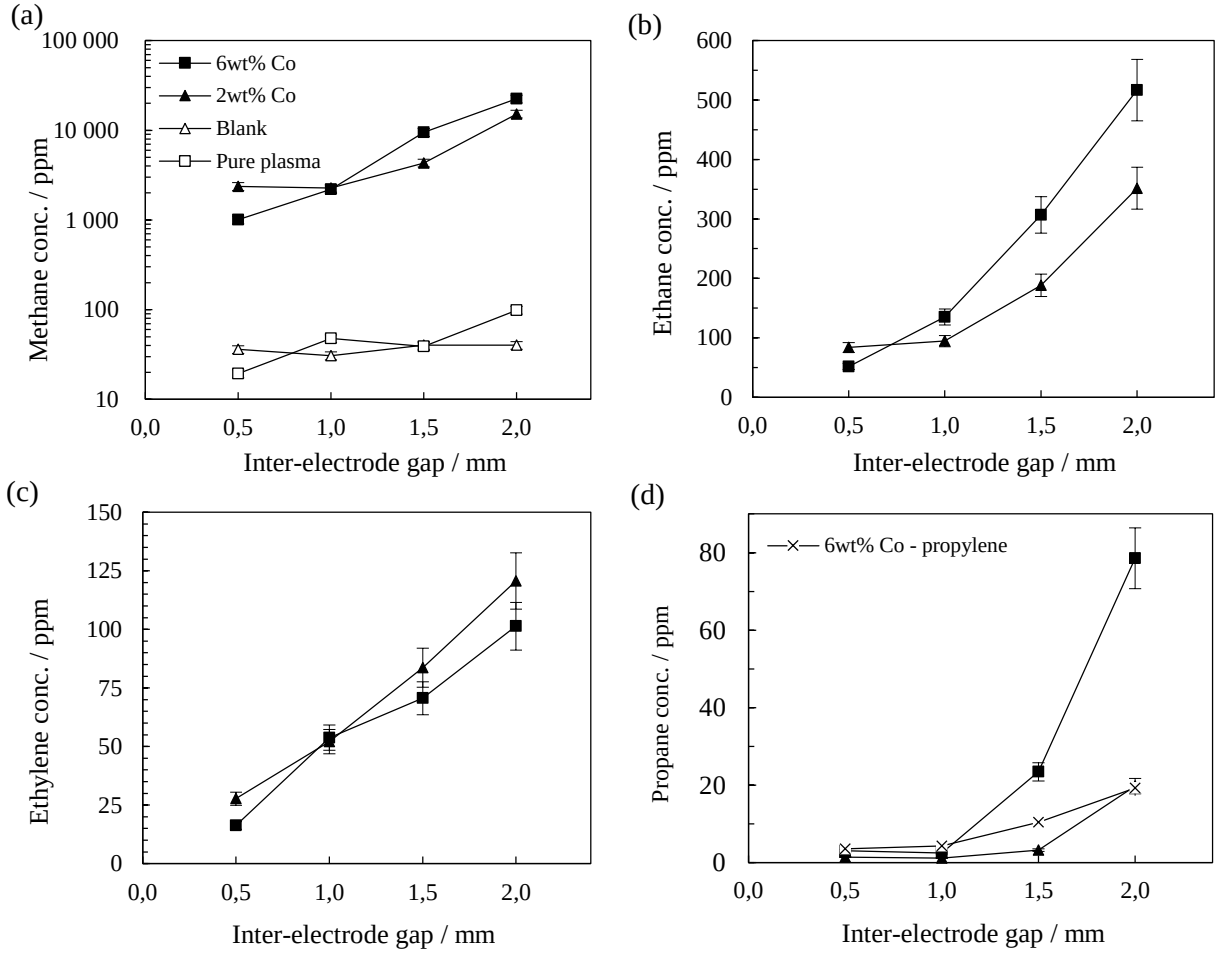

Figure 6.14: The influence of inter-electrode gap on hydrocarbon concentration for pure plasma and plasma-catalytic FTS (NTP + Blank, 2 or 6 wt% Co catalyst) at a discharge time of 60 s; (a) methane, (b) ethane, (c) ethylene and (d) propane/propylene. **Legend:** ■ – 6 wt% Co; ▲ – 2 wt% Co; ∆ – Blank; □ – Pure plasma; **x** - 6 wt% Co (propylene). **Operating conditions:** Syngas ratio: 2.2:1; pressure: 2 MPa; current: 350 mA; wall temperature: 25°C. **Error bars (vertical):** Expanded experimental hydrocarbon concentration uncertainty of ±11%.

The above-mentioned fixed conditions were used as they led to relatively high product yields and a stable arc discharge in the pressure variation study.

An increase in the inter-electrode gap denoted an increase in the arc length and volume of syngas being treated. The concentrations of methane (22 424 ppm), ethane (517 ppm), ethylene (101 ppm), propane (79 ppm) and propylene (19 ppm) for the 6 wt% Co catalyst at an inter-electrode gap of 2 mm were approximately 22, 10, 6, 26 and 5 times greater, respectively, than the hydrocarbon yields obtained at 0.5 mm.

In contrast, the methane and ethane yields for pure plasma FTS increased from 0.5 to 2 mm by factors of only 5 and 2 respectively. In addition, the pure plasma ethylene and C_3 hydrocarbon yields remained below 1 ppm (not shown in Figure 6.14). These results indicated that the inter-electrode gap had a more significant influence on hydrocarbon production in Co-based plasma-catalytic FTS.

The considerable differences in the pure plasma and plasma-catalytic concentration-gap yields were attributed to their active arc discharge volume differences. For pure plasma FTS, increasing the inter-electrode gap by a factor of 4 (from 0.5 to 2 mm) corresponded to a fourfold increase in the discharge volume assuming a linear relationship. The same increase in the inter-electrode gap for plasma-catalytic systems not only caused a fourfold increase in the arc discharge volume, but also a fourfold increase in the catalyst surface area exposed to the discharge, leading to activation of more Co particles. This behaviour was verified at the widest discharge gap of 2 mm, where methane, ethane, ethylene and propane concentrations for the 6 wt% Co catalyst were 226, 210, 278 and 1353 times greater, respectively, than that obtained for pure plasma. For pure plasma between 250 and 450 mA, the ethane concentrations were between 0.2 and 2.5 ppm, whereas ethylene and propane concentrations were lower than 1 ppm and propylene was not produced (note that these concentration values are not presented in Figures 6.14.a to 6.14.d above). Furthermore, similar product yields were obtained for the blank catalyst.

The hydrocarbon yields obtained for the 6 wt% Co catalyst exceeded those of the 2 wt% Co catalyst for most discharge gaps investigated. However, the opposite trend was seen for methane, ethane and ethylene at 0.5 mm, which was especially evident for ethylene between 1 and 2 mm. The lower 6 wt% Co catalyst's ethylene yields at the 1 and 2 mm discharge gaps could be due to these larger discharge volumes causing an increase in the catalyst surface temperature, probably triggering ethylene readsorption followed by secondary reactions such as hydrogenation to ethane or reinsertion into propane or propylene chains (phenomena described for the pressure variation study in Section 6.2.1.6). These reaction phenomena describing the lower ethylene yields at 1 and 2 mm for the 6 wt% Co catalyst, were verified by the 38 and 71% higher ethane and propane concentrations, respectively, and the exclusive production of propylene (not detected for the 2 wt% Co catalyst system). In addition, the mentioned ethylene secondary reactions

occurring for the 6 wt% Co catalyst seemed to be much more prevalent at higher discharge gaps than at higher pressures in the pressure variation study (discussed in Section 6.2.1.6).

The maximum product yields for the plasma-catalytic systems, discussed above, were related to the energy consumption, discussed below, in order to determine the optimum operating conditions for the inter-electrode gap variation study.

6.4.2 The influence of the inter-electrode gap on energy consumption

An increase in the inter-electrode gap from 0.5 to 2 mm at a fixed current of 350 mA caused an increase in the voltage as shown in Figure 6.15. The voltage increase was necessary for sustaining the arc discharge.

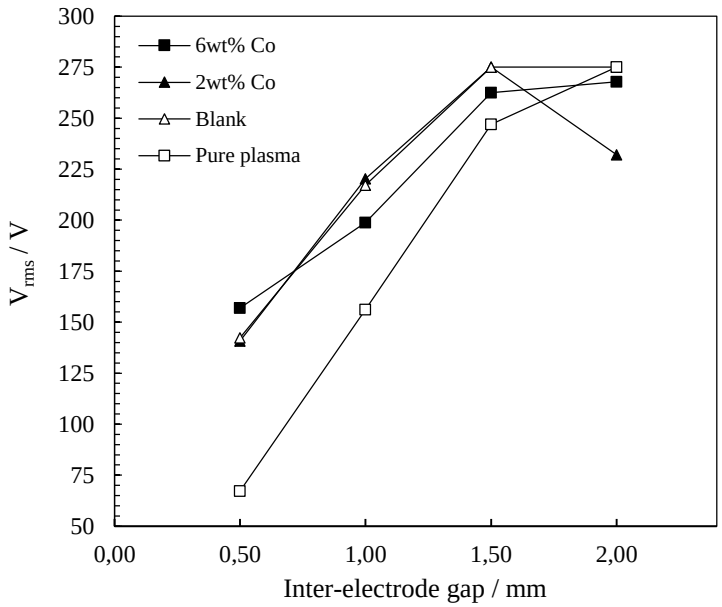

Figure 6.15: The influence of inter-electrode gap on rms voltage for pure plasma and plasma-catalytic FTS (NTP + Blank, 2 or 6 wt% Co catalyst) at a discharge time of 60 s. **Legend:** ■ – 6 wt% Co; ▲ – 2 wt% Co; ∆ – Blank; □ – Pure plasma. **Operating conditions:** Syngas ratio: 2.2:1; pressure: 2 MPa; current: 350 mA; wall temperature: 25^{o}C.

This increasing voltage-gap trend could be explained in terms of the various regions constituting the arc discharge, namely the near-cathode and near-anode border zones (more non-equilibrium in nature) and positive arc column (less non-equilibrium in nature due to its higher inherent electrical resistivity). The thicknesses of these arc regions usually vary with the inter-electrode gap [43, 60].

For wide inter-electrode gaps (2 mm in this work), the positive arc column was long and was therefore more influential in controlling the discharge behaviour. The long arc column had a high electrical resistivity leading to a more thermal plasma (greater convective losses). In order to sustain these thermal processes, comparatively high input voltages were required (275 V for pure plasma as shown in Figure 6.15 above).

In contrast to the wide discharge gaps, for short discharge gaps (0.5 mm in this work), the non-equilibrium border zones governed the electrical behaviour of the discharge, leading to a lower voltage requirement (67 V for pure plasma as shown in Figure 6.15 above). This arc zone-gap behaviour also extended to the plasma-catalytic systems. In addition to these arc zones, the higher specific input energy (SIE) values at wider inter-electrode gaps (Figure 6.16) also indicated that the plasma was further from non-equilibrium.

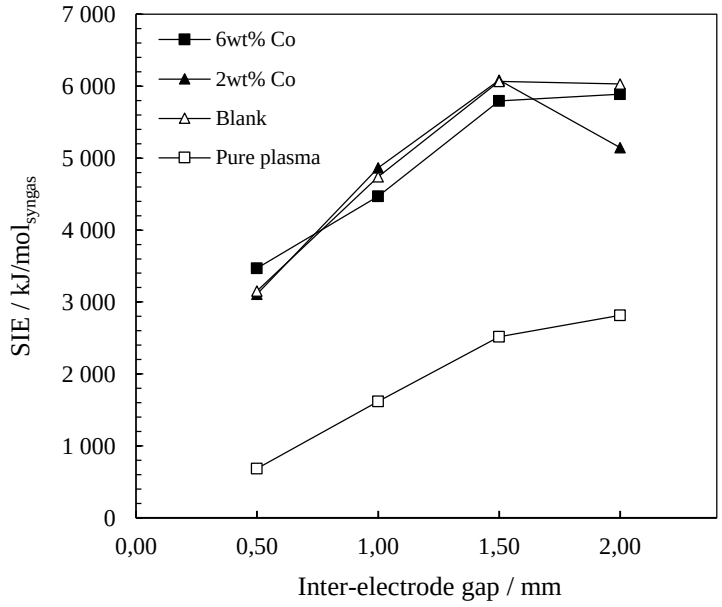

Figure 6.16: Specific input energy (kJ/mol$_{syngas}$) as a function of inter-electrode gap for pure plasma and plasma-catalytic FTS (NTP + Blank, 2 or 6 wt% Co catalyst) at a discharge time of 60 s. **Legend:** ■ – 6 wt% Co; ▲ – 2 wt% Co; ∆ – Blank; □ – Pure plasma. **Operating conditions:** Syngas ratio: 2.2:1; pressure: 2 MPa; current: 350 mA; wall temperature: 25ºC.

The specific required energy (SRE) values, shown in Figure 6.17 below, decreased significantly from 0.5 to 2 mm for the 2 and 6 wt% Co catalysts, revealing that 1.5 to 2 mm was the optimum inter-electrode gap range in terms of energy efficiency and hydrocarbon yields. At 2 mm, the SRE values for the 2 wt% Co catalyst (224 MJ/mol$_{methane,prod}$) and 6 wt% Co catalyst (265 MJ/mol$_{methane,prod}$) were factors of approximately 126 and 107, respectively, lower than that of pure plasma.

Although the SRE value for both Co catalysts were similar between 1.5 and 2 mm, the 6 wt% Co catalyst produced significantly greater quantities of paraffins and propylene (not produced by the other three systems) in this gap range. Therefore, this catalyst was again shown to be the most suitable for promoting chain growth. However, if higher ethylene yields were desired, then the 2 wt% Co catalyst operating between 1.5 and 2 mm would be favoured.

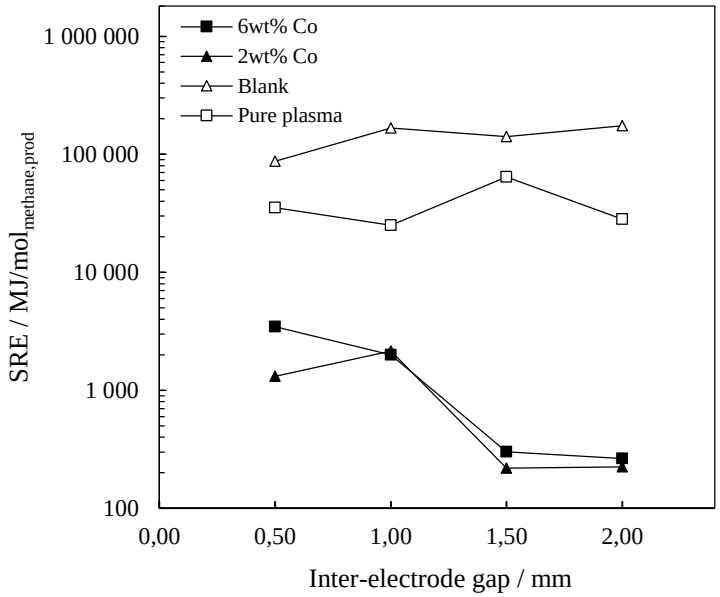

Figure 6.17: Specific required energy ($MJ/mol_{methane,prod}$) as a function of inter-electrode gap for pure plasma and plasma-catalytic FTS (NTP + Blank, 2 or 6 wt% Co catalyst) at a discharge time of 60 s. **Legend:** ■ – 6 wt% Co; ▲ – 2 wt% Co; ∆ – Blank; □ – Pure plasma. **Operating conditions:** Syngas ratio: 2.2:1; pressure: 2 MPa; current: 350 mA; wall temperature: 25ºC.

In conclusion, for the pressure, current and inter-electrode gap variation studies (discussed in Sections 6.2 to 6.4), it was shown that the 2 and 6 wt% Co catalysts systems unanimously improved the C_1-C_3 hydrocarbon product yields and energy consumption compared to the blank catalyst and pure plasma FTS systems. The optimum operating parameters for chain growth and energy efficiency for the 2 and 6 wt% Co catalysts were: (i) 10 MPa at 10 s and 2 MPa at 60 s for the pressure variation study (0.5 to 10 MPa); (ii) 250 mA for the current variation study (200 to 450 mA) and; (iii) 2 mm for the inter-electrode gap variation study (0.5 to 2 mm). At these optimum conditions, the 6 wt% Co catalyst was generally the most effective for catalysing FTS reactions, thus encouraging the use of higher cobalt loadings in future plasma-catalytic FTS investigations.

In order to better understand the influence of plasma on the catalyst and their related interactions, the catalyst was characterised using various microscopic probing tools. These findings are presented in Section 6.5.

6.5 Catalyst Characterisation

The effect of plasma on the blank, 2 and 6 wt% Co catalysts was investigated using transmission electron microscopy (TEM), scanning electron microscopy (SEM), energy dispersive x-ray (EDX) and x-ray diffraction (XRD). A discussion of these diagnosis is provided here.

6.5.1 Transmission electron microscopy (TEM)

6.5.1.1 Cobalt loading

The effects of cobalt in the 2 and 6 wt% Co catalysts were clearly seen in the previous sections by the significantly higher product yields and wider product distribution than that obtained using the blank catalyst and pure plasma systems. In order to further understand the effects of cobalt loading on plasma-catalytic interactions, the cobalt particle size analysis and particle distribution were determined using transmission electron microscopy (TEM) analysis.

Figure 6.18.a below showed a TEM micrograph of an alumina coated catalyst without cobalt loaded (blank). TEM micrographs of the 2 wt% Co catalyst, shown in Figures 6.18.b to 6.18.d below, revealed the presence of cobalt particles on mullite (Al_2O_3/SiO_2), seen as dark isolated clusters (enclosed by white circles). The cobalt aggregates were clearly noticeable in comparison to the lighter mullite particles in the blank catalyst image.

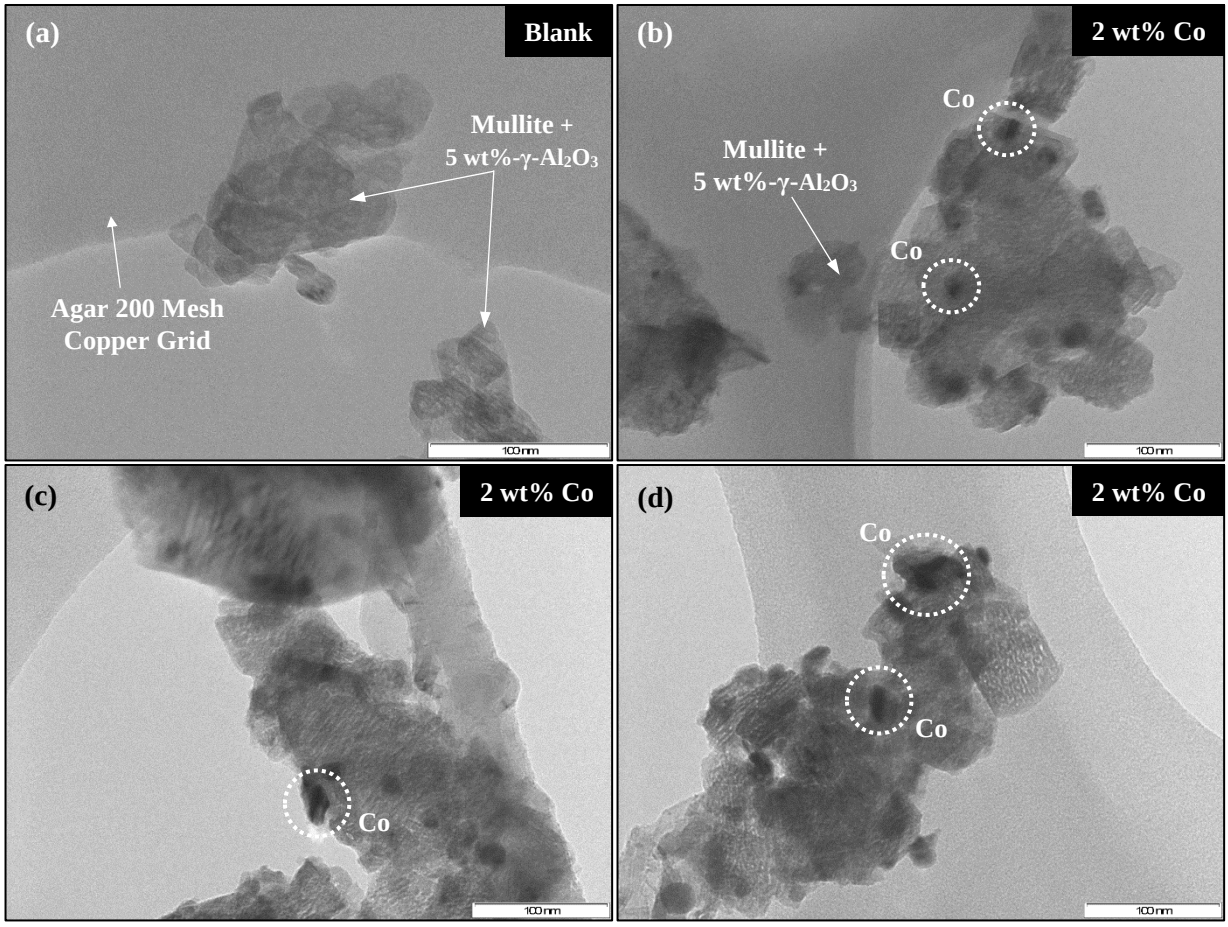

Figure 6.18: TEM micrographs of used catalysts; (a) blank, (b-d) 2 wt% Co.
(N.B. Examples of cobalt clusters are enclosed by white circles).

TEM images of the 6 wt% Co catalyst, shown in Figures 6.19.a and 6.19.b below, revealed larger clusters than the 2 wt% Co. The cobalt clusters in the TEM images were assumed to be mainly metallic cobalt, with minor quantities of cobalt oxides - CoO or Co_3O_4. This assumption was supported by SEM analysis (discussed in Section 6.5.2 below), which indicated that the reductive CO/H_2 plasma environment could have led to the reduction of unreduced cobalt oxides to metallic cobalt.

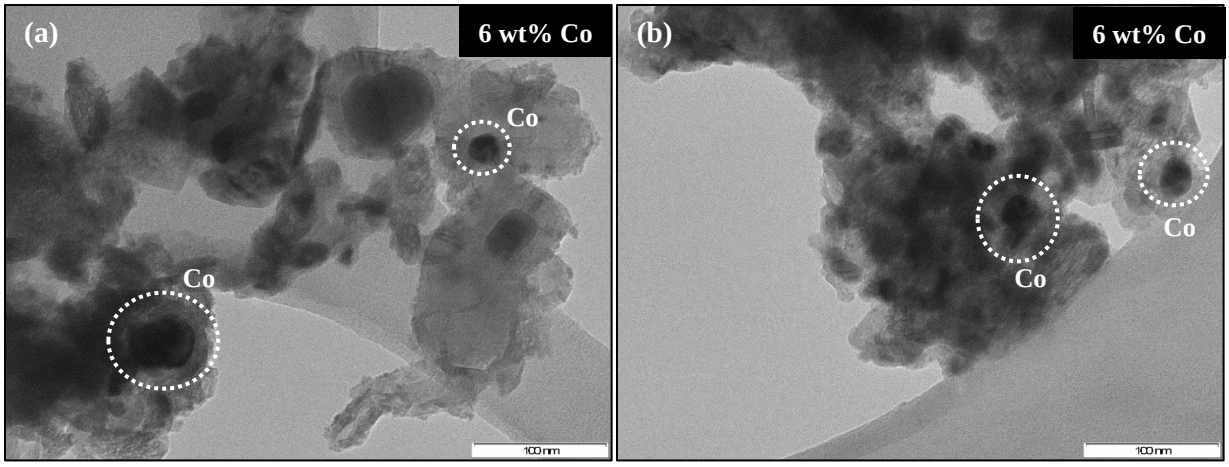

Figure 6.19: TEM micrographs of used catalysts; (a, b) 6 wt% Co.
(N.B. Examples of cobalt clusters are enclosed by white circles).

With the above assumption that the cobalt particles in the TEM images were metallic cobalt, the cobalt particle size distribution was evaluated. The distribution, presented in Figure 6.20 below, was determined by measuring 100 cobalt clusters for each of the 2 and 6 wt% Co catalyst using iTEM image analysis software. The size of the 6 wt% cobalt clusters were between 6 and 57 nm with 84% of the particles in the range of 6 to 25 nm. The size of the 2 wt% cobalt particles were between 2 and 35 nm with 95% of the particles in the range of 2 to 19 nm. The average particle size for the 2 and 6 wt% cobalt catalysts were estimated to be 10 and 19 nm respectively. The larger cobalt particles of the 6 wt% Co catalyst corresponded to higher C_1-C_3 hydrocarbon yields, improved chain growth and propylene formation (absent in the pure plasma, blank catalyst and 2 wt% Co catalyst), indicating that chain growth was promoted by the higher cobalt loading as demonstrated in the literature [216-218].

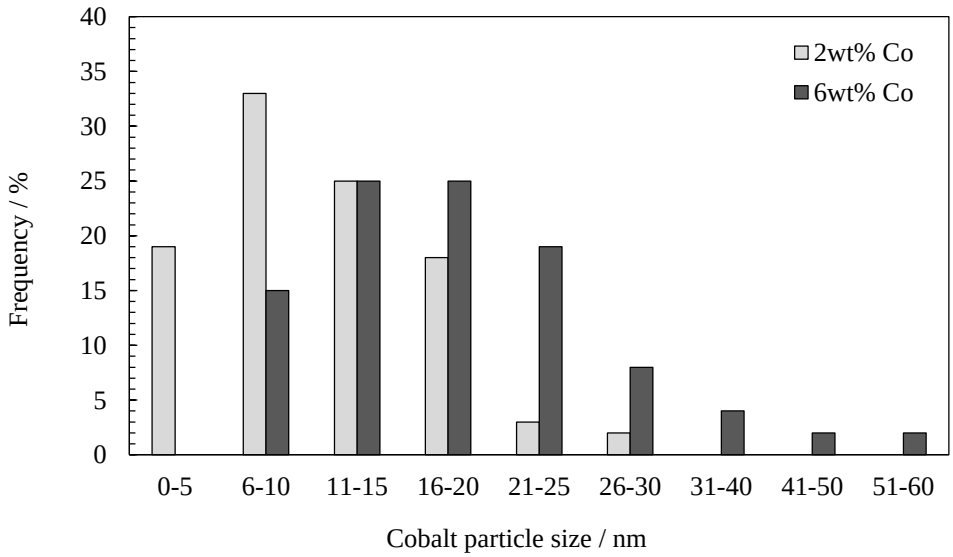

Figure 6.20: Particle size histogram of the 2 wt% (■) and 6 wt% (■) cobalt catalysts.

The study by Tavasoli et al. [218], in particular, explained the cobalt loading and particle size trends evaluated by TEM in this work. They showed that larger clusters were formed for higher loadings of cobalt (8 to 40 wt%) that were supported on Al_2O_3. As in this work, their study revealed that more cobalt was loaded onto the same support surface for higher loadings, resulting in agglomeration of cobalt crystal particles to form larger cluster sizes.

They associated larger clusters with weaker cobalt metal-support interactions leading to better reducibility of the catalyst [216, 217], thus creating more active sites for FTS reactions. It was also suggested that larger clusters could lower steric hindrance for dissociative adsorption of CO [218], which might lead to an increase in chain growth monomer formation. In contrast to higher loadings, they reported that lower cobalt loadings led to stronger metal-support interactions possibly forming cobalt aluminate ($CoAl_2O_4$), which can hinder the catalyst reducibility [218]. However, cobalt aluminate, analysed via Raman spectroscopy (plots not presented here), was not detected in the 2 and 6 wt% Co catalysts, but could have been present in minute quantities that were below the detection limit.

6.5.1.2 Carbon nanotubes (CNTs)

In addition to TEM being utilised to determine the cobalt particle size distribution, it was also used to detect carbonaceous species on the catalyst. Unexpectedly, carbon nanotubes (CNTs) were detected, which were only found on the higher loaded 6 wt% Co catalyst shown in Figures 6.21.a to 6.21.d below. This was an interesting finding as CNTs are not formed in conventional FTS due to low temperature operation. The only known association between CNTs and conventional FTS was the use of CNTs as catalyst supports, which are briefly discussed in Appendix E.

An important requirement for CNT growth is that precursor decomposition occurs on the catalyst surface [219], which in this work was probably induced in the form of molecular CO and C_1-C_3 hydrocarbons [220-222] decomposing on the cobalt surface at high temperatures (600 to 1200^{o}C), as in thermal chemical vapour deposition (CVD), less likely, or by carbon-plasma (pre-dissociated CO) deposition on the cobalt surface at lower temperatures (as low as 120^{o}C), as in plasma-enhanced chemical vapour deposition (PECVD) [222, 223]. In addition, graphite, detected in the used cobalt catalysts in this work using x-ray diffraction (discussed in Section 6.5.4), may have been a CNT precursor or remnant that failed to grow due to encapsulation of the catalyst by carbon i.e. CNTs are essentially cylindrical graphene sheets in which graphene is a single layer of graphite.

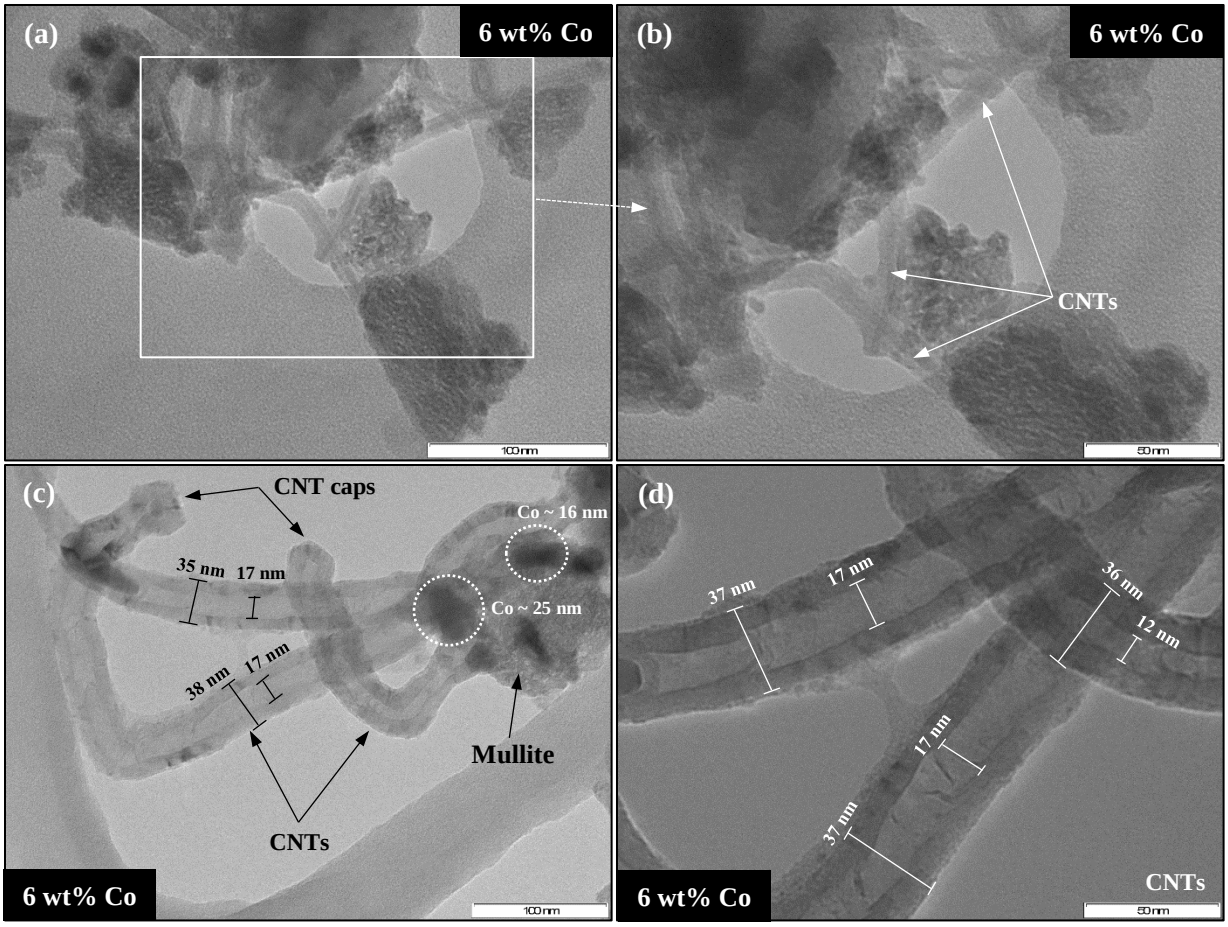

Figure 6.21: TEM micrographs of used catalysts; (a-d) 6 wt% Co.

The CNTs seemed to originate from the cobalt clusters that were firmly rooted to the γ-Al_2O_3/mullite support and then appeared to protrude away from the cobalt cluster. This suggests the applicability of the base-growth mechanism for describing CNT formation: a growth mechanism that occurs due to the strong interaction between Co and γ-Al_2O_3. The above mechanisms are extensively described in Appendix E.

The appearance of these CNTs corresponded to that of multi-walled CNTs (MWCNTs), similar to MWNTs in other works [220, 224]. The MWCNTs had inner diameters between 12-17 nm and outer diameters between 36-38 nm, measured visually from the TEM micrographs in Figures 6.21.c and 6.21.d above using iTEM software.

6.5.2 Scanning electron miscroscopy (SEM)

SEM was used to determine the catalyst coating thickness (Section 6.5.2.1) and surface topography (Section 6.5.2.2).

6.5.2.1 Catalyst coating thickness

The SEM micrographs in Figure 6.22 revealed the coating thicknesses of the used cobalt catalysts. The washcoat layer thicknesses, measured at 20 different locations for the blank, 2 and 6 wt% Co used catalysts, ranged between 21-49 µm, 34-67 µm, and 41-75 µm, respectively, with average coating thicknesses of 37, 49 and 51 µm respectively.

The average coating thicknesses increased with increasing cobalt loading. These were both related to FTS hydrocarbon production, where C_1-C_3 hydrocarbon yields increased with layer thickness (cobalt loading). Similarly, Bakhtiari el al. [171] found that the C_{5+} selectivity increased with coating thickness (or increased with cobalt loading from 15 to 33 wt%) for FTS using a monolithic reactor (pure catalysis). The coating thickness is important in continuous monolith reactors where mass transfer limitations are directly affected by the diffusion length (coating thickness) [171], which was not as significant for the batch process in this work.

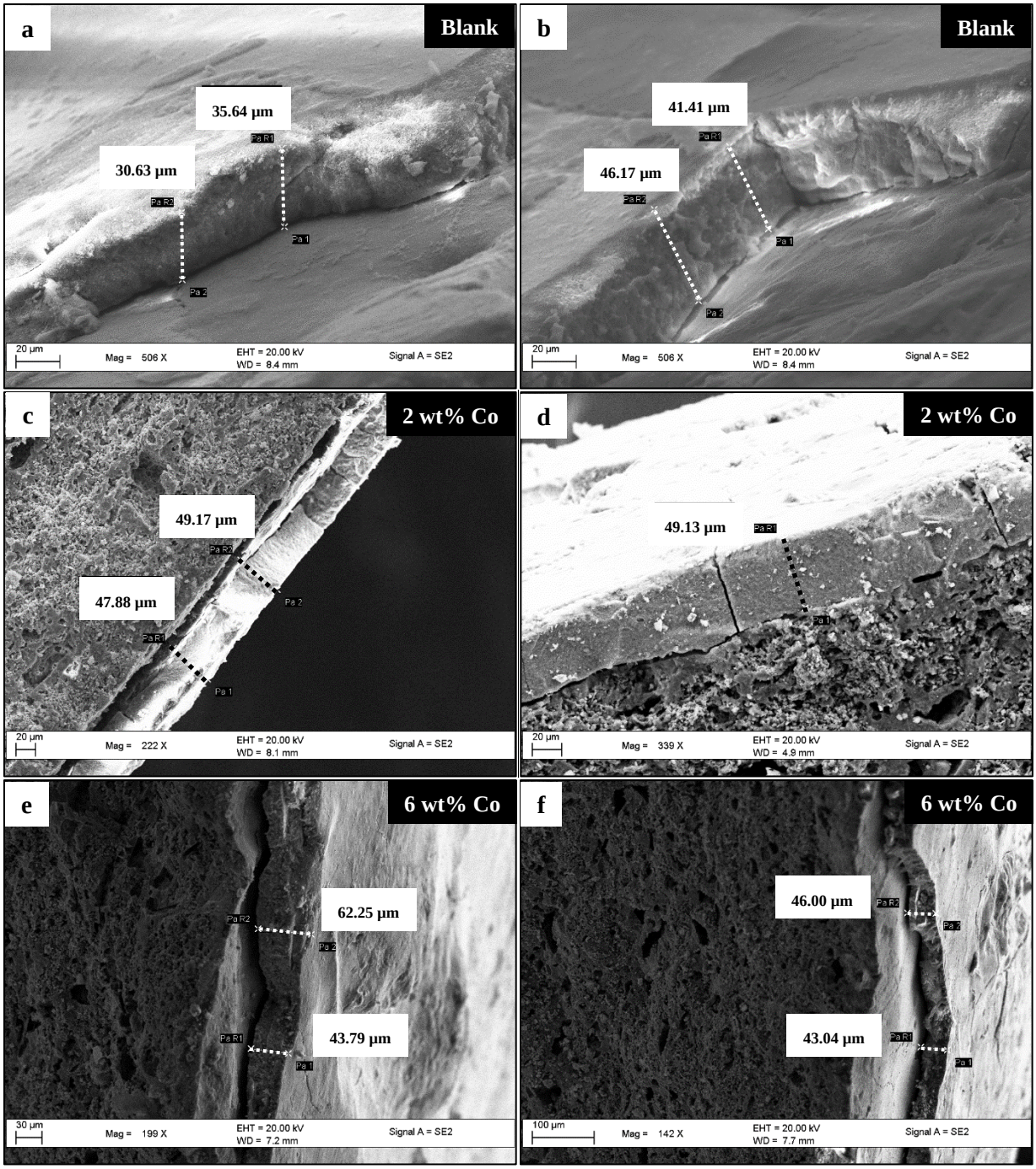

Figure 6.22: SEM images of catalyst coating thickness; (a, b) blank, (c, d) 2 wt% Co, (e, f) 6 wt% Co.

6.5.2.2 Catalyst surface topography

In addition to the catalyst coating thickness, SEM was also utilised to reveal the catalysts surface characteristics. A SEM micrograph of fresh uncoated mullite, not containing γ-Al_2O_3 and Co, is shown in Figure 6.23.a. In contrast, γ-Al_2O_3 clusters were clearly seen on the fresh blank catalyst in Figure 6.23.b.

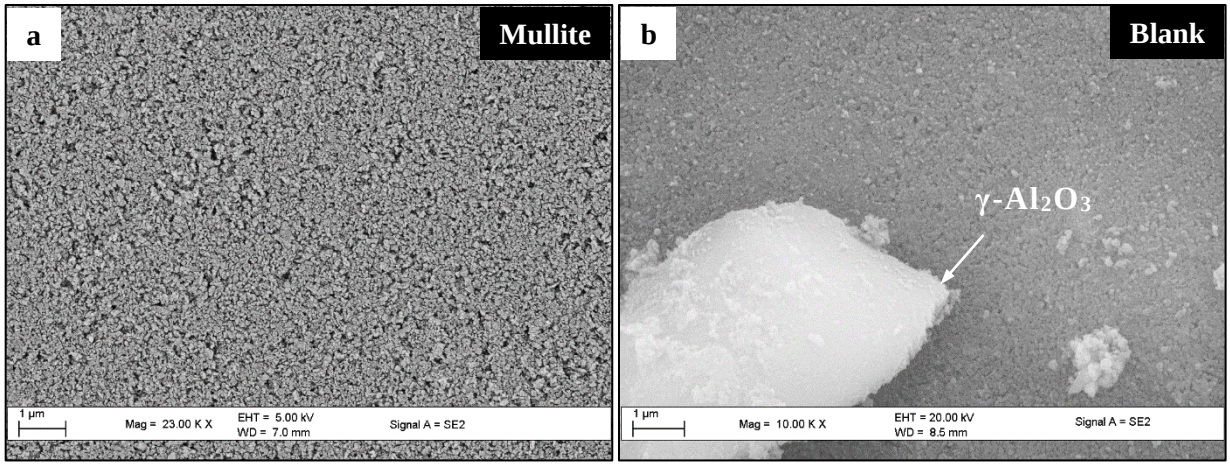

Figure 6.23: SEM micrographs of catalysts; (a) uncoated mullite (no γ-Al_2O_3 and Co), (b) blank catalyst.

The SEM images of the inner surfaces of the 2 and 6 wt% Co catalysts, shown in Figures 6.24 and 6.25 below, respectively, revealed the difference between fresh and used cobalt catalysts. Large agglomerates were seen on the fresh (calcined/reduced) 2 wt% Co catalyst (Figure 6.24.a) and 6 wt% Co catalyst (Figures 6.25.a and 6.25.b). However, smaller and more highly dispersed particles were visible on the used 2 wt% Co catalyst (Figure 6.24.b) and 6 wt% Co catalyst (Figure 6.25.c and 6.25.d).

In conventional FTS, De la Pena O'Shea [197] showed that an increase in pressure from 2 to 4 MPa using a Co/SiO_2 led to a higher dispersion of cobalt particles on silica than that activated with pure H_2, which they attributed to stronger CO chemisorption at higher pressure causing segregation of cobalt particles and an increase in the catalytic surface area.

Therefore, high operating pressures (0.5 to 10 MPa), beyond that of conventional FTS, coupled with the pre-dissociated CO plasma species, were the likely cause of the high cobalt dispersion shown in Figures 6.24.b, 6.25.c and 6.25.d. In addition, the reduction of unreduced Co oxides to smaller Co metal particles reported in other plasma-catalytic studies [32, 66, 93, 102], could also explain the reduced particles sizes in the SEM images below.

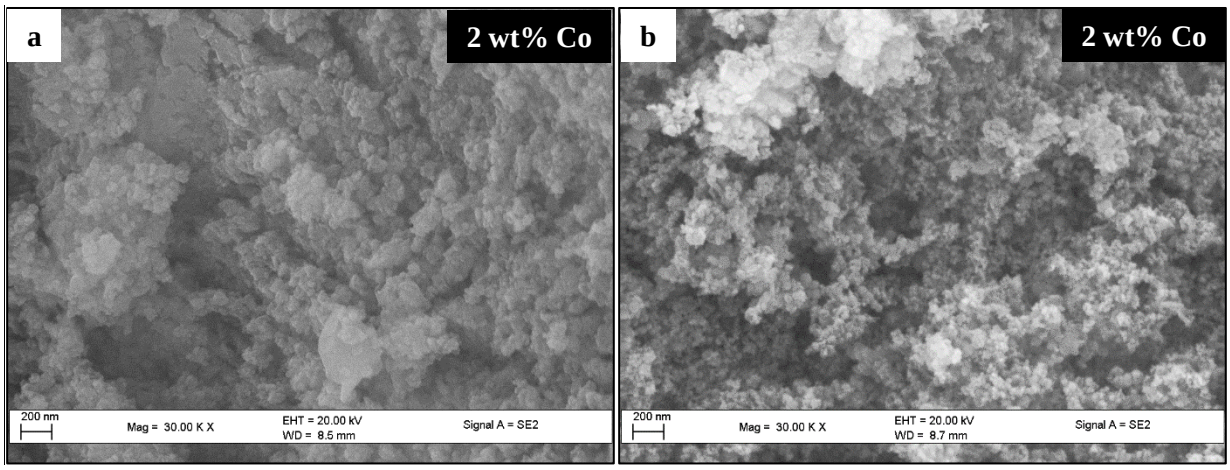

Figure 6.24: SEM micrographs of 2 wt% Co catalysts; (a) fresh catalyst, (b) used catalyst.

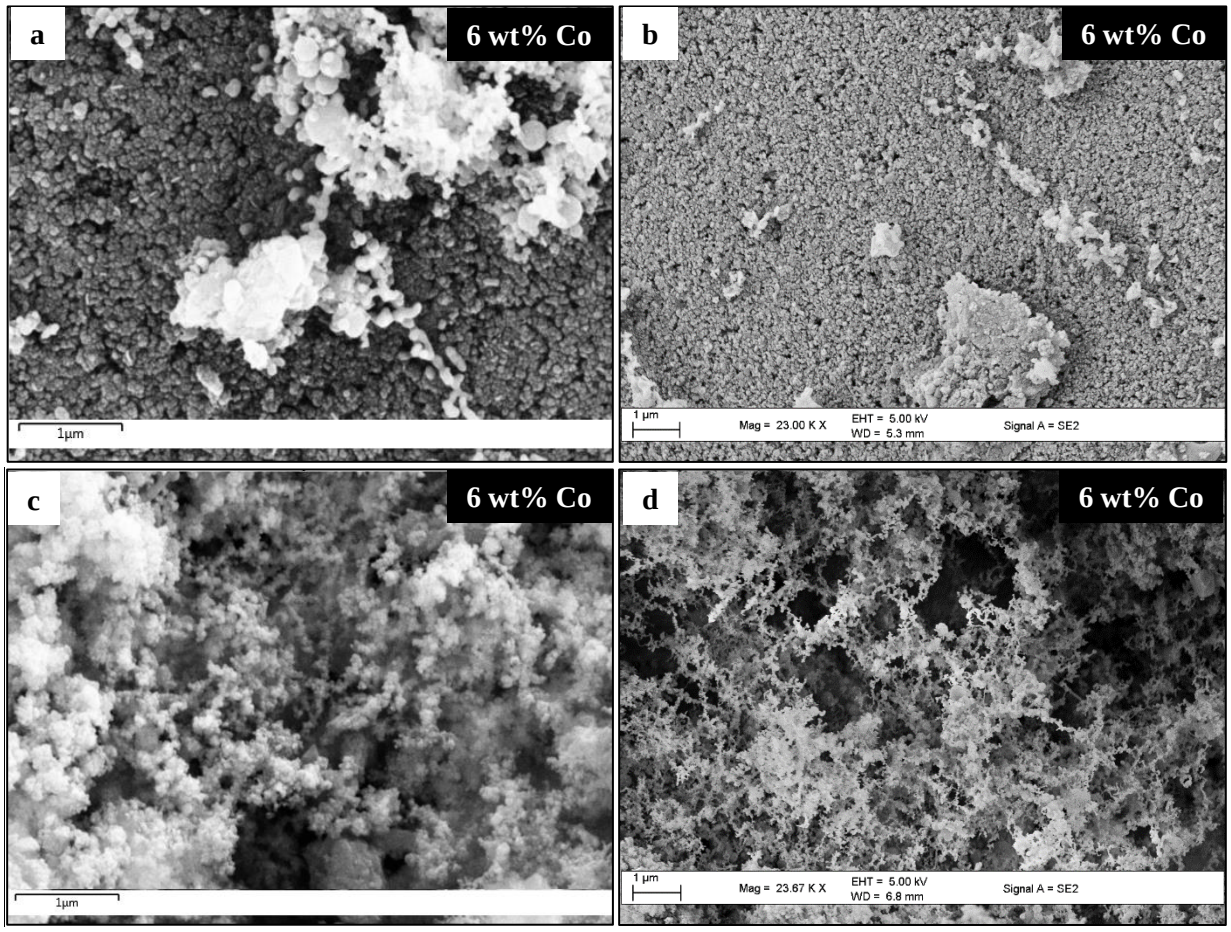

Figure 6.25: SEM micrographs of 6 wt% Co catalysts; (a-b) fresh catalyst, (c-d) used catalyst.

Different degrees of plasma treatment for the 6 wt% Co catalyst were observed, as seen in Figures 6.25.c and 6.25.d, where greater catalyst modification could be seen by the smaller clusters in Figure 6.25.d, which

could be due to this section of catalyst residing closer to the arc discharge (probably directly above the arc discharge) resulting in hotspots being formed, a phenomenon also observed in the plasma-catalysis literature [74].

In the final SEM analysis, SEM was coupled with energy dispersive spectroscopy to determine the qualitative distribution of cobalt on the catalyst surface, discussed in the next section.

6.5.3 Energy dispersive x-ray (EDX)

EDX dot mapping, a quantitative analysis tool combining SEM and EDX, was used to identify the various elements constituting the catalyst and determine the distribution of these elements. Oxygen bound to aluminium (Al_2O_3) and silica (SiO_2) were neglected in the mapping process in order to ensure that the dominant components (Co, Al and Si) were clearly distinguishable.

EDX dot mapping images of coating thicknesses for the used 2 and 6 wt% Co catalysts are presented in Figures 6.26 and 6.27, respectively, which revealed the distinction between the γ-Al_2O_3/Co coating layer and mullite substrate (72 wt%-Al_2O_3/SiO_2). The images showed a higher cobalt coverage for the 6 wt% Co catalyst (Figure 6.27), as expected, whereas less cobalt and more γ-Al_2O_3 was visible in the coating layer for the 2 wt% Co catalyst (Figure 6.26).

These elemental distributions on the coating thicknesses were confirmed by the dot mapping images of the inner surfaces of the 2 and 6 wt% Co catalysts presented in Figures 6.28 and 6.29 below, respectively, which include graphs of the relative elemental peak intensities. Collectively, these images showed that plasma treatment led to uniform dispersion of the active metal for both cobalt catalysts and that the cobalt in the 6 wt% Co catalyst was present in a greater quantity and was more highly dispersed than the 2 wt% Co catalyst, corroborating the results obtained in SEM (Section 6.5.2) and TEM (Section 6.5.1) analysis.

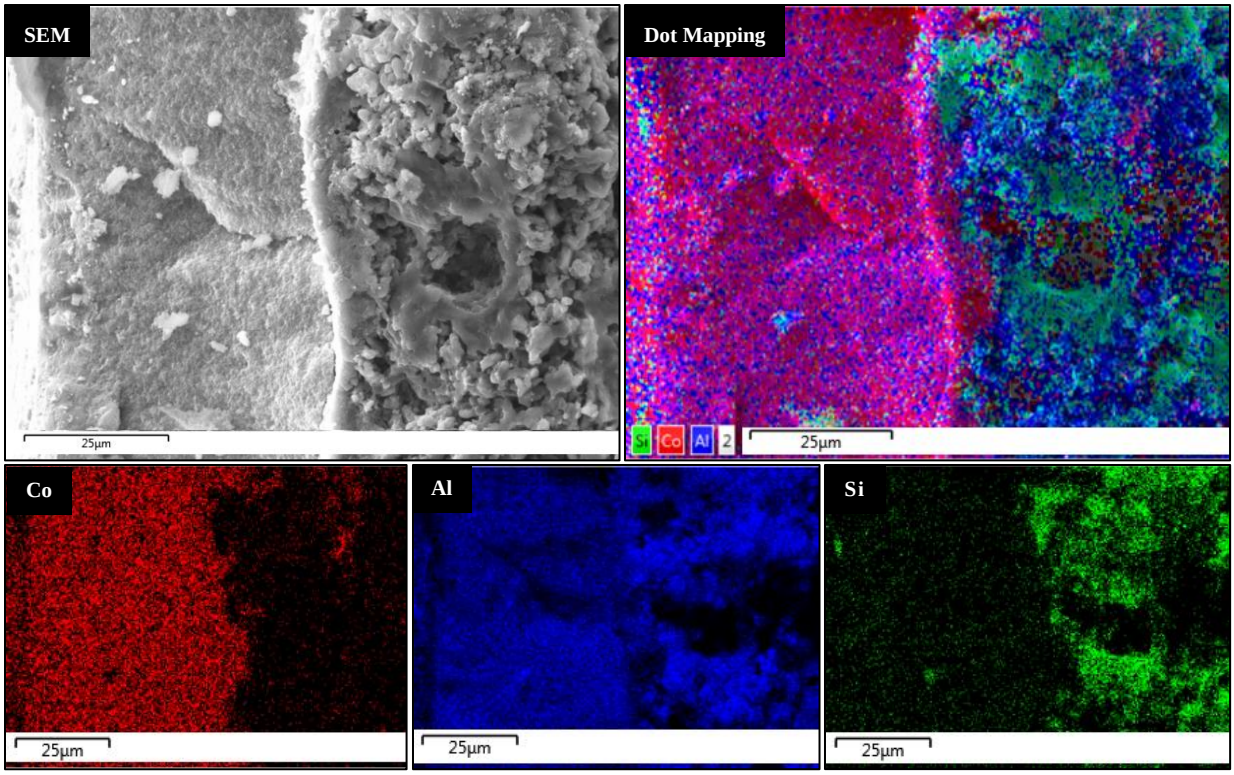

Figure 6.26: EDX dot mapping analysis of the coating thickness for a used 2 wt% Co catalyst.

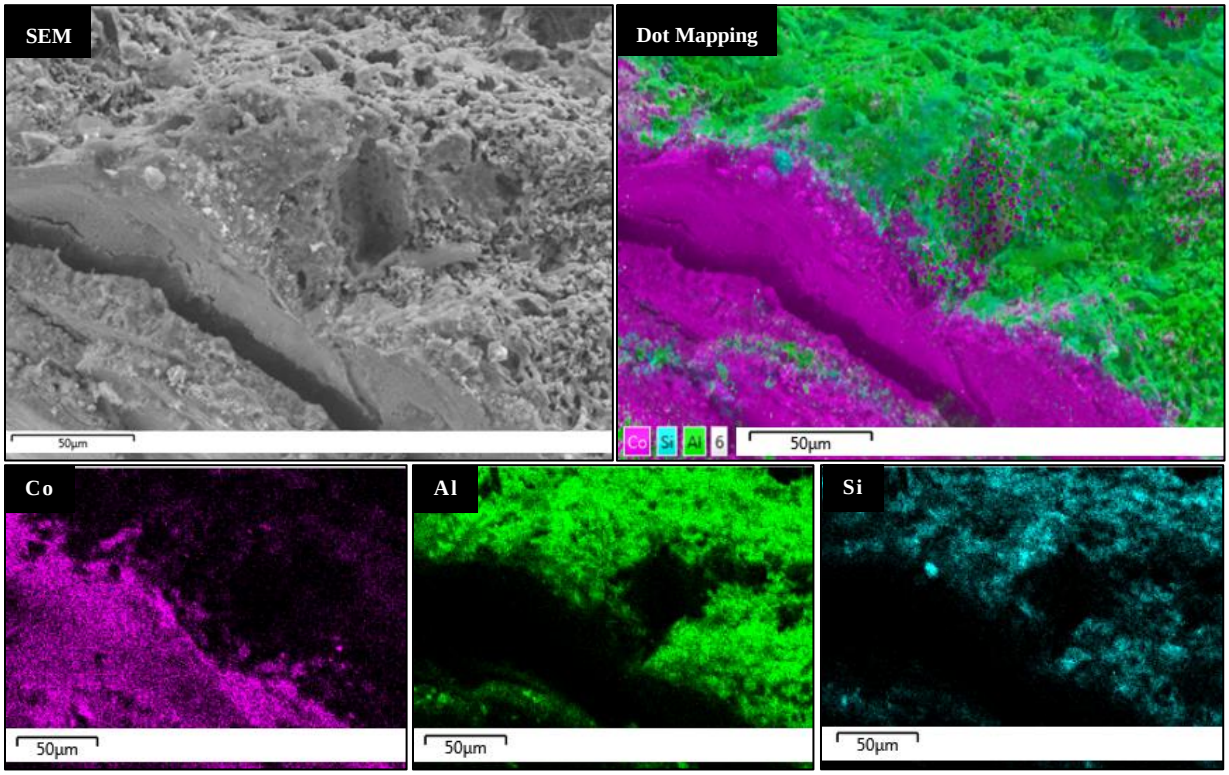

Figure 6.27: EDX dot mapping analysis of the coating thickness for a used 6 wt% Co catalyst.

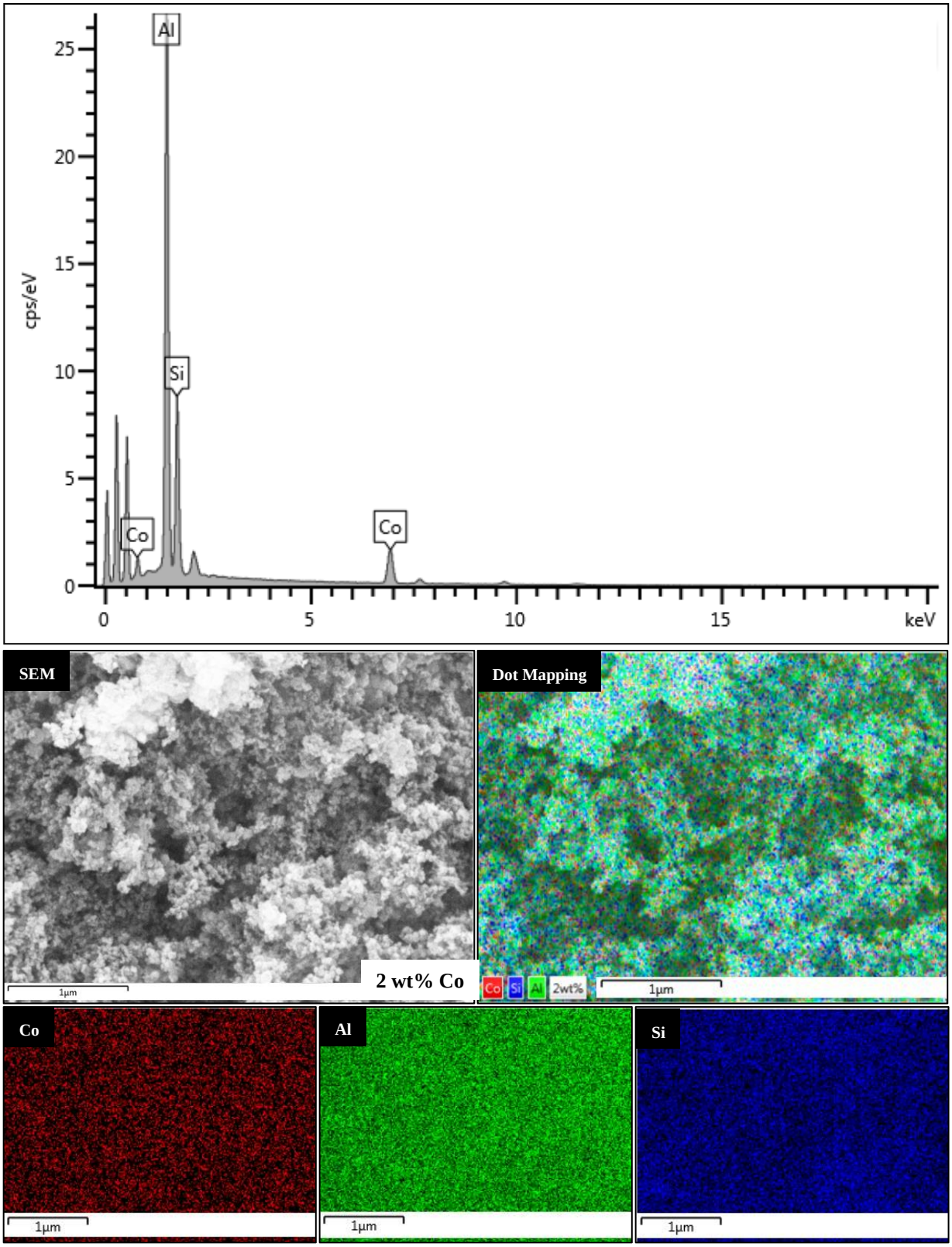

Figure 6.28: EDX dot mapping analysis of the surface of a used 2 wt% Co catalyst.

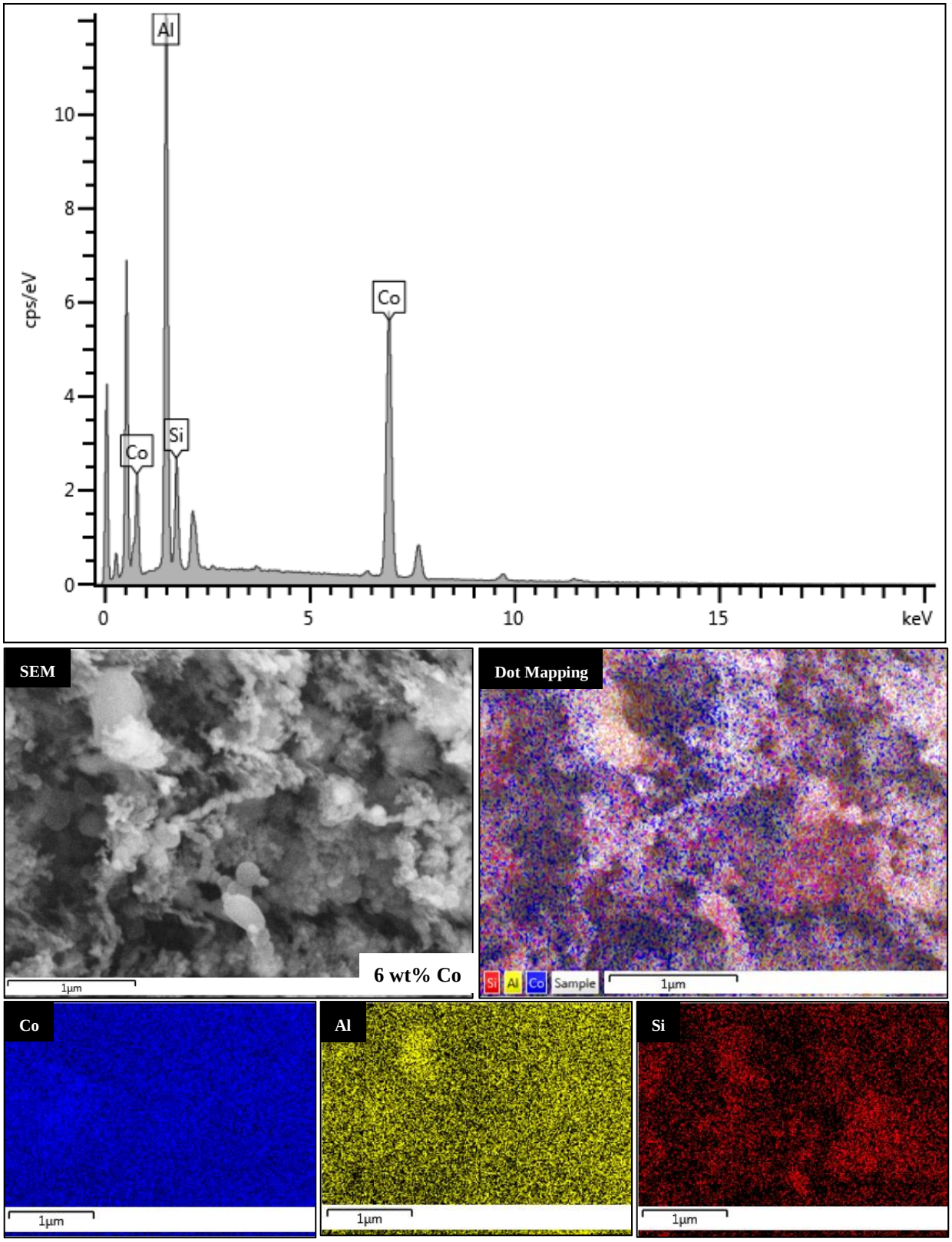

Figure 6.29: EDX dot mapping analysis of the surface of a used 6 wt% Co catalyst.

The final catalyst characterisation tool used was x-ray diffraction. The analysis is discussed in Section 6.5.4.

6.5.4 X-ray diffraction (XRD)

Powder XRD with a cobalt radiation source was used to identify the molecular compounds in the blank, 2 and 6 wt% cobalt catalysts. The catalyst spectra, shown in Figure 6.30.a, were identified by comparison to reference peak patterns (Figure 6.30.b), which were acquired from the HighScore Plus database that listed the potential peak matches in order of probability.

XRD failed to detect cobalt or cobalt carbides in the 2 and 6 wt% cobalt catalysts probably due to the high dispersion of low metal loadings that may have existed below the instrument detection limit. However, mullite and alumina diffraction patterns were dominant in the catalyst spectra. Reference peak patterns for mullite and alumina matched the catalyst peaks with the highest probability. The highest peak for each reference component corresponded to 100% intensity with the remaining peaks having relative intensities. The blank, 2 and 6 wt% cobalt catalysts exhibited the same peak patterns as seen in Figure 6.30.a. In addition, the 2 and 6 wt% Co catalysts' peak intensities for mullite and alumina were comparatively similar, but the mullite/alumina peaks at 62^{o}, 63^{o}, 67^{o}, 71^{o}, 76^{o}, 79^{o}, 81^{o}, 84^{o} and 89^{o} for the blank catalyst were slightly higher, which was due to the presence of more mullite and alumina in the absence of cobalt.

In addition to mullite and alumina, hexagonal graphite (2H) was detected in all catalysts. Graphite 2H, the most commonly occurring form of graphite (the other form being rhombohedral graphite (3R)) is comprised of carbon atoms covalently bonded to surrounding carbon atoms to form hexagonal networks, which are further layered [225]. XRD was capable of detecting crystalline phases of graphite and related carbon species but was unable to identify non-crystalline phases such as amorphous polymeric carbon. Graphite was estimated to exist in minute quantities (< 1 %) by the Rietveld refinement tool in HighScore Plus. Some of the reference peaks for graphite such as the peaks at 30^{o}, 49^{o}, 59^{o} and 71^{o} overlap those of mullite, with the peak at 71^{o} also closely corresponding to alumina, making it difficult to identify graphite. However, the peak at 52^{o} (highlighted by the dashed line), which was absent in mullite and alumina, suggests that graphite was deposited on all catalysts.

The formation of graphite was verified by it being a precursor in the synthesis of carbon nanotubes (CNTs), which were detected by TEM analysis (Section 6.5.1). The temperatures of graphite formation are closely related to that of CNTs. Higher temperatures promote the conversion of surface carbon species into more stable species with a lower affinity for hydrogenation. Nakamura et al. [226] showed that carbidic carbon

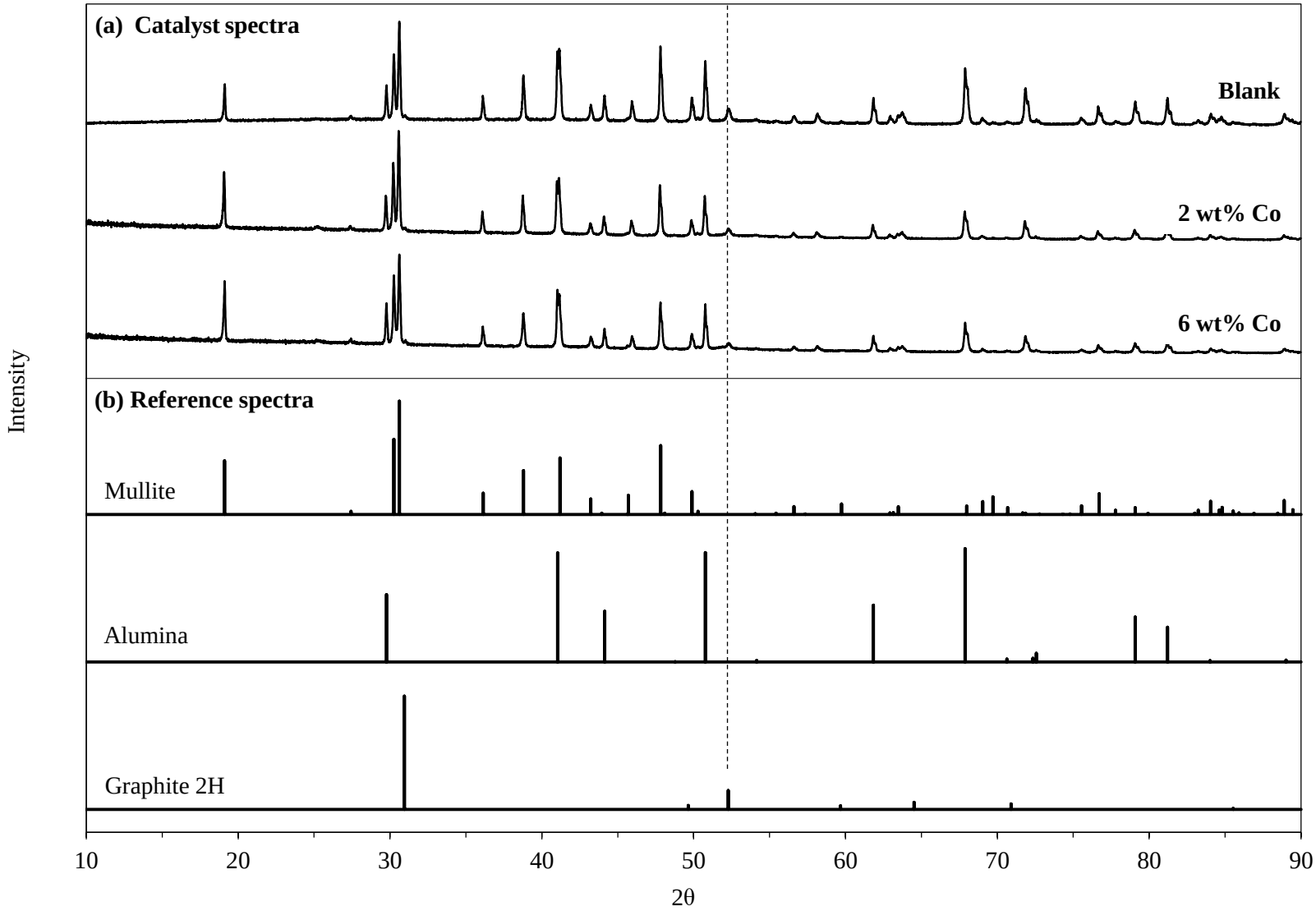

Figure 6.30: XRD plots of (a) catalyst peaks and (b) reference peak patterns.

was formed by the carburization of a Co/Al_2O_3 catalyst (via CO disproportionation) at temperatures exceeding 230°C, which was converted to graphite when the temperature was raised to about 430°C. In addition, Tan et al. [227] observed the occurrence of graphene peaks at 400 and 470°C. Some authors indicated that graphite and graphene hydrogenation occurs above 600°C for cobalt catalysts [228, 229]. Lee et al. [230] obtained similar results to Nakamura et al. [226] for 2-20wt% Co/Al_2O_3 catalysts and also found that some carbon species were resistant to hydrogenation at 600°C. Their FTS experiments showed that the catalyst activity was lower than that of fresh catalyst due to the blockage of active cobalt sites by irreversibly bound graphitic and polymeric carbon.

In this work, graphite could have either hydrogenated to form hydrocarbons or grew to form CNTs at the temperatures mentioned above. However, such high temperatures, required for pure catalytic operations, were also destructive towards the catalyst's structural integrity causing loss of activity. Plasma-catalysis could have lowered the activation temperature for graphite and CNT formation as the catalyst activity was not dramatically modified after more than 40 experiments.

In addition, the longer treatment time of 60 s would have increased the time for CO disproportionation, thus leading to the formation of more stable graphite and CNT products as shown by Nakamura et al. [231]. Furthermore, graphite, in conjunction with other carbonaceous species, is electrically conductive [214]. Therefore, the deposition of carbonaceous species (graphite) on the catalyst surfaces of the blank, 2 and 6 wt% Co catalysts could have modified the plasma electrical properties. These species may have contributed to the deviations in the FTS behaviour for the 2 and 6 wt% Co catalysts from the pure plasma system, as deposits were not detected for pure plasma FTS.

Carbon deposits were also observed on the cathode and anode surfaces for the 2 wt% Co catalyst system, as shown in Photograph 6.2 in Section 6.2.1.6. These deposits were visually observed to interfere with the arc stability. The stability was also represented by the voltage fluctuations [60], determined from the standard deviation errors of 60 000 rms voltage values determined for individual pressures between 1 and 10 MPa for the pressure variation study at 60 s (mentioned in Section 6.2.2). These deviations were then averaged for each system. The resulting average voltage errors for the pure plasma, blank catalyst, 2 and 6 wt% Co catalysts systems were 1.5, 1.2, 2.9 and 1.4% respectively. The highest error for the 2 wt% Co catalyst verified that carbon deposition on the electrodes caused arc fluctuations or deformation, which would have occurred by the arc unhinging from the anodic root and re-hinging on the electrically conductive carbon deposits. Furthermore, the arc interactions with internal components of the reactor caused by the deposits were problematic as it hampered the operability and performance of the reactor. This provides

further support for favouring of the 6 wt% Co catalyst and the future investigation of higher cobalt loadings.

In Section 6.5, the catalyst characterisation analysis performed via TEM, SEM, EDX and XRD, showed that the catalyst properties were enhanced by the non-thermal plasma (NTP), which most likely contributed to the improved performance of the plasma-catalytic FTS process using the cobalt catalysts.

In the final section of Chapter 6, Section 6.6, the results and phenomena of the operating parameter studies (Sections 6.2 to 6.4) were coupled with the catalyst characterisation analysis (Section 6.5), in order to describe the potential reaction pathways that may have occurred in plasma-catalytic FTS.

6.6 Plasma-catalyst interactions

In plasma-catalytic FTS, hydrocarbons were presumed to be synthesised via a combination of the following reaction pathways:

i. Plasma reactions emanated in the arc core as in pure plasma FTS (Section 6.6.1);
ii. Surface reactions were induced on the 2 and 6 wt% Co catalysts due to plasma-thermal activation of the catalyst, as in conventional (pure catalytic) FTS (Section 6.6.2);
iii. Surface reactions were induced on the 2 and 6 wt% Co catalysts via plasma-dissociated CO and H_2 species contacting the catalyst at near room temperature, as in atmospheric pressure NTPs generated by the DBD and corona discharges (Section 6.6.3).

6.6.1 Plasma reactions in the arc core

The first plasma-catalytic reaction route that could have occurred was probably that of pure plasma FTS. In pure plasma FTS, as mentioned in Section 6.2.1.1, electrons in the hot arc core possessed sufficient energy (1 to 20 eV) for dissociation of CO (11.16 eV) and H_2 (4.25 eV) molecules. H_2 was more rapidly dissociated than CO (rate limiting step) due to the lower activation barrier, which when compounded with syngas containing mostly H_2 (68.75 mol%), led to hydrogen being the dominant atomic species in the arc core. Due to the abundance of dissociated hydrogen and the high arc temperature, the rate of hydrogenation of CH_x species to form methane exceeded that of C_2 and C_3 hydrocarbon chain growth. For example, CH_4 (772 ppm) >> C_2H_6 (16.3 ppm) > C_2H_4 (3.4 ppm) > C_3H_8 (2.8 ppm) > C_3H_6 (not detected), where the concentration of methane was 47 times more than ethane for the pure plasma study at 10 MPa and 60 s.

The product distribution for plasma-catalytic FTS, using 2 and 6 wt% cobalt catalysts, was similar to that of pure plasma FTS, especially where methane was the main product. It could be assumed therefore that the overall plasma-catalytic reaction scheme was controlled mainly by the active plasma species i.e. plasma

reactions were rapid compared to slower catalytic reactions. The latter reactions usually benefited from longer residence periods, where the time-on-stream for effective production in industrial and lab-scale FTS ranged from hours to weeks [140].

Despite a high methane content as in pure plasma FTS, the presence of the catalyst and the influence of different cobalt loadings, were noticeable. That is, tripling of the cobalt loading from 2 wt% (0.21g) to 6 wt% (0.65 g), contributed to a considerable increase in the hydrocarbon production rate, and process energy efficiency, proving that the catalyst was active for FTS.

6.6.2 Catalytic reactions by plasma-thermal activation

The second plasma-catalytic reaction route that could have occurred was the thermal activation of the cobalt catalyst by the high temperature arc discharge. Prior to discussing the reactions, the heating effect of the arc discharge on the catalyst and their associated interactions are discussed.

Arc discharge: nature

The non-thermal arc discharge in this work differed from other non-thermal plasmas (NTPs) in that it possessed a hybrid nature. The arc core had a local thermal equilibrium (LTE) nature, with temperatures estimated to range between 10 000 and 20 000 K (based on a helium arc discharge MHD model [158, 211]). However, the bulk gas contained in the arc discharge reactor was minimally heated and remained close to ambient temperature, indicative of a NTP. This overall non-thermal state was achieved as a result of the arc being generated at low currents (250-450 mA) and narrow discharge gaps (0.5-2 mm). These conditions led to the generation of a narrow arc column that was contained between the electrodes i.e. the arc core volume was estimated to be between 0.071 and 0.080 mm^3, which was approximately more than 30 000 times the total volume of the reactor [5].

Since the maximum current used in this work was 0.45 A (450 mA), thermionic emission (where electrons are transferred from the metal surface), and its associated effects on electrode consumption, were negligible. This was verified by the electrode length remaining relatively constant after about 40 to 50 experiments (inclusive of the pressure, current and inter-electrode gap variation studies); after which period the catalyst was removed and a new catalyst was inserted into the reactor. This electrode behaviour contrasted with thermal arcs, where thermionic emission caused by high current generation ($I > 10$ A) [49] usually leads to excessive electrode consumption.

Arc discharge: Heating of the catalyst

The arc discharge reactor was not externally heated for thermal activation of the cobalt catalyst, but instead was kept at room temperature using a cooling jacket. Hence, catalyst heating was solely as a result of the high temperature of the arc discharge, as described above. Plasma-heating of the catalyst depended on the process conditions (pressure, current and inter-electrode gap), which controlled the distance of the hot arc from the catalyst surface.

In most cases there was no direct contact between the arc and the catalyst surface, as viewed through the sightglass. Such contact would have melted the catalyst. That is, the melting point of mullite (~1830^{o}C)[176] was much lower than the arc core temperature. This was due to a clearance of approximately 3.5 mm from the conical tip of the cathode, where the arc was initiated, and a clearance of at least 1.5 mm on the flat anode edge, where the arc hinged (illustrated in Figure 5.3). The arc continuously changed its hitching point on the anode surface resulting in a variable distance between the arc and catalyst surface throughout the treatment period. The variable distances were due to the arc column itself tending to extend or curve towards the top of the reactor due, primarily, to convective forces. This curved arc column most likely heated the catalyst, with the catalyst surface directly above the arc column being heated to the greatest extent.

On the assumption that the arc itself did not contact the catalyst, it was likely that the temperature of the catalyst was indirectly heated by the arc. That is, the catalyst temperature was raised by the heated bulk gas near the catalyst surface, driven by the large temperature gradients that existed between the hot arc and cold bulk gas. These temperature gradients could have existed throughout the reactor, leading to the catalyst surface being non-uniformly heated. Heating of the different locations on the catalyst surface, in order of decreasing surface temperature, was probably as follows: upper surface of the catalyst directly above the arc > catalyst surface below the arc > upper and lower surfaces of the catalyst at an axial distance from the arc.

The non-uniformity of the catalyst heating could have reduced the extent of thermal activation and plasma interaction farther away from the arc core, whereas the area closest to the arc core was expected to experience the greatest extent of thermal activation and thus would have contributed the most to hydrocarbon production. The effects of wide temperature gradients and localised heating across the catalyst surface were observed from SEM micrographs of the 6 wt% Co catalyst presented in Section 6.5.2.2. The SEM images verified that the upper surface of the catalyst, the surface in closer proximity to the curved arc column, was modified to a greater extent during plasma treatment.

Arc discharge: Thermal catalytic reactions

Heating of the catalyst by the hot arc, discussed above, could have led to thermal activation of the catalyst as in conventional FTS. The catalysts in conventional FTS are thermally activated in order to adsorb H_2 and CO, where CO is adsorbed in various states: molecular, dissociative or associative, depending on the catalyst temperature and operating pressure. At higher temperature [133] and pressure [197], CO is more strongly adsorbed on the catalyst surface than H_2, usually present in the associative state [133], leading to higher CO conversion and a broad spectrum of products (C_1 to at least C_{30} hydrocarbons).

Similar thermal activation mechanisms could have occurred during plasma-catalytic FTS, suggested by the increase in hydrocarbon yields with operating pressure and bulk gas temperature (a function of the arc temperature). However, in contrast to conventional FTS, excessive methane yields, and a narrow C_1-C_3 hydrocarbon product distribution, were obtained, as revealed by the results in Chapter 6.

In conventional FTS; high methane yields, limited olefin formation and poor hydrocarbon chain growth were the result of high catalyst temperatures [232]. Therefore, despite similar operating pressures to conventional FTS (2 MPa) [202], the contrasting high arc core temperatures appeared to have favoured methanation and impeded chain growth in both pure plasma and plasma-catalytic FTS. The high temperature operation may have also led to liquid products (undetected by GC) being bypassed, which instead promoted the formation of carbonaceous species.

According to these results, a lowering of the arc temperature was required whilst a high operating pressure was maintained. However, the arc temperature was fully dependent on the operating pressure; contrasting with conventional FTS, in which the operating pressure and catalyst temperature are autonomously controlled.

6.6.3 Catalytic surface reactions by plasma species

The final route for plasma-catalytic reactions were based on the interaction between plasma species and the catalyst. As mentioned in Section 6.6.2, the arc-catalyst distance varied during each experiment as the arc tended to fluctuate in response to load variations; with greater fluctuations possible at higher pressures, currents and inter-electrode gaps. At wider arc-catalyst distances, the active plasma species may have been de-excited and returned to the ground state when moving from the hot arc to cold bulk gas. However, at shorter arc-catalyst distances, it was likely that the arc got close enough to the catalyst surface to enable catalyst interaction with short living active plasma species, which could have migrated to, and reacted on cobalt particles.

In atmospheric pressure non-thermal plasmas (NTPs), vibrationally excited molecules, and radicals, are known to react with the catalyst surface, whereas ions and electronically excited molecules are considered to be de-energised before significant interactions occur [35]. Furthermore, the influence of rotational and translational excitation (controlling the bulk gas temperature) are ignored in regards to surface reactions. In sub-atmospheric pressure plasmas, electronic excitation is more prominent due to wider temperature gaps between the electrons and bulk gas [233].

Based on these trends of low to atmospheric pressure NTPs, in this work, the effect of electronic excitation should have diminished as the pressure was increased and a more thermal equilibrium state was approached. Whereas, vibrationally excited CO molecules and CO radicals could have interacted more strongly with the catalyst leading to a lower catalyst temperature (activation barrier) than that required for ground state CO molecules [74, 77]. The adsorbed or plasma-activated CO on the catalyst surface could then react with associatively adsorbed H_2 (thermally induced), or more likely plasma-dissociated H_2, which should have been abundantly available due to its lower dissociation energy than CO [66], leading to the formation of chain growth monomer species (CH_x).

6.6.4 Catalyst surface temperature: limitations

The plasma-catalytic reaction mechanisms described in Sections 6.6.1 to 6.6.3 were dependent on the catalyst surface temperature as in conventional FTS. However, the catalyst surface temperature was not measured directly as the thermocouple was located away from the arc discharge region in order to avoid electrical interference with the arc, maintaining its stability, as well as avoiding exposure of the thermocouple to high arc temperatures. Despite these limitations, a temperature range could only be estimated based on the reaction products formed.

It was likely that the catalyst was heated to at least 220^{o}C, which was required for thermal activation of a cobalt catalyst in order to promote CO disproportionation in conventional FTS. In addition, the formation of graphite suggested that the catalyst may have been heated to a minimum temperature range of 230-430^{o}C [226]; whereas carbon nanotubes suggested that the catalyst was heated to around 430-600^{o}C, according to CVD mechanisms [210], or as low as 120^{o}C according to PECVD [222, 223]. The temperature-pressure trends in Figure 6.6 showed that there were increases in the bulk gas temperature of only 3.3^{o}C (6 wt%), 0.1^{o}C (2 wt%), 3.2 ^{o}C (0wt%) and 5.8 ^{o}C (pure plasma) for an increase in pressure from 1 to 10 MPa. This minimal variation of the gas temperature could imply that the catalyst temperature remained fairly constant for the pressure ranges investigated.

Alternatively, as mentioned in Section 6.6.3, the catalyst activation temperature could have been reduced due to the active plasma (pre-dissociated) species possessing higher internal energies than ground state molecules in pure catalytic FTS, thus lowering the activation temperature below that of pure catalytic processes. This temperature reduction by plasma has been reported in other plasma-catalytic applications such as hydrocarbon reforming [75-88] and pollutant treatment [89, 90], with temperatures being reduced from as high as 750^{o}C to room temperature [87, 88].

6.6.5 Summary of plasma-catalytic reactions

The conclusion is therefore drawn regarding plasma-catalytic mechanisms: The active plasma species and ground state molecules, reacting on the catalyst surface, combined with reactions within the arc core, were the major reaction pathways. These pathways could have led to plasma-catalytic FTS producing higher hydrocarbon yields, a lower methane/ethane ratio, and higher energy efficiency than pure plasma FTS.

The C_1-C_3 hydrocarbon product distribution for plasma-catalytic FTS using a 2 and 6 wt% cobalt catalysts was similar to that of pure plasma FTS, especially with methane being the major product. This indicated that the overall reaction scheme was controlled mainly by the active plasma species. That is, plasma reactions were rapid, compared to slower catalytic reactions that usually benefited from longer residence periods. Periods where the time-on-stream for effective production in industrial and lab-scale FTS ranged from hours to weeks [140].

Apart from the rapid plasma reactions, the low cobalt loading could have also contributed to high methane yields and a narrow product distribution. This trend was seen in the Co/Al_2O_3 study by Tavasoli et al. [218], who found that the cobalt loadings in the lower range of 8-40 wt% led to a more selective catalyst for methane and light C_2-C_4 hydrocarbons.

However, despite the rapid plasma reactions and low cobalt loadings leading to high methane yields, the presence of the catalyst, and the influence of cobalt loadings, were clearly noticeable when compared to the pure plasma process. Both the 2 and 6 wt% Co catalysts improved the hydrocarbon production by a factor of > 200, and energy consumption by a factor of > 100 (for the inter-electrode gap study). Furthermore, a reasonable improvement of these performance factors were observed from a tripling of the cobalt loading from 2 wt% (0.21g) to 6 wt% (0.65 g). More importantly, the 6 wt% Co catalyst system did not significantly interfere with the arc stability, as was the case for the 2 wt% Co catalyst system (arising from high carbon deposition on the electrodes). The above mentioned findings suggested that the catalyst was certainly active for FTS.

A detailed explanation for these plasma-catalytic interactions could not be ascertained at this exploratory stage of research, due to the complex plasma chemistry and catalytic interactions involved. In addition, there were limitations in the experimental setup, which included not having the facilities to measure the catalyst and arc temperatures.

6.6.6 Catalytic activity

In addition to plasma-catalytic interactions leading to higher product yields and improved chain growth (discussed in Sections 6.6.1 to 6.6.4 above), these interactions also affected the catalyst activity and stability.

The low cobalt loadings of 2 and 6 wt% (compared to 10 to 40 wt% in conventional FTS) may have contributed to the prominence of methanation and carbon deposition in this work. In addition to carbon deposition; unreduced cobalt oxide, oxidation of metallic cobalt by water and sintering are also known to decrease the catalyst activity [234]. These factors, if present, did not lead to a decline in catalytic activity. In some cases, repetition of experiments led to higher hydrocarbon yields within the ±11% expanded experimental concentration uncertainty, probably due to a low degree of carbon deposition resulting in the high availability of catalytic sites for adsorption.

The catalytic activity may have been maintained due to several factors: Firstly, the reducible environment, created by the combination of the hot arc core and highly reductive gases (H_2 and CO); secondly, the high operating pressures, which are shown to cause catalyst re-construction in conventional FTS as well as to inhibit catalytic re-oxidation caused by water [197] and; finally, the reduction of cobalt oxides to smaller metallic cobalt particles.

The occurrence of these phenomena, evident in the SEM images (Section 6.5.2.2), where cobalt particles that were exposed to plasma were smaller in size and more uniformly dispersed than the particles in fresh catalysts, were likely to be responsible for the consistent catalyst activity and good stability of the 2 and 6 wt% Co catalysts.

Chapter 7
CONCLUSIONS

The purpose of the exploration was to ascertain whether the product yields and energy efficiency of pure plasma FTS (no catalyst) could be improved upon by plasma-catalytic FTS, under the scope of pressure (0.5 to 10 MPa), current (250 to 450 mA) and inter-electrode gap (0.5 to 2 mm).

The trace hydrocarbons produced by the pure plasma, 2 and 6 wt% Co catalytic systems, decreased in the order: methane >> ethane > ethylene > propane > propylene. Methane, the dominant product, exhibited similar qualitative trends in pure plasma and plasma-catalytic systems, indicating that the high temperature of the arc core, and active plasma species within the hot arc, induced plasma-chemical reactions at a much faster rate than catalytic surface reactions, thus directing the reaction pathway towards methanation and impeding chain growth in plasma-catalysis.

Despite the high methane yields, the introduction of a catalyst into the discharge region did however shift the FTS reaction pathways. The blank catalyst led to considerably lower C_1-C_3 hydrocarbon yields than those of pure plasma FTS. In contrast, the 2 and 6 wt% Co catalytic systems led to higher C_1-C_3 hydrocarbons yields than both pure plasma and the blank catalyst, as well as higher olefinicity, higher energy efficiencies (lower specific required energy (SRE)), and the formation of propylene (produced almost exclusively by the 6 wt% Co catalyst). These findings indicated that the Co catalyst was activated by plasma (in the absence of external heating) to promote FTS reactions, either by thermal activation of adsorbed H_2 and CO ground state molecules and/or radicals and vibrationally-excited CO.

The optimum operating conditions, based on the highest C_2 and C_3 hydrocarbon yields, lower methane/ethane and ethane/ethylene ratios, and a comparatively lower energy consumption (assumed to have originated from the above-stated reaction mechanisms), were as follows; (i) 10 MPa at 10 s (most favourable for C_3 hydrocarbon production), and 2 MPa at 60 s (most favourable for C_2 hydrocarbon production), for the pressure variation study (0.5 to 10 MPa); (ii) 250 mA for the current variation study (250 to 450 mA), due to this relatively low current leading to a more non-equilibrium plasma nature, which resulted in a glow-like or arc-to-glow transition type plasma developing at 250 and 300 mA in the presence of the 6wt% Co catalyst (a phenomena reported in the literature as a result of plasma-catalyst interaction [74, 100, 109]); and (iii) the widest discharge gap of 2 mm for the inter-electrode gap variation study (0.5

to 2 mm), due to this gap producing the largest discharge volume and largest surface area for catalytic heating.

These results showed that the inter-electrode gap was the most influential operating parameter on hydrocarbon production and energy consumption, followed by current and pressure, which can be further optimised. At 2 mm using the 6wt% Co catalyst, the methane, ethane, ethylene and propane concentrations of 22 424 (2.24 mol%), 517, 101, 79 and 19 ppm, respectively, were 1.5, 1.5, 0.8 and 4 times greater than the 2 wt% Co catalyst concentrations and 227, 210, 278, 1353 times greater than the pure plasma concentrations. In addition, at 2 mm, the 6 wt% Co catalyst (265 $MJ/mol_{methane,prod}$) used slightly more energy than the 2 wt% Co catalyst (224 $MJ/mol_{methane,prod}$) and ~107 times less energy to produce a mole of methane than the pure plasma system.

Catalyst characterisation tools were used to understand the effect of different cobalt loadings on FTS and to evaluate the influence of plasma on the catalyst. TEM analysis showed that the 6 wt% Co catalyst contained larger cobalt clusters (19 nm) than the 2 wt% Co catalyst (10 nm). The large clusters were considered to improve catalyst reducibility, providing a larger surface area of active sites for surface reactions. This cobalt loading trend was in agreement with conventional FTS [218]. TEM also showed that carbon nanotubes were synthesised exclusively by the 6 wt% Co catalyst, which is not produced under conventional FTS conditions. XRD analysis revealed traces of graphite deposits on the blank, 2 and 6 wt% Co catalysts, which are known to be precursors for carbon nanotube synthesis. SEM-EDX analysis showed that the coating thicknesses increased with cobalt loading from 2 wt% (49 μm) to 6 wt% (51 μm) as observed in the literature [171], corresponding to the increase in cluster sizes with cobalt loading evaluated using TEM.

SEM-EDX also showed that the 2 and 6 wt% Co catalyst surfaces were modified by plasma treatment to different degrees, producing a more uniform dispersion and possibly reducing cobalt oxides to metallic cobalt due to the reductive syngas environment and high pressure operation. These modifications, which are similar to that observed in other plasma-catalytic studies [32, 66, 93, 102], may have contributed to the sustaining of the catalyst activity in this work. Furthermore, the catalyst surface closer to the arc discharge seemed to be modified to a greater extent, suggesting the formation of hotspots, a phenomenon that has been observed in the literature [74].

The temperature of the catalyst and arc discharge could not be measured in this work. These are vital for understanding the plasma and catalyst surface chemistries. However, the catalyst temperature may be

estimated based on the products formed; for example, 230°C for synthesis in conventional FTS. However, it was likely that the plasma species lowered the activation barriers for formation of these species as reported in other plasma-catalytic processes [87, 88]

Finally, the results in this work showed that the plasma-catalytic system with the higher cobalt catalyst loading of 6 wt%, generally produced the highest hydrocarbon yields for most operating conditions investigated. It also led to a more stable arc discharge (related to lower carbon deposition) than the 2 wt% Co catalyst. Therefore, higher cobalt loadings between 10 and 40 wt% (used in conventional FTS) [145] should be investigated in order to realise the potential of plasma-catalytic FTS.

In regards to the field of non-thermal plasma-catalysis, to the best of the author's understanding, this was the first study undertaken at high pressure, demonstrating that an arc discharge could be ignited and sustained at high pressure in the presence of a catalyst. The novelty of this work also prompted the implementation of a preparation technique that combined the washcoating method used in monolithic catalysis and a catalyst-reactor configuration used in atmospheric pressure plasma-catalysis.

The results obtained by the combination of these technologies could incentivize the application of plasma-catalysis in other reactive systems; systems that would benefit from the synergy between non-thermal plasma, high pressure and a catalyst. This provides the additional advantages of fast treatment times and compact equipment setup, unique to non-thermal plasma reactors.

Chapter 8
RECOMMENDATIONS

Future work should include the following modifications to the equipment and experimental techniques:

8.1 Arc discharge reactor

- An automated anode retraction system to improve inter-electrode gap reproducibility.
- A heated reactor system with the capacity of at least 100°C, which will prevent condensation of water at higher pressures, as liquid water was found to extinguish the arc at 10 MPa for the 6 wt% Co catalytic system. Additional studies should investigate the effect of heating the reactor up to the conventional FTS temperature range of 200 to 250°C, with the catalyst present and absent, in order to determine the contribution of thermal catalytic activation in plasma-catalytic FTS.
- Internal or external mixing of the reactor contents. Such a modification may require major equipment modifications. This idea should be further contemplated in order to increase the volume of treated gas, which is strictly constrained by the low arc discharge/reactor volume ratio.
- An on-line analysis of the product stream in order to reduce sampling error.
- An investigation of pure plasma and plasma-catalytic FTS with the arc discharge reactor arranged in a vertical configuration, which was demonstrated by Lebouvier et al. [211] to produce a more stable CF_4 arc discharge.

8.2 Catalyst

- Employ higher cobalt loadings between 10 and 40 wt%, which is the typical range used in conventional FTS. The effects of high cobalt loadings (8-40 wt%) was seen in the study by Tavasoli et al. [218]. In their work, lower cobalt loadings deposited onto an Al_2O_3 support led to a more selective catalyst for methane (as in this work) and light C_2-C_4 hydrocarbons; whereas higher loadings decreased lighter hydrocarbon production and promoted higher molecular chain growth, resulting in a greater than 60% improvement in C_5^+ selectivity as a result of an increase in cobalt loading from 8 to 40 wt%. Therefore, by increasing the cobalt loading in plasma-catalytic FTS, similar improvements in the product distribution and yields may occur.
- Optimisation of the catalyst preparation method i.e. coating, calcination and reduction.
- Addition of a reduction promoter, such as platinum, to facilitate reduction of cobalt oxides into active metallic cobalt [118].
- Addition of a manganese (Mn) promoter, suggested to reduce methane selectivity and increase activity for cobalt catalysts [202].

REFERENCES

[1] Takeshita T, Yamaji K, (2008), Important roles of Fischer–Tropsch synfuels in the global energy future, Energy Policy 36: 2773-2784.

[2] Morales F, Weckhuysen BM, (2006), Promotion effects in Co-based Fischer-Tropsch catalysis, Catalysis 19.

[3] Aranda G, van der Drift A, Smit R, (2014), The Economy of Large Scale Biomass to Substitute Natural Gas (bioSNG) plants.

[4] Iwarere S, Rohani V, Ramjugernath D, Fabry F, Fulcheri L, (2014), Hydrocarbons synthesis from syngas by very high pressure plasma, Chem. Eng. J. 241: 1-8.

[5] Rohani V, Iwarere S, Fabry F, Mourard D, Izquierdo E, Ramjugernath D, Fulcheri L, (2011), Experimental study of hydrocarbons synthesis from syngas by a tip–tip electrical discharge at very high pressure, Plasma Chem. Plasma Process. 31: 663-679.

[6] Rajanikanth B, Shimizu K, Okumoto M, Katsura S, Mizuno A, (1995),Application of pulsed discharge plasma for methanol synthesis, in: Industry Applications Conference, 1995. Thirtieth IAS Annual Meeting, IAS'95., Conference Record of the 1995 IEEE, IEEE, pp. 1459-1462.

[7] Zhou LM, Xue B, Kogelschatz U, Eliasson B, (1998), Partial Oxidation of Methane to Methanol with Oxygen or Air in a Nonequilibrium Discharge Plasma, Plasma Chem. Plasma Process. 18: 375-393.

[8] Kraus M, Eliasson B, Kogelschatz U, Wokaun A, (2001), CO 2 reforming of methane by the combination of dielectric-barrier discharges and catalysis, PCCP 3: 294-300.

[9] Cho W, Baek Y, Moon S-K, Kim YC, (2002), Oxidative coupling of methane with microwave and RF plasma catalytic reaction over transitional metals loaded on ZSM-5, Catal. Today 74: 207-223.

[10] Kogelschatz U, Eliasson B, (1995),Ozone generation and applications, Handbook of Electrostatic Processes (JS Chang, AJ Kelly, JM Crowley, eds), in, Marcel Dekker, New York, pp. 581.

[11] Lu B, Zhang X, Yu X, Feng T, Yao S, (2006), Catalytic oxidation of benzene using DBD corona discharges, J. Hazard. Mater. 137: 633-637.

[12] Ye Z, Zhang Y, Li P, Yang L, Zhang R, Hou H, (2008), Feasibility of destruction of gaseous benzene with dielectric barrier discharge, J. Hazard. Mater. 156: 356-364.

[13] Futamura S, Zhang A, Prieto G, Yamamoto T, (1998), Factors and intermediates governing byproduct distribution for decomposition of butane in nonthermal plasma, Industry Applications, IEEE Transactions on 34: 967-974.

[14] Ogata A, Mizuno K, Kushiyama S, Yamamoto T, (1998), Methane Decomposition in a Barium Titanate Packed-Bed Nonthermal Plasma Reactor, Plasma Chem. Plasma Process. 18: 363-373.

[15] Ogata A, Ito D, Mizuno K, Kushiyama S, Gal A, Yamamoto T, (2002), Effect of coexisting components on aromatic decomposition in a packed-bed plasma reactor, Applied Catalysis A: General 236: 9-15.

[16] Gervasini A, Ragaini V, (2000), Catalytic technology assisted with ionization/ozonization phase for the abatement of volatile organic compounds, Catal. Today 60: 129-138.

[17] Wang Y-F, Lee W-J, Chen C-Y, Hsieh L-T, (1999), Decomposition of Dichlorodifluoromethane by Adding Hydrogen in a Cold Plasma System, Environ. Sci. Technol. 33: 2234-2240.

[18] Oda T, (2003), Non-thermal plasma processing for environmental protection: decomposition of dilute VOCs in air, J. Electrostatics 57: 293-311.

[19] Gal A, Kurahashi M, Kuzumoto M, (1999), An energy-consumption and byproduct-generation analysis of the discharge nonthermal plasma-chemical NO-reduction process, J. Phys. D: Appl. Phys. 32: 1163.

[20] Li R, Yan K, Miao J, Wu X, (1998), Heterogeneous reactions in non-thermal plasma flue gas desulfurization, Chem. Eng. Sci. 53: 1529-1540.

[21] Stoffels E, Flikweert A, Stoffels W, Kroesen G, (2002), Plasma needle: a non-destructive atmospheric plasma source for fine surface treatment of (bio) materials, Plasma Sources Sci. Technol. 11: 383.

[22] Leduc M, Guay D, Leask R, Coulombe S, (2009), Cell permeabilization using a non-thermal plasma, New Journal of Physics 11: 115021.

[23] Pochner K, Beil S, Horn H, Blömer M, (1997), Treatment of polymers for subsequent metallization using intense UV radiation or plasma at atmospheric pressure, Surf. Coat. Technol. 97: 372-377.

[24] Seeböck R, Esrom H, Charbonnier M, Romand M, Kogelschatz U, (2001), Surface modification of polyimide using dielectric barrier discharge treatment, Surf. Coat. Technol. 142–144: 455-459.

[25] Xu W, Liu X, (2003), Surface modification of polyester fabric by corona discharge irradiation, Eur. Polym. J. 39: 199-202.

[26] Kline L, (1986), Electron and chemical kinetics in the low-pressure RF discharge etching of silicon in SF6, Plasma Science, IEEE Transactions on 14: 145-155.

[27] Kim J, Byun D, Kim J-s, Kum D-W, (2000), Low-temperature growth of GaN by atomic nitrogen based on a dielectric barrier discharge, J. Cryst. Growth 210: 478-486.

[28] Jiang N, Qian SF, Wang L, Zhang HX, (2001), Localized material growth by a dielectric barrier discharge, Thin Solid Films 390: 119-122.

[29] Goossens O, Dekempeneer E, Vangeneugden D, Van de Leest R, Leys C, (2001), Application of atmospheric pressure dielectric barrier discharges in deposition, cleaning and activation, Surf. Coat. Technol. 142: 474-481.

[30] Kim S-S, Lee H, Na B-K, Song HK, (2004), Plasma-assisted reduction of supported metal catalyst using atmospheric dielectric-barrier discharge, Catal. Today 89: 193-200.

[31] Dhar R, Pedrow PD, Liddell KC, Ming Q, Moeller TM, Osman M, (2005), Plasma-enhanced metal-organic chemical vapor deposition (PEMOCVD) of catalytic coatings for fuel cell reformers, Plasma Science, IEEE Transactions on 33: 138-146.

[32] Cheng D-G, (2008), Plasma decomposition and reduction in supported metal catalyst preparation, Catalysis Surveys from Asia 12: 145-151.

[33] Sharma R, Rimmer RD, Gunamgari J, Shekhawat RS, Davis BJ, Mazumder MK, Lindquist D, (2005), Plasma-assisted activation of supported Au and Pd catalysts for CO oxidation, Industry Applications, IEEE Transactions on 41: 1373-1376.

[34] GyoáKoo I, SeokáLee M, HeeáShim J, HwanáAhn J, MooáLee W, (2005), Platinum nanoparticles prepared by a plasma-chemical reduction method, J. Mater. Chem. 15: 4125-4128.

[35] Liu C-j, Vissokov GP, Jang BW-L, (2002), Catalyst preparation using plasma technologies, Catal. Today 72: 173-184.

[36] Waymouth JF, (1971), Electrical discharge lamps, Cambridge, MA: MIT Press.

[37] Cho G, Lee JY, Lee DH, Kim SB, Song HS, Koo J, Kim BS, Kang JG, Choi EH, Lee UW, (2005), Glow discharge in the external electrode fluorescent lamp, Plasma Science, IEEE Transactions on 33: 1410-1415.

[38] Fridman A, (2008), Plasma chemistry, Cambridge University Press.

[39] Takenaka Y, Kuzumoto M, Yasui K, Yagi S, Tagashira M, (1991), High power and high focusing CWCO 2 laser using an unstable resonator with a phase-unifying output coupler, Quantum Electronics, IEEE Journal of 27: 2482-2487.

[40] Boyd IW, Zhang J-Y, (2001), Photo-induced growth of dielectrics with excimer lamps, Solid·State Electron. 45: 1413-1431.

[41] Boeuf J, (2003), Plasma display panels: physics, recent developments and key issues, J. Phys. D: Appl. Phys. 36: R53.

[42] Petitpas G, Rollier JD, Darmon A, Gonzalez-Aguilar J, Metkemeijer R, Fulcheri L, (2007), A comparative study of non-thermal plasma assisted reforming technologies, Int. J. Hydrogen Energy 32: 2848-2867.

[43] Benilov M, (2008), Understanding and modelling plasma–electrode interaction in high-pressure arc discharges: a review, J. Phys. D: Appl. Phys. 41: 144001.

[44] Benilov M, Naidis G, (2003), Modelling of low-current discharges in atmospheric-pressure air taking account of non-equilibrium effects, J. Phys. D: Appl. Phys. 36: 1834.

[45] Bromberg L, Cohn D, Rabinovich A, Heywood J, (2001), Emissions reductions using hydrogen from plasmatron fuel converters, Int. J. Hydrogen Energy 26: 1115-1121.

[46] Kogelschatz U, (2004), Atmospheric-pressure plasma technology, Plasma Phys. Controlled Fusion 46: B63.

[47] Kalra CS, Gutsol AF, Fridman A, (2005), Gliding arc discharges as a source of intermediate plasma for methane partial oxidation, Plasma Science, IEEE Transactions on 33: 32-41.

[48] Arkhipenko V, Kirillov A, Safronau YA, Simonchik L, Zgirouski S, (2009), Self-sustained dc atmospheric pressure normal glow discharge in helium: from microamps to amps, Plasma Sources Sci. Technol. 18: 045013.

[49] Staack D, Farouk B, Gutsol A, Fridman A, (2005), Characterization of a dc atmospheric pressure normal glow discharge, Plasma Sources Sci. Technol. 14: 700.

[50] Lowke J, (1979), Simple theory of free-burning arcs, J. Phys. D: Appl. Phys. 12: 1873.

[51] Turchi P, Rutberg P, Kulishevich A, Hohman K, Kamhawi H, Mikellides I, Mikellides P, Schmahl C, Tegmeyer R, Gibson J, (1994),Development of a high power and high pressure plasma flow facility, in: 30th joint propulsion conference and exhibition, Indianapolis, pp. 27-29.

[52] Horn D, Felderman E, MacDermott W, (1996), Impacts of external magnetic fields applied to high-pressure electric arc heaters, J. Propul. Power 12: 1093-1098.

[53] Schmidt H-P, Speckhofer G, (1996), Experimental and theoretical investigation of high-pressure arcs. I. The cylindrical arc column (two-dimensional modeling), Plasma Science, IEEE Transactions on 24: 1229-1238.

[54] Terashima K, Howald L, Haefke H, Güntherodt H-J, (1996), Development of a mesoscale/nanoscale plasma generator, Thin Solid Films 281: 634-636.

[55] Montgomery P, Smith D, Sheeley J, Felderman E, (2004),The quest for higher total pressures: justification and current development efforts for a higher pressure arc-heater facility, USAF developmental test and evaluation summit, Woodland Hills, 16–18 Nov 2004, in, AIAA-2004-6815.

[56] Dubreus TM, Sheeley JM, Stewart JH, Development of a Mid-Pressure Arc-Heated Facility for Hypersonic Vehicle Testing, in: US Air Force T&E Days 2010, 2010, pp. 1732.

[57] Tachibana K, (2006), Current status of microplasma research, IEEJ Transactions on Electrical and Electronic Engineering 1: 145-155.

[58] Izquierdo E, Gonzalez-Aguilar J, Fulcheri L, (2008),Theoretical and experimental study of an argon free burning arc dicharge at very high-pressure and low-intensity, in: Plasma Science, 2008. ICOPS 2008. IEEE 35th International Conference on, IEEE, pp. 1-1.

[59] Izquierdo E, Aguilar JG, Fulcheri L, (2009), Electrical characterisation of very high pressure Ar/H2 low current arc discharge, High Temperature Material Processes: An International Quarterly of High-Technology Plasma Processes 13.

[60] Fulcheri L, Rohani V, Fabry F, Traisnel N, (2010), Experimental electrical characterization of a low-current tip–tip arc discharge in helium atmosphere at very high pressure, Plasma Sources Sci. Technol. 19: 045010.

[61] Iwarere SA, Lebouvier A, Fulcheri L, Ramjugernath D, (2014), Experimental study on the formation of higher fluorocarbons from CF 4 by a tip–tip electrical arc discharge at very high pressure, J. Fluorine Chem. 166: 96-103.

[62] Iwarere SA, Rohani V-J, Ramjugernath D, Fulcheri L, (2015), Dry reforming of methane in a tip–tip arc discharge reactor at very high pressure, Int. J. Hydrogen Energy 40: 3388-3401.

[63] Jager B, Espinoza R, (1995), Advances in low temperature Fischer-Tropsch synthesis, Catal. Today 23: 17-28.

[64] Sie S, (1998), Process development and scale up: IV. Case history of the development of a Fischer-Tropsch synthesis process, Rev. Chem. Eng. 14: 109-157.

[65] Dry M, (1981), The Fischer-Tropsch Synthesis, Catalysis science and technology 1: 159-255.

[66] Al-Harrasi WS, Zhang K, Akay G, (2013), Process intensification in gas-to-liquid reactions: plasma promoted Fischer-Tropsch synthesis for hydrocarbons at low temperatures and ambient pressure, Green Process. Synth. 2: 479-490.

[67] Vandenbroucke A, Morent R, De Geyter N, Nguyen Dinh M, Giraudon J, Lamonier J, Leys C, (2010), Plasma-catalytic decomposition of TCE, Int J plasma environ sci technol 4: 135-138.

[68] Whitehead JC, (2010), Plasma catalysis: a solution for environmental problems, Pure Appl. Chem. 82: 1329-1336.

[69] Chae JO, Demidiouk V, Yeulash M, Choi IC, Jung TG, (2004), Experimental study for indoor air control by plasma-catalyst hybrid system, Plasma Science, IEEE Transactions on 32: 493-497.

[70] Bromberg L, Cohn D, Rabinovich A, Alexeev N, Samokhin A, Hadidi K, Palaia J, Margarit-Bel N, (2006), Onboard plasmatron hydrogen production for improved vehicles. 2006, Massachusetts Institute of Technology, Plasma Fusion and Science Center.

[71] Tu X, Whitehead J, (2012), Plasma-catalytic dry reforming of methane in an atmospheric dielectric barrier discharge: Understanding the synergistic effect at low temperature, Applied Catalysis B: Environmental 125: 439-448.

[72] Gallon HJ, Tu X, Twigg MV, Whitehead JC, (2011), Plasma-assisted methane reduction of a NiO catalyst—Low temperature activation of methane and formation of carbon nanofibres, Applied Catalysis B: Environmental 106: 616-620.

[73] Holzer F, Roland U, Kopinke F-D, (2002), Combination of non-thermal plasma and heterogeneous catalysis for oxidation of volatile organic compounds: Part 1. Accessibility of the intra-particle volume, Applied Catalysis B: Environmental 38: 163-181.

[74] Neyts E, Bogaerts A, (2014), Understanding plasma catalysis through modelling and simulation—a review, J. Phys. D: Appl. Phys. 47: 224010.

[75] Amouroux J, Cavadias S, Doubla A, (2011),Carbon Dioxide reduction by non-equilibrium electrocatalysis plasma reactor, in: IOP Conference Series: Materials Science and Engineering, IOP Publishing, pp. 012005.

[76] Nikoo MK, Sharifi MA, Amin NS, (2011), Carbon dioxide reforming of methane by catalytic-plasma reactor over Cu/Zn/γ-Al2O3, Jurnal Teknologi (Sciences and Engineering) 56: 75-86.

[77] Chen HL, Lee HM, Chen SH, Chao Y, Chang MB, (2008), Review of plasma catalysis on hydrocarbon reforming for hydrogen production—interaction, integration, and prospects, Applied Catalysis B: Environmental 85: 1-9.

[78] Eliasson B, Kogelschatz U, Xue B, Zhou L-M, (1998), Hydrogenation of Carbon Dioxide to Methanol with a Discharge-Activated Catalyst, Ind. Eng. Chem. Res. 37: 3350-3357.

[79] Li M-W, Tian Y-L, Xu G-H, (2007), Characteristics of carbon dioxide reforming of methane via alternating current (AC) corona plasma reactions, Energy & fuels 21: 2335-2339.

[80] Wallis AE, Whitehead J, Zhang K, (2007), The removal of dichloromethane from atmospheric pressure air streams using plasma-assisted catalysis, Applied Catalysis B: Environmental 72: 282-288.

[81] Nozaki T, Muto N, Kado S, Okazaki K, (2004), Dissociation of vibrationally excited methane on Ni catalyst: Part 1. Application to methane steam reforming, Catal. Today 89: 57-65.

[82] Nozaki T, Muto N, Kadio S, Okazaki K, (2004), Dissociation of vibrationally excited methane on Ni catalyst: part 2. Process diagnostics by emission spectroscopy, Catal. Today 89: 67-74.

[83] Pietruszka B, Anklam K, Heintze M, (2004), Plasma-assisted partial oxidation of methane to synthesis gas in a dielectric barrier discharge, Applied Catalysis A: General 261: 19-24.

[84] Wang Q, Yan B-H, Jin Y, Cheng Y, (2009), Dry reforming of methane in a dielectric barrier discharge reactor with Ni/Al2O3 catalyst: interaction of catalyst and plasma, Energy & Fuels 23: 4196-4201.

[85] Kappes T, Schiene W, Hammer T, (2002),Energy balance of a Dielectric Barrier Discharge reactor for hydrocarbon steam reforming, in: 8th International Symposium on High Pressure Low Temperature Plasma Chemestry proceedings, HAKONE, Citeseer.

[86] Sobacchi M, Saveliev A, Fridman A, Kennedy LA, Ahmed S, Krause T, (2002), Experimental assessment of a combined plasma/catalytic system for hydrogen production via partial oxidation of hydrocarbon fuels, Int. J. Hydrogen Energy 27: 635-642.

[87] Li M-W, Liu C-P, Tian Y-L, Xu G-H, Zhang F-C, Wang Y-Q, (2006), Effects of catalysts in carbon dioxide reforming of methane via corona plasma reactions, Energy & fuels 20: 1033-1038.

[88] Pham M, Goujard V, Tatibouet J, Batiot-Dupeyrat C, (2011), Activation of methane and carbon dioxide in a dielectric-barrier discharge-plasma reactor to produce hydrocarbons—Influence of La 2 O 3/γ-Al 2 O 3 catalyst, Catal. Today 171: 67-71.

[89] Marques R, Da Costa S, Da Costa P, (2008), Plasma-assisted catalytic oxidation of methane: On the influence of plasma energy deposition and feed composition, Applied Catalysis B: Environmental 82: 50-57.

[90] Magureanu M, Mandache NB, Eloy P, Gaigneaux EM, Parvulescu VI, (2005), Plasma-assisted catalysis for volatile organic compounds abatement, Applied catalysis B: environmental 61: 12-20.

[91] Kim H-H, Ogata A, Futamura S, (2008), Oxygen partial pressure-dependent behavior of various catalysts for the total oxidation of VOCs using cycled system of adsorption and oxygen plasma, Applied Catalysis B: Environmental 79: 356-367.

[92] Guo Y-F, Ye D-Q, Chen K-F, He J-C, Chen W-L, (2006), Toluene decomposition using a wire-plate dielectric barrier discharge reactor with manganese oxide catalyst in situ, J. Mol. Catal. A: Chem. 245: 93-100.

[93] Zhang Y-P, Ma P-S, Zhu X, Liu C-J, Shen Y, (2004), A novel plasma-treated Pt/NaZSM-5 catalyst for NO reduction by methane, Catal. Commun. 5: 35-39.

[94] Guo Y-f, Ye D-q, Chen K-f, He J-c, (2007), Toluene removal by a DBD-type plasma combined with metal oxides catalysts supported by nickel foam, Catal. Today 126: 328-337.

[95] Pribytkov A, Baeva G, Telegina N, Tarasov A, Stakheev AY, Tel'nov A, Golubeva V, (2006), Effect of electron irradiation on the catalytic properties of supported Pd catalysts, Kinet. Catal. 47: 765-769.

[96] Wallis AE, Whitehead JC, Zhang K, (2007), The removal of dichloromethane from atmospheric pressure nitrogen gas streams using plasma-assisted catalysis, Applied Catalysis B: Environmental 74: 111-116.

[97] Kizling MB, Järås SG, (1996), A review of the use of plasma techniques in catalyst preparation and catalytic reactions, Applied Catalysis A: General 147: 1-21.

[98] Kang WS, Park JM, Kim Y, Hong SH, (2003), Numerical study on influences of barrier arrangements on dielectric barrier discharge characteristics, Plasma Science, IEEE Transactions on 31: 504-510.

[99] Holzer F, Kopinke F, Roland U, (2005), Influence of ferroelectric materials and catalysts on the performance of non-thermal plasma (NTP) for the removal of air pollutants, Plasma Chem. Plasma Process. 25: 595-611.

[100] Chen HL, Lee HM, Chen SH, Chang MB, Yu SJ, Li SN, (2009), Removal of volatile organic compounds by single-stage and two-stage plasma catalysis systems: a review of the performance enhancement mechanisms, current status, and suitable applications, Environ. Sci. Technol. 43: 2216-2227.
[101] Kim H-H, Ogata A, Futamura S, (2006), Effect of different catalysts on the decomposition of VOCs using flow-type plasma-driven catalysis, Plasma Science, IEEE Transactions on 34: 984-995.
[102] Cheng D-g, Zhu X, Ben Y, He F, Cui L, Liu C-j, (2006), Carbon dioxide reforming of methane over Ni/Al 2 O 3 treated with glow discharge plasma, Catal. Today 115: 205-210.
[103] Roland U, Holzer F, Kopinke F-D, (2002), Improved oxidation of air pollutants in a non-thermal plasma, Catal. Today 73: 315-323.
[104] Morent R, Dewulf J, Steenhaut N, Leys C, Van Langenhove H, (2006), Hybrid plasma-catalyst system for the removal of trichloroethylene in air, Journal of Advanced Oxidation Technologies 9: 53-58.
[105] Ogata A, Yamanouchi K, Mizuno K, Kushiyama S, Yamamoto T, (1999), Decomposition of benzene using alumina-hybrid and catalyst-hybrid plasma reactors, Industry Applications, IEEE Transactions on 35: 1289-1295.
[106] Tao K, Ohta N, Liu G, Yoneyama Y, Wang T, Tsubaki N, (2013), Plasma enhanced catalytic reforming of biomass tar model compound to syngas, Fuel 104: 53-57.
[107] Van Durme J, Dewulf J, Sysmans W, Leys C, Van Langenhove H, (2007), Efficient toluene abatement in indoor air by a plasma catalytic hybrid system, Applied Catalysis B: Environmental 74: 161-169.
[108] Chao Y, Huang C-T, Lee H-M, Chang M-B, (2008), Hydrogen production via partial oxidation of methane with plasma-assisted catalysis, Int. J. Hydrogen Energy 33: 664-671.
[109] Van Durme J, Dewulf J, Leys C, Van Langenhove H, (2008), Combining non-thermal plasma with heterogeneous catalysis in waste gas treatment: a review, Applied Catalysis B: Environmental 78: 324-333.
[110] Huang H, Ye D, Leung DY, Feng F, Guan X, (2011), Byproducts and pathways of toluene destruction via plasma-catalysis, J. Mol. Catal. A: Chem. 336: 87-93.
[111] Mizuno A, (2013), Generation of non-thermal plasma combined with catalysts and their application in environmental technology, Catal. Today 211: 2-8.
[112] Van Wesenbeeck K, Hauchecorne B, Lenaerts S, (2013), Integration of a photocatalytic coating in a corona discharge unit for plasma assisted catalysis, Journal of Environmental Solutions 2: 16-24.
[113] Kim HH, (2004), Nonthermal plasma processing for air-pollution control: a historical review, current issues, and future prospects, Plasma Processes and Polymers 1: 91-110.
[114] Chang MB, Lee HM, (2004), Abatement of perfluorocarbons with combined plasma catalysis in atmospheric-pressure environment, Catal. Today 89: 109-115.
[115] Yu SJ, Chang MB, (2001), Oxidative conversion of PFC via plasma processing with dielectric barrier discharges, Plasma Chem. Plasma Process. 21: 311-327.

[116] Chen X, Rozak J, Lin J-C, Suib SL, Hayashi Y, Matsumoto H, (2001), Oxidative decomposition of chlorinated hydrocarbons by glow discharge in PACT (plasma and catalyst integrated technologies) reactors, Applied Catalysis A: General 219: 25-31.

[117] Wilhelm D, Simbeck D, Karp A, Dickenson R, (2001), Syngas production for gas-to-liquids applications: technologies, issues and outlook, Fuel Process. Technol. 71: 139-148.

[118] Vogel A, van Dyk B, Saib A, (2016), GTL using efficient cobalt Fischer-Tropsch catalysts, Catal. Today 259: 323-330.

[119] Šimáček P, Kubička D, Pospíšil M, Rubáš V, Hora L, Šebor G, (2013), Fischer–Tropsch product as a co-feed for refinery hydrocracking unit, Fuel 105: 432-439.

[120] Fischer F, Tropsch H, (1923), Uber die Herstellung synthetischer olgemische (Synthol) durch Aufbau aus Kohlenoxyd und Wasserstoff, Brennst. Chem 4: 276-285.

[121] Fischer F, Tropsch H, (1925), Patent-Nr. 484337, Verfahren zu Gewinnung mehrgliedriger Paraffinkohlenwasserstoffe aus Kohlenoxyden und Wasserstoff auf katalytischem Wege, Deutsches Reichspatentamt.

[122] Dry ME, (1990), The Fischer-Tropsch process-commercial aspects, Catal. Today 6: 183-206.

[123] Dry ME, (2002), The Fischer–Tropsch process: 1950–2000, Catal. Today 71: 227-241.

[124] Dry ME, (2002), High quality diesel via the Fischer–Tropsch process–a review, J. Chem. Technol. Biotechnol. 77: 43-50.

[125] Lobo P, Hagen DE, Whitefield PD, (2011), Comparison of PM emissions from a commercial jet engine burning conventional, biomass, and Fischer–Tropsch fuels, Environ. Sci. Technol. 45: 10744-10749.

[126] Schihl P, Hoogterp-Decker L, Gingrich E, (2012),The Ignition Behavior of a Coal to Liquid Fischer-Tropsch Jet Fuel in a Military Relevant Single Cylinder Diesel Engine, in, SAE Technical Paper.

[127] Wang H, Oehlschlaeger MA, (2012), Autoignition studies of conventional and Fischer–Tropsch jet fuels, Fuel 98: 249-258.

[128] Beyersdorf A, Timko M, Ziemba L, Bulzan D, Corporan E, Herndon S, Howard R, Miake-Lye R, Thornhill K, Winstead E, (2014), Reductions in aircraft particulate emissions due to the use of Fischer–Tropsch fuels, Atmos. Chem. Phys. 14: 11-23.

[129] Best LM, Ana B, Bradford RL, Hepp AF, (2012), Characterization of Catalyst Materials for Production of Aerospace Fuels, National Aeronautics and Space Administration, Glenn Research Center.

[130] Anderson RB, (1956), Kinetics and reaction mechanism of the Fischer-Tropsch synthesis, Catalysis 4: 257-372.

[131] Anderson RB, (1956), Catalysts for the Fischer-Tropsch synthesis, Van Nostrand-Reinhold: New York.

[132] Mirzaei AA, Arsalanfar M, Bozorgzadeh HR, Samimi A, (2014), A review of Fischer-Tropsch synthesis on the cobalt based catalysts, Physical Chemistry Research 2: 179-201.

[133] Van Der Laan GP, Beenackers A, (1999), Kinetics and selectivity of the Fischer–Tropsch synthesis: a literature review, Catalysis Reviews 41: 255-318.

[134] Valero MC, Raybaud P, (2013), Cobalt Catalyzed Fischer–Tropsch Synthesis: Perspectives Opened by First Principles Calculations, Catal. Lett. 143: 1-17.

[135] Wojciechowski B, (1988), The kinetics of the Fischer-Tropsch synthesis, Catalysis Reviews Science and Engineering 30: 629-702.

[136] Novak S, Madon R, Suhl H, (1981), Models of hydrocarbon product distributions in Fischer–Tropsch synthesis. I, The Journal of Chemical Physics 74: 6083-6091.

[137] Chai G-Y, Falconer JL, (1985), Alkali promoters on supported nickel: Effect of support, preparation, and alkali concentration, J. Catal. 93: 152-160.

[138] Van de Loosdrecht J, Van der Kraan A, Van Dillen A, Geus J, (1997), Metal-support interaction: titania-supported and silica-supported nickel catalysts, J. Catal. 170: 217-226.

[139] Vannice M, (1977), The catalytic synthesis of hydrocarbons from H2CO mixtures over the Group VIII metals: V. The catalytic behavior of silica-supported metals, J. Catal. 50: 228-236.

[140] Khodakov AY, Chu W, Fongarland P, (2007), Advances in the development of novel cobalt Fischer-Tropsch catalysts for synthesis of long-chain hydrocarbons and clean fuels, Chem. Rev. 107: 1692-1744.

[141] Dry ME, (1996), Practical and theoretical aspects of the catalytic Fischer-Tropsch process, Applied Catalysis A: General 138: 319-344.

[142] Hindermann J, Hutchings G, Kiennemann A, (1993), Mechanistic aspects of the formation of hydrocarbons and alcohols from CO hydrogenation, Catalysis Reviews—Science and Engineering 35: 1-127.

[143] de Smit E, Weckhuysen BM, (2008), The renaissance of iron-based Fischer–Tropsch synthesis: on the multifaceted catalyst deactivation behaviour, Chem. Soc. Rev. 37: 2758-2781.

[144] Botes F, Niemantsverdriet J, Van De Loosdrecht J, (2013), A comparison of cobalt and iron based slurry phase Fischer–Tropsch synthesis, Catal. Today 215: 112-120.

[145] Khodakov AY, (2009), Fischer-Tropsch synthesis: Relations between structure of cobalt catalysts and their catalytic performance, Catal. Today 144: 251-257.

[146] Diehl F, Khodakov AY, (2009), Promotion of cobalt Fischer-Tropsch catalysts with noble metals: a review, Oil & Gas Science and Technology-Revue de l'IFP 64: 11-24.

[147] Rytter E, Holmen A, (2015), Deactivation and Regeneration of Commercial Type Fischer-Tropsch Co-Catalysts—A Mini-Review, Catalysts 5: 478-499.

[148] Van Berge PJ, Visagie JL, Van De Loosdrecht J, Van Der Walt TJ, Sollie JC, Veltman HM, (2009),Process for activating cobalt catalysts, in, Google Patents.

[149] Geerlings JJC, Huisman HM, Mesters CMAM, (2000),Cobalt based fischer-tropsch catalyst, in, Google Patents.

[150] Clavenna LR, Woo HS, Mauldin CH, Wachter WA, (2003),Cobalt catalyst compositions useful for conducting carbon monoxide hydrogenation reactions, in, Google Patents.

[151] Eri S, Kinnari KJ, Schanke D, Hilmen A-M, (2008),Fischer-tropsch catalyst, preparation, and use thereof, in, Google Patents.

[152] Oukaci R, Singleton AH, Goodwin JG, (1999), Comparison of patented Co F–T catalysts using fixed-bed and slurry bubble column reactors, Applied Catalysis A: General 186: 129-144.

[153] Donnelly TJ, Satterfield CN, (1989), Product distributions of the Fischer-Tropsch synthesis on precipitated iron catalysts, Applied Catalysis 52: 93-114.

[154] Rofer-DePoorter CK, (1981), A comprehensive mechanism for the Fischer-Tropsch synthesis, Chem. Rev. 81: 447-474.

[155] Iwarere SA, (2013),PhD thesis: Syntheis of hydrocarbons and fluorocarbons in a tip-tip arc discharge reactor at high pressure, in, Universty of KwaZulu-Natal.

[156] Davis BH, (2005), Fischer–Tropsch synthesis: overview of reactor development and future potentialities, Top. Catal. 32: 143-168.

[157] Steynberg A, Dry M, (2004), Fischer-Tropsch Technology, Elsevier.

[158] Lebouvier A, Iwarere S, Ramjugernath D, Fulcheri L, (2013), 3D magnetohydrodynamic modelling of a dc low-current plasma arc batch reactor at very high pressure in helium, J. Phys. D: Appl. Phys. 46: 145203.

[159] Pacheco J, Soria G, Pacheco M, Valdivia R, Ramos F, Frías H, Durán M, Hidalgo M, Greenhouse gas treatment and H2 production, by warm plasma reforming, Int. J. Hydrogen Energy.

[160] Rueangjitt N, Sreethawong T, Chavadej S, Sekiguchi H, (2011), Non-oxidative reforming of methane in a mini-gliding arc discharge reactor: effects of feed methane concentration, feed flow rate, electrode gap distance, residence time, and catalyst distance, Plasma Chem. Plasma Process. 31: 517-534.

[161] Rueangjitt N, Sreethawong T, Chavadej S, Sekiguchi H, (2009), Plasma-catalytic reforming of methane in AC microsized gliding arc discharge: effects of input power, reactor thickness, and catalyst existence, Chem. Eng. J. 155: 874-880.

[162] Hilmen A-M, Bergene E, Lindvåg O, Schanke D, Eri S, Holmen A, (2001), Fischer–Tropsch synthesis on monolithic catalysts of different materials, Catal. Today 69: 227-232.

[163] Hilmen A-M, Bergene E, Lindvg O, Schanke D, Eri S, Holmen A, (2000), Fischer-Tropsch synthesis using monolithic catalysts, Stud. Surf. Sci. Catal. 130: 1163-1168.

[164] Tomašić V, Jović F, (2006), State-of-the-art in the monolithic catalysts/reactors, Applied Catalysis A: General 311: 112-121.

[165] Bodke A, Bharadwaj S, Schmidt L, (1998), The effect of ceramic supports on partial oxidation of hydrocarbons over noble metal coated monoliths, J. Catal. 179: 138-149.

[166] de Deugd RM, Chougule RB, Kreutzer MT, Meeuse FM, Grievink J, Kapteijn F, Moulijn JA, (2003), Is a monolithic loop reactor a viable option for Fischer–Tropsch synthesis?, Chem. Eng. Sci. 58: 583-591.

[167] de Deugd RM, Kapteijn F, Moulijn JA, (2003), Using monolithic catalysts for highly selective Fischer–Tropsch synthesis, Catal. Today 79: 495-501.

[168] Moreno-Castilla C, Pérez-Cadenas AF, (2010), Carbon-based honeycomb monoliths for environmental gas-phase applications, Materials 3: 1203-1227.

[169] Kapteijn F, de Deugd RM, Moulijn JA, (2005), Fischer–Tropsch synthesis using monolithic catalysts, Catal. Today 105: 350-356.

[170] Guettel R, Knochen J, Kunz U, Kassing M, Turek T, (2008), Preparation and Catalytic Evaluation of Cobalt-Based Monolithic and Powder Catalysts for Fischer− Tropsch Synthesis, Ind. Eng. Chem. Res. 47: 6589-6597.

[171] Bakhtiari M, Khorasheh F, Zamanian A, Nakhaeipour A, Irani M, (2008), Preparation, Evaluation and Characterization of Monolithic Catalysts for Fischer-Tropsch Synthesis, Petroleum & Coal 50: 56-61.

[172] Liu W, Hu J, Wang Y, (2009), Fischer–Tropsch synthesis on ceramic monolith-structured catalysts, Catal. Today 140: 142-148.

[173] Avila P, Montes M, Miro EE, (2005), Monolithic reactors for environmental applications: A review on preparation technologies, Chem. Eng. J. 109: 11-36.

[174] Panneerselvam M, Rao K, (2003), Novel microwave method for the synthesis and sintering of mullite from kaolinite, Chem. Mater. 15: 2247-2252.

[175] Chaudhuri S, Patra S, Chakraborty A, (1999), Electrical resistivity of transition metal ion doped mullite, J. Eur. Ceram. Soc. 19: 2941-2950.

[176] Schneider H, Schreuer J, Hildmann B, (2008), Structure and properties of mullite—a review, J. Eur. Ceram. Soc. 28: 329-344.

[177] Liguras DK, Goundani K, Verykios XE, (2004), Production of hydrogen for fuel cells by catalytic partial oxidation of ethanol over structured Ni catalysts, J. Power Sources 130: 30-37.

[178] Zhao X, Cong Y, Lv F, Li L, Wang X, Zhang T, (2010), Mullite-supported Rh catalyst: a promising catalyst for the decomposition of N 2 O propellant, Chem. Commun. 46: 3028-3030.

[179] Schimmoeller B, Schulz H, Pratsinis SE, Bareiss A, Reitzmann A, Kraushaar-Czarnetzki B, (2006), Ceramic foams directly-coated with flame-made V 2 O 5/TiO 2 for synthesis of phthalic anhydride, J. Catal. 243: 82-92.

[180] Ma W, Jacobs G, Ji Y, Bhatelia T, Bukur DB, Khalid S, Davis BH, (2011), Fischer–Tropsch synthesis: influence of CO conversion on selectivities, H2/CO usage ratios, and catalyst stability for a Ru promoted Co/Al2O3 catalyst using a slurry phase reactor, Top. Catal. 54: 757-767.

[181] Villegas L, Masset F, Guilhaume N, (2007), Wet impregnation of alumina-washcoated monoliths: Effect of the drying procedure on Ni distribution and on autothermal reforming activity, Applied Catalysis A: General 320: 43-55.

[182] Johnson BG, Bartholomew CH, Goodman DW, (1991), The role of surface structure and dispersion in CO hydrogenation on cobalt, J. Catal. 128: 231-247.

[183] Geerlings J, Wilson J, Kramer G, Kuipers H, Hoek A, Huisman H, (1999), Fischer–Tropsch technology—from active site to commercial process, Applied Catalysis A: General 186: 27-40.

[184] Lebouvier A, Iwarere SA, d'Argenlieu P, Ramjugernath D, Fulcheri L, (2013), Assessment of carbon dioxide dissociation as a new route for syngas production: a comparative review and potential of plasma-based technologies, Energy & Fuels 27: 2712-2722.

[185] Fairbairn AR, (1969), The Dissociation of Carbon Monoxide, Proceedings of the Royal Society of London. Series A, Mathematical and Physical Sciences 312: 207-227.

[186] Iza F, Hopwood JA, (2004), Rotational, vibrational, and excitation temperatures of a microwave-frequency microplasma, Plasma Science, IEEE Transactions on 32: 498-504.

[187] Rethwisch DG, Dumesic J, (1986), Effect of metal-oxygen bond strength on properties of oxides. 1. Infrared spectroscopy of adsorbed carbon monoxide and carbon dioxide, Langmuir 2: 73-79.

[188] Tanabe K, (1981), Solid acid and base catalysts, Catalysis science and technology 2: 255.

[189] Pines H, Haag WO, (1960), Alumina: Catalyst and Support. I. Alumina, its Intrinsic Acidity and Catalytic Activity1, J. Am. Chem. Soc. 82: 2471-2483.

[190] Cabrejas Manchado M, Guil J, Perez Masia A, Ruiz Paniego A, Trejo Menayo J, (1994), Adsorption of H2, O2, CO, and CO2 on a. gamma.-Alumina: Volumetric and Calorimetric Studies, Langmuir 10: 685-691.

[191] Sun H, Page MI, Atherton JH, Hall A, (2014), Kinetics of the conversion of methyl benzoate to benzamide by the alumina catalysed reaction with liquid ammonia at 120° C, Catalysis Science & Technology 4: 3870-3878.

[192] Roland U, Holzer F, Kopinke F-D, (2005), Combination of non-thermal plasma and heterogeneous catalysis for oxidation of volatile organic compounds: Part 2. Ozone decomposition and deactivation of γ-Al2O3, Applied Catalysis B: Environmental 58: 217-226.

[193] Conner Jr WC, Falconer JL, (1995), Spillover in heterogeneous catalysis, Chem. Rev. 95: 759-788.

[194] Bhatelia T, Li Ce, Sun Y, Hazewinkel P, Burke N, Sage V, (2014), Chain length dependent olefin re-adsorption model for Fischer–Tropsch synthesis over Co-Al 2 O 3 catalyst, Fuel Process. Technol. 125: 277-289.

[195] Zabidi NAM, Ali S, Subbarao D, (2014), Effects of Pressure on the Performance of CNTs-Supported Catalyst in a Fischer-Tropsch Reaction, Journal of Materials Science and Engineering. B 4.

[196] Petitto SC, Marsh EM, Carson GA, Langell MA, (2008), Cobalt oxide surface chemistry: the interaction of CoO (100), Co 3 O 4 (110) and Co 3 O 4 (111) with oxygen and water, J. Mol. Catal. A: Chem. 281: 49-58.

[197] De la Pena O'Shea V, Alvarez-Galvan M, Campos-Martin J, Fierro J, (2005), Strong dependence on pressure of the performance of a Co/SiO2 catalyst in Fischer–Tropsch slurry reactor synthesis, Catal. Lett. 100: 105-116.

[198] Elbashir N, Dutta P, Manivannan A, Seehra M, Roberts C, (2005), Impact of cobalt-based catalyst characteristics on the performance of conventional gas-phase and supercritical-phase Fischer–Tropsch synthesis, Applied Catalysis A: General 285: 169-180.

[199] Borg Ø, Eri S, Blekkan EA, Storsæter S, Wigum H, Rytter E, Holmen A, (2007), Fischer–Tropsch synthesis over γ-alumina-supported cobalt catalysts: effect of support variables, J. Catal. 248: 89-100.

[200] Bukur DB, Pan Z, Ma W, Jacobs G, Davis BH, (2012), Effect of CO conversion on the product distribution of a Co/Al2O3 Fischer–Tropsch synthesis catalyst using a fixed bed reactor, Catal. Lett. 142: 1382-1387.

[201] Botes FG, (2009), Influences of water and syngas partial pressure on the kinetics of a commercial alumina-supported cobalt Fischer− Tropsch catalyst, Ind. Eng. Chem. Res. 48: 1859-1865.

[202] Yang J, Ma W, Chen D, Holmen A, Davis BH, (2014), Fischer–Tropsch synthesis: A review of the effect of CO conversion on methane selectivity, Applied Catalysis A: General 470: 250-260.

[203] Iglesia E, Reyes SC, Madon RJ, Soled SL, Selectivity Control and Catalyst Design in the Fischer-Tropsch Synthesis: Sites, Pellets, and Reactors, in: D.D. Eley HP, Paul BW (Eds.) Advances in Catalysis, Academic Press, 1993, pp. 221-302.

[204] Madon RJ, Iglesia E, Reyes SC, (1993),Non-Flory product distributions in Fischer-Tropsch synthesis catalyzed by Ruthenium, Cobalt, and Iron, in: ACS Symp. Ser., AMER CHEMICAL SOC 1155 16TH ST, NW, WASHINGTON, DC 20036, pp. 383-396.

[205] Dinse A, Aigner M, Ulbrich M, Johnson GR, Bell AT, (2012), Effects of Mn promotion on the activity and selectivity of Co/SiO 2 for Fischer–Tropsch Synthesis, J. Catal. 288: 104-114.

[206] Tavasoli A, Khodadadi A, Mortazavi Y, Sadaghiani K, Ahangari M, (2006), Lowering methane and raising distillates yields in Fischer–Tropsch synthesis by using promoted and unpromoted cobalt catalysts in a dual bed reactor, Fuel Process. Technol. 87: 641-647.

[207] Komaya T, Bell AT, (1994), Estimates of rate coefficients for elementary processes occurring during Fischer-Tropsch synthesis over RuTiO2, J. Catal. 146: 237-248.

[208] Kuipers E, Scheper C, Wilson J, Vinkenburg I, Oosterbeek H, (1996), Non-ASF product distributions due to secondary reactions during Fischer–Tropsch synthesis, J. Catal. 158: 288-300.

[209] Iglesia E, Reyes SC, Madon RJ, (1991), Transport-enhanced α-olefin readsorption pathways in Ru-catalyzed hydrocarbon synthesis, J. Catal. 129: 238-256.

[210] Sinnott S, Andrews R, Qian D, Rao A, Mao Z, Dickey E, Derbyshire F, (1999), Model of carbon nanotube growth through chemical vapor deposition, Chem. Phys. Lett. 315: 25-30.

[211] Lebouvier A, Iwarere S, Ramjugernath D, Fulcheri L, (2013), Investigation of tetrafluoromethane as a plasma gas in a very high pressure/low current dc batch reactor by means of 3D MHD modelling, J. Phys. D: Appl. Phys. 46: 355206-355214.

[212] Kunhardt EE, (2000), Generation of large-volume, atmospheric-pressure, nonequilibrium plasmas, Plasma Science, IEEE Transactions on 28: 189-200.

[213] Fan HY, (1939), The transition from glow discharge to arc, Phys. Rev. 55: 769.

[214] Deprez N, McLachlan D, (1988), The analysis of the electrical conductivity of graphite conductivity of graphite powders during compaction, J. Phys. D: Appl. Phys. 21: 101.

[215] Benilov M, Marotta A, (1995), A model of the cathode region of atmospheric pressure arcs, J. Phys. D: Appl. Phys. 28: 1869.

[216] Jacobs G, Das TK, Zhang Y, Li J, Racoillet G, Davis BH, (2002), Fischer–Tropsch synthesis: support, loading, and promoter effects on the reducibility of cobalt catalysts, Applied Catalysis A: General 233: 263-281.

[217] Jacobs G, Patterson PM, Zhang Y, Das T, Li J, Davis BH, (2002), Fischer–Tropsch synthesis: deactivation of noble metal-promoted Co/Al 2 O 3 catalysts, Applied Catalysis A: General 233: 215-226.

[218] Tavasoli A, Sadaghiani K, Nakhaeipour A, Ghalbi Ahangari M, (2007), Cobalt Loading Effects on the Structure and Activity for Fischer-Tropsch and Water–gas Shift Reactions of Co/Al2O3 Catalysts, Iran. J. Chem. Chem. Eng. Vol 26.

[219] Kuzmany H, Kukovecz A, Simon F, Holzweber M, Kramberger C, Pichler T, (2004), Functionalization of carbon nanotubes, Synth. Met. 141: 113-122.

[220] Kumar M, Ando Y, (2010), Chemical vapor deposition of carbon nanotubes: a review on growth mechanism and mass production, Journal of nanoscience and nanotechnology 10: 3739-3758.

[221] Meyyappan M, Delzeit L, Cassell A, Hash D, (2003), Carbon nanotube growth by PECVD: a review, Plasma Sources Sci. Technol. 12: 205.

[222] Meyyappan M, (2009), A review of plasma enhanced chemical vapour deposition of carbon nanotubes, J. Phys. D: Appl. Phys. 42: 213001.

[223] Bell MS, Teo KB, Lacerda RG, Milne W, Hash DB, Meyyappan M, (2006), Carbon nanotubes by plasma-enhanced chemical vapor deposition, Pure Appl. Chem. 78: 1117-1125.

[224] Hou Y, Tang J, Zhang H, Qian C, Feng Y, Liu J, (2009), Functionalized few-walled carbon nanotubes for mechanical reinforcement of polymeric composites, ACS nano 3: 1057-1062.

[225] Shi H, Barker J, Saidi M, Koksbang R, Morris L, (1997), Graphite structure and lithium intercalation, J. Power Sources 68: 291-295.

[226] Nakamura J, Tanaka K-i, Toyoshima I, (1987), Reactivity of deposited carbon on Co□ Al 2 O 3 catalyst, J. Catal. 108: 55-62.

[227] Tan KF, Xu J, Chang J, Borgna A, Saeys M, (2010), Carbon deposition on Co catalysts during Fischer–Tropsch synthesis: A computational and experimental study, J. Catal. 274: 121-129.

[228] Keyvanloo K, Fisher MJ, Hecker WC, Lancee RJ, Jacobs G, Bartholomew CH, (2015), Kinetics of deactivation by carbon of a cobalt Fischer–Tropsch catalyst: Effects of CO and H 2 partial pressures, J. Catal. 327: 33-47.

[229] Potoczna-Petru D, (1991), The interaction of model cobalt catalysts with carbon, Carbon 29: 73-79.

[230] Lee D-K, Lee J-H, Ihm S-K, (1988), Effect of carbon deposits on carbon monoxide hydrogenation over alumina-supported cobalt catalyst, Applied catalysis 36: 199-207.

[231] Nakamura J, Toyoshima I, Tanaka K-i, (1988), Formation of carbidic and graphite carbon from CO on polycrystalline cobalt, Surf. Sci. 201: 185-194.

[232] Espinoza R, Steynberg A, Jager B, Vosloo A, (1999), Low temperature Fischer–Tropsch synthesis from a Sasol perspective, Applied Catalysis A: General 186: 13-26.

[233] Dakin JT, (1991), Nonequilibrium lighting plasmas, Plasma Science, IEEE Transactions on 19: 991-1002.

[234] Tsakoumis NE, Rønning M, Borg Ø, Rytter E, Holmen A, (2010), Deactivation of cobalt based Fischer–Tropsch catalysts: a review, Catal. Today 154: 162-182.

[235] Jeon I-Y, Chang DW, Kumar NA, Baek J-B, (2011),Functionalization of Carbon Nanotubes, Carbon Nanotubes - Polymer Nanocomposites, in: Yellampalli DS (Ed.), InTech.

[236] Moisala A, Nasibulin AG, Kauppinen EI, (2003), The role of metal nanoparticles in the catalytic production of single-walled carbon nanotubes—a review, J. Phys.: Condens. Matter 15: S3011.

[237] Prasek J, Drbohlavova J, Chomoucka J, Hubalek J, Jasek O, Adam V, Kizek R, (2011), Methods for carbon nanotubes synthesis—review, J. Mater. Chem. 21: 15872-15884.

[238] van Steen E, Prinsloo FF, (2002), Comparison of preparation methods for carbon nanotubes supported iron Fischer–Tropsch catalysts, Catal. Today 71: 327-334.

[239] Abbaslou RMM, Tavassoli A, Soltan J, Dalai AK, (2009), Iron catalysts supported on carbon nanotubes for Fischer–Tropsch synthesis: Effect of catalytic site position, Applied Catalysis A: General 367: 47-52.

[240] Tavasoli A, Abbaslou RMM, Trepanier M, Dalai AK, (2008), Fischer–Tropsch synthesis over cobalt catalyst supported on carbon nanotubes in a slurry reactor, Applied Catalysis A: General 345: 134-142.

[241] Xiong H, Motchelaho MA, Moyo M, Jewell LL, Coville NJ, (2011), Correlating the preparation and performance of cobalt catalysts supported on carbon nanotubes and carbon spheres in the Fischer–Tropsch synthesis, J. Catal. 278: 26-40.

[242] Trépanier M, Tavasoli A, Dalai AK, Abatzoglou N, (2009), Co, Ru and K loadings effects on the activity and selectivity of carbon nanotubes supported cobalt catalyst in Fischer–Tropsch synthesis, Applied Catalysis A: General 353: 193-202.

[243] Trépanier M, Tavasoli A, Dalai AK, Abatzoglou N, (2009), Fischer–Tropsch synthesis over carbon nanotubes supported cobalt catalysts in a fixed bed reactor: Influence of acid treatment, Fuel Process. Technol. 90: 367-374.

[244] Tavasoli A, Trépanier M, Abbaslou RMM, Dalai AK, Abatzoglou N, (2009), Fischer–Tropsch synthesis on mono-and bimetallic Co and Fe catalysts supported on carbon nanotubes, Fuel Process. Technol. 90: 1486-1494.

[245] Guczi L, Stefler G, Geszti O, Koppány Z, Kónya Z, Molnár É, Urbán M, Kiricsi I, (2006), CO hydrogenation over cobalt and iron catalysts supported over multiwall carbon nanotubes: effect of preparation, J. Catal. 244: 24-32.

[246] Bahome MC, Jewell LL, Padayachy K, Hildebrandt D, Glasser D, Datye AK, Coville NJ, (2007), Fe-Ru small particle bimetallic catalysts supported on carbon nanotubes for use in Fischer–Tröpsch synthesis, Applied Catalysis A: General 328: 243-251.

[247] Bezemer G, Van Laak A, Van Dillen A, De Jong K, (2004), Cobalt supported on carbon nanofibers-a promising novel Fischer-Tropsch catalyst, Stud. Surf. Sci. Catal. 147: 259-264.

[248] Eschemann TO, Lamme WS, Manchester RL, Parmentier TE, Cognigni A, Rønning M, de Jong KP, (2015), Effect of support surface treatment on the synthesis, structure, and performance of Co/CNT Fischer–Tropsch catalysts, J. Catal. 328: 130-138.

[249] Serp P, Castillejos E, (2010), Catalysis in carbon nanotubes, ChemCatChem 2: 41-47.

[250] Tasis D, Tagmatarchis N, Bianco A, Prato M, (2006), Chemistry of carbon nanotubes, Chem. Rev. 106: 1105-1136.

[251] Castillejos E, Debouttière PJ, Roiban L, Solhy A, Martinez V, Kihn Y, Ersen O, Philippot K, Chaudret B, Serp P, (2009), An efficient strategy to drive nanoparticles into carbon nanotubes and the remarkable effect of confinement on their catalytic performance, Angew. Chem. Int. Ed. 48: 2529-2533.

[252] Chen W, Fan Z, Pan X, Bao X, (2008), Effect of confinement in carbon nanotubes on the activity of Fischer− Tropsch iron catalyst, J. Am. Chem. Soc. 130: 9414-9419.

Appendix A
GC CALIBRATION

The thermal conductivity detector (TCD) was calibrated for the reactant gases (CO and H_2) and the flame ionisation detector (FID) was calibrated for the hydrocarbon product gases (methane, ethane, ethylene, propane and propylene). Due to the low concentrations (< 1-3 mol%) of products, calibration was performed using pure hydrocarbon gases and hydrocarbon gases diluted in helium (> 95 mol%) in order to generate a calibration curve that could be more accurately extrapolated from the dilute region to the origin. For calibration of the dilute region, hydrocarbon gases were mixed with helium in a mixing vessel rated at approximately 30 bar. The mixing vessel was initially evacuated using a Edwards vacuum pump and the hydrocarbon and helium gases were introduced separately into the mixing vessel based on the required partial pressures. The mass of each gas was recorded, from which the molarity was calculated. Pre-determined volumes of the pure and diluted hydrocarbon gases were injected into the FID channel and the corresponding GC peak areas were processed. The extended calibration curves for the number of mols of hydrocarbons injected into the GC (calculated using the ideal gas law, n=PV/RT) versus GC peak as well as the residual plot for the dilute region are presented in Figures A.1 to A.14.

A.1 Hydrocarbon gases detected by FID

Methane

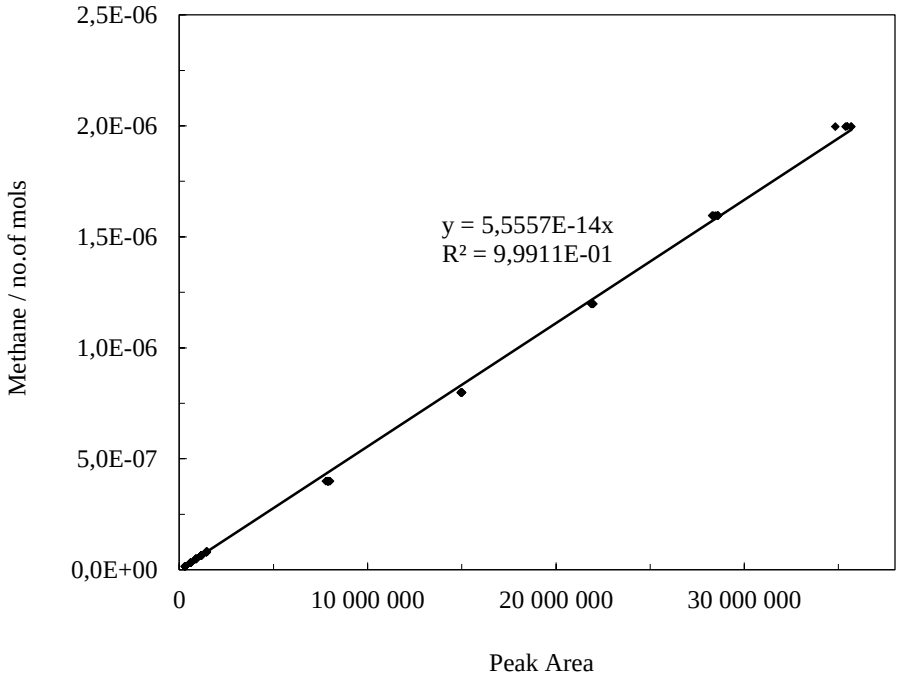

Figure A.1: GC calibration curve for methane.

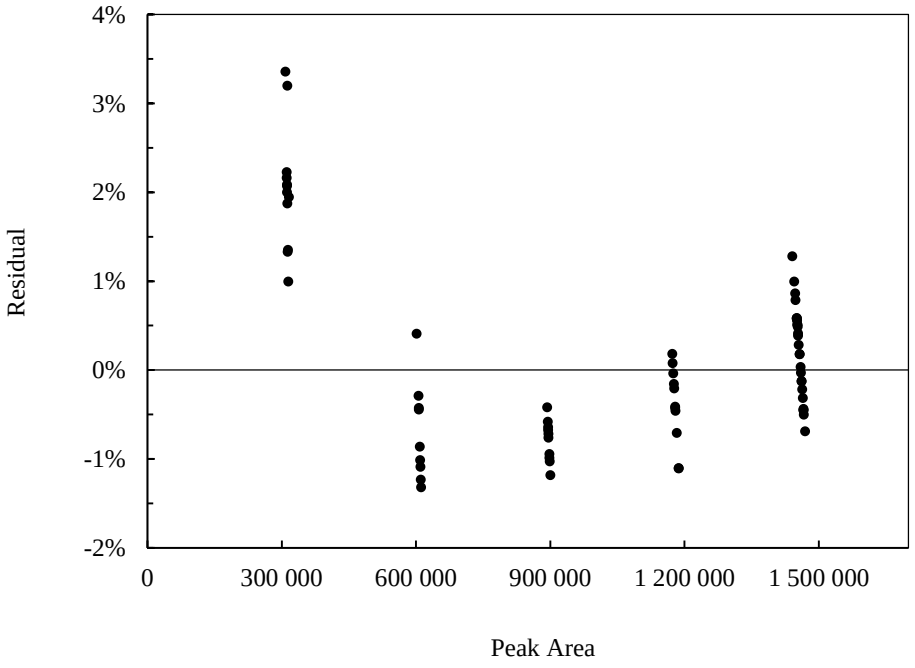

Figure A.2: Residual plot for no. of mols of methane versus peak area.

Ethane

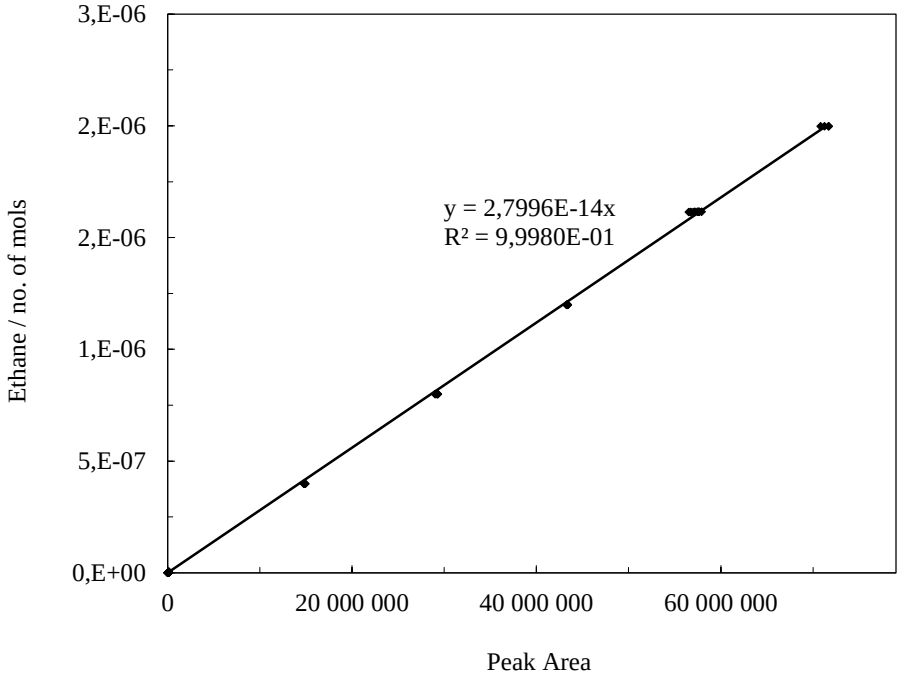

Figure A.3: GC calibration curve for ethane.

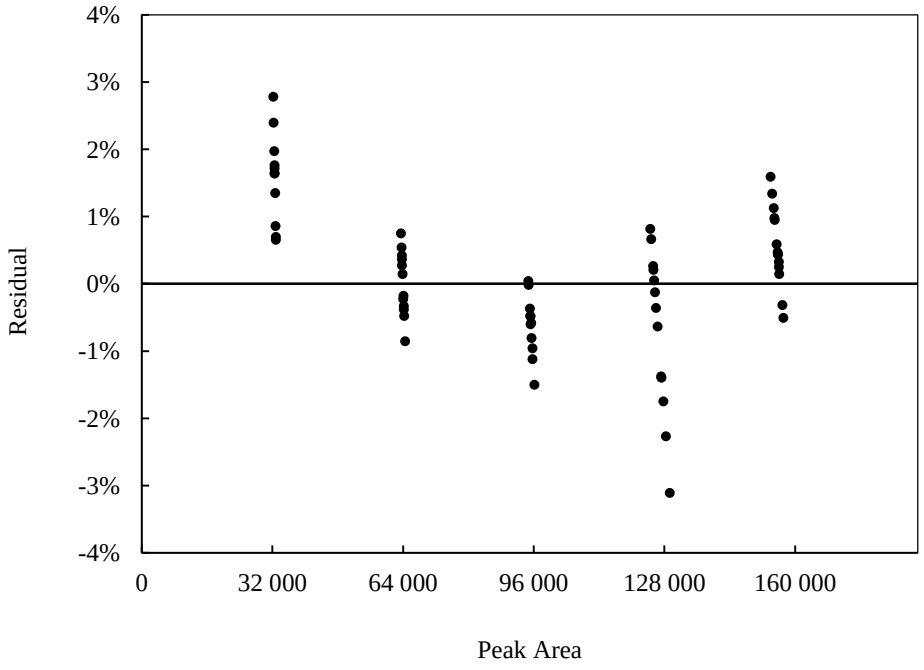

Figure A.4: Residual plot for no. of mols of ethane versus peak area.

Ethylene

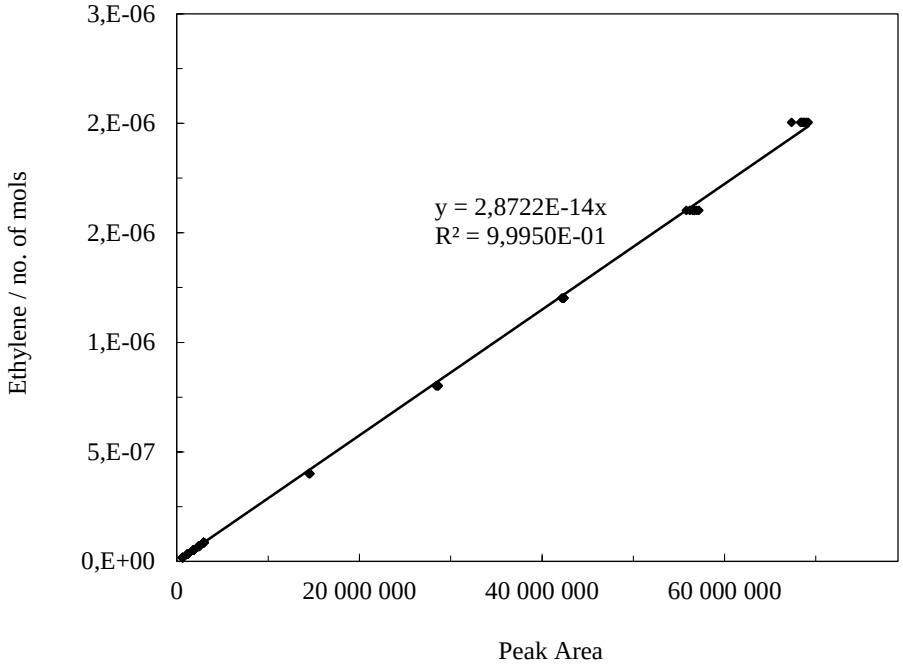

Figure A.5: GC calibration curve for ethylene.

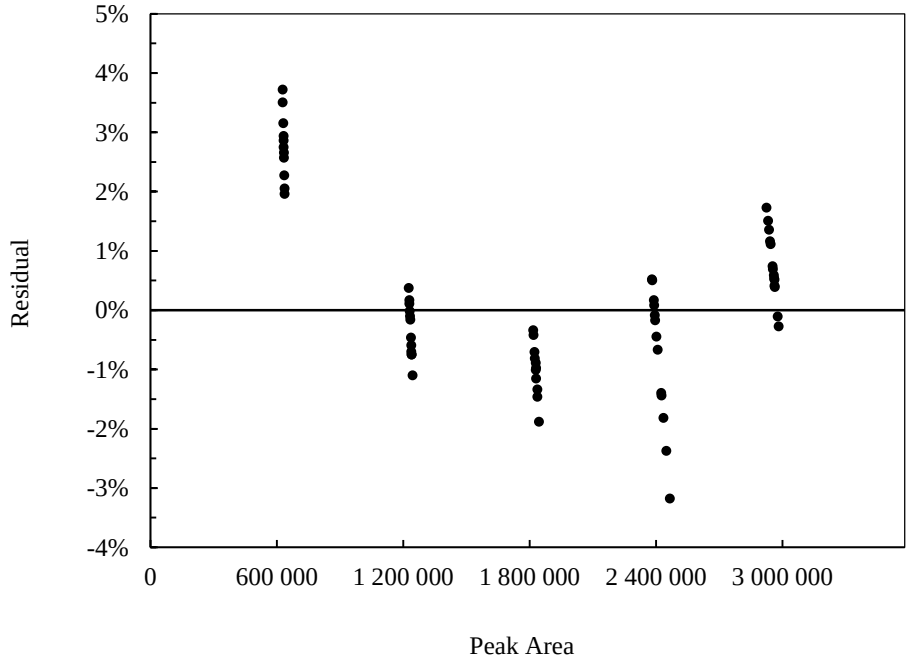

Figure A.6: Residual plot for no. of mols of ethylene versus peak area.

Propane

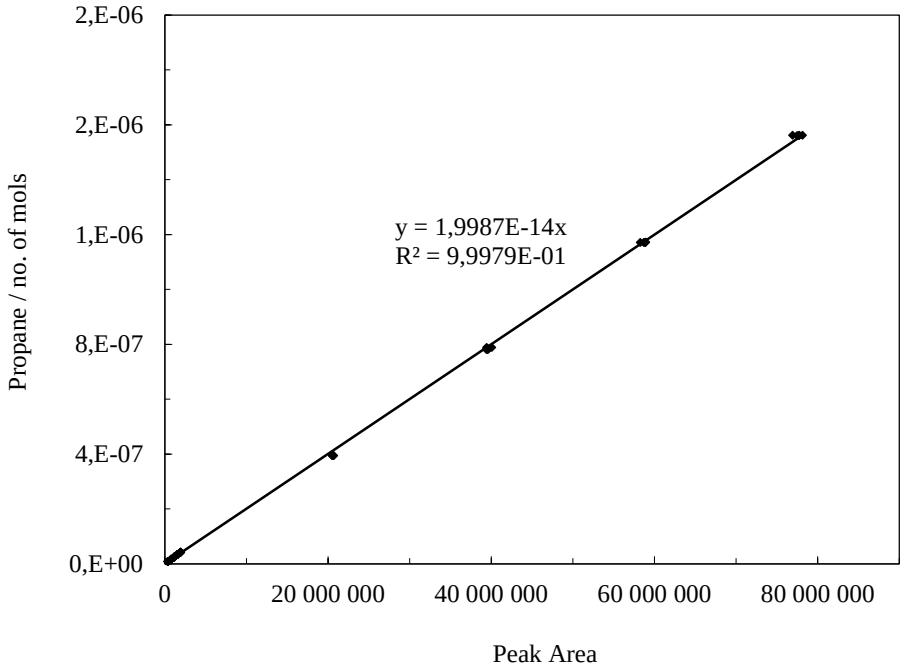

Figure A.7: GC calibration curve for propane.

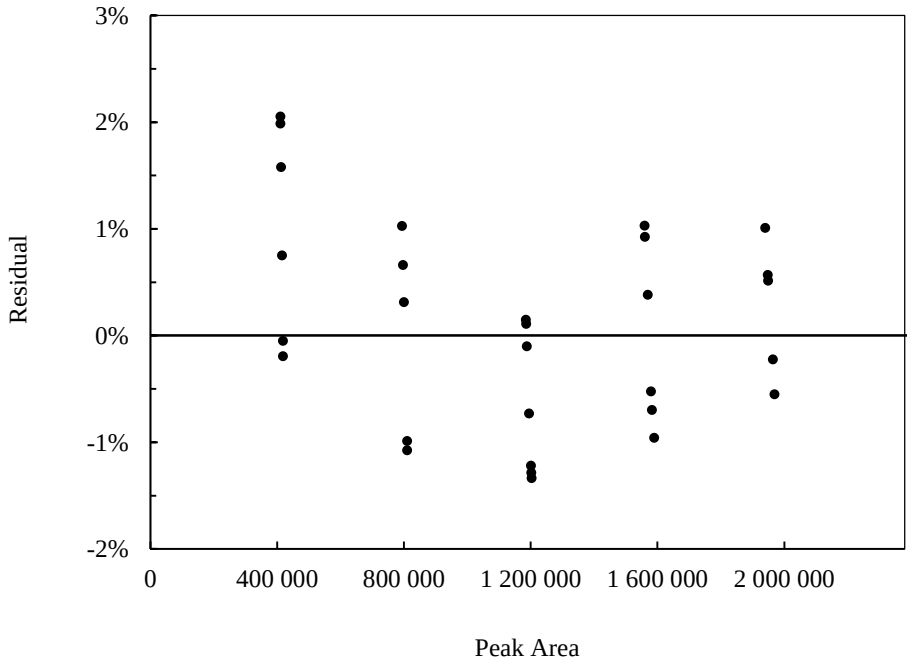

Figure A.8: Residual plot for no. of mols of propane versus peak area.

Propylene

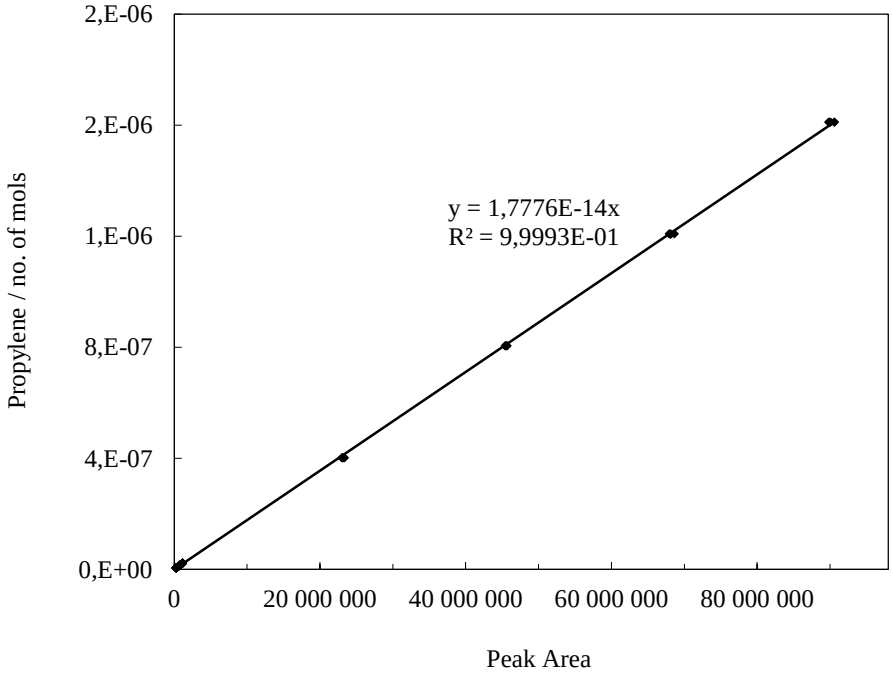

Figure A.9: GC calibration curve for propylene.

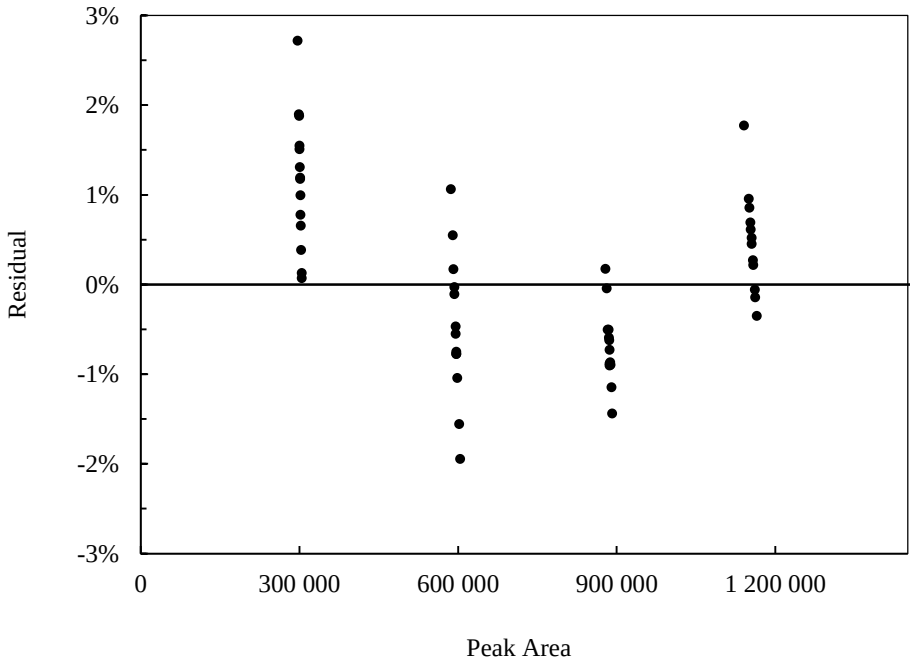

Figure A.10: Residual plot for no. of mols of propylene versus peak area.

A.2 Permanent gases detected by TCD

Hydrogen

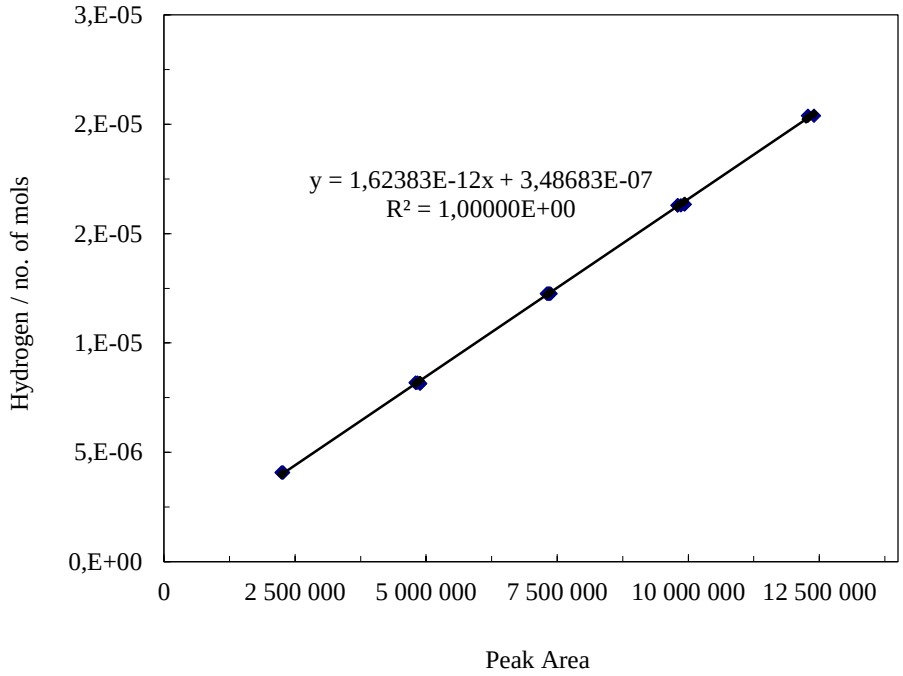

Figure A.11: GC calibration curve for hydrogen.

(N.B. The second term of the linear equation is negligible).

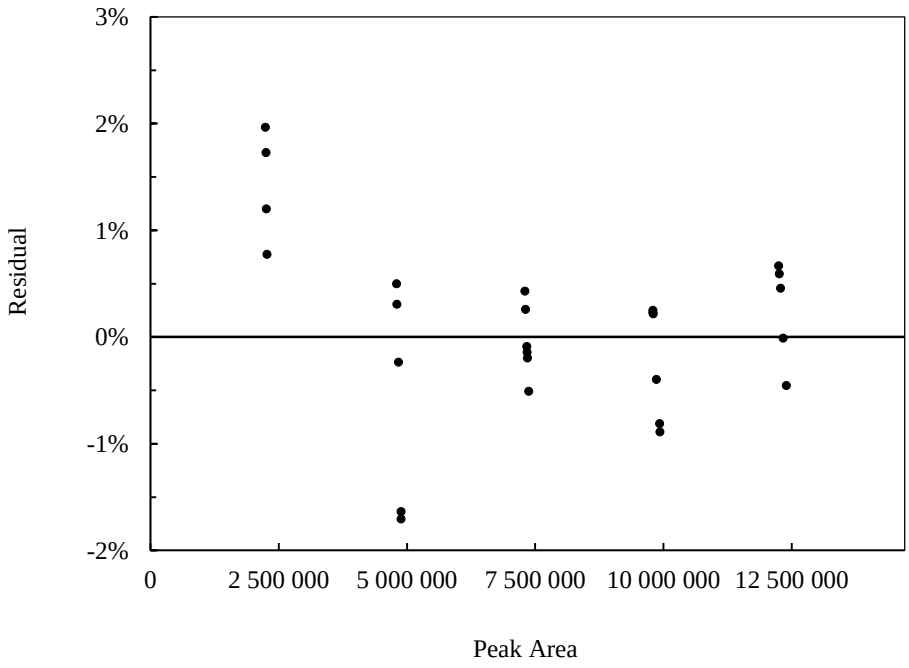

Figure A.12: Residual plot for no. of mols of hydrogen versus peak area.

Carbon monoxide

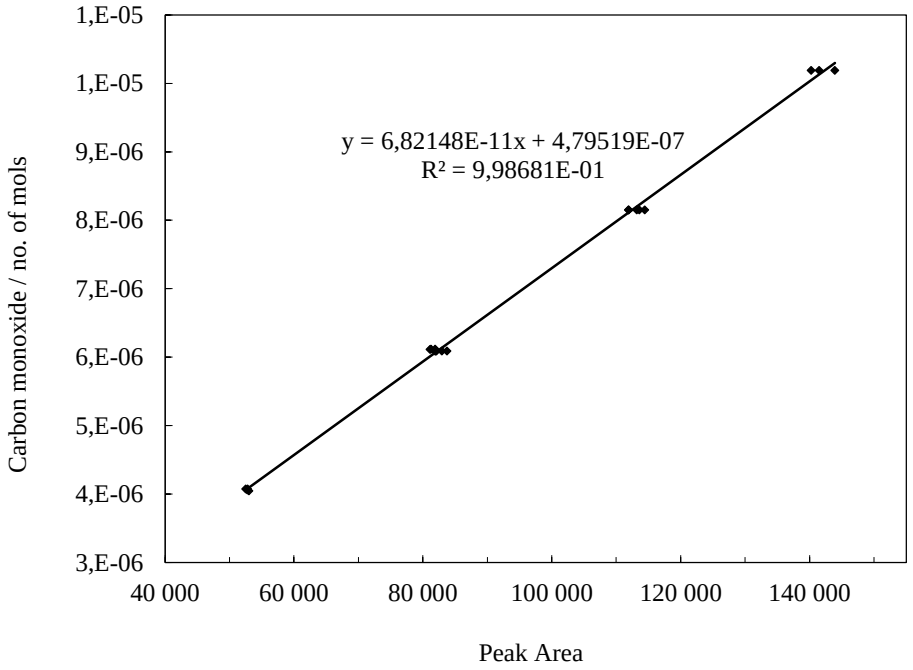

Figure A.13: GC calibration curve for carbon monoxide.

(N.B. The second term of the linear equation is negligible).

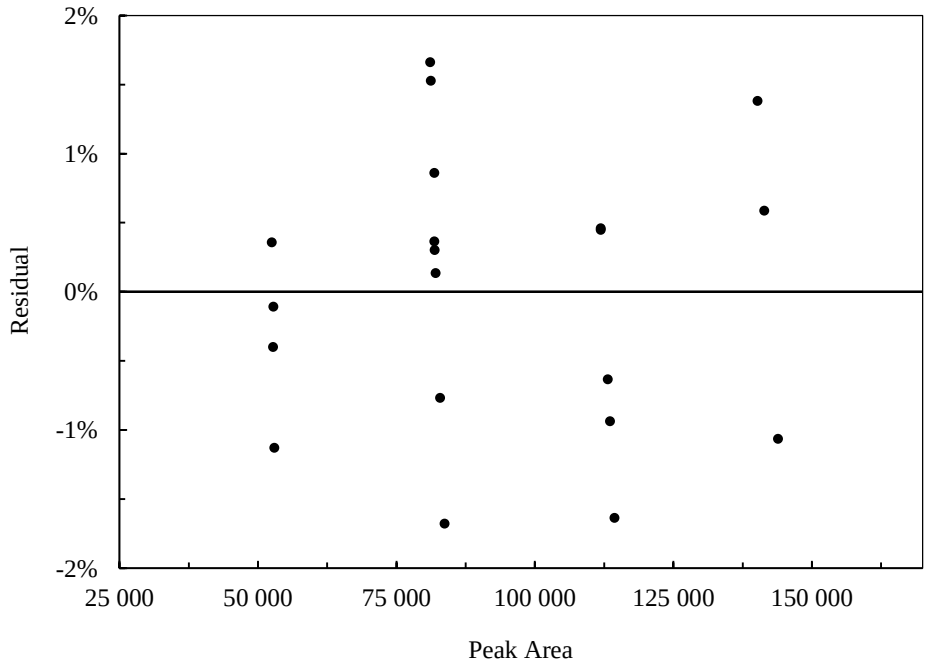

Figure A.14: Residual plot for no. of mols of carbon monoxide versus peak area.

Appendix B
EXPERIMENTAL UNCERTAINTIES

The experimental uncertainties evaluated for the C_1-C_3 hydrocarbon product molar concentrations (in ppm) are discussed in Appendix D. The major contributions to the concentration uncertainties were errors emerging from the GC calibration method (Sections B.2 and B.3) and arc discharge reactor sampling procedure (Section B.4).

B.1 GC calibration uncertainties

A Shimadzu 2010-plus GC was calibrated using pure and diluted C_1-C_3 hydrocarbon gases. The moles of gas injected into the GC by a syringe were determined by the ideal gas law (equation B.1).

$$n_1 = x_1\left(\frac{PV}{RT}\right) \tag{B.1}$$

Errors incurred during the calibration process were assigned to the ideal gas parameters: pressure, volume, temperature and mole fraction of hydrocarbon species contained in the syringe.

$$u_{calib}(n_1) = f(P, V, T, x_1)$$

The calibration was undertaken at atmospheric pressure (measured using a barometer) and at ambient temperature (measured using a mercury thermometer). The volume of hydrocarbon gas injected into the GC by a Hamilton 50 uL gastight syringe, ranged between 10 and 50 uL. The mole fraction of a pure hydrocarbon gas was unity but ranged between 0.001 and 0.04 for a hydrocarbon gas diluted in helium.

The mole fraction errors (x_1) arising from the dilution process are discussed in Section B.2 and the ideal gas law parametric errors (*P, V and T*) are described in Section B.3.

(N.B. certain sources of error in the calibration process such as hydrocarbon purity and molecular weight were neglected as there minor error contributions were swamped by the major sources discussed in Section B.2).

B.2 GC calibration: Mole fraction uncertainties

In order to accurately extend the GC calibration curve to the dilute region, calibrations were undertaken using a hydrocarbon gas diluted in helium. The C_1-C_3 hydrocarbon gas and helium were introduced separately into an evacuated stainless steel mixing vessel, which were weighed using an OHAUS Explorer Pro EP6102 mass balance. The major sources of error in the gas dilution technique arose from the weighing process. The mass uncertainty for component 1 (hydrocarbon) and component 2 (helium) of the gas mixture encompassed the mass balance uncertainty contributions: readability, repeatability and linearity, as shown in equation B.2.

$$u(m_1) = u(m_2) = n\sqrt{[u_{read}(m)]^2 + \left[u_{rep}(m)\right]^2 + [u_{linear}(m)]^2} \tag{B.2}$$

$$u(m_1) = u(m_2) = n\sqrt{\left[\frac{\sigma_{read}}{\sqrt{3}}\right]^2 + \left[\frac{\sigma_{rep}}{\sqrt{3}}\right]^2 + \left[\frac{\sigma_{linear}}{\sqrt{3}}\right]^2}$$

The three individual uncertainty contributions were evaluated using a rectangular distribution of the mass balance standard deviation errors (σ):

$$\sigma_{read} = 0.01\ g; \quad \sigma_{rep} = 0.02\ g; \quad \sigma_{linear} = 0$$

The evaluated mass uncertainties were then used to determine the hydrocarbon mole fraction uncertainty:

$$u(x_1) = f(m_1, m_2)$$

To evaluate the above uncertainty, the mole fraction of component 1 (x_1) was rearranged to incorporate the mass of components 1 and 2:

$$x_1 = \frac{n_1}{n_1 + n_2}$$

$$x_1 = \left(1 + \frac{M_1}{m_1}\frac{m_2}{M_2}\right)^{-1} \tag{B.3}$$

Based on the mass-related from of the mole fraction equation above, the mole fraction uncertainty of methane, ethane, ethylene, propane and propylene was determined as follows:

$$u(x_1) = \sqrt{\left[\frac{\partial x_1}{\partial m_1}u(m_1)\right]^2 + \left[\frac{\partial x_1}{\partial m_2}u(m_2)\right]^2} \tag{B.4}$$

Where $\frac{\partial x_1}{\partial m_1} = \frac{M_1}{m_1^2}\frac{m_2}{M_2}\left(1 + \frac{M_1}{m_1}\frac{m_2}{M_2}\right)^{-2}$ and $\frac{\partial x_1}{\partial m_2} = -\frac{M_1}{m_1}\frac{1}{M_2}\left(1 + \frac{M_1}{m_1}\frac{m_2}{M_2}\right)^{-2}$

The mole fraction and mole fraction uncertainties in molar units and as a percentage, determined by equation B.4, are listed in Table B.1. The uncertainties vary due to the compositional differences of the mixtures. Methane and propane were mixed separately with helium, whereas ethane/ethylene and propylene/acetylene (not detected) were mixed with helium. Due to these mixture variations, the general (but not strict) trend was that higher uncertainties were obtained for lower quantities of hydrocarbons mixed with helium.

Table B.1: Mole fraction uncertainties for C_1-C_3 hydrocarbons.

Component 1	x_1	**u(x_1)**	**u(x_1)**
methane	0.04048	0.00079	2.0%
ethane	0.00197	0.00008	4.1%
ethylene	0.04277	0.00009	0.2%
propane	0.02207	0.00020	0.9%
propylene	0.01437	0.00047	3.3%

The mole fraction uncertainties were incorporated into the ideal gas law for the dilute region, which is discussed in Section B.3.

B.3 GC calibration: Molar concentration uncertainties

The mole fraction and mole fraction uncertainty, u(x_1), evaluated for the dilute region (Section B.2), were incorporated into the ideal gas law in order to determine the molar concentration of each hydrocarbon species. The mole fraction for the pure gas calibration was unity; hence, the uncertainty term was neglected.

$$n_1 = x_1 \frac{PV}{RT}$$

The combined calibration uncertainty, $u_{c,calib}$ (n), encompassed the standard uncertainty contributions of the hydrocarbon correlations equations (Appendix A) and the repeatability of the calibration.

$$u_{calib}(n) = n\sqrt{\left[u_{rep}(n)\right]^2 + \left[u_{corr}(n)\right]^2}$$

As mentioned in Section B.1, errors incurred during the calibration process were assigned to the ideal gas parameters: pressure, volume, temperature and mole fraction of hydrocarbon species contained in the syringe. The combination of these contributions were encompassed in the calibration repeatability uncertainty:

$$u_{rep}(n) = n\sqrt{\left[\frac{u(P)}{P}\right]^2 + \left[\frac{u(V)}{V}\right]^2 + \left[\frac{u(T)}{T}\right]^2 + \left[\frac{u(x_1)}{x_1}\right]^2} \quad \text{(B.5)}$$

Where the pressure, volume and temperature uncertainties were evaluated using rectangular distributions.

$$u(P) = \frac{1\ kPa}{\sqrt{3}}; \quad u(V) = \frac{2\% \times V}{\sqrt{3}}; \quad u(T) = \frac{2\ K}{\sqrt{3}}$$

The calibration repeatability uncertainty determined for the pure and dilute methane, determined for an injection volume of 50 uL, are listed in Table B.2.

Table B.2: Calibration repeatability uncertainty for pure and diluted methane.

V (uL)	P (kPa)	T (ºC)	$[u(V)/V]^2$	$[u(P)/P]^2$	$[u(T)/T]^2$	$[u(x_1)/x_1]^2$	n (mols)	$u_{rep}(n)$
			Pure methane					
50	100.04	28.1	1.33E-04	3.33E-05	1.47E-05	0.00	1.997E-06	2.69E-08
40	99.94	28.0	1.33E-04	3.34E-05	1.47E-05	0.00	1.597E-06	2.15E-08
30	99.98	28.0	1.33E-04	3.33E-05	1.47E-05	0.00	1.198E-06	1.61E-08
20	100.01	28.0	1.33E-04	3.33E-05	1.47E-05	0.00	7.989E-07	1.08E-08
10	100.03	28.0	1.33E-04	3.33E-05	1.47E-05	0.00	3.995E-07	5.38E-09
			Dilute methane region					
50	99.49	27.2	1.33E-04	3.37E-05	1.48E-05	3.85E-04	8.064E-08	1.92E-09
40	99.52	27.1	1.33E-04	3.37E-05	1.48E-05	3.85E-04	6.455E-08	1.54E-09
30	99.59	27.0	1.33E-04	3.36E-05	1.48E-05	3.85E-04	4.847E-08	1.15E-09
20	99.58	27.0	1.33E-04	3.36E-05	1.48E-05	3.85E-04	3.231E-08	7.69E-10
10	99.46	27.2	1.33E-04	3.37E-05	1.48E-05	3.85E-04	1.612E-08	3.84E-10

In addition to the calibration repeatability error, the uncertainties arising from the hydrocarbon correlation equation were calculated using equation B.6.

$$u_{corr}(n) = \frac{n_{i,true}\left(\left|\frac{n_{i,true} - n_{i,calc}}{n_{i,true}}\right|_{max}\right)}{\sqrt{3}} \quad \text{(B.6)}$$

Where $n_{i,true}$ (listed in Table B.2 was calculated from the ideal gas equation) and $n_{i,calc}$ was evaluated from the hydrocarbon calibration correlations in Appendix A, which for methane was:

$$n_{i,calc} = 5.556 \times 10^{-14} \times GC\ Peak\ Area$$

The resultant calibration uncertainty, listed in Table B.3, was calculated by combining the calibration correlation uncertainty, $u_{corr}(n)$, and calibration repeatability uncertainty, $u_{rep}(n)$, for each hydrocarbon component. Both error sources provided similar contributions to the final uncertainties for ethylene, propane and propylene.

Table B.3: Final calibration uncertainty for C_1-C_3 hydrocarbons.

Hydrocarbon	**n / mols**	**$u_{corr}(n)$**	**$u_{rep}(n)$**	**u_{calib} (mols)**	**u_{calib} (%)**
methane	6.45E-08	5.83E-10	1.54E-09	1.64E-09	**2.5**
ethane	4.00E-07	1.12E-08	5.39E-09	1.24E-08	**3.1**
ethylene	5.16E-08	5.65E-10	7.03E-10	9.02E-10	**1.7**
propane	3.95E-07	9.46E-09	5.31E-09	1.08E-08	**2.7**
propylene	4.03E-07	7.42E-09	5.42E-09	9.19E-09	**2.3**

B.4 Reactor sampling: Experimental uncertainties

In addition to the GC calibration uncertainty, evaluated in Sections B.3 and B.4, the arc discharge reactor product sampling method also manufactured major sources of error.

After a reaction period of either 10 or 60 s in the arc discharge reactor, a sample was extracted via a sampling port and injected into the calibrated GC. Between 3 and 5 samples were analysed in order to improve statistical repeatability. The experimental repeatability, the major source of uncertainty in pure plasma and plasma-catalytic FTS, was determined by equation B.7.

$$u_{exp}(n) = \frac{(\sigma(n)/\overline{n})}{\sqrt{3}} \quad \text{and} \quad \sigma(n) = \sqrt{\frac{\sum(n-\bar{n})^2}{a}} \tag{B.7}$$

Where $\sigma(n)$ denotes the standard deviation, which indicates the measurement precision, $\bar{n}$ denotes the average number of moles of a hydrocarbon species, *a* represents the number of samples analysed (typically between 3 and 5). A rectangular distribution was used to convert the standard deviation to a standard uncertainty. The standard uncertainties were evaluated for each C_1-C_3 hydrocarbon component in the pure

plasma and plasma-catalytic FTS product streams for all experiments conducted in the pressure, current and inter-electrode gap variation studies.

A sample of the standard uncertainties determined for plasma-catalytic FTS using a 6 wt% Co catalyst is presented in Table B.4. These results revealed that higher standard uncertainties were observed for lower average product concentrations, depicted by $\bar{n}$ (presented in ppm and moles), as a result of the higher sensitivity of the dilute region of the GC calibration. The lowest uncertainties (< 1%) were obtained for the inter-electrode gap study and the highest uncertainties (4%) were obtained for the current study. Due to the variability of the standard uncertainty with the molar concentration, a standardized uncertainty of 4.5%, the maximum obtained, was applied in the experimental results.

Table B.4: Experimental uncertainties for plasma-catalysis using a 6 wt% Co catalyst.

Component	$\bar{n}$ /ppm	$\bar{n}$ /mols	$\sigma(n)$	$u_{rep}(n)$ / mols	$u_{rep}(n)$ / %
		Pressure variation study at 10 MPa and 10 s.			
methane	5 200	1.13E-07	1.45E-09	8.37E-10	0.7%
ethane	57	1.23E-09	2.67E-11	1.54E-11	1.3%
ethylene	4.9	1.07E-10	2.65E-12	1.53E-12	1.4%
propane	12	2.52E-10	8.53E-12	4.92E-12	1.9%
propylene	4.8	1.04E-10	2.95E-12	1.70E-12	1.6%
		Current variation study at 450 mA			
methane	1 773	3.73E-08	2.79E-09	1.61E-09	4.3%
ethane	68	1.43E-09	9.92E-11	5.73E-11	4.0%
ethylene	19	3.99E-10	2.85E-11	1.65E-11	4.1%
propane	2.3	4.92E-11	3.12E-12	1.80E-12	3.7%
propylene	3.7	7.69E-11	5.31E-12	3.07E-12	4.0%
		Inter-electrode gap study at 2 mm			
methane	22 424	4.33E-07	5.99E-09	3.46E-09	0.8%
ethane	517	9.98E-09	1.54E-10	8.91E-11	0.9%
ethylene	101	1.96E-09	3.08E-11	1.78E-11	0.9%
propane	79	1.52E-09	1.78E-11	1.03E-11	0.7%
propylene	19	3.71E-10	4.36E-12	2.52E-12	0.7%

B.5 Combined and expanded uncertainties

The standard molar uncertainties evaluated for both the GC calibration (ranging between 1.7 and 3.1% in Section B.3), and the experimental analyses (4.5% in Section B.4), were integrated to produce the combined uncertainty:

$$u_c(n) = n\sqrt{\left[u_{exp}(n)\right]^2 + [u_{calib}(n)]^2} \quad \text{(B.8)}$$

A coverage factor (k = 2) was applied to the combined uncertainty resulting in the expanded uncertainties for hydrocarbon molar concentrations (equation B.9), which was the final form reported in Chapter 6. There was level of confidence of ~95% that the error was distributed within the expanded uncertainty interval.

$$U_c(n) = \pm k u_c(n) \quad \text{(B.9)}$$

The maximum expanded uncertainties for the major hydrocarbon species are listed in Table B.5. Due to similar uncertainties being obtained for all species, a standardized expanded uncertainty of ±11% (rounded off uncertainty values) was used for all species, which were represented by vertical error bars in the hydrocarbon concentration (ppm) versus pressure, current or inter-electrode gap plots in Chapter 6.

Table B.5: Expanded uncertainties for various hydrocarbons.

Hydrocarbon	**u_c (n) / %**	**$\pm U_c$ (n) / %**
methane	5.2	±10.3
ethane	5.5	±10.9
ethylene	4.8	±9.7
propane	5.3	±10.5
propylene	5.0	±10.1

Appendix C
PRESSURE CALIBRATION

The pressure calibration curve for the WIKA S-10 high pressure transmitter (0-250 bar~25 MPa) fitted to the arc discharge reactor is presented below. The reference pressure was measured using a WIKA Mensor CPC8000 pressure controller.

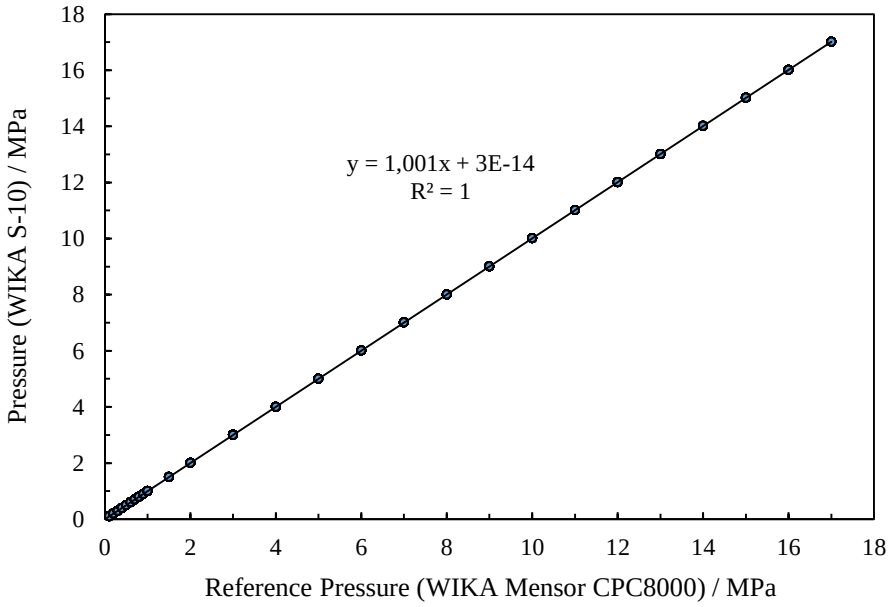

Figure C.1: Pressure calibration curve for the WIKA S-10 high pressure transmitter.

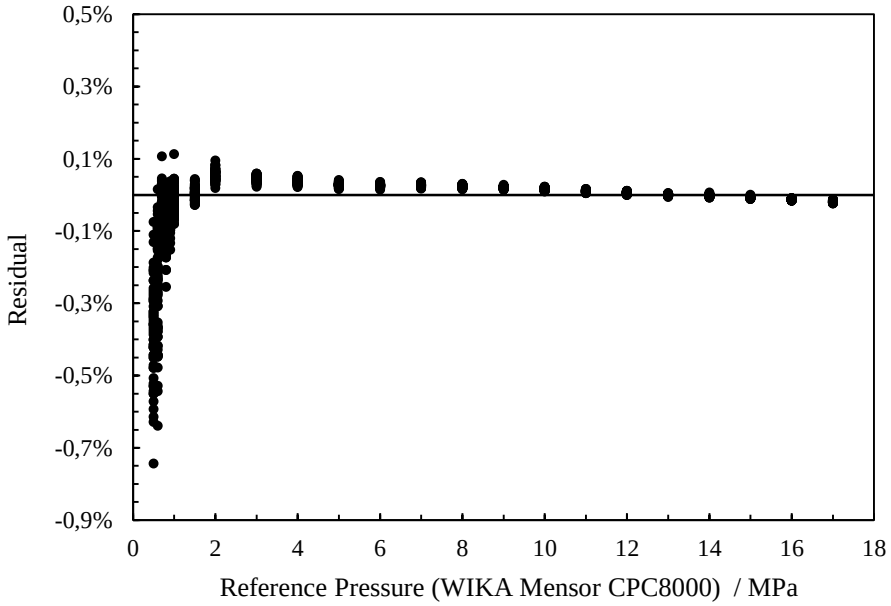

Figure C.2: Residual plot for the WIKA S-10 high pressure transmitter.

Appendix D
RMS VOLTAGE CALCULATIONS

The Visual Basic (VBA) code presented below, was used to extract up to 60 000 voltage data points from Excel spreadsheet files (recorded via a digital oscilloscope software), which were compiled in order to calculate the rms voltage according to the equations D.1.

$$V_{rms} = \sqrt{\frac{\sum_1^n (V^2)}{n}} \tag{D.1}$$

Where *V* is the voltage obtained from the oscilloscope measurements and *n* is the number of voltage data points between 10 000 and 60 000.

Visual Basic code

```
Option Explicit
   Dim wrdarray(), DateTimeArray() As String
   Dim fileDate, fileTime As String
   Dim sourceFile, sourceFolder As String
   Dim wrkBk As Workbook

Sub copyFiles()

   Dim sheetNo, sheetRow As Integer
   sheetNo = 1
   sheetRow = 2

   On Error Resume Next
   Application.ScreenUpdating = False      'Opens the folder selector dialog screen to allow user selection

   With Application.FileDialog(msoFileDialogFolderPicker)

      .Title = "Please select a folder"
      .Show
```

```
        .AllowMultiSelect = False

        If .SelectedItems.count = 0 Then        'If a folder is not selected, then abort
            MsgBox "You did not select a folder"
           Exit Sub
        End If

        sourceFolder = .SelectedItems(1) & "\"          'Assign user selected folder to SourceFolder

    End With

    sourceFile = Dir(sourceFolder)              'DIR attains the first file of the folder
                                                'Loops through all files in folder until DIR no more are found
    Do While sourceFile <> ""                   'Opens the file and assigns a variable to the workBk for future use

        Set wrkBk = Workbooks.Open(Filename:=sourceFolder & sourceFile)
        Call RootMeanSquare
        wrkBk.Close savechanges:=False
        sourceFile = Dir                        'DIR attains the next file in the folder
        sheetRow = sheetRow + 1

    Loop

Application.ScreenUpdating = True
End Sub
```

```
Sub RootMeanSquare()

    Dim j, voltColumn, currentColumn As Integer
    Dim count As Double   'no. of points in each sheet
    Dim k As Long
    Dim V2Sum, I2Sum As Double
    Dim V2, I2 As Double
    Dim voltDot, currentDot As String
    Dim voltComma, currentComma As String
    Dim Mean As Single
```

```
Dim printSheet As String
Dim sheetnum As Integer
Dim printFileName, printCount, printV2, printI2 As Integer

printSheet = "MAIN" ' sheet for outputing of rms data
printFileName = 1
printCount = 4
printV2 = 5
printI2 = 6
voltColumn = 1
currentColumn = 2
j = 0
k = 0
count = 0
V2Sum = 0
I2Sum = 0
sheetnum = 1

With ThisWorkbook.Sheets(printSheet)

    Do          'Find first voltage value
       j = j + 1
    Loop Until wrkBk.Sheets(sheetnum).Cells(j, voltColumn) = "Ch1 V"

       k = j + 1          'Row Index of cell containing the first voltage

    Do While IsEmpty(wrkBk.Sheets(sheetnum).Cells(k, voltColumn)) = False

       'Sum of Squares: Voltage
       V2 = ((wrkBk.Sheets(sheetnum).Cells(k, voltColumn).Value) * -1000) ^ 2
     'Convert from mV to V
       V2Sum = V2Sum + V2

       'Sum of Squares: Current
       I2 = ((wrkBk.Sheets(sheetnum).Cells(k, currentColumn).Value) * 10) ^ 2
     'Convert from V to A. Conversion -- (V)*(A/100mV)*(1000mV/V)
```

```
            I2Sum = I2Sum + I2

            k = k + 1
            count = count + 1
          Loop

        .Cells(printRow, printFileName).Value = sourceFile

         Call SplitDateTime


         Cells(printRow, printCount).Value = count
         Cells(printRow, printV2).Value = V2Sum
        . Cells(printRow, printI2).Value = I2Sum

        j = 0
        k = 0
        count = 0
        V2Sum = 0
        I2Sum = 0

    End With
End Sub
```

```
Function printRow() As Integer

    With ThisWorkbook.Sheets("MAIN")
    Dim rows As Integer
    rows = 6

       Do Until .Cells(rows, 6) = ""              ' Search last column of current row
          rows = rows + 1
       Loop

    printRow = rows
```

```
    End With
End Function
```

```
Function FileDateAndTime()        ' Get last modified date and time of file

    FileDateAndTime = FileDateTime(ActiveWorkbook.FullName)

End Function
```

```
Function SplitDateTime()
    Dim n As Integer
    Dim printDate, printTime As Integer
    Dim column As Integer

    printDate = 2
    printTime = 3

    DateTimeArray() = Split(FileDateAndTime)

    ThisWorkbook.Sheets(1).Cells(printRow, printDate).Value = DateTimeArray(0)  'Output modified file date
    ThisWorkbook.Sheets(1).Cells(printRow, printTime).Value = DateTimeArray(1)  'Output modified file time

 End Function
```

Appendix E
CARBON NANOTUBE SYNTHESIS

Carbon nanotubes (CNTs) were synthesized during Fischer-Tropsch synthesis (FTS) experiments in this work. Therefore, a brief discussion of the common synthesis methods are discussed in this section. CNTs consist of sp^2 bonded carbon atoms (stronger than sp^3 bonds found in diamonds) with each carbon bonded to three others as in graphite [235]. CNTs have been synthesised in the literature by either physical methods such as arc discharge and laser-ablation or by chemical methods such as thermal chemical vapour deposition (CVD), plasma enhanced chemical vapour deposition (PECVD) or by aerosol synthesis [236].

E.1 Arc discharge method

CNT formation using a DC arc discharge involves ignition of an arc between two graphite electrodes with diameters in the range of 6 to 12 mm, contained in a discharge chamber usually filled with helium or in some studies methane or hydrogen. In this process, CNTs are formed by the consumption of the graphite electrodes. A multi-walled CNT (MWCNT) is formed without using a catalyst, whereas a single-walled CNT (SWCNT), requires a catalyst such as Ni, Fe, Co, etc. SWCNTs formed using an arc discharge combined with several catalysts, including cobalt, were reported to have diameters between 1 to 3 nm [237]. However, the arc discharge (> 1400^{o}C) and laser-ablation methods have been replaced by lower temperature (< 800^{o}C) CVD, which allows precise control of the purity, physical and dimensional properties of the CNT [237]. Although an arc discharge is in operation in this work, tungsten electrodes are used, thus indigenous graphite is not present as the CNT precursor. In addition, low currents (I < 1 A) are used here compared to required currents above 10 A. In regards to the aerosol synthesis, catalyst particles are produced in-situ during CNT formation [236], which is not applicable to this work.

E.2 Chemical vapour deposition (CVD)

The conditions for CNT synthesis in this work are similar to those in CVD and PECVD processes. Therefore, the conditions for CVD are briefly described. CVD typically involves the decomposition of a hydrocarbon gas in the presence of a supported metal catalyst at high temperatures between 600 and 1200^{o}C and pressures ranging from sub-atmospheric to more recently investigated atmospheric environments, which promote the growth of the CNT on the metal surface [220, 237]. Cobalt, iron and nickel are typically used for CNT synthesis by CVD as these metals offer high carbon solubility at high temperatures and high diffusion rate of carbon [220]. In addition, they possess high melting temperatures and low equilibrium-

vapour pressures, which provide a large temperature range for a wide range of carbon precursors to participate in CVD [220]. Moisala et al. [236] reviewed several works using these catalysts to produce CNTs.

The general outline for CNT growth via CVD (still being deliberated by the CNT community) is as follows; (a) hydrocarbon vapors contact the heated nano-sized metal particle, (b) carbon dissolves into the metal while hydrogen is released, (c) when the carbon-solubility limit is reached at the operating temperature, the dissolved carbon precipitates and crystallizes in the form of a tubular structure, which has no detached bonds and is stable [220]. There are two types of growth mechanisms, tip-growth model and base-growth model, which are governed by the catalyst metal-support interaction. A weak catalyst-support interaction leads to the diffused-CNT precipitating from below the metal particle and pushing it off the support as shown in Figure E.1. The CNT continues to grow from the metal towards the support (tip-growth model) until the metal is encapsulated with carbon rendering the metal inactive. In contrast, when the catalyst-support interactions are strong the CNT cannot push the metal particle off the support causing the CNT to precipitate from the apex of the metal in the form of a graphitic cylinder [220], with growth continuing from the metal upwards (base-growth model).

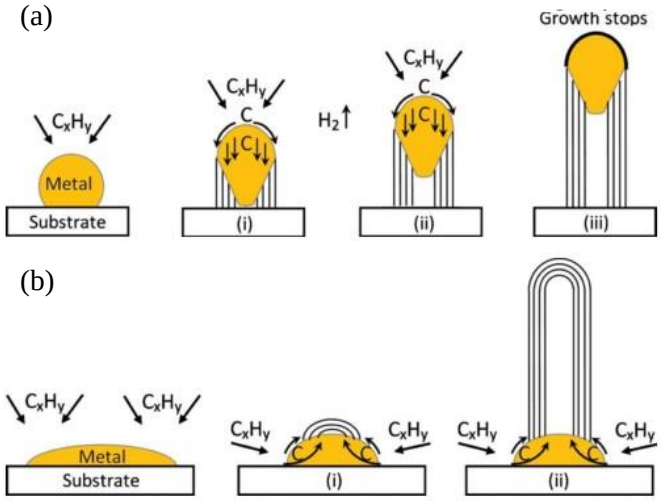

Figure E.1: Growth mechanisms for CNTs;
(a) tip-growth model, (b) base-growth model (extracted from [220]).

E.3 CNTs as catalyst supports in FTS

CNTs are not usually formed under conventional FTS condition, However, from 2002 [238] several papers have been published on the use of CNTs as a support for FTS catalysts [239-248]. CNTs have been utilized as a support due to their high purity, electrical conductivity, mechanical strength, the absence of

microporosity (eradicating diffusion effects and intra-particle mass transfer), the ability to tune the metal-support interactions [249], control of metal dispersion due to easy surface functionalization [250] and the flexibility to deposit the active metal within the tubes or on the outer surface [251, 252].